EPFL

Thèse n° 10 462

The role of secondary ice production in mixed-phase clouds

Présentée le 1er décembre 2023

Faculté de l'environnement naturel, architectural et construit
Laboratoire des processus atmosphériques et leurs impacts
Programme doctoral en génie civil et environnement

pour l'obtention du grade de Docteur ès Sciences

par

Paraskevi GEORGAKAKI

Acceptée sur proposition du jury

Prof. G. Manoli, président du jury
Prof. A. Nenes, directeur de thèse
Prof. A. Ekman, rapporteuse
Prof. C. Hoose, rapporteuse
Dr J. Grazioli, rapporteur

École polytechnique fédérale de Lausanne

2023

“Don’t forget: beautiful sunsets need cloudy skies.”

– Paulo Coelho

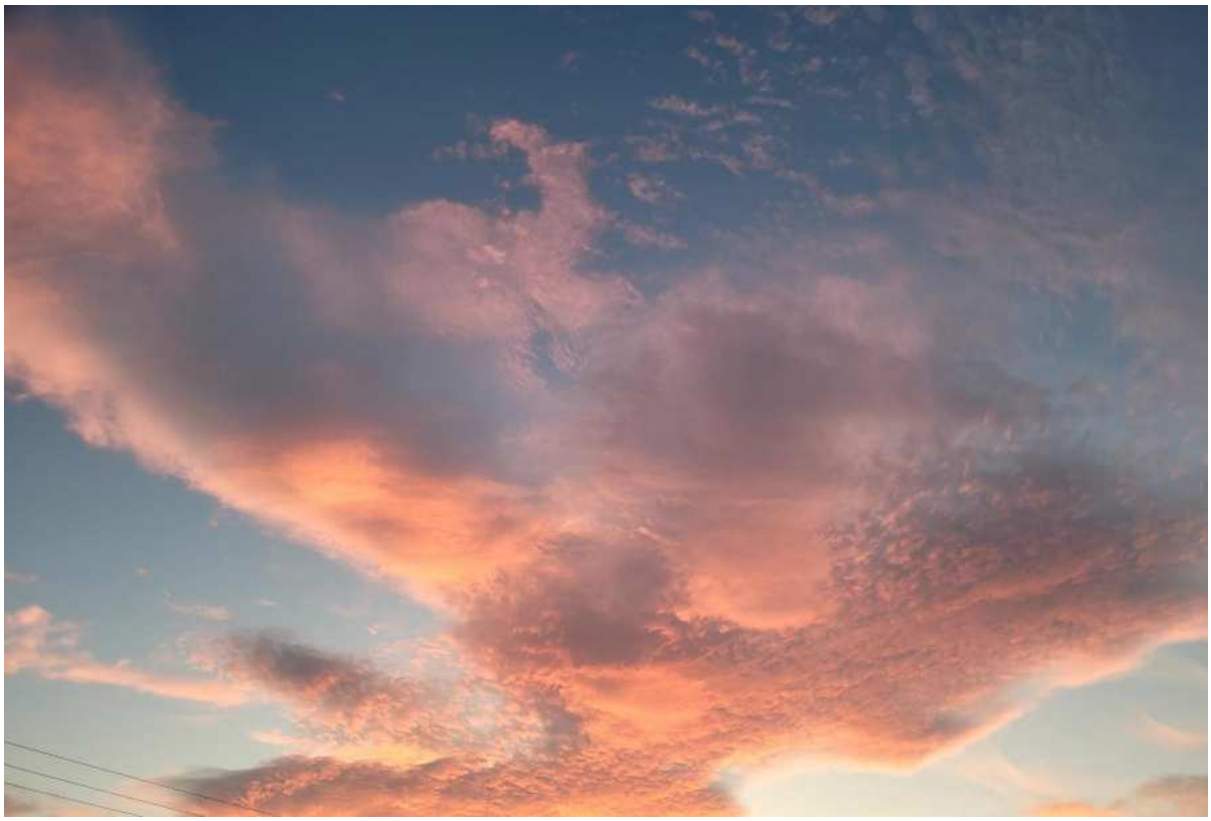

Devoted to our forever young – Angelos

Στον Αγγελούκο μας

Acknowledgments

This PhD thesis marks the conclusion of a remarkable 4-year journey, filled with adventures and joyful experiences that will forever hold a special place in my heart. As I reflect on this journey, I am deeply grateful for the collaboration, shared laughter, and support from the remarkable individuals who have been an integral part of this transformative experience.

First, I would like to sincerely thank my advisor, **Prof. Athanasios Nenes**, for giving me the opportunity to pursue this exciting PhD research in the laboratory of atmospheric processes and their impacts (LAPI). His encouragement allowed me the freedom to explore diverse research avenues aligned with my interests, fostering both personal and academic growth. I am thankful for the numerous scientific discussions and brainstorming that have been instrumental in shaping the trajectory of this thesis.

I extend my gratitude to the members of my thesis jury, **Prof. Annica Ekman**, **Prof. Corinna Hoose**, **Dr. Jacopo Grazioli** and **Prof. Gabriele Manoli** for reviewing this work and for infusing their passion for cloud microphysics into my private defense bringing forth insightful discussions and invaluable perspectives.

I am also grateful to **Prof. Georgia Sotiropoulou** for introducing me to the exciting world of ice microphysics, engaging in countless scientific and non-scientific discussions, and consistently offering her assistance while encouraging me to find my own solutions. I will always cherish the moments of coding, debugging, and, of course, the fun we had together.

I greatly appreciated being part of the **FORCeS** project, which gave me the chance to collaborate with brilliant scientists, increasing the visibility and impact of my PhD research. Special credits to the members of the model intercomparison project, **Montse**, **Georgia**, **Luisa**, **Hannah**, **María** and **Ulrike**, whose collaborative modeling efforts and positive attitude transformed the implementation of the new ice multiplication parameterization into an enjoyable task. Many thanks also to **Alexandros** and **Iris** for the unforgettable memories during our annual meetings.

I would also like to thank the Profs. **Spyros Pandis** and **Maria Kanakidou** along with all members of the **C-STACC** group and the **ECPL** lab. Their expertise seamlessly blended with that of our LAPI lab, contributing to the success of our weekly joint seminars and fostering engaging discussions among scientists passionate about atmospheric chemistry and physics.

This PhD thesis would never be as it is without all the fantastic bunch of people who made up the LAPI team, shaping the spirit of our lab with the motto “Don't worry, be LAPI”. Despite varying scientific backgrounds and interests that sometimes limited our research conversations, I am profoundly thankful and inspired by each LAPI member for their motivation, intelligence, and kindness. My heartfelt thanks go out to **Kalliopi**, who generously shared her experience, offered valuable advice, and kept my Cretan dialect alive; **Nikunj** for his unique perspective and for ruling the dance floor with us; **Roy** for his positivity and modesty, for being the best seminar guru and for being a source of inspiration to all of us; **Andrea** for his scientific enthusiasm and calm strength; **Kunfeng** for his generosity and

the warmth he brought to our hearts with his fine gastronomical creations; **Maria** who inspired me with her dedication and persistence; **Satoshi** and **Alexandros** for sharing their passion for science; **Marcela**, for her continuous assistance and for adding vibrant colors to our WhatsApp group; **Sandra**, for her invaluable support at the beginning of my PhD, which greatly aided my adjustment to the Swiss life; **Virginia** for the shared laughter and for reminding me of my early-PhD self; **Romanos** for evoking happy memories from our bachelor's and master's years; my top modelers **Giannis** and **Eemeli** for the drinks that accompanied our secondary ice discussions and coding endeavors; **Eliot**, for kindly encouraging me to express my research ideas in simpler words; **Ali**, for his amazing motivation during his summer internship; and our new members **Berkay** and **Zohreh**, for their eagerness for what lies ahead. I saved a special thanks for my office mates, the "VGL crew", for bringing a touch of craziness to our shared space, making my PhD journey a little bit more colorful. Thanks to **Ghislain** for never losing his hope to motivate me with outdoor activities, adding a unique rhythm into our workdays with his imaginary drums, and always contributing a positive atmosphere to our VGL office. Thanks also to my partner in crime, **Lucile**, for her motivation (and patience) in teaching me French, for serving as LAPI's pastry chef, for being the most welcoming hostess at our parties, and for being my travel buddy through these years and beyond. I've found a lifelong friend. The moments we've all shared, from our picnics to after-work outings, will forever bring a smile to my face.

I extend my gratitude to the next-door lab, LTE, for bringing joy and laughter in our lovely GR corridor. Special thanks to **Prof. Alexis Berne**, whose door was always open for discussions, offering his invaluable insights and support. During the early stages of my PhD, I was fortunate to have **Dr. Étienne Vignon** as a neighbor, generously sharing his advice and WRF expertise, which laid the foundation for my research. Thanks to **Adrien**, **Gionata**, **Monika**, **Rebecca** and **Alfonso** for always bringing their smile to our coffee and lunch breaks. A special mention goes to my beloved **Anne-Claire**, who has been a bright and constant companion from the first classes of our PhD journey until our defenses, and I'm looking forward to all the joyful moments that await.

There wasn't much time left to reconnect with my childhood friends, **Maria**, **Vaso**, **Manos**, and **Nafsika**, but I owe them a big thanks for the wonderful moments we've shared since our youth. Saying goodbye to them was always difficult, and I find myself eagerly counting the days until our next reunion. I would also like to thank my friends **Valia, Christoforos, Andreas** and **Markos**, for all the memories we've shared since our undergraduate years in Heraklion. I am also grateful to have met two incredible individuals during my master's, **Christianna**, with whom an instant and enduring bond was formed, and **Cheng**, who has shared in some of the most memorable moments during my ERASMUS internship in Stockholm. Despite being scattered across the globe, you've always been a part of my life as we've been supporting each other me from afar.

In closing, I would like to convey my love and appreciation to my **family** for their continuous encouragement and for bearing with my intrinsic need to talk about what are fluffy clouds made of. Special credits go to my aunt, **Stella**, whose curious nature sparked the investigation of Storm Carmel, later evolving into a research paper during my PhD. I also want to express my admiration for my **grandparents**, who have efficiently embraced technology, bridging the physical distance that separates us. A profound thank you goes to my **parents**, Giannis and Georgia, for instilling in me the courage to pursue my unique path and for their unconditional love and support in all my endeavors despite the difficulties. You've truly been my rock. Of course, I consider myself truly blessed to have my **sister**, Maria, whose strength and enigmatic nature has always been a powerful source of inspiration for me. Thank you for believing in me and for always having my back.

Last but certainly not least, my deepest love and gratefulness are reserved for **Nikos**, for the immeasurable help throughout all those years of our shared journey. Thanks for making my life brighter and for being my anchor, my source of encouragement, a shoulder to lean on through the most difficult times and a genuine source of joy during times of success. Your patience and support means the world to me!

Bussigny, November, 2023 Vivi Georgakaki

Abstract

Clouds are omnipresent in the Earth's atmosphere. Their phase composition significantly modulates their interaction with solar and terrestrial radiation, as well as precipitation formation. Particularly for clouds containing both phases, known as mixed-phase clouds, a thorough understanding of the processes governing the distribution of both liquid water and ice is imperative for their accurate representation in models, which is achieved through empirical parameterizations. Compared to liquid-phase processes, mechanisms related to ice formation have been notably understudied, with most weather prediction and global climate models still lacking descriptions of critical ice multiplication processes, capable of efficiently amplifying ice crystal concentrations at relatively warm subzero temperatures.

This PhD thesis aims to investigate microphysical processes that play a crucial role in determining the ice- and liquid-phase partitioning of mixed-phase clouds. We first demonstrated the ability to accurately predict cloud droplet numbers in orographic mixed-phase clouds using cloud parcel theory, along with in-situ aerosol measurements and remotely-sensed updraft velocities. Additionally, we established a relationship that could potentially be applied to decipher cloud droplet formation regimes in virtually any type of non-precipitating boundary-layer clouds.

With a primary focus on the overlooked ice-related processes, we updated the microphysics scheme of a widely-used numerical weather prediction model, to account for previously neglected ice multiplication processes. We found that the combined effect of crystal fragmentation due to collisions with seeding ice particles from above the cloud, and to a lesser extent those lofted from the snow-covered surface, significantly increased modeled ice crystal concentrations, aligning them with in-situ observations of low-level orographic clouds. These findings were further corroborated through comparisons with ground-based radar measurements in a mountainous region, underscoring the need for models to incorporate additional secondary ice processes for accurate simulations of the amount of snowfall on the ground. By coupling the model with a radar simulator, we further proposed an interpretation of complex radar signatures linked to distinct ice growth and multiplication processes.

Lastly, we introduced a novel framework to represent the impact of ice multiplication in polar stratiform mixed-phase clouds, identified as the most radiatively important cloud type. This framework, developed by applying machine learning techniques to regional climate simulations, demands fewer inputs for predicting ice multiplication, making integration into large-scale models more straightforward compared to conventional secondary ice schemes.

In summary, this thesis advances our understanding of microphysical processes in mixed-phase clouds from various perspectives, characterizing the droplet formation regime and identifying conditions favoring secondary ice production in polar and orographic clouds, inferring potential signatures of ice growth and multiplication from radar observations, and introducing a novel methodological tool to parameterize its impact in large-scale models. These outputs open new avenues for microphysical process descriptions in global climate models, with expected improvements in predicting precipitation patterns and the radiative properties of mixed-phase clouds on a global scale.

Résumé

Les nuages sont omniprésents dans l'atmosphère terrestre. Leur composition en phases modifie considérablement leurs interactions avec le rayonnement solaire et terrestre, ainsi que la formation des précipitations. En particulier, pour les nuages contenant les deux phases, appelés nuages mixtes, une compréhension approfondie des processus régissant la répartition de l'eau liquide et de la glace est impérative pour leur représentation précise dans les modèles, qui est obtenue par des paramétrisations empiriques. Comparativement aux processus en phase liquide, les mécanismes liés à la formation de la glace ont été largement sous-étudiés, la plupart des modèles de prévision météorologique et de climatologie mondiale manquant encore de descriptions des processus critiques de multiplication de la glace, capables d'amplifier efficacement les concentrations de cristaux de glace même à des températures sous zero relativement douces.

Cette thèse de doctorat vise à étudier les processus microphysiques qui jouent un rôle crucial dans la détermination de la répartition des phases de glace et de liquide dans les nuages mixtes. Nous avons d'abord démontré la capacité de prédire avec précision les nombres de gouttelettes de nuage dans les nuages mixtes orographiques en utilisant la théorie des paquets de nuages, ainsi que des mesures in situ des aérosols et des vitesses de courant ascendant détectées à distance. De plus, nous avons établi une relation qui pourrait potentiellement être appliquée pour décrypter les régimes de formation des gouttelettes de nuage dans pratiquement n'importe quel type de nuage de couche limite sans précipitations.

Avec un accent particulier sur les processus liés à la glace, largement sous-étudiés, nous avons mis à jour le schéma de microphysique d'un modèle de prévision météorologique numérique largement utilisé pour tenir compte des processus de multiplication de la glace précédemment négligés. Nous avons constaté que l'effet combiné de la fragmentation des cristaux due aux collisions avec des particules de glace ensemencées depuis le dessus du nuage, et dans une moindre mesure celles soulevées depuis la surface couverte de neige, a considérablement augmenté les concentrations de cristaux de glace modélisées, les alignant avec les observations in situ des nuages orographiques de bas niveau. Ces conclusions ont été corroborées par des comparaisons avec des mesures radar au sol dans une région montagneuse, soulignant la nécessité pour les modèles d'incorporer des processus de glace secondaire supplémentaires pour des simulations précises de la quantité de neige au sol. En couplant le modèle avec un simulateur radar, nous avons en outre proposé une interprétation des signatures radar complexes liées à des processus distincts de croissance et de multiplication de la glace.

Enfin, nous avons introduit un nouveau cadre pour représenter l'effet de la multiplication de la glace dans les nuages mixtes stratiformes polaires, identifiés comme le type de nuage dont l’impact radiatif est le plus important. Ce cadre, utilisant des techniques d'apprentissage automatique appliquées à des simulations climatiques régionales, demande moins d'entrées pour prédire les contributions de multiplication de la glace, facilitant l'intégration dans les modèles à grande échelle par rapport aux schémas de glace secondaire conventionnels.

En résumé, cette thèse améliore notre compréhension des processus microphysiques dans les nuages mixtes sous différentes approches, notamment la caractérisation du régime de

formation des gouttelettes et l'identification des conditions favorables à la production de glace secondaire dans les nuages polaires et orographiques, l'inférence de signatures potentielles de croissance et de multiplication de la glace à partir d'observations radar, et l'introduction d'un nouvel outil méthodologique pour paramétrer son impact dans les modèles à grande échelle. Ces résultats ouvrent de nouvelles perspectives pour les descriptions des processus microphysiques dans les modèles climatiques mondiaux, avec des améliorations attendues dans la prédiction des schémas de précipitations et des propriétés radiatives des nuages mixtes à l'échelle mondiale.

Contents

List of acronyms

The table below presents the most important acronyms utilized within this thesis.

Acronyms	Description
2D-S	2-dimensional stereo probe
3V-CPI	3-view cloud particle imager
AGL	Above ground level
AML/AMSL	Above mean sea level
ARW	Advanced research WRF
BB	Biomass burning
BIPS	Blowing snow ice particles
BL	Boundary layer
BR	Ice-ice collisional break-up
CALISHTO	Cloud-AerosoL InteractionS in the Helmos background TropOsphere
CCN	Cloud condensation nuclei
CDP	Cloud droplet probe
CFSTGC	Single-column continuous-flow streamwise thermal gradient chamber
CLACE	Cloud and Aerosol Characterization Experiment
CMIP6	Coupled Model Intercomparison Project phase 6
CRF	Cloud radiative forcing
CR-SIM	Cloud Resolving Model Radar Simulator
DGL	Dendritic growth layer
DMT	Droplet Measurement Technologies
DNS	Direct Numerical Simulation
DS	Droplet shattering during freezing
ECMWF	European Centre for Medium Range Weather Forecasts
ERA5	Fifth generation of the ECMWF atmospheric reanalyses dataset
FMCW	Frequency-modulated continuous wave
FT	Free troposphere
ICNC	Ice crystal number concentration
INP	Ice nucleating particle
GCMs	Global Climate Models
GFS	Global Forecasting System
HAC	Helmos Hellenic Atmospheric Aerosol and Climate Change
HM	Hallett-Mossop process
IEF/IMF	Ice enhancement/multiplication factor
IoA	Index of agreement
JFJ	Jungfraujoch
LES	Large Eddy Simulation
LW	Longwave

M05	Microphysics scheme of Morrison et al. (2005)
ML	Machine learning
MODIS	Moderate Resolution Imaging Spectroradiometer
MPC	Mixed-phase cloud
MSE	Mean Squared Error
MYJ	Mellor–Yamada–Janjic
MYNN	Mellor-Yamada-Nakanishi-Niino
NCEP	National Centers for Environmental Protection
NN	Neural network
NPF	New particle formation
NWP	Numerical weather prediction
OPC	Optical Particle Counter
PBL	planetary boundary layer
PDF	Probability density functions
PINE	Portable Ice Nucleation Experiment
PIP	Primary ice production
PSD	Particle size distribution
PVM-100	Particulate Volume Monitor
RACLETS	Role of Aerosols and Clouds Enhanced by Topography on Snow
RaFSIP	Random Forest Secondary Ice Production
RF	Random forest
RFR	Random Forest Regressor
RMSE	Root mean square error
RRTMG	Rapid Radiative Transfer Model for General Circulation Models
SEA	Southeast Atlantic
SEUS	Southeast United States
SIP	Secondary ice production
SLW	Supercooled liquid water
SMPS	Scanning mobility particle sizers
SUBBR	Sublimational break-up
SW	Shortwave
VL	Vathia Lakka
WBF	Wegener–Bergeron–Findeisen
WFJ	Weissfluhjoch
WOP	Wolfgang Pass
WProf	W-band profiler
WRF	Weather Research and Forecasting model

List of symbols

The table below presents the most important symbols utilized within this thesis, along with their corresponding units.

Symbol	Units	Description
ε_{org}	[-]	equivalent organic mass fraction
κ	[-]	Hygroscopicity parameter
λ	[m^{-1}]	Slope parameter of the gamma distribution
μ	[-]	Spectral index of the gamma distribution
N_0	[kg^{-1} m^{-1}]	Intercept of gamma distribition
ρ_h	[kg m^{-3}]	Hydrometeor bulk density
d_{aer}	[µm]	Aerodynamic diameter
d_{opc}	[µm]	Optical particle counter diameter
D_r	[µm]	Freezing droplet diameter
ICWC	[kg m^{-2}]	Integrated condensed water content
IWC	[g m^{-3}]	Ice water content
K_0	[J]	Initial kinetic energy
LWC	[g m^{-3}]	Liquid water content
LWP	[g m^{-2}]	Liquid water path
MDV	[m s^{-1}]	Mean Doppler velocity
N_{aer}	[cm^{-3}]	Total aerosol number concentration
$n_{aer,0.5}$	[scm^{-3}]	Number concentration of aerosols with sizes larger than 0.5 µm aerodynamic diameter
N_B	[-]	Number of big secondary ice fragments per frozen drop
NBIPS	[L^{-1}]	Number concentrations of blowing snow ice particles
N_{BR}	[-]	Number of secondary ice fragments per collision
N_d	[cm^{-3}]	cloud droplet number
N_{DS} *or* N_T	[-]	Number of tiny ice splinters per frozen drop
N_g	[L^{-1}]	Number concentration of graupel particles
N_i	[L^{-1}]	Number concentration of cloud ice particles
N_{isg}	[L^{-1}]	Total ice crystal concentrations (cloud ice + snow + graupel)
N_s	[L^{-1}]	Number concentration of snow particles
N_{SUBBR}	[-]	Number of secondary ice fragments generated after sublimational break-up
p_{fr}	[-]	Freezing probability
p_{sh}	[-]	Shattering probability

r_{eff}	[µm]	Droplet effective radius
RH_i	[%]	Relative humidity with respect to ice
S_{cr}	[%]	Critical supersaturation
S_{max}	[%]	Maximum in-cloud supersaturation
SS	[%]	Supersaturation level
TWC	[g m^{-3}]	Total water content
Ze_w	[dBZ] or [$mm^6 m^{-3}$]	W-band equivalent radar reflectivity factor

1. Introduction

1.1 Motivations

Predicting the Earth's surface temperature response following a doubling of atmospheric carbon dioxide – a parameter termed climate sensitivity – ranks among the greatest challenges faced by the atmospheric modeling community (Gettelman et al., 2019; Zelinka et al., 2022). Accurate responses to this question involve addressing a primary source of uncertainty in future climate projections: clouds. In a warming climate, cloud patterns and composition undergo gradual shifts that can either amplify or mitigate global warming, giving rise to the so-called *cloud-phase feedback* (Murray et al., 2021). The latest generation of Global Climate Models (GCMs) participating in the recent Coupled Model Intercomparison Project phase 6 (CMIP6) has demonstrated increased climate sensitivity compared to their predecessors. This increase is primarily attributed to the refined representation of middle- to high-latitude mixed-phase clouds (MPCs; Bodas-Salcedo et al., 2019; Ceppi & Nowack, 2021; Zelinka et al., 2020). This underscores the critical importance of accurately representing these clouds in GCMs to reduce inter-model discrepancies in climate predictions.

Accurate representation of MPCs in models requires a precise description of the mechanisms governing their liquid- and ice-phase partitioning. The processes driving cloud and precipitation formation and evolution span scales from sub-micron to centimeters. This poses significant challenges in their model depiction, considering that numerical weather prediction (NWP) models and GCMs typically project atmospheric processes onto horizontal grid spacings that range from a few kilometers to approximately 100 kilometers. Interaction between processes occurring at finer scales than the spatial grid resolution – termed subgrid-scale microphysical processes – and resolved model scales occurs solely through parameterizations, which are tuned to enhance agreement with theoretical principles or observations (Hourdin et al., 2017).

Recognizing the significance of microphysical processes, the cloud modeling community has progressively advanced cloud microphysical schemes with increasing sophistication (e.g., Morrison et al., 2005; Seifert & Beheng, 2006). Yet, ice formation remains among the most poorly understood and parameterized microphysical processes. This limitation introduces persistent radiative model biases, particularly over climatologically-sensitive high-latitude regions where MPCs are abundant (Shaw et al., 2022; Sledd & L'Ecuyer, 2021; Tan & Storelvmo, 2019). Given that the majority of global precipitation, especially in midlatitudes, originates in the ice phase (Heymsfield et al., 2020; Mülmenstädt et al., 2015), the imperative for intensifying collaborative efforts in refining modeling of ice-related processes is further underscored.

An unresolved scientific enigma revolves around ice crystal number concentrations (ICNCs) within MPCs. Typically, ICNCs in surface-decoupled MPCs lacking seeding from higher-level clouds are expected to align with the number of pre-existing ice nucleating particles (INPs), as the latter are required to facilitate ice nucleation within the mixed-phase temperature regime (Hoose & Möhler, 2012; Murray et al., 2012). However, a body of airborne studies investigating cloud microstructure has yielded evidence indicating that INPs can be orders of magnitude less abundant than ICNCs (Järvinen et al., 2022; Korolev et al., 2022).

This disparity highlights the existence of additional microphysical processes capable of amplifying ICNCs in MPCs without necessitating further INP action. These processes, known as secondary ice production (SIP) or ice multiplication, were studied in laboratory settings during the late 1950s to the 1970s, leading to the proposition of six possible mechanisms (Field et al., 2017; Korolev & Leisner, 2020). However, only three of these mechanisms – rime splintering, also known as the Hallett-Mossop process (HM), ice-ice collisional break-up (BR), and droplet shattering during freezing (DS) – have been observed in real atmospheric conditions (Järvinen et al., 2022; Korolev et al., 2020; Pasquier et al., 2022). Nevertheless, the relative contributions and precise physics of the proposed SIP mechanisms have remained persistently uncertain. This PhD thesis addresses this research gap, aiming to advance our comprehension of SIP processes in MPCs.

From the modeling perspective, more sophisticated expressions have recently emerged to represent the frequently-acknowledged SIP processes, amalgamating prior experimental observations (Deshmukh et al., 2022; Phillips et al., 2017a; Phillips et al., 2018). However, despite growing recognition of the significance of SIP through experimental, in-situ, remote sensing, and modeling studies (Field et al., 2017), most GCMs and NWP models still rely on simplistic parameterizations solely for the HM process. As a result, these models lack a potentially critical source of ice particles, which has implications for simulated cloud radiative impacts and precipitation patterns (e.g., Vergara-Temprado et al., 2018). A number of promising modeling efforts have aimed to incorporate parameterizations for additional SIP mechanisms, with the majority of them confined to single case studies with limited horizontal and temporal scales (e.g., Karalis et al., 2022; Sotiropoulou, Vignon, et al., 2021; Waman et al., 2022), while only one examines the global importance of SIP (Zhao & Liu, 2021). All modeling efforts consistently confirm substantial ICNC elevation due to SIP mechanisms in stratiform, frontal, multilayer, cumulus, orographic, and deep convective clouds (Hoose, 2022).

When parameterizing new processes, modelers must strike a balance between model complexity and computational efficiency. This balance is particularly pertinent to microphysical processes, which demand handling a large amount of information in simulations (Morrison et al., 2020). Incorporating SIP in large-scale models comes with the need to make certain assumptions, as it involves describing numerous empirical parameters not explicitly resolved within their microphysics scheme. As the complexity of GCMs increases, their results may become less interpretable, emphasizing the importance of model simplification (Proske et al., 2022, 2023). In the era of big data, physics-guided machine learning (ML) algorithms offer a promising avenue for simplifying models and elucidating processes within GCMs (e.g., Beucler et al., 2021).

This PhD thesis aims to tackle the mentioned challenges through a cascade of approaches. It focuses on two important types of MPCs: orographic clouds, which play a pivotal role in the hydrological cycle, and Arctic clouds, strongly associated with enhanced surface warming – a phenomenon known as Arctic Amplification. Relying primarily on cloud modeling and machine learning techniques, evaluated against in-situ and ground-based remote sensing observations, this PhD research aims to enhance the comprehension of droplet formation and ice multiplication within MPCs.

1.2 Microphysical processes in mixed-phase clouds

At temperatures between 0 and -38˚C, although the solid phase of water is thermodynamically favored, liquid cloud droplets do not freeze spontaneously in the atmosphere. Indeed, at temperatures below freezing cloud droplets persist in a metastable state known as supercooling. Within this temperature range, supercooled droplets can coexist with heterogeneously frozen ice crystals (Section 1.2.2) within the same cloud volume, resulting in the formation of mixed-phase cloud conditions. This chapter will explore the complex microphysical processes that take place in this context, forming the main focus of this PhD research.

Mixed-phase conditions can arise within various cloud types, such as wave, frontal, convective, and stratiform clouds, under a range of meteorological conditions. The lower saturation vapor pressure over ice compared to supercooled liquid water renders the mixture of ice and liquid thermodynamically unstable (Section 1.2.3), resulting in rapid glaciation (e.g. Korolev et al., 2017). However, a substantial body of literature has documented their unexpected persistence in diverse locations, spanning from the tropics (e.g., Lawson et al., 2015; Riihimaki et al., 2012) to higher latitudes and the poles (e.g., D'Alessandro et al., 2023; Shupe et al., 2011; Xi et al., 2022). Mixed-phase conditions are also frequently observed in orographic clouds forming over mountainous terrain, like the Swiss Alps. A complex interplay involving cloud microphysics, large-scale moisture advection, radiative cooling and turbulent fluxes is critical in sustaining liquid droplets below freezing temperatures in Arctic clouds (Morrison et al., 2012). In contrast, orographic clouds rely more prominently on orographically-induced updraft velocities to maintain liquid-phase supersaturation, thereby enabling the simultaneous growth of liquid and ice condensate (Lohmann et al., 2016).

1.2.1 Cloud droplet formation and susceptibility to aerosol or dynamical forcing

The formation of cloud droplets in the atmosphere requires the presence of soluble or hydrophilic aerosol particles, such as sea salt or sulfate. This subset of the aerosol particles, termed cloud condensation nuclei (CCN), can undergo hygroscopic growth into aqueous droplets, triggering cloud droplet activation once a critical supersaturation level is attained. The key factors driving CCN activation encompass their number, size, chemical composition reflected in the hygroscopicity parameter (κ), and the occurrence of updrafts inducing supersaturated conditions at the cloud base.

Plotting the number of cloud droplets against the total aerosol concentration usually demonstrates an increasing trend, indicating that cloud droplet formation is primarily influenced by aerosol availability. This regime of droplet formation is termed "aerosol-limited". As the droplet number increases, the fierce competition for available water vapor molecules depletes cloud supersaturation, preventing the activation of additional cloud droplets. When cloud supersaturation drops below approximately 0.1% (e.g., Kacarab et al., 2020), droplet formation becomes insensitive to aerosol changes, transitioning into a new regime driven entirely by fluctuations in vertical velocity. This is known as the "velocity-limited" regime. Between these two limiting cases, a transitional regime is expected to exist, where cloud droplet formation is sensitive to both updraft velocity and aerosol properties (Reutter et al., 2009). In the remote Alpine atmosphere, cloud droplet number concentrations are predominantly influenced by aerosol availability (Hoyle et al., 2016), except during periods of enhanced anthropogenic activity, related to for example biomass-burning emissions (Georgakaki et al., 2021). The same applies to the pristine Arctic atmosphere, where velocity-limited conditions are rarely met except for short periods during the Arctic haze in early spring (Motos et al., 2023).

1.2.2 Heterogeneous ice nucleation

At temperatures below freezing, the nucleation of a new stable phase requires an energy barrier to be surpassed, which is dictated by an intermediate maximum in the Gibbs free energy of the system. Below -38˚C, the energy barrier for the phase transition from liquid to ice is so minimal that even a slight rearrangement of molecular structure can convert liquid or solution cloud droplets into ice – a process known as homogeneous freezing. At warmer temperatures, however, insoluble aerosols are needed to lower the energy barrier and catalyze the ice nucleation processes, which is therefore called *heterogeneous freezing*. INPs provide a solid surface that facilitates the formation of stable ice clusters. In contrast to CCN, only approximately one in a million aerosol particles can serve as INPs (Murray et al., 2012). The most prevalent INPs include mineral dust, biological particles, bacteria, ash,

pollen and sea-spray (Kanji et al., 2017). Ice formation in the atmosphere, whether homogeneous or heterogeneous, is termed primary ice production (PIP), contrasting with SIP, which arises from the multiplication of pre-existing ice particles and is discussed further in Section 1.2.4.1.

Heterogeneous freezing can be initiated through one of four freezing modes, as illustrated in Figure 1.1 and briefly discussed below:

- *Contact freezing*: An INP comes into contact with a supercooled droplet, initiating ice nucleation at the phase boundaries among the droplet, particle, and surrounding air. This pathway triggers ice formation at warmer temperatures (> -10˚C) compared to the other freezing modes (Ladino Moreno et al., 2013).
- *Immersion freezing*: This mode is initiated from within a cloud or solution droplet, where an INP is already immersed. Freezing of the cloud droplet occurs upon cooling. This is believed to be the dominant nucleation mode in most MPCs (Whale, 2017).
- *Condensation freezing*: This process occurs in two stages. First, the soluble component of the INP acts as a CCN to form a cloud droplet when saturation with respect to liquid water is achieved. Then, the insoluble part of the INP facilitates the freezing of the cloud droplet. It is still unclear whether this process differentiates from immersion freezing (Vali et al., 2015).
- *Deposition nucleation*: Water vapor molecules deposit directly onto the INP surface, provided that the environment is supersaturated with respect to ice. The occurrence of this mechanism is still controversial due to the generally unfavorable nature of a phase transition from vapor to solid. A recent proposal suggests that the actual process behind deposition nucleation is pore condensation and freezing, where liquid water can condense under water subsaturated conditions (David et al., 2019).

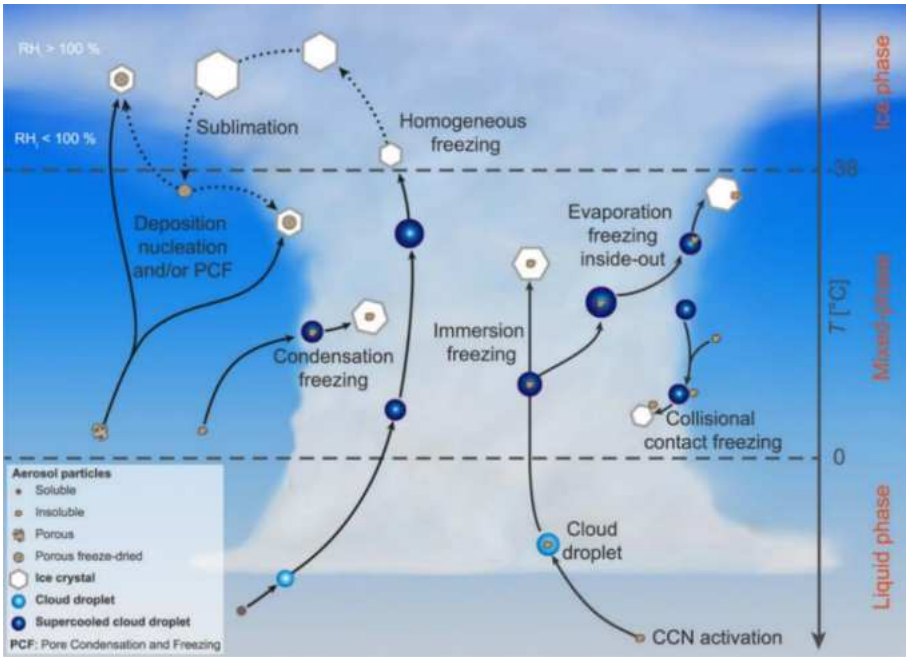

Figure 1.1 Overview of different heterogeneous freezing modes that can take place within the mixed-phase temperature regime of a thunderstorm cloud. Figure adapted from Kanji et al. (2017).

The relative importance of each nucleation mode within the atmosphere heavily depends on the ambient temperature and supersaturation, as well as the INP size, composition and morphology

(Hoose & Möhler, 2012; Knopf & Alpert, 2023). In the Swiss Alps, INP concentrations may vary from 10^{-3} up to over 100 L^{-1} (e.g., Lacher et al., 2017). Free-tropospheric INP observations collected at the high-altitude Jungfraujoch (JFJ) station have shown that Saharan dust intrusions enrich the atmosphere with mineral dust particles acting as INPs at temperatures around -30˚C (Brunner et al., 2021). Aged sea-spray aerosols arriving via long-range transport can also serve as effective INPs (Lacher et al., 2021). However, at moderate supercooling (temperatures > -15˚C), the majority of INPs were found to originate from epiphytic bacteria or fungi (Conen et al., 2022). In the remote Arctic atmosphere, INPs are mostly found to vary between 10^{-5} and 1 L^{-1} (e.g., Wex et al., 2019). Mineral dust particles from local sources in summer and long-range transport in winter were again identified as important INP contributors (Abbatt et al., 2019). Marine biogenic particles resulting from cracks and open leads in the sea ice are another important INP source in the high Arctic, capable of initiating ice nucleation at temperatures as high as -7.5˚C (Hartmann et al., 2020). The origin of these INPs is linked to phytoplankton blooms (Creamean et al., 2019) or the emission of sea-spray aerosols during bubble bursting at the atmosphere-ocean interface (Wilson et al., 2015).

Within MPCs, changes in the number of available INPs may carry important implications for their radiative properties. Generally speaking, in a warming climate, replacement of ice with liquid is expected to enhance their reflectivity to shortwave (SW) solar radiation, resulting in a negative cloud-phase feedback that counters initial warming (Tan & Storelvmo, 2019; Vergara-Temprado et al., 2018). This scenario, however, becomes more complex if we also consider potential changes in INP concentrations. For instance, in a warming climate, diminished sea ice concentrations in polar regions might result in higher atmospheric INP levels, driven by increased biogenic emissions from the open ocean (Carlsen & David, 2022). Consequently, MPCs would contain ice crystals at warmer temperatures than previously estimated, rendering them optically thinner and resulting in a positive cloud-phase feedback (Murray et al., 2021). This underscores the intricacy of ice-related processes and the necessity for their accurate representation in GCMs.

1.2.3 Ice growth processes in mixed-phase clouds

What makes the study of ice crystals so intriguing is their unique individuality. When ice germs form in the atmosphere, rapid vapor diffusion drives their growth into what is termed *pristine ice crystals*. This process is called *growth by vapor deposition*. Laboratory experiments have yielded a well-recognized diagram that elucidates how ambient temperature and ice supersaturation govern the resulting morphology of ice crystals, denoted as *ice crystal habits* (Libbrecht, 2017). For instance, columnar and needle-like ice crystals are formed at temperatures between -5 and -10°C, followed by planar, dendritic ice structures at temperatures between roughly -10 and -20°C. This temperature regime is known as *dendritic growth layer* (DGL). Below -20°C, planar or columnar shapes may emerge depending on the prevailing ice supersaturation. More complex shapes as presented in picture iv of Figure 1.2 can arise when a pristine ice crystal continues its growth under new environmental conditions. Understanding the growth history of such intricate ice crystal habits is not trivial. The growth history of two complex, fragile ice structures was recently inferred from observations of MPCs in the Arctic (Pasquier et al., 2023).

In MPCs, the difference between the saturation vapor pressure over ice than over liquid creates a vapor pressure gradient from the higher pressure region surrounding the droplets to the lower pressure surrounding the ice crystals. When the environment becomes subsaturated with respect to liquid water, cloud droplets start evaporating as water vapor molecules rapidly diffuse toward neighboring ice crystals. This mechanism, in which ice crystals grow at the expense of surrounding evaporating supercooled droplets, is known as the *Wegener–Bergeron–Findeisen* (WBF) process. WBF can efficiently glaciate MPCs within minutes to tens of minutes (Korolev & Mazin, 2003). However, the efficiency of this process might be strongly dependent on the MPC cloud morphology. Indeed,

observations of MPCs have revealed the potential for either uniform mixing or spatial separation between liquid droplets and ice crystals. This implies that clusters of either liquid or ice phase can be enclosed within extended glaciated or liquid clouds at spatial scales below 100 m (Korolev & Milbrandt, 2022). This configuration limits interactions between the two phases and may favor the preservation of supercooled droplets within MPCs. Nevertheless, this subgrid scale phase heterogeneity is currently absent from large-scale models and could serve as a significant source of biases.

Following the initial depositional growth, ice particles in MPCs can further augment their size through collisional processes, either with other ice crystals or cloud droplets/raindrops. Within mixed-phase conditions, when ice particles fall and collide with supercooled droplets or raindrops, a portion of the liquid-phase hydrometeor can freeze onto them, resulting in the formation of an ice shell. This process is known as *riming* and contributes to the transfer of mass from the liquid to the ice phase. As a result, the ice particle becomes more spherical, and massive, therefore increasing its terminal velocity. Riming has been identified as enhancing surface precipitation by 20-50% (e.g., Borys et al., 2003; Lowenthal et al., 2016). Graupel particles commonly emerge as the end products of the riming process, while intense riming present in vigorous convective clouds can lead to the creation of large hailstones.

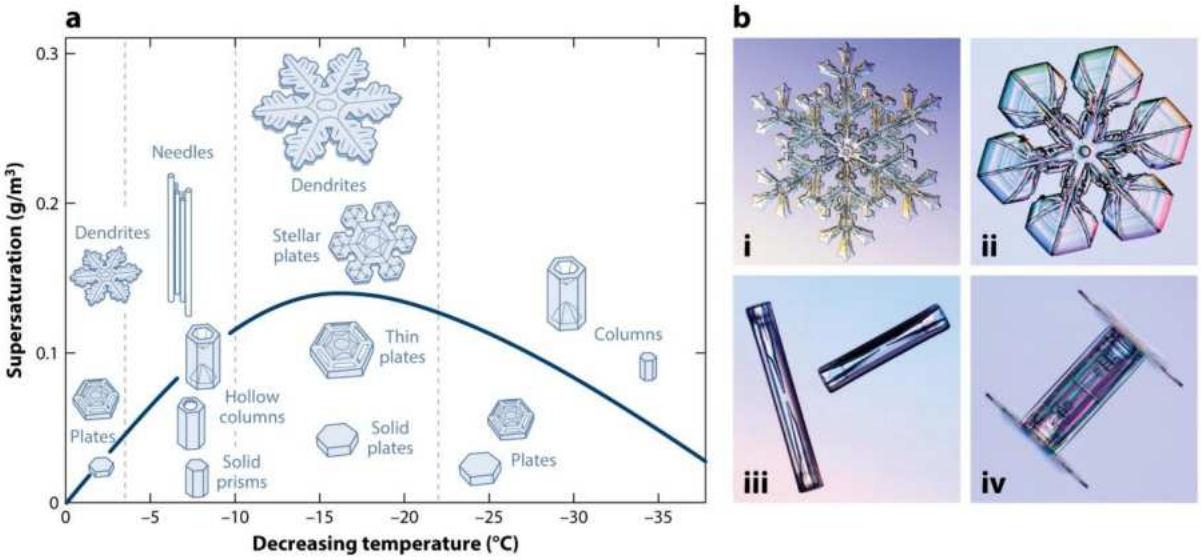

Figure 1.2 (a) Ice crystal habits growing in atmospheric air as a function of temperature and supersaturation with respect to ice. The solid curve represents the supersaturation with respect to the liquid phase of water. (b) Pictures of pristine ice crystals: (i), (ii) planar, dendritic ice particles, (iii) columnar, and (iv) capped-column ice crystals. Figure adapted from Libbrecht (2017).

Aggregation occurs when ice crystals collide and adhere, resulting in the creation of larger aggregated snowflakes. This growth mechanism exhibits greater efficiency within two distinct temperature ranges: (i) at temperatures spanning from -10 to -15°C, where the dendritic structure of ice particles is favored, particularly when high ice supersaturation prevails. This is because the entanglement of two branched ice structures becomes more likely upon collision. (ii) at temperatures near 0°C, where a thick quasi-liquid layer forms on the surface of the melting ice particles, significantly enhancing their sticking ability. However, radar observations from Arctic MPCs have suggested the suppressed role of aggregation at such warm subzero temperatures (Chellini et al., 2022). Turbulence in the atmosphere

(Sheikh et al., 2022) or varying terminal velocities of ice hydrometeors further promote aggregational growth. Given that riming can increase differential settling and the chance of collisions, the formation of aggregates becomes more likely if riming initially occurs in the atmosphere.

1.2.4 Discrepancies between ice crystal numbers and ice nucleating particles

1.2.4.1 Secondary ice production

Brewer and Palmer (1949) introduced the concept that the splintering of ice crystals from growing snowflakes or hailstones could elevate ICNCs beyond the levels of INPs, effectively transforming a water cloud into an ice cloud. Subsequent global field campaigns have consistently reported substantial disparities between the two, confirming that ICNCs can exceed INPs by several orders of magnitude (e.g., Huang et al., 2022; Lawson et al., 2023; O'Shea et al., 2017; Rangno & Hobbs, 2001; Young et al., 2016). In cases where MPCs are decoupled from the surface and lack seeding from upper-level clouds, an ice enhancement factor (IEF) or ice multiplication factor (IMF) can be calculated as the ratio between ICNCs and INPs, serving as an indicator of the prevalence of SIP. Both observational (e.g., Korolev et al., 2022; Wieder et al., 2022) and modeling studies (e.g., Waman et al., 2022; Zhao et al., 2023) have contributed to literature-derived IMF values.

The schematic depiction in Figure 1.3 summarizes the IMF outcomes from various field observations conducted over the past decade, spanning maritime convective (Stith et al., 2011), continental (Crawford et al., 2012; Taylor et al., 2016), tropical (Ladino et al., 2017; Lasher-Trapp et al., 2016), orographic (Lauber et al., 2021; Mignani et al., 2019; Wieder et al., 2022), and Arctic (Pasquier et al., 2022) MPCs. SIP is observed across temperatures ranging from nearly 0 to approximately -25°C. Predominantly, within warmer temperatures below the -15°C isotherm, SIP substantially augments ICNCs by over four orders of magnitude compared to ambient INP concentrations. In colder conditions, IMF calculations are scarcer, yet still manifest ICNC enhancements surpassing a factor of 100.

After over a decade of continuous research both in laboratory settings and in the field, contributing to advancements in our comprehension of primary ice formation (e.g., DeMott et al., 2011, 2018), SIP is a process that has gained considerably less attention within the scientific community. Unlike PIP, the most pioneering laboratory experiments concerning SIP date back several decades (early '70s), carried out using simplified setups that posed technological challenges given the available resources at the time (Hallett & Mossop, 1974; Takahashi et al., 1995; Vardiman, 1978). The outcomes of these experiments laid the groundwork for all present-day SIP parameterizations found in cloud models (Field et al., 2017). Nowadays, more intricate and precise experiments and observations are feasible due to the advancement of high-speed video microscopy (e.g., Lauber et al., 2018) and the utilization of anti-shatter cloud probe tips that mitigate data contamination by shattering artifacts (Korolev et al., 2013).

Field et al. (2017) and Korolev and Leisner (2020) offer a comprehensive overview of current SIP knowledge. Since these comprehensive papers, further evidence for the significance of SIP in clouds has emerged from various observational and laboratory studies utilizing sophisticated equipment (Keinert et al., 2020; Kleinheins et al., 2021; Mignani et al., 2019). Hartmann et al. (2023) aimed to quantify ice splinters ejected when droplets rime onto ice particles within the HM temperature range, finding limited action of this mechanism. This contrasts with the hundreds of SIP particles per mg rime discovered in the Hallett and Mossop (1974) optimal setup. Recently, increased attention from the cloud research modeling community has been directed towards SIP due to the need for more advanced microphysical parameterizations (e.g., Fridlind et al., 2007; Listowski & Lachlan-Cope, 2017; Phillips et al., 2018; Phillips et al., 2017a; Yano et al., 2016). While uncertainties persist in the modeling parameterization of SIP, modeling studies unanimously converge on the conclusion that accounting

for SIP can effectively bridge the gap between model predictions and observations in various MPC types (e.g., Dedekind et al., 2021; Sotiropoulou, Vignon, et al., 2021; Waman et al., 2022; Zhao et al., 2023). These factors underscore the urgency of revisiting key SIP experiments with modern instrumentation and advancing our in-situ observations of SIP. This is to better quantify the contribution of these mechanisms to observed ICNC enhancements and the necessary and sufficient conditions for SIP initiation, which will ultimately advance the way these processes are parameterized in models.

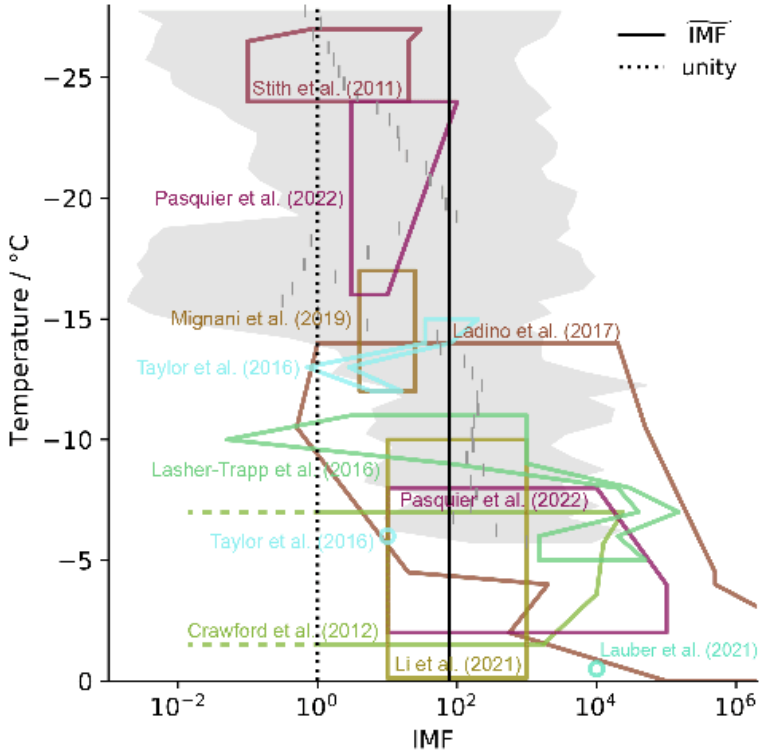

Figure 1.3 Literature review of ice multiplication factors derived from field observations across various types of MPCs, plotted against their respective temperature ranges. SIP is recognized when the IMF exceeds unity, denoted by the vertical black dashed line. Figure adapted from Wieder et al. (2022), with the range of their findings in alpine clouds indicated by the gray shaded region and their median predictions represented by the black solid line.

In recent decades, several SIP-identifying mechanisms have emerged in literature, as detailed in Field et al. (2017) and Korolev and Leisner (2020). A concise overview of the four significant SIP mechanisms explored within this PhD thesis is presented below. This review encompasses laboratory and field observations, modeling, and atmospheric remote sensing, all of which have contributed to our understanding of these mechanisms:

a. *Droplet shattering during freezing:* Historically, this was the first SIP mechanism reported in clouds (e.g. Cannon et al., 1974; Langham & Mason, 1958; Mason & Maybank, 1960). DS occurs when a drizzle droplet, typically larger than ~50 µm, collides with either an INP or an ice particle. Upon contact, the droplet begins freezing from the outside in, creating a solid ice shell around it (e.g., Griggs & Choularton, 1983) (Figure 1.4a). As freezing progresses inward, pressure builds, leading to fragmentation, which can result in the droplet breaking in two halves, cracking, bubble bursting, or jetting (e.g., Keinert et al., 2020). These processes may be accompanied by the

ejection of small ice fragments, the number of which was the research focus of individual freezing experiments reporting the maximum fragmentation rate at temperatures between ∼-10 and -15˚C (Kleinheins et al., 2021; Lauber et al., 2018).

DS efficiently operates in vigorous convective updrafts (Korolev et al., 2020; Lawson et al., 2015; Qu et al., 2020), which do not meet the criteria for HM. Sullivan, Hoose, et al. (2018) demonstrated that DS is significant for clouds formed above the freezing level, provided that limited INPs and intermediate to high updrafts are present (refer to their Figure 8b and 9). In slightly supercooled Arctic MPCs, remote sensing observations indicate that DS can be more conducive to SIP than the well-established HM process (Luke et al., 2021). This aligns with in-situ observations from Ny-Ålesund and single-column simulations conducted by (Zhao et al., 2021), but contrasts with smaller-scale modeling studies suggesting that DS is ineffective in polar regions (Fu et al., 2019; Sotiropoulou et al., 2020). Through refinement of SIP and PIP parameterizations in the Community Earth System Model version 2, Zhao et al. (2023) discovered that DS accounts for about 75% of simulated ICNCs in Southern Ocean MPCs, within the temperature range of -15 to -10˚C (see pie charts in their Figure S4).

In wintertime orographic clouds, radar measurements implied the importance of DS in cloud regions with high liquid water content (LWC; Billault-Roux et al., 2023), or in cloud top generating cells (Ramelli et al., 2021a). Additionally, in-situ data suggest the increasing efficiency of this process at temperatures warmer than -3˚C (Lauber et al., 2021)l, attributed to a raindrop recirculation theory (Korolev et al., 2020) facilitated by orographically-induced updrafts passing through the melting layer. However, mesoscale model simulations of the same type of MPCs formed at temperatures colder than -8˚C indicate that DS has minimal contribution to the modeled ICNCs (Dedekind et al., 2021; Georgakaki et al., 2022). This might, however, be related to the challenging representation of DS in bulk microphysics schemes, with the models following a bin-emulated framework systematically reporting higher efficiency of this process (Sotiropoulou et al., 2022; Zhao & Liu, 2022).

b. *The rime splintering or Hallett-Mossop process:* HM stands out as the most extensively studied and firmly established SIP mechanism. It operates effectively within a specific temperature range, spanning from -3˚C to -8˚C, where supercooled liquid droplets sized between 13 µm and 25 µm (Choularton et al., 1980; Hallett & Mossop, 1974) freeze onto the surfaces of ice particles (Figure 1.4b). Nevertheless, aircraft measurements (e.g., Korolev et al., 2020, 2022) have revealed instances of high ICNCs even when the conditions required for the HM mechanism are not met. Even under favorable conditions, the HM process alone may prove insufficient to account for observed ice crystal production rates in MPCs (Hobbs & Rangno, 1990; Korolev et al., 2020).

Observationally, signatures of HM can be inferred more readily than other SIP mechanisms due to its constrained temperature ranges, which favor the growth of ejected ice splinters into needle-like or columnar ice habits (Figure 1.2). During field campaigns, the potential presence of HM is therefore speculated based on in-situ imagery where heavily rimed particles (e.g., graupel), liquid droplets, and small columns/needles coexist (e.g., Grazioli et al., 2015; Järvinen et al., 2022; Lloyd et al., 2015). The presence of distinct hydrometeor modes with different morphologies and habits further facilitates the inference of HM through vertically-pointing radar spectrograms (e.g., Luke et al., 2021; Oue et al., 2015; Sinclair et al., 2016).

From the modeling perspective, parameterized expressions of HM have been extensively implemented in NWP models and GCMs with explicit microphysics. However, uncertainties persist regarding this mechanism, such as the rate of splinters ejected per mass of rime

(Hartmann et al., 2023). Atlas et al. (2022) supported the significant impact of HM on the simulated cloud radiative forcing (CRF) of low cumulus clouds over the Southern Ocean, yet highlighted a significant shortcoming in the representation of this process in models. Specifically, the initiation of HM in models necessitates arbitrary, non-physically based thresholds in the mixing ratios of ice and liquid hydrometeors to be achieved. Multiple modeling studies have indicated that removing these thresholds could enhance the efficiency of HM in models (e.g., Atlas et al., 2020; Young et al., 2019). Nonetheless, even after eliminating these thresholds, the representation of HM does not always bridge the gap with observed ICNCs, underscoring the complementary role of other SIP mechanisms (Karalis et al., 2022; Sotiropoulou et al., 2020).

c. *Fragmentation due to ice-ice collision:* Collisions between delicate ice particles leading to mechanical break-up (Figure 1.4c) have been identified as an effective SIP mechanism across a broad temperature range, showing a distinct peak in ice splinter production at around -15˚C (Grzegorczyk et al., 2023; Takahashi et al., 1995). Our understanding of this mechanism remains limited due to sparse airborne investigations (e.g., Schwarzenboeck et al., 2009; Takahashi, 1993) and a scarcity of laboratory studies (Griggs & Choularton, 1986; Takahashi et al., 1995; Vardiman, 1978) utilizing simplified experimental setups, which have raised concerns about result accuracy. Recent efforts have focused on studying graupel-graupel and graupel-aggregate collisions in a wind tunnel laboratory with improved experimental designs, aiming to reproduce and validate earlier findings (Grzegorczyk et al., 2023).

Signatures of BR activity can be deduced from in-situ particle images showing a combination of large rimed particles and smaller irregular-shaped particles like broken-off arms of dendritic crystals and aggregates. The action of BR has been recognized in various cloud types, including the mature stage of convective clouds (Huang et al., 2022; Waman et al., 2022), cold-air outbreaks (Karalis et al., 2022), stratiform conditions, especially within multilayer cloud systems formed in orographic terrain (Ramelli et al., 2021a; Georgakaki et al., 2022), as well as in the Arctic (Pasquier et al., 2022) and the Southern Ocean (Jarvinen et al., 2022). The occurrence of BR, resulting from collisions among fragile dendritic crystals formed between -20 and -10˚C, can also be inferred from ground-based remote sensing observations (von Terzi et al., 2022). Unlike the columnar-ice mode often associated with HM, the presence of a disk-like mode in turbulent cloud regions at colder temperatures may indicate BR activity (Billault-Roux et al., 2023).

In modeling approaches, three different methods have been employed to parameterize the impact of BR-induced SIP. These methods either entail prescribing a constant number of fragments generated per collision (e.g., Hoarau et al., 2018), parameterizing the fragment count using simple exponential fits to the experimental findings of Takahashi et al. (1995) (Dedekind et al., 2023; Sullivan, Hoose, et al., 2018), or utilizing more sophisticated expressions dependent on initial kinetic energy, colliding particle size, and rimed fraction (Sotiropoulou, Ickes, et al., 2021; Zhao & Liu, 2022). BR parameterizations have been tested across small-scale, mesoscale, and GCMs confirming the efficacy of this mechanism in increasing modeled ICNCs by up to ∼3 orders of magnitude.

d. *Sublimational break-up:* When dendritic or heavily rimed particles descend within subsaturated cloudy regions, they may undergo sublimation, causing certain portions of these particles to become detached from the main ice structure (such as the arms of dendrites, Figure 1.4e). Termed as SUBBR, this process was initially identified through laboratory investigations in the 1980s and 1990s. Oraltay and Hallett (1989) documented the fracturing of dendrites under subzero temperatures and relative humidities over ice of less than 70%. Subsequent to this, Dong

et al. (1994) and Bacon et al. (1998) observed the fragmentation of rimed and frost ice particles, respectively. Combining the collective experimental findings, Deshmukh et al. (2022) formulated two empirical parameterizations for SUBBR in graupel and dendritic snow. The number of fragments produced due to SUBBR was parameterized as a function of temperature, supersaturation, ice particle size, and a ventilation coefficient dependent on the particle's fall speed.

For ice fragments formed during sublimation to contribute to ice multiplication, they must re-enter a supersaturated cloud region. This raises concerns about the effectiveness of this mechanism under real atmospheric conditions, given the small size and consequently low terminal velocities of the resulting ice fragments (Korolev & Leisner, 2020). Nonetheless, idealized simulations estimated an IMF of approximately 5 (10) following SUBBR of dendritic snow (graupel) particles in a deep convective descent of ~2 m s^{-1} (Deshmukh et al., 2022). SUBBR might also become active within the subsaturated layer of air separating a multilayer cloud system within a *seeder-feeder cloud configuration* (Section 1.2.4.2). The first modeling study encompassing all four SIP mechanisms found that SUBBR can be the second most significant SIP process after BR, generating an IMF of up to ~10^2 in the fastest downdrafts (> -5 m s^{-1}) of a continental convective storm (Waman et al., 2022). Incorporating this mechanism into GCM simulations of Arctic MPCs revealed minimal efficiency, constrained to lower atmospheric levels, with ice production rates being at least one order of magnitude lower than those of other SIP mechanisms (Sotiropoulou et al., 2022). This was attributed to the generally high relative humidities prevailing in polar MPCs.

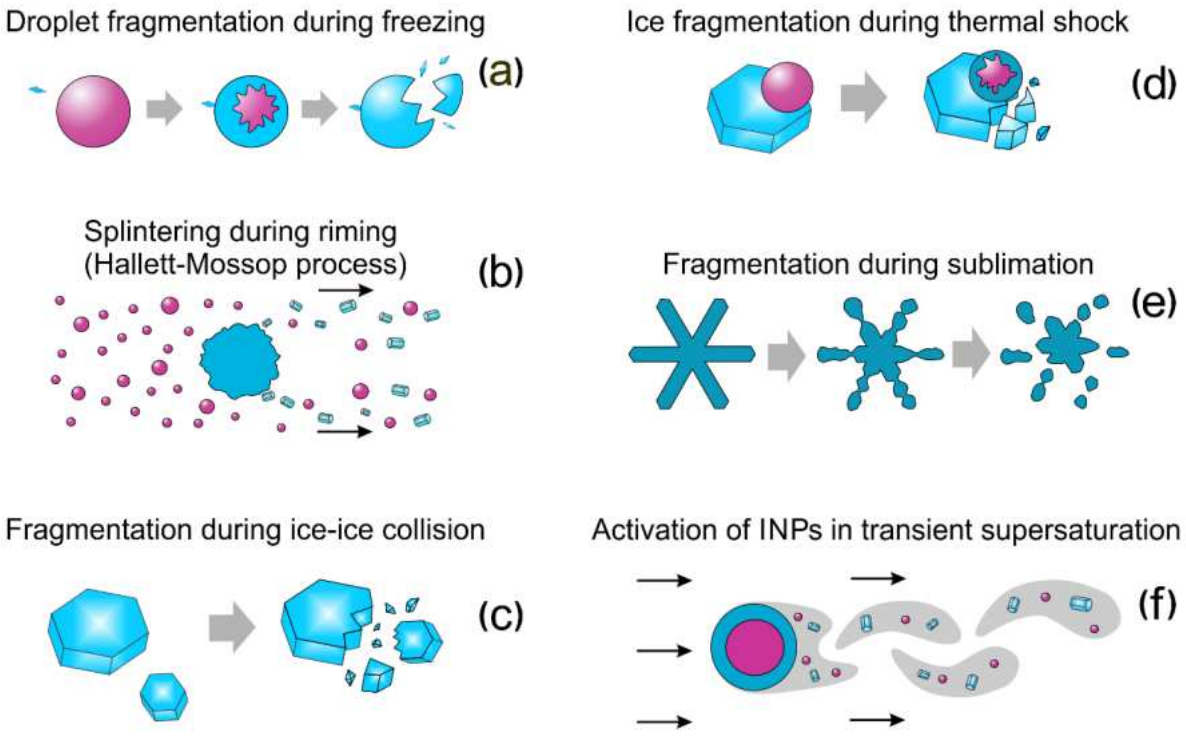

Figure 1.4 Schematic illustration presenting a summary of six proposed SIP mechanisms: (a) droplet-shattering, (b) Hallett-Mossop, (c) ice-ice collisional break-up, (d) thermal shock ice fragmentation, (e) sublimational break-up, and (f) INP activation in transient supersaturation. Figure adapted by Korolev & Leisner (2020).

Two additional ice multiplication mechanisms have been identified and presented in Korolev and Leisner (2020). Thermal shock-induced fragmentation (Figure 1.4d) can occur in the atmosphere when a supercooled cloud droplet rimes onto the surface of an ice crystal (King & Fletcher, 1976). This collision releases latent heat from the freezing droplet, raising the temperature of the ice crystal to its melting point. This differential expansion of the ice crystal may lead to its fragmentation. Another proposed SIP mechanism involves again the latent heat release during the freezing of a falling warm hydrometeor, which generates a temperature difference between the surface of the freezing hydrometeor and the surrounding air. In this case, water vapor evaporates from the surface of the frozen hydrometeor generating regions of high transient supersaturation in the cold cloudy air, activating virtually all interstitial aerosol that can act as INPs (Krayer et al., 2021; Prabhakaran et al., 2020), as illustrated in Figure 1.4f. These two mechanisms have received limited investigation, and their potential for ice multiplication remains uncertain. This PhD research primarily aims to improve the representation of SIP within NWP models and GCMs, and to create methods that can potentially be applied to detect SIP signs from remote sensing observations.

1.2.4.2 Seeder-feeder mechanism

Elevated ICNCs in low-level MPCs, exceeding what can be explained by the presence of a few INPs, are sometimes found to result from the seeder-feeder process. This mechanism involves the sedimentation of ice particles either within layered clouds or internally within a single cloud (Proske et al., 2021; Roe, 2005), leading to two distinct cloud configurations:

- *External seeder-feeder*: ice particles fall from an upper-level (glaciated) seeder cloud through subsaturated cloud-free air, surviving sublimation and re-entering supersaturated conditions upon reaching the lower-level (mixed-phase or liquid-only phase) cloud.
- *In-cloud seeding*: large ice particles precipitate from higher (glaciated) parts of a cloud to lower lying (mixed-phase or liquid-phase) parts of the same cloud. In this case, a vertical continuum of cloud condensates spans between the seeder and feeder regions, and the falling ice particles do not encounter subsaturated conditions.

Both configurations are characteristic of orographic clouds frequently associated with precipitation enhancement and cloud glaciation over mountains (e.g., Mott et al., 2014; Purdy et al., 2005; Roe, 2005). Satellite remote sensing analysis over an 11-year span (2006-2017) by Proske et al. (2021) indicated that in Switzerland, in-cloud seeding occurred in 18% of observations, while the external seeder-feeder mechanism appeared 15% of the time for cirrus cloud seeders. Beyond orographic terrain, the Arctic region also frequently experiences multilayer clouds. Satellite data analysis revealed that such cloud systems occur between 15-25% of the time in the Arctic – a possibly conservative estimate due to retrieval uncertainties over the high-albedo surfaces of the polar regions (Liu et al., 2012). Combining ground-based remote sensing with in-situ measurements over a year in the Arctic, Vassel et al. (2019) found ice seeding in 23% of total measurements. Interestingly, even in the absence of ice seeding, the two clouds in the seeder-feeder system can still interact radiatively. This is because the upper-level cloud is anticipated to enhance downwelling longwave (LW) radiation reaching the lower-level cloud, which reduces cloud-top radiative cooling – critical for turbulent mixing and low-level cloud maintenance (e.g., Christensen et al., 2013).

Another significant aspect of ice seeding cases is their association with SIP events. This link has been highlighted by several modeling (e.g., Georgakaki et al., 2022; Sotiropoulou, Vignon, et al., 2021) and observational studies in the Alpine (Ramelli et al., 2021a) and the Arctic region (Pasquier et al., 2022), as well as in the Southern Ocean (Järvinen et al., 2022), underscoring its significance given the frequency of such cloud configurations.

1.2.4.3 Surface-induced ice particles

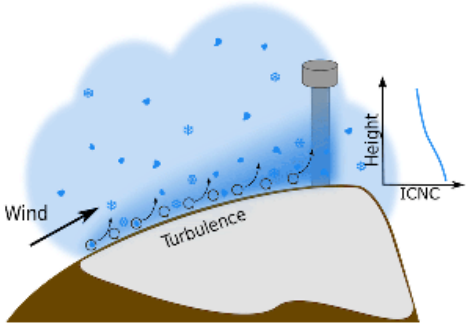

Figure 1.5 Illustration of the effect of wind-induced surface snowflakes (blowing snow) on the ice crystal number concentrations found in orographic mixed-phase clouds. Figure cropped and adapted from Beck et al. (2018).

Over the complex, mountainous terrain, surprisingly high ICNCs are often attributed to surface processes, such as blowing snow, surface hoar frost detachment, turbulent effects near mountain surfaces, ice particle convergence due to orographic lifting, and riming on snow-covered surfaces (Beck et al., 2018; Geerts et al., 2015; Rogers & Vali, 1987). Among these processes, the impact of blowing snow ice particles has been extensively studied, either using mountain observations (e.g., Lowenthal et al., 2019), and remote sensing (e.g., Geerts et al., 2015; Vali et al., 2012), or snow-cover models (e.g., Lehning et al., 2006) sometimes coupled with atmospheric models (e.g., Sharma et al., 2023; Vionnet et al., 2014). Blowing snow particles can stay suspended near the surface provided that the wind speed exceeds a threshold value, which varies between 4 and 13 m s^{-1} (e.g., Mahesh et al., 2003), depending on the snowpack properties and the prevailing atmospheric conditions. Simplified methods have been employed to model surface-based processes in orographic MPC development, as demonstrated in Farrington et al. (2016) and Georgakaki et al. (2022). To achieve a more precise representation of lower atmospheric processes and assess their potential in contributing to ice-related processes in near-surface MPCs, coupling NWP models with advanced surface snow models, as demonstrated by Gerber et al. (2023) and Sharma et al. (2023), would be necessary.

1.2.5 Indirect aerosol effects via mixed-phase clouds

Improving our understanding of the intricate microphysical processes within MPCs is important for better quantifying *aerosol indirect effects*, which refer to alterations in cloud properties driven by variations in atmospheric particulate matter, or simply aerosols. In purely liquid-phase clouds it is recognized that changes in the aerosol concentrations serving as CCN can modify liquid cloud droplet concentrations as well as their cloud radiative properties and lifetime through different indirect effects (Albrecht, 1989; Twomey, 1974). Yet, the response of ice-containing clouds, such as MPCs, to changes in the aerosol loading is less understood. This is largely because of the complex and nonlinear microphysical pathways that can influence the properties and evolution of MPCs. Three indirect aerosol-cloud interactions have been proposed to act in MPCs:

- The *glaciation indirect effect*, where increased aerosol concentrations are followed by an increase in the available INPs, allowing for more ice crystals to be nucleated in the atmosphere. This is expected to speed up the WBF process and augment ice-phase precipitation until complete cloud glaciation is achieved (Lohmann, 2002).
- The *riming indirect effect* (Lance et al., 2011; Lohmann & Feichter, 2005) opposes the glaciation indirect effect. It highlights how elevated CCN concentrations can result in clouds with numerous, smaller cloud droplets, reducing the riming of ice crystals and, consequently, the mass of ice particles and precipitation (Borys et al., 2003; Lohmann, 2017).
- The *thermodynamic indirect effect* (Lohmann & Feichter, 2005), elucidates that an increase in CCN and subsequent reduction in the effective radius of cloud droplets can delay the onset of freezing

in clouds. This is due to the decreased probability of heterogeneous immersion freezing and/or SIP processes, which therefore suppresses precipitation and cloud glaciation.

1.3 Representing ice microphysics in models

Cloud microphysics encompasses numerous and nonlinear interactions among hydrometeors, with the most intricate likely occurring in the context of cold cloud microphysics, which was the primary focus of Section 1.2. Microphysics schemes in atmospheric models aim to capture the behavior of cloud and precipitation particles and their impacts on weather patterns, climate, and radiative fluxes. As summarized in Morrison et al. (2020), microphysics schemes confront two primary challenges, partly stemming from representing the cloud and precipitation particle population due to computational limitations, and from uncertainties arising from gaps in cloud physics understanding.

Cloud microphysics schemes typically fall into two categories: spectral or bin microphysics and bulk microphysics (Figure 1.6). The key distinction lies in how they handle particle size distributions (PSDs). Bin schemes divide PSDs of ice and liquid hydrometeors into discrete size or mass intervals ("bins"), modeling the evolution of each bin individually. In contrast, bulk microphysics schemes do not explicitly track the entire spectrum of particle sizes but assume some functional form for the particles' PSDs. The predicted microphysical quantities in bulk schemes are typically moments or weighted integrals of the assumed PSDs. Bin schemes provide more degrees of freedom allowing for a more realistic representation of the hydrometeor PSDs, yet they are considerably more computationally demanding than bulk schemes – typically one to two orders of magnitude higher. This computational burden has confined bin schemes primarily to research modeling, while bulk schemes continue to serve operational and long-range climate studies (e.g., Milbrandt et al., 2016). Bulk schemes can be either single- or double-moment, depending on whether they predict solely the hydrometeors mass mixing ratio or both their number concentration and mixing ratio, being the zeroth and first moment of the assumed distributions, respectively.

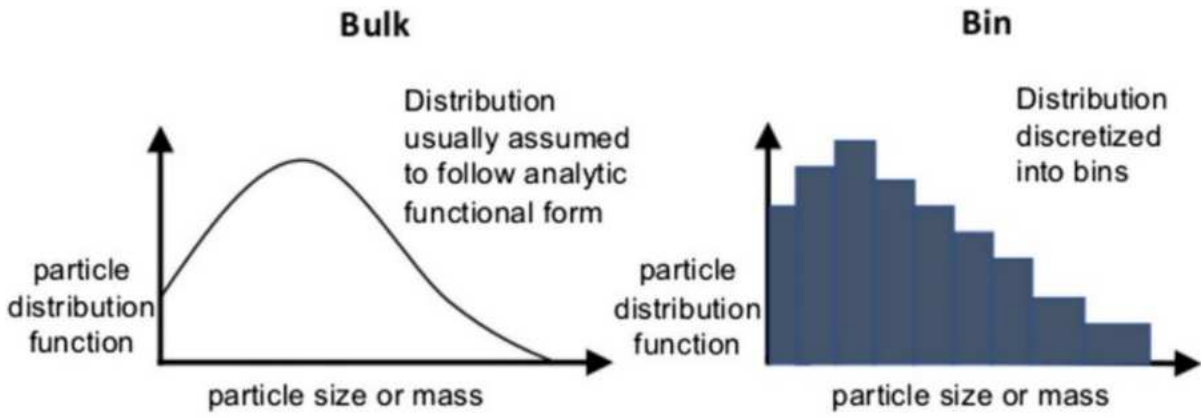

Figure 1.6 Comparison of cloud and precipitation particle size distributions using bulk (left) and bin (right) microphysics schemes. The horizontal axes represent particle size or mass, while the vertical axes indicate the number density distribution. Cropped and adapted from Morrison et al. (2020).

Figure 1.7 illustrates the considerable scale variability addressed by the microphysics component of the model. Microscopic entities, such as individual ice crystals and cloud droplets can measure just a few microns in size, whereas heavily rimed structures like hailstones can extend to centimeter scales.

The diverse and intricate nature of these processes cannot be numerically captured within the coarse horizontal grid spacing of large-scale models. Only Direct Numerical Simulation (DNS) models explicitly resolve the myriad of hydrometeors – albeit within spatially-limited cloudy volumes. Transitioning to cloud-scale motions, these can be largely resolved by Large Eddy Simulation (LES) models with horizontal resolutions around tens of meters. However, for larger-scale regional or GCMs with grid spacings of approximately 100 km or more, subgrid-scale processes necessitate approximations or parameterizations to interact effectively with the broader resolved model scales. As individual clouds and their dynamical motions become progressively unresolved from left to right in the schematic shown in Figure 1.7, the emergence of microphysics parameterizations as a complex yet indispensable aspect of atmospheric modeling becomes evident.

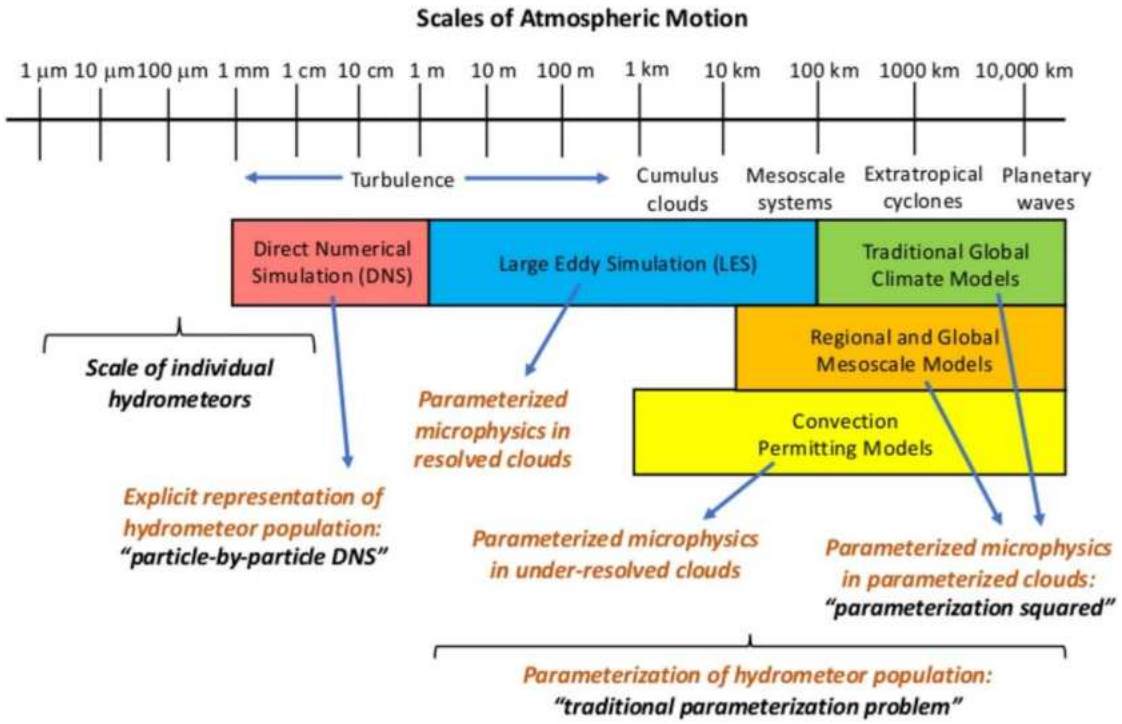

Figure 1.7 Schematic representation of atmospheric motion scales across a range of atmospheric models, illustrated within color-coded boxes. Figure adapted from Morrison et al. (2020).

1.3.1 Machine learning for parameterization development

Artificial intelligence, employing ML techniques, has made significant advancements across various scientific disciplines over recent decades. Within the atmospheric sciences, its contributions are widely acknowledged (e.g., Irrgang et al., 2021; Reichstein et al., 2019) as it unlocks possibilities such as purely data-driven weather forecasting (e.g., Weyn et al., 2020) and climate modeling (Rasp et al., 2018; Yuval & O'Gorman, 2020). ML algorithms operate by identifying complex relationships and generalizing statistical associations to establish a function that maps inputs to outputs. This is achieved through minimizing predefined loss metrics tailored to a specific task.

ML for climate modeling shows great promise, particularly in addressing computational challenges and bottlenecks associated with traditional physically-based parameterizations (e.g., Gentine et al., 2018; Grundner et al., 2022). Two ML methods, neural networks (NNs) and random forests (RFs), have been used to develop parameterizations for GCMs. RF, an ensemble learning algorithm composed of

multiple decision trees, preserves physical properties by averaging predictions from subsets of training samples (Breiman, 2001). This conservative behavior leads to more stable GCM simulations compared to NNs, which may deviate from the training data pool (Han et al., 2020; O'Gorman & Dwyer, 2018). NN parameterizations, while memory-efficient in GCMs, can introduce numerical instabilities and result in model blow ups or climate drift (Brenowitz & Bretherton, 2018, 2019; Rasp et al., 2018). Stable long-term simulations require post-prediction adjustments and accurate processing of the training dataset (Rasp, 2020; Yuval et al., 2021).

Parameterizing cloud microphysical processes and aerosol-cloud interactions is among the most challenging aspects of climate simulations (e.g., Liu et al., 2023; Morrison et al., 2020). Parameterizations for bulk microphysics schemes are often derived from fitting techniques applied to bin scheme outputs (e.g., Barahona & Nenes, 2007; Seifert, 2008) or laboratory results (e.g., Deshmukh et al., 2022; Sullivan, Hoose, et al., 2018), or by analytically solving equations governing the microphysical processes (e.g., Barahona & Nenes, 2009). Attempts have already been made to simplify the representation of warm cloud microphysical processes, such as autoconversion or accretion, using ML approaches (Chiu et al., 2021; Gettelman et al., 2021; Seifert & Rasp, 2020). However, addressing cold cloud microphysics remains more complex, with no tailored ML-based attempt to date. A first attempt will be presented in Chapter 5.

1.3.2 The Weather Research and Forecasting Model

The Weather Research and Forecasting (WRF) model is an open-source mesoscale NWP model employing the Advanced Research WRF (ARW) dynamical core. WRF operates on horizontal scales ranging from a few kilometers to several hundred kilometers, designed for both atmospheric research and operational forecasting. It is suitable for simulations under actual atmospheric or idealized conditions, aiding physical parameterization development and testing. While a comprehensive technical description exists in Skamarock et al. (2008), a succinct overview is provided here.

WRF operates as a fully compressible and nonhydrostatic model, resolving vertical pressure distribution without the hydrostatic approximation. Among the prognostic variables are the horizontal velocity, perturbation potential temperature, geopotential and surface pressure of dry air, water vapor mixing ratio and the microphysical variables for each hydrometeor species considered. ARW employs an Arakawa-C grid staggering, locating horizontal velocity and geopotential components at the edge of the grid cells to capture the advection of variables. The rest of prognostic are positioned at the center of the grid cells. Vertically, WRF utilizes a terrain-following hybrid sigma-pressure coordinate system. Temporal integration employs the 3rd order Runge-Kutta integration scheme, while spatial integration employs 2nd to 6th order advection schemes.

WRF offers a range of microphysics options, which encompass bin models and single- or double-moment bulk schemes. These schemes predict the mass mixing ratios of hydrometeor species and, in the case of double-moment schemes, also include their number concentrations. Among the microphysics schemes available in WRF, the Morrison double-moment bulk scheme (Morrison et al., 2005; Morrison et al., 2009; hereafter M05) was chosen to simulate cloud microphysics throughout the modeling studies of this PhD research, and will be detailed in the following section.

1.3.2.1 The Morrison Double-Moment Microphysics Scheme

The performance of the M05 scheme has been rigorously validated in the literature across various types of MPCs found in Arctic (Cho et al., 2020), Antarctic (Vignon et al., 2019), and Alpine (Farrington et al., 2016) regions. This scheme is well-suited for stratiform MPCs in large-scale models and can also handle convective clouds when the horizontal resolution allows it (< 3 km). Otherwise, for shallow-

convection subgrid processes, a cumulus scheme is recommended. M05 accounts for two liquid hydrometeor species: cloud droplets and raindrops, and three ice species: cloud ice, snow, and graupel. Prognostic equations describe both the mass and number concentration of all hydrometeor species, except for liquid cloud droplets, whose single-moment representation requires defining a prescribed cloud droplet number concentration. The hydrometeor sizes are represented by gamma functions, as described below:

$$f(D) = N_0 D^{\mu} e^{-\lambda D}, \tag{1.1}$$

where D refers to the hydrometeor diameter, μ is the spectral index, while

$$\lambda = \left[\frac{\alpha N \Gamma(\mu+\beta+1)}{q\Gamma(\mu+1)}\right]^{\frac{1}{\beta}}, \tag{1.2}$$

is the slope parameter (in m^{-1}) and

$$N_0 = \frac{N\lambda^{\mu+1}}{\Gamma(\mu+1)}, \tag{1.3}$$

is the intercept (in kg^{-1} m^{-1}). Except for cloud droplets, where μ is determined as a function of cloud and thermodynamic properties (see Equation 30 in Morrison et al., 2005), all other hydrometeors exhibit $\mu = 0$, indicating their distributions follow an exponential form. In Equations (1.2) and (1.3), q and N represent the hydrometeor mass mixing ratio (in kg kg^{-1}) and number concentration (in kg^{-1}), respectively. The parameter $\beta = 3$ and $\alpha = \frac{\rho_h \pi}{6}$, where ρ_h is the particle's bulk density (in kg m^{-3}) following (Reisner et al., 1998). Assumed to be spherical, all hydrometeors conform to the mass-diameter relationship as follows:

$$m = \alpha D^{\beta}. \tag{1.4}$$

Figure 1.8 presents a condensed overview of the microphysical interactions encompassed by the M05 scheme in WRF. It is important to note that interactions involving graupel particles are omitted from this schematic. At the end of each model timestep, equations governing the Eulerian tendencies of mixing ratios and number concentrations for all five hydrometeor species are updated. The number tendency of cloud ice particles has the following form:

$$\frac{dN_i}{dt} = \text{Advection + Primary ice production + Ice multiplication –}$$
$$\text{Autoconversion – Sublimation/melting – Sedimentation – Collection} \tag{1.5}$$

The equation above summarizes all potential sources and sinks of small cloud ice particles in the M05 scheme. Within a specific model grid point, cloud ice particles can undergo advection through horizontal transport or form through primary ice nucleation or ice multiplication. Primary ice nucleation is parameterized using several simplified temperature-dependent schemes, including immersion freezing of cloud droplets or large raindrops (Bigg, 1953), contact freezing (Meyers et al., 1992), which accounts for the collection of INPs by cloud droplets through Brownian motion, and deposition/condensation freezing nucleation (Cooper, 1986).

Regarding ice multiplication, the default M05 scheme includes only the HM mechanism. However, as will be discussed in detail in Chapters 3 and 4, the M05 scheme was updated to incorporate state-of-the-art SIP parameterizations for all four important SIP mechanisms (Section 1.2.4.1). Small ice particles can grow either through vapor deposition or by collecting cloud droplets (provided they exceed 100 μm in size). Once they surpass a characteristic diameter of 250 μm, they are converted into the snow category through autoconversion. The number of ice particles may decrease due to

sublimation, melting, sedimentation, or if they are collected by larger snow or graupel particles or by raindrops.

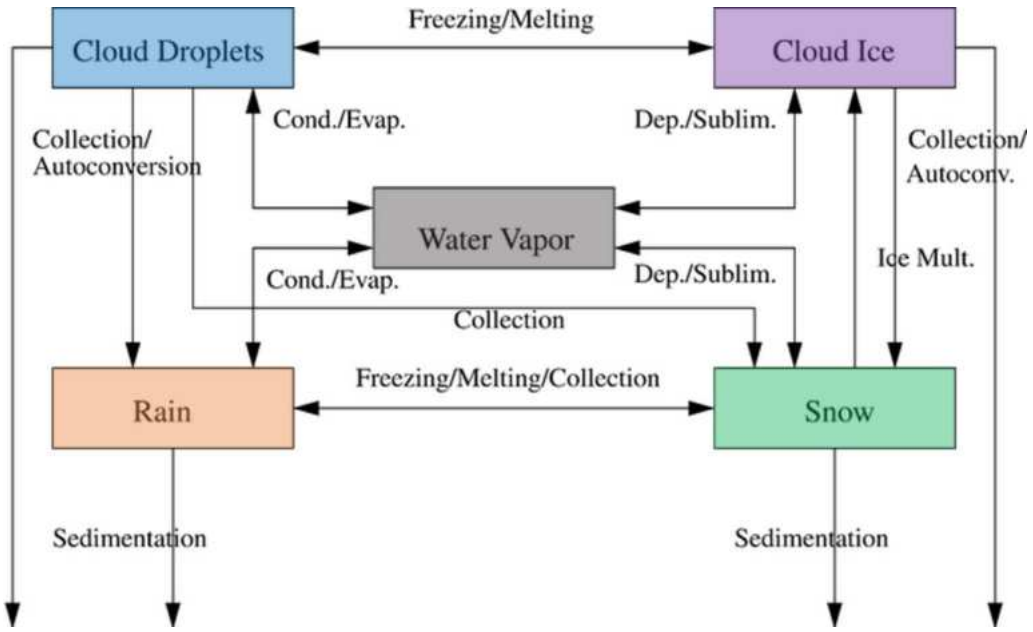

Figure 1.8 A box diagram summarizing the microphysical processes described in the Morrison microphysics scheme of WRF. Note that cloud droplet and raindrop riming that can lead to the formation of graupel are not included in this schematic. Figure adjusted and adapted from Morrison et al. (2005).

Equation (1.5) will be slightly modified when applied to the snow particle species. Snow can be generated within the model through ice-to-snow autoconversion or as a result of collisions between ice and rain particles. In M05, snow aggregation, parameterized according to Passarelli (1978) and Reisner et al. (1998), serves as an efficient source of snowflakes. Snow particles may also be subject to removal via sedimentation or transformed into graupel following collisions with the two liquid hydrometeors.

The formation of graupel particles in the model occurs through riming, where either cloud droplets or raindrops collide with snow, or through the collection of cloud ice by raindrops. This transformation takes place when specific thresholds in the mass mixing ratios of the involved hydrometeors are exceeded. It is worth noting that the choice of these thresholds is rather arbitrary and lacks strong physical justification, yet their choice can influence simulation results. This was addressed in Morrison and Grabowski (2008), where the variability in threshold values was found to limit graupel formation and subsequently reduce the mean fall speed of hydrometeors, thereby impacting surface precipitation.

1.4 Particular objectives

Given the radiative and hydrological impact of MPCs, and particularly of ice formation therein, the overall goal of this PhD project is to bring a step further our understanding of microphysical processes occurring in this climatologically important cloud type. The coexistence of ice and liquid phase in the same cloud volume makes the study of MPCs more intriguing – as both phases are interlinked into a

complex web of ice growth and multiplication processes that can significantly affect the cloud radiative forcing and lifetime (Section 1.2.5) dictating their glaciation fraction and precipitation produced. Reviewing the present state of literature (Sections 1.2 and 1.3), it becomes clear that it is rather recent when both experimental and modeling communities turned their attention to ice multiplication processes. From the modeling point-of-view, significant work remains to incorporate state-of-the-art SIP descriptions in NWP models and GCMs, as their role in affecting the modeled liquid-ice phase partitioning in clouds is already demonstrated.

With the aim to extend the current knowledge and understanding of microphysical properties and processes in orographic as well as polar MPCs, the main points that will be addressed within this PhD research are the following:

1. *Do changes in cloud dynamics or aerosol content influence cloud droplet formation in the Alpine region?*
    a) To what extent can cloud parcel modeling, when combined with in-situ and remote-sensing observations, predict cloud droplet numbers in orographic clouds?
    b) Is there a relationship that characterizes the shift from aerosol-limited to velocity-limited cloud conditions?
    c) Can we deduce information about the distribution of updraft velocities when velocity-limited conditions occur, and what are the implications for the ice-phase of clouds?

2. *Does inclusion of SIP descriptions in an NWP model help explain the elevated ice crystals found in orographic MPCs*?
    a) How do seeding ice particles influence the low-level MPCs?
    b) Which is the dominant SIP process?
    c) Do wind-induced ice particles influence the simulated ice crystal concentrations close to the surface?
    d) What is the impact of these processes in total accumulated precipitation?

3. *Can we infer signatures of SIP from radar observations of orographic clouds*?
    a) Does coupling a SIP-aware NWP model with a forward radar simulator produce the measured reflectivities?
    b) What are the environmental conditions promoting SIP?
    c) What is the role of snowflake aggregation?
    d) Do SIP processes within the DGL produce characteristic signatures in the full Doppler spectra?
    e) Is there an indication of SIP in the standard radar moments?

4. *Can the combined effect of SIP in stratiform MPCs be parameterized in large-scale models using an ML-framework?*
    a) What are the most important parameters for describing the effects of SIP in large-scale models?
    b) What is the offline performance of the ML-based SIP algorithm?
    c) Does replacing the detailed SIP descriptions in an NWP model with the ML-based SIP scheme impact the performance of the model?
    d) Are there any effects on computational efficiency or numerical stability in simulations?
    e) To what extent does the ML framework replicate the SIP physics from conventional parameterizations it was trained on?

The structure of this PhD thesis is outlined as follows: In the following three chapters, the focus will be on orographic MPCs. **Chapter 2** presents an analysis of the factors influencing droplet variability in

Alpine MPCs. This analysis utilizes in-situ and remote-sensing observations collected during the Role of Aerosols and Clouds Enhanced by Topography on Snow (RACLETS) field campaign in Davos, Switzerland. Moving on to **Chapter 3**, the primary emphasis is on the impact of SIP processes in orographic clouds. This is accomplished through numerical modeling and model evaluation using field observations from the Cloud and Aerosol Characterization Experiment (CLACE) 2014 campaign in the Swiss Alps. In **Chapter 4**, an intensive snowfall event documented during the Cloud-AerosoL InteractionS in the Helmos background TropOsphere (CALISHTO) campaign at Mount Helmos, Greece, is examined. A synergistic approach, which combines modeling tools and remote sensing observations, is presented for inferring SIP from radar data. The updated microphysics code developed as part of the research in Chapter 3 serves as the foundation for the development of a new ML parameterization for SIP, designed for seamless integration into large-scale models. This ML framework is the subject of **Chapter 5**. The thesis concludes with **Chapter 6**, which offers a final discussion, outlining perspectives as well as open questions.

2. On the drivers of droplet variability in alpine mixed-phase clouds

This chapter investigates whether cloud droplet formation in the Alpine region is modulated by variations in cloud dynamics or aerosol concentrations. The analysis is based on in-situ observations gathered during the RACLETS campaign in the Davos region, Switzerland, during February and March 2019. The research involves post-processing of in-situ aerosol and remote sensing data, along with cloud parcel model simulations. The text is adapted from the postprint version of the article:

- **Georgakaki, P.**, Bougiatioti, A., Wieder, J., Mignani, C., Ramelli, F., Kanji, Z. A., Henneberger, J., Hervo, M., Berne, A., Lohmann, U., and Nenes, A. (2021): On the drivers of droplet variability in alpine mixed-phase clouds, *Atmospheric Chemistry and Physics*, 21, 10993–11012, doi: 10.5194/acp-21-10993-2021.

The presented cloud droplet analysis and processing of the CCN data was carried out by Paraskevi Georgakaki with inputs and supervision from Athanasios Nenes. The CCN instrumentation was setup by Aikaterini Bougiatioti, the aerosol instrumentation and inlet setup were done by Jörg Wieder, Claudia Mignani, and Zamin A. Kanji, the cloud data by Fabiola Ramelli and Jan Henneberger, and the lidar data by Maxime Hervo. The original manuscript was written by Paraskevi Georgakaki and Athanasios Nenes, with input from all authors.

2.1 Summary

Droplet formation provides a direct microphysical link between aerosols and clouds (liquid or mixed-phase), and its adequate description poses a major challenge for any atmospheric model. Observations are critical for evaluating and constraining the process. To this end, aerosol size distributions, cloud condensation nuclei (CCN), hygroscopicity, and lidar-derived vertical velocities were observed in alpine mixed-phase clouds during the Role of Aerosols and Clouds Enhanced by Topography on Snow (RACLETS) field campaign in the Davos, Switzerland, region during February and March 2019. Data from the mountain-top site of Weissfluhjoch (WFJ) and the valley site of Davos Wolfgang are studied. These observations are coupled with a state-of-the-art droplet activation parameterization to investigate the aerosol–cloud droplet link in mixed-phase clouds. The mean CCN-derived hygroscopicity parameter, κ, at WFJ ranges between 0.2–0.3, consistent with expectations for continental aerosols. κ tends to decrease with size, possibly from an enrichment in organic material associated with the vertical transport of fresh ultrafine particle emissions (likely from biomass burning) from the valley floor in Davos. The parameterization provides a droplet number that agrees with observations to within ∼25 %. We also find that the susceptibility of droplet formation to aerosol concentration and vertical velocity variations can be appropriately described as a function of the standard deviation of the distribution of updraft velocities, σ_w, as the droplet number never exceeds a characteristic limit, termed the "limiting droplet number", of ∼150-550 cm^{-3}, which depends solely on σ_w. We also show that

high aerosol levels in the valley, most likely from anthropogenic activities, increase the cloud droplet number, reduce cloud supersaturation (< 0.1 %), and shift the clouds to a state that is less susceptible to changes in aerosol concentrations and very sensitive to vertical velocity variations. The transition from an aerosol to velocity-limited regime depends on the ratio of cloud droplet number to the limiting droplet number, as droplet formation becomes velocity limited when this ratio exceeds 0.65. Under such conditions, droplet size tends to be minimal, reducing the likelihood that large drops are present that would otherwise promote glaciation through rime splintering and droplet shattering. Identifying regimes where droplet number variability is dominated by dynamical – rather than aerosol – changes is key for interpreting and constraining when and which types of aerosol effects on clouds are active.

2.2 Introduction

Orographic clouds, and the precipitation they generate, play a major role in Alpine weather and climate (e.g., Grubisic & Billings, 2008; Lloyd et al., 2015; Roe, 2005; Saleeby et al., 2013; Vosper et al., 2013). The formation and evolution of orographic clouds involves a rich set of interactions at different spatial and temporal scales encompassing fluid dynamics, cloud microphysics and orography (Roe, 2005; Rotunno & Houze, 2007). Atmospheric aerosol particles modulate the microphysical characteristics of orographic clouds by serving as cloud condensation nuclei (CCN) that form droplets, or ice nucleating particles (INPs) that form ice crystals (Muhlbauer & Lohmann, 2009; Pruppacher & Klett, 1997; Saleeby et al., 2013; Zubler et al., 2011).

Emissions of aerosol particles acting as CCN and INPs can affect the microphysical and radiative properties of clouds with strong (but highly uncertain) effects on local and regional climate (IPCC, 2013; Seinfeld et al., 2016). Aerosol interactions with orographic clouds are subject to even larger uncertainties, owing in part to the complex flows generated by the interaction of the large-scale flow with the mesoscale orographic lifting and condensation and complex anisotropic turbulent air motions that arise (Roe, 2005; Rotunno & Houze, 2007; Smith, 2006). Most importantly, orographic clouds are often mixed-phase clouds (MPCs), which are characterized by the simultaneous presence of supercooled liquid water droplets and ice crystals (Farrington et al., 2016; Henneberg et al., 2017; Lloyd et al., 2015; Lohmann et al., 2016). MPCs remain one of the least understood cloud types, due to the multiple and highly nonlinear cloud microphysical pathways that can affect their properties and evolution. MPCs tend to glaciate (i.e., transition to pure ice clouds) over time because of the Bergeron–Findeisen process, which is the rapid growth of ice crystals at the expense of the evaporating cloud droplets, owing to the higher saturation vapor pressure of liquid water over ice (Bergeron, 1935; Findeisen, 1938). Aerosol concentrations may also alter the microphysical pathways active in MPCs and ultimately drive their glaciation state. For instance, an increase in CCN concentrations leads to more numerous and smaller cloud droplets, reducing the riming efficiency of ice crystals and therefore the hydrometeor crystal mass and the amount of precipitation (Lance et al., 2011; Lohmann & Feichter, 2005; Lohmann, 2017). This mechanism counters the glaciation indirect effect, where increases in INP concentrations elevate ice crystal number concentration (ICNC) and promotes the conversion of liquid water to ice and therefore the amount of ice-phase precipitation (Lohmann, 2002). Increases in CCN can also decrease cloud droplet radius and impede cloud glaciation, owing to reductions in secondary ice production (SIP), which includes rime splintering, collisional break-up, and droplet shattering (Field et al., 2017; Sotiropoulou et al., 2020; Sotiropoulou, Vignon, et al., 2021).

Cloud-scale updraft velocity (i.e., the part of the vertical velocity spectrum with positive values) is the major driver of droplet formation, owing to the supersaturation generated from adiabatic expansion and cooling (Ghan et al., 2011; Nenes et al., 2001). Despite its importance, the simulation of updraft velocity by atmospheric models is rarely constrained by observations, which can lead to large uncertainties in climate and numerical weather prediction models (Sullivan et al., 2016; Sullivan,

Barthlott, et al., 2018). Reutter et al. (2009) pointed out that droplet formation in clouds can be limited by the amount of CCN present (called the "aerosol-limited" regime), or by the vertical velocity that generates supersaturation in the cloudy updrafts (called the "velocity-limited" regime). Over the complex Alpine terrain, vertical motions can be significantly shaped by the effects of orography (Lohmann et al., 2016). Orographic MPCs have been frequently observed in the Swiss Alps under high updraft velocity conditions, where supersaturation with respect to liquid water is formed faster than it is depleted by diffusional and collisional ice growth processes (Korolev & Isaac, 2003) leading to persistent MPCs (Lohmann et al., 2016).

Given the importance of droplet number for the radiative cloud properties and microphysical evolution of alpine MPCs, it is essential to understand the main aerosol and dynamics properties that drive droplet formation. A limited number of studies exist that discuss this very important topic, although they focus on liquid-phase clouds (Hammer et al., 2014, 2015; Hoyle et al., 2016). Hoyle et al. (2016) showed that 79% of the variance in droplet number in warm clouds formed at the high-altitude research station of Jungfraujoch in the Swiss Alps (3450 m a.s.l.) is driven by variations in potential CCN concentration (i.e., aerosol particles with a dry diameter > 80nm). Using a cloud parcel model, Hammer et al. (2015) also investigated the influence of updraft velocity, particle concentration, and hygroscopicity on liquid cloud formation in the alpine region and found that variations in vertical wind velocity have the strongest influence on the aerosol activation. We are not aware of existing in situ studies assessing cloud droplet closure in MPCs where the existence of ice crystals can deplete supersaturation or the low temperatures may decrease CCN activity through the formation of glassy aerosols.

Here we analyze observational data collected as part of the Role of Aerosols and Clouds Enhanced by Topography on Snow (RACLETS) field campaign, which was held in the region of Davos, Switzerland, during February and March 2019. This intensive field campaign aims to address questions related to the modulators of orographic precipitation, the drivers of the enhanced ice-crystal number concentrations observed in MPCs, as well as the human-caused pollution effects on cloud microphysical and optical properties. In this study we focus on a two-week period and seek to unravel the complex aerosol–droplet–updraft velocity interactions that occur in the orographic MPCs. For this, we combine CCN number concentrations with the particle size distributions to understand the variations in hygroscopicity over time and for sites located in the valley and a nearby mountain-top site. The in situ measurements are subsequently coupled with a state-of-the-art droplet parameterization to determine the potential droplet numbers and the corresponding maximum supersaturation achieved in cloudy updrafts. The predicted droplet numbers are evaluated against direct observations and the degree to which droplet formation is velocity or aerosol limited is determined for the whole time series.

2.3 Methods

2.3.1 Observational datasets

This analysis utilizes measurements collected during the RACLETS campaign, which took place from 8 February to 28 March 2019 (https://www.envidat.ch/group/about/raclets-field-campaign, last access: 17 December 2020 (Lauber et al., 2020; Mignani et al., 2021; Ramelli et al., 2021a; Ramelli et al., 2021b). This joint research project offers a unique dataset of orographic clouds, precipitation, and snow measurements in an effort to shed light on some fundamental microphysical processes present in subsequent stages of the life cycle of clouds (i.e., cloud formation, precipitation onset, and cloud dissipation). All measurements presented in this paper were performed at two distinct observation stations near Davos, Switzerland (Figure A1 in Appendix A). A measurement site is located at Davos Wolfgang, which is the pass between Davos (1560 m a.s.l.) in the south and Klosters (1200 m a.s.l.) in

the north and is otherwise known as Wolfgang Pass (WOP; 1630 m a.s.l., 46°50'08.076"N 9°51'12.939"E). Measurements were also conducted at the mountain-top station Weissfluhjoch (WFJ; 2700 m a.s.l., 46°49'58.670"N 9°48'23.309"E), which is located ~1km above the valley floor in Davos, in the eastern part of the Swiss Alps. The current study primarily focuses on data collected during a two-week period of interest, which spans from 24 February to 8 March 2019. During the RACLETS campaign, a defective sheath air filter affected the CCN measurements collected at WFJ, thus inhibiting data usage from the instrument for a large duration of the campaign. Therefore, we limit our analysis to the abovementioned period when the CCN counter was fully operational. In addition, during the selected period two distinct weather patterns were observed (fair weather conditions interrupted by a precipitating period), allowing for a contrasting analysis of the observed scenarios. The following description refers to the measurements that provided the basis for the present analysis (see Table 2.1).

2.3.1.1 Aerosol particle size distribution measurements

Particle size distributions were continuously monitored at WOP and WFJ using commercially available scanning mobility particle sizers (SMPS; Model 3938, TSI Inc., US). At both stations, the systems consisted of a differential mobility analyzer (Model 3081, TSI Inc., US), a soft X-ray neutralizer (Model 3088, TSI Inc., US), and a water-based condensation particle counter (Model 3787 at WOP, Model 3788 at WFJ, TSI Inc., US). Running the particle counters in low flow mode (0.6 L min^{-1}), using a sheath flow of 5.4 L min^{-1}, and applying a total scanning time of 2 min (scan time: 97 s; retrace time: 3 s; purge time: 10 s), particle size distributions between 11.5 and 469.8 nm diameter were monitored.

2.3.1.2 CCN measurements

A Droplet Measurement Technologies (DMT) single-column continuous-flow streamwise thermal gradient chamber (CFSTGC; Roberts & Nenes, 2005) was used to carry out in situ measurements of CCN number concentrations for different supersaturations (SS). The CFSTGC consists of a cylindrical flow tube with wetted walls, inside which SS is developed by applying a linear streamwise temperature gradient between the column top and bottom. Owing to the greater mass diffusivity of water vapor than the thermal diffusivity of air, a constant and controlled SS is generated with a maximum at the centerline of the flow tube. The SS is mainly dependent on the applied temperature gradient, flow rate and pressure (Roberts & Nenes, 2005). An aerosol sample flow is introduced at the column centerline and those particles having a critical supersaturation lower than the instrument SS will activate to form droplets and will afterward be counted and sized by an optical particle counter (OPC) located at the base of the CFSTGC column. The SS developed within the instrument responds linearly to changes in pressure, since its operation relies on the difference between heat and mass diffusivity. Calibration of the instrument, which determines the output supersaturation, was performed by the manufacturer at ~800 mbar, while throughout the campaign the CFSTGC was operating at a lower pressure ~735 mbar, therefore the SS reported by the instrument is adjusted by a factor of $\frac{735}{800} = 0.92$, which accounts for the difference between the ambient and the calibration pressure (Roberts & Nenes, 2005). CCN concentrations were measured at a specific SS for approximately 10 min; the instrument was cycled between six discrete values ranging from 0.09% to 0.74% supersaturations, producing a full spectrum every hour. Each 10 min segment of the raw CCN data is filtered to discount periods of transient operation (during supersaturation changes) and whenever the room temperature housing the instrument changed sufficiently to induce a reset in column temperature (the instrument

control software always sets the column temperature to be at least 1.5° above the room temperature to exclude spurious supersaturation generation in the column inlet). The CFSTGC was deployed on the mountain-top site of WFJ with the intention of relating the CCN measurements directly to the size distribution and total aerosol concentration data measured by the SMPS instrument at the same station.

2.3.1.3 Cloud microphysical measurements

In situ observations of the cloud microphysical properties were obtained with the tethered balloon system HoloBalloon (Ramelli et al., 2020). The main component of the measurement platform is the holographic cloud imager HOLIMO 3B, which uses digital in-line holography to image an ensemble of cloud particles in the size range from 6 µm to 2 mm diameter in a three-dimensional detection volume. Note that particles smaller than 6 µm are not detected by HOLIMO, which means that the droplet number concentration may be underestimated. Based on a set of two-dimensional images, information about the particle position, size, and shape can be obtained. The detected particles can be classified as cloud droplets and ice crystals using supervised machine learning (Fugal et al., 2009; Touloupas et al., 2020). The differentiation between cloud droplets (circular) and ice crystals (non-circular) is done for particles exceeding 25 µm diameter based on their shape (Henneberger et al., 2013). From the classification, the phase-resolved size distribution, concentration, and content can be derived (Henneberger et al., 2013; Ramelli et al., 2020). The HoloBalloon platform was flying at WOP and provided vertical profiles of the cloud properties within the lowest 300 m of the boundary layer (BL). The current analysis utilizes the cloud droplet number concentration and liquid water content (LWC) measurements. Note that the LWC is calculated based on the size distribution of the cloud droplets using a liquid water density (ρ_w) of 1000 kg m^{-3} and is therefore dominated by large cloud particles.

2.3.1.4 Meteorological data

During the measurement period, meteorological parameters (e.g., pressure, temperature, precipitation, and horizontal wind speed and direction) were continuously monitored by the permanent MeteoSwiss observation station at WFJ. Additionally, a weather station was installed on the OceaNet container (Griesche et al., 2020) deployed at WOP, which also hosted several remote sensing instruments (e.g., cloud radar, Raman lidar, and microwave radiometer) and a particle size velocity (Parsivel) disdrometer (Parsivel2, OTT HydroMet GmbH, Germany; Tokay et al., 2014) to measure precipitation. As there was no wind sensor included in the weather station on the OceaNet container, we utilized the horizontal wind speed and direction measurements from the nearby MeteoSwiss station in Davos, assuming that they provide a good proxy for the wind regime in the valley. Vertical wind speed profiles were obtained with a wind Doppler lidar (WindCube 100S, manufactured by Leosphere) at WOP. Throughout the campaign the wind lidar measured from 200 to 8100 m above ground level (AGL) with high temporal (5 s max) and vertical resolution (50 m). The wind lidar operated following the Doppler beam switching technique with an elevation of 75°. More information about the remote sensing measurements can be found in Ramelli et al. (2021a).

Table 2.1 Overview of data sources from the RACLETS campaign used for this study. Along with the observed parameters, the corresponding instrumentation, measurements range, and time resolutions are listed.

Measured parameter	Measurement site	Instrument	Measurement range	Time resolution
Aerosol number size distribution	WOP/ WFJ	Scanning Mobility Particle Sizer	11.5 – 469.8 nm	2 min
CCN number concentration	WFJ	Continuous flow streamwise thermal gradient CCN counter	SS = 0.09 – 0.74%	1 s
Cloud droplet number concentration and liquid water content	WOP	Holographic cloud imager HOLIMO	6 µm – 2 mm	10 – 20 s
Precipitation	WOP/ WFJ	Parsivel disdrometer/ MeteoSwiss weather station	0.2 mm – 25 mm	30 s
Horizontal wind speed and direction	WOP/ WFJ	MeteoSwiss weather station	–	10-min averages
Profiles of vertical wind speed	WOP	Wind Doppler Lidar	200 m – 8100 m AGL	5 s max

2.3.2 Aerosol hygroscopicity

The aerosol hygroscopicity parameter, κ, encompasses the impact of particle chemical composition on its subsaturated water uptake and CCN activity (Petters & Kreidenweis, 2007). Here, we determine κ similarly to the approach of Moore et al. (2011), Jurányi et al. (2011), Lathem et al. (2013), Kalkavouras et al. (2019), Kacarab et al. (2020), and others by combining the CCN measurements with the SMPS aerosol size distribution data as follows. For each SMPS scan, the particle size distribution is integrated backward starting from the bin with the largest-size particles, which corresponds to the CCN with the lowest critical supersaturation, S_{cr}. We then successively add bins with smaller and smaller diameters until the aerosol number matches the CCN concentration observed for the same time period as the SMPS scan. The particles in the smallest size bin, which we call critical dry diameter, D_{cr}, correspond to the CCN with the highest S_{cr} possible, which is the instrument supersaturation (SS). From D_{cr} and SS we determine κ from Köhler theory (Petters & Kreidenweis, 2007) assuming the particle chemical composition is internally mixed:

$$\kappa = \frac{4A^3}{27 D_{cr}^3 SS^2} \tag{2.2}$$

where $A = \frac{4M_w\sigma_w}{RT\rho_w}$ is the Kelvin parameter, in which M_w (kg mol^{-1}) is the molar mass of water, σ (J m^{-2}) is the surface tension of the solution droplet, R is the universal gas constant, and T (K) is the ambient temperature. Here, we assume the surface tension of the solution droplet is equal to that of pure water ($\sigma = \sigma_w$) by convention. The κ determined above represents the composition of particles with diameter D_{cr} (large particles can have a different κ but still activate given that their S_{cr} is lower than the prevailing SS in the CCN chamber). This means that over the course of an hour, over which a full SS cycle is completed, κ is determined for a range of D_{cr}, which in our case were in the range of 50–200 nm (Section 2.4.1). This size-resolved κ information provides insights on the possible origin and chemical components of the aerosol, which is important given that there is no other measurement available to constrain chemical composition during RACLETS. From κ, we infer an equivalent organic mass fraction, ε_{org}, assuming that the aerosol is composed of an organic–inorganic mixture:

$$\varepsilon_{org} = \frac{(\kappa - \kappa_i)}{(\kappa_o - \kappa_i)} \tag{2.2}$$

where κ_i = 0.6 and κ_o = 0.1 are characteristic hygroscopicity values for the inorganic fraction of an aerosol (represented by ammonium sulfate) and organic aerosol, respectively (Dusek et al., 2010; Petters & Kreidenweis, 2007; Wang et al., 2008). Note that these values for a continental aerosol are supported by observations and analyses (e.g., Andreae & Rosenfeld, 2008; Pringle et al., 2010; Rose et al., 2008).

2.3.3 Cloud droplet number and cloud maximum supersaturation

Here, we apply adiabatic cloud parcel theory to the observational datasets to determine the maximum in-cloud supersaturation (S_{max}) and cloud droplet number (N_d) that would form over both measurement sites throughout the observation period. Droplet calculations are carried out with the physically based aerosol activation parameterization of Nenes and Seinfeld (2003), with extensions introduced by Fountoukis and Nenes (2005), Barahona et al. (2010), and Morales and Nenes (2014). Each N_d calculation requires knowledge of the observed pressure, temperature, vertical winds, aerosol size distribution, and hygroscopicity. For the WFJ site, all data are available as described in the sections above. For the WOP site, CCN (hence hygroscopicity) data are not available so we carry out N_d calculations at two κ values, 0.1 and 0.25, which are the upper and the lower limit determined from the WFJ analysis (Section 2.4.1). The ability to reproduce observed cloud droplet number concentrations (Section 2.4.2.1) further supports the selection of these values.

The wind lidar measurements conducted at WOP (Section 2.3.1.4) are used to determine the prevailing vertical velocities at both sites. Data extracted from the first bin of the lidar at 200 m AGL are considered representative for WOP as the wind lidar has no values very close to the ground, while measurements extracted for 1100 m AGL are used as a proxy for the vertical velocities at WFJ. The high-resolution wind lidar data are grouped by hour and each fitted to half Gaussian probability density functions (PDFs) with zero mean and standard deviation σ_w. An hourly PDF of updraft velocities is provided in the Supplement as an example of the calculation method we followed here (Figure A2). Employing the "characteristic velocity" approach of Morales and Nenes (2010), the PDF-averaged values of N_d and S_{max} are calculated by applying the parameterization using a single characteristic velocity, w^*=0.79σ_w. This approach has been shown to successfully predict cloud-scale values of N_d in field studies for cumulus and stratocumulus clouds (e.g., Conant et al., 2004; Fountoukis et al., 2007; Kacarab et al., 2020; Meskhidze et al., 2005). The droplet closure carried out in this study is also used to support the validity of this approach for alpine MPCs. To determine the σ_w values used in the closure

study (Section 2.4.2.1), we isolated the segments of the wind lidar measurements that correspond to each cloud event observed by the HoloBalloon platform. The subsequent fitting of the measured updraft velocities to half Gaussian PDFs revealed a σ_w value representative of each cloud. The accuracy of the wind lidar products is affected by precipitation, as the measured updraft velocities might be masked by the terminal fall velocity of the hydrometeors. We therefore use disdrometer measurements to identify and exclude precipitating periods from our analysis. Aiming to examine how N_d responds to different vertical velocity–aerosol situations, potential N_d for both sites are calculated at 10 values of σ_w between 0.1 and 1.0 m s^{-1} (Section 2.4.2.4). Note that we use the term "potential" droplet number throughout this study, as its calculation is performed regardless of the actual existence of clouds over the measurement sites.

2.4 Results and discussion

2.4.1 Particle number, CCN concentration, and κ at WOP and WFJ

The total aerosol number concentration (N_{aer}) time series (integrated aerosol size distribution) together with horizontal wind speed and direction measurements are depicted for both sites in Figure 2.1. The N_{aer} data points of WFJ are colored by κ (Section 2.3.2), while the orange solid line is used as a trace for WOP time series, as κ was not determined for the site owing to a lack of corresponding CCN measurements. Aiming to interpret the aerosol variations and the potential differences observed between valley and high-altitude measurements, the two-week period of interest is divided into two different subperiods. During 24 and 28 February, a high-pressure system was dominant over Europe with clear skies and elevated temperatures (Figure A3). During this first subperiod, the N_{aer} varies considerably and tends to follow a diurnal cycle that anticorrelates between the two sites (Figure 2.1a). As expected, most of the time the concentrations at WOP are elevated with respect to WFJ because the N_{aer} in the valley is influenced by local sources, which during this time of the year includes emissions from biomass burning (BB) (Lanz et al., 2010). N_{aer} at WOP peaks in the evening, reaching up to $\sim 10^4$ cm^{-3}, presumably because of BB emissions in the valley, which seem to stop around midnight (Figure 2.1a). Up to 2 orders of magnitude lower N_{aer} is measured at the same time at the WFJ site. In the afternoon, N_{aer} at WFJ approach those observed at WOP, indicating that the two sites are possibly experiencing similar air masses. The κ for WFJ seems to follow a clear temporal pattern as well, ranging between ~0.1–0.4 with a minimum in the afternoon when the two sites experience the same air masses. Low N_{aer} values are accompanied by higher κ, while at higher N_{aer} conditions less hygroscopic aerosols are recorded (Figure 2.1a).

The above diurnal cycles and their relationships can be understood in terms of BL dynamics typically occurring in mountain–valley systems (Chow et al., 2013). During daytime under clear sky conditions, the slopes and the valley itself are warmed by solar radiation, causing rising of the BL and additionally the production of buoyant air masses that rise up the slope toward the summit (through "upslope" and "up-valley" winds) (Okamoto & Tanimoto, 2016). This hypothesis can be further supported by the fair weather recorded by the weather station at WFJ until 28 February (Figure A3). The buoyant upslope flow could then transport polluted air masses originating from the BL of the valley up to the WFJ site, elevating the concentrations of less hygroscopic aerosols observed in the afternoon. The situation reverses during nighttime, when cold air descends from the slopes (downslope winds) and flows out of the valley (down-valley winds) due to the radiative cooling of the surface. The less polluted air observed during the early hours of the day before sunrise indicates that the WFJ station remained in the free troposphere (FT), with lower N_{aer} and more aged air (i.e., larger κ) with a more prominent

accumulation mode (Baltensperger et al., 1997; Jurányi et al., 2011; Kammermann et al., 2010; Seinfeld & Pandis, 2006, pp. 376–378).

Another consideration is that the upslope flow that "connects" the valley and the mountain-top site may not only be driven by thermal convection but also from mechanically forced lifting. The latter mechanism is caused by the deflection of strong winds by a steep mountain slope and it can be of great importance depending mainly on the height of the mountain and the mean speed of the wind (Kleissl et al., 2007). The local wind effects can be further interpreted looking at the MeteoSwiss time series of wind speed and direction for both stations (Figure 2.1b, c). Wind measurements at the WFJ station recorded a strong wind speed reaching up to ~11 m s^{-1} from the easterly–northeasterly directions between 24 and 28 February. The wind direction measured at WFJ coincides with the relative location of WOP site (see black dashed line in Figure 2.1c). The steep orography over the Alps would transform part of this strong horizontal motion into vertical motion and transport air from WOP to WFJ, as seen in other alpine locations like Jungfraujoch (e.g., Hoyle et al., 2016). A detailed analysis, however, is out of the scope of this study.

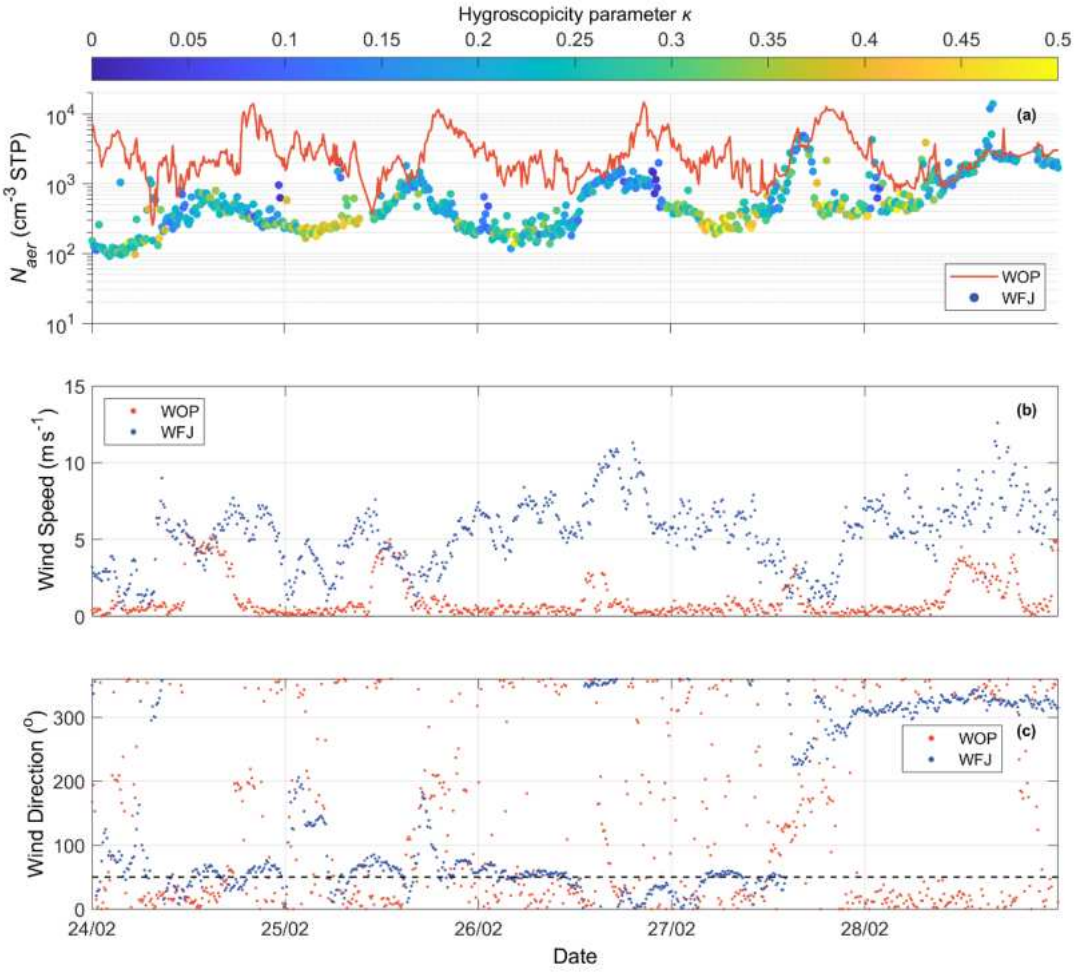

Figure 2.1 (a) N_{aer} under standard temperature and pressure conditions (cm^{-3} STP) at WOP (orange line) and at WFJ (circles colored by κ), (b) wind speed (m s^{-1}), and (c) wind direction (in degrees) obtained from the MeteoSwiss observation stations at WFJ (blue dots) and Davos (orange dots) between 24 and 28 February 2019. The black dashed line indicates the relative direction of WOP to WFJ. Each day is referenced to 00:00 UTC.

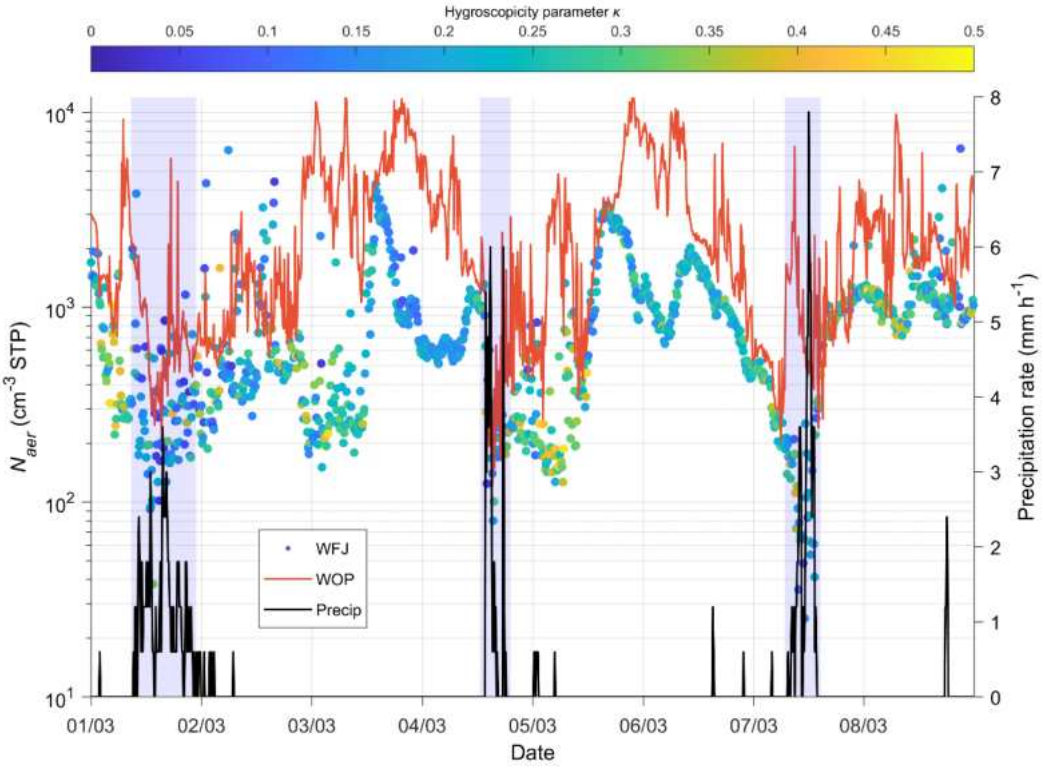

Figure 2.2 N_{aer} (cm^{-3} STP) at WOP (orange line) and at WFJ (circles colored by κ). The black solid line represents the precipitation rate (mm h^{-1}) recorded from the MeteoSwiss observation station for each 10 min interval at WFJ between 1 and 8 March 2019. The blue shaded areas represent the periods when precipitation recorded at the WFJ site is most intense.

Similar to Figure 2.1a, Figure 2.2 illustrates the N_{aer} time series measured at both sites along with the precipitation rate recorded by the MeteoSwiss station at WFJ during the time period between 1 and 8 March 2019. Meteorological observations show the pressure and temperature dropping (Figure A3) together with intense snow and rain events, associated with the passage of cold fronts over the region. Three intense precipitation events are visible in our dataset occurring on 1, 4, and 7 March 2019 (blue shaded areas in Figure 2.2) creating up to 7.8 mm h^{-1} of precipitation. The most intense drop in N_{aer} is seen to occur during and after the precipitation events, with the aerosol concentrations dropping to less than 200 cm^{-3} (100 cm^{-3}) at WOP (WFJ). This is not the case for the last event, where a big "spike" of N_{aer} is observed before the precipitation event in the WOP time series, which is in contrast with the concurrent sharp decrease in N_{aer} (< 20 cm^{-3}) observed at WFJ. This could be an indication of a local source affecting the N_{aer} recorded in the valley. During dry weather conditions, we can notice again the aerosol time series correlating during the afternoon and anticorrelating later in the evening and early morning hours. On 3 March, a steep increase in N_{aer} is seen in the WFJ time series reaching up to ~4000 cm^{-3}, which is followed by a period of several hours with low hygroscopicity values (κ < 0.2) indicating once more the influence of freshly emitted particles arriving at WFJ from the BL of lower altitudes. Additionally, between 1 and 8 March, the diurnal cycle of particle hygroscopicity is less pronounced compared to the period between 24 and 28 February. Especially on 1 and 7 March, less hygroscopic aerosols (κ < 0.1) – hence less effective CCN particles – are found at WFJ (Figure 2.2). This is likely from either precipitation removing aerosol particles through diffusive and impaction processes or the removal of aerosol particles that first activate and then are removed by precipitation. Also,

because N_{aer} drops, fresh local emissions become more important, further justifying the predominance of low κ values.

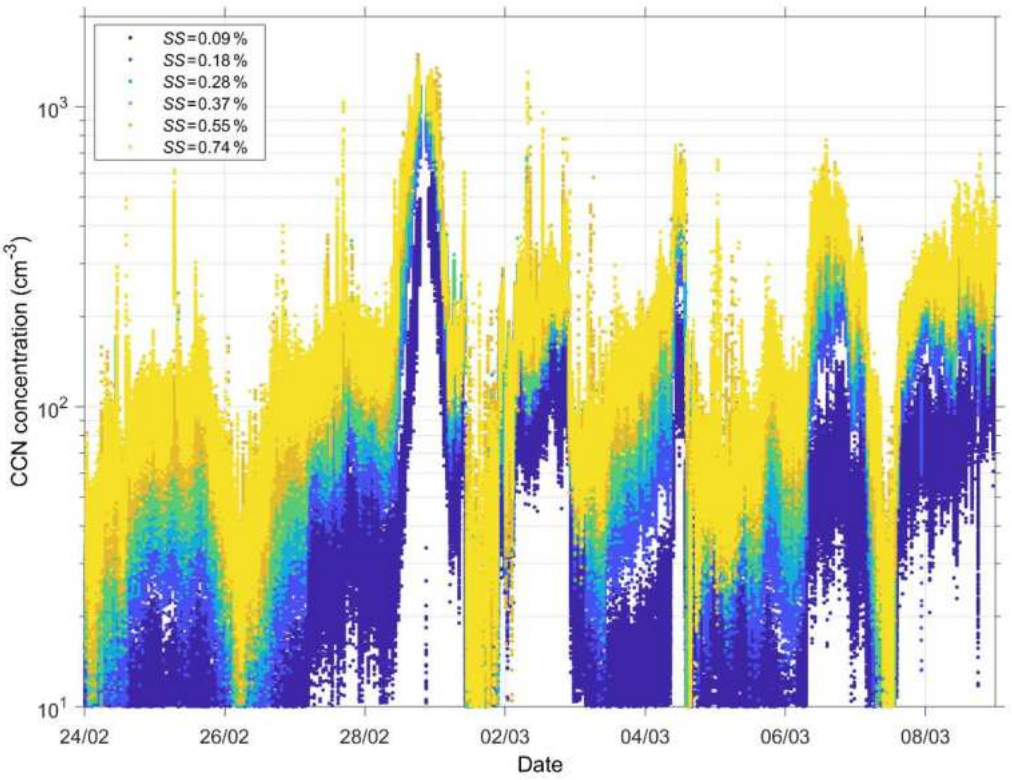

Figure 2.3 Time series of in situ CCN number concentrations (cm^{-3}) at WFJ for different levels of supersaturation (SS) with respect to water between 24 February and 8 March 2019.

Figure 2.3 presents the CCN number concentration time series measured at ambient conditions at WFJ for all six supersaturations. Throughout the two-week measurement period the recorded CCN number concentrations do not seem to follow a clear temporal pattern. The absence of a diurnal cycle in CCN properties measured at Jungfraujoch during winter was also pointed out in the study by Jurányi et al. (2011) because the site is mainly in free tropospheric conditions during most of the winter. According to Figure 2.3, the observed CCN concentrations tend to be low ($\sim 10^2$ cm^{-3}) even at the highest SS (0.74%), which is expected given that WFJ is a remote continental measurement site with CCN concentrations that are typical of free tropospheric continental air (Fanourgakis et al., 2019; Hoyle et al., 2016; Jurányi et al., 2010, 2011). This is again in line with the measured monthly median values of CCN (at SS=0.71%) reported by Jurányi et al. (2011) being equal to 79.1 and 143.4 cm^{-3} for February and March 2009, respectively. Some local CCN spikes are, however, recorded during the evening of 28 February and at the beginning of March (e.g., on 2, 4 and 6 March), with the observed values of CCN reaching up to 650 cm^{-3} at SS=0.09% (lowest SS) and 1361 cm^{-3} at SS=0.74% (highest SS). Considering that WFJ is a site frequently located in the FT, sudden fluctuations in the CCN concentrations could be related to the vertical transport of freshly emitted particles (e.g., wood burning or vehicle emissions) from the valley floor in Davos. It is also worth noting that some aerosol spikes observed on the 3 March ($\sim$3350 cm^{-3}) and the 5 March ($\sim$2100 cm^{-3}) in the WFJ time series (Figure 2.2) are not accompanied by a corresponding peak in the CCN time series. This indicates the presence of small aerosol particles that activate above 0.74% supersaturation (i.e., particles with a diameter smaller than $\sim$25 nm). This

case could also be associated with new particle formation (NPF) events. A previous study by Herrmann et al. (2015) reported the aerosol number size distribution at Jungfraujoch over a 6-year period indicating that NPF was observed during 14.5% of the time without a seasonal preference. Tröstl et al. (2016) also showed that NPF significantly adds to the total aerosol concentration at Jungfraujoch and is favored only under perturbed FT conditions (i.e., BL injections). Finally, during the three intense precipitation events (on 1, 4 and 7 March) we can identify again that the wet removal of the more hygroscopic aerosols (Figure 2.2) suppresses the presence of cloud-activating particles, at times depleting the atmosphere almost completely from CCN (Figure 2.3). This is clearly shown on 1 and 7 March, when the CCN number measured at 0.74% supersaturation drops below 10 cm^{-3}, which is extremely low for BL concentrations.

The aerosol hygroscopicity parameter derived from all CCN data collected between 24 February and 8 March is presented in Figure 2.4a. The red solid line represents the hourly averaged hygroscopicity values over one complete instrument supersaturation cycle. The hygroscopic properties of the particles at WFJ vary as a function of supersaturation, exhibiting on average lower values (∼0.1) at high SS and higher values (∼0.3) at the lower SS. Since the supersaturation inversely depends on particle size, Figure 2.4a indicates that the hygroscopicity of the particles drops by almost 60% as the particles are getting smaller (i.e., as the supersaturation increases). Table 2.2 summarizes the mean values of κ and D_{cr} and their standard deviations, as calculated for each measured SS. The anticorrelation seen between the instrument SS and D_{cr} is reasonable if we consider that the latter represents the minimum activation diameter in a population of particles; therefore, only the particles with a D_{cr} > 193.54 nm are able to activate into cloud droplets at low D_{cr} values (0.09%). The hourly averaged κ at each SS slot falls within a range of ∼0.2 and ∼0.3, which is a representative value of continental aerosols (Andreae and Rosenfeld, 2008; Rose et al., 2008).

Table 2.2 Average κ and D_{cr} values at WFJ for each SS measured between 24 February and 8 March 2019. Uncertainty for each value is expressed by the standard deviation.

SS (%)	κ_{mean}	$D_{cr,mean}$
0.09	0.26 ± 0.10	193.54 ± 29.58
0.18	0.31 ± 0.13	116.80 ± 22.20
0.28	0.25 ± 0.13	96.69 ± 21.62
0.37	0.24 ± 0.13	82.67 ± 20.93
0.55	0.20 ± 0.12	68.30 ± 20.95
0.74	0.19 ± 0.11	58.11 ± 17.54

The hygroscopicity parameter κ along with the inferred ε_{org} (Equation 2.2) are shown in Figure 2.4b as a function of particle size. Compared to smaller particles, the higher κ of larger particles (> 100 nm) is consistent with them being more aged and with a lower fraction of organics. The smaller particles are possibly enriched in organic species, which is consistent with the notion that air masses in the valley can contain large amounts of freshly emitted BB smoke with lower κ. Aerosol particles in the FT are considerably more aged (Seinfeld and Pandis, 2006, pp. 376–378) and exhibit higher values of κ and consequently lower values of ε_{org}. The chemical composition of sub-100 nm particulate matter was therefore presumably dominated by organic material transported from the valley, while the higher κ

values characterizing the larger particles are consistent with the more aged character of free tropospheric aerosols (e.g., Jurányi et al., 2011). The higher ε_{org} inferred for the smaller particles suggests that mixing between fresh emissions in the valley and the free tropospheric aerosols might also be taking place at WFJ.

2.4.2 Droplet formation in the alpine region

2.4.2.1 Method evaluation against direct observations

During the RACLETS campaign, planar and dendritic ice particles were collected from supercooled clouds at WFJ aiming to examine their refreezing ability. A detailed description of the sampling methodology can be found in Mignani et al. (2019). Between 1 and 7 March, images of single dendrites were taken and analyzed visually for the degree of riming (Figure A4). The estimated riming degree varies from 1 (lightly rimed) to 4 (heavily rimed) following the categorization of Mosimann et al. (1994). Some representative images of each measured riming degree are shown in Figure A4b in the Supplement. Although images were captured intermittently, they were taken within all three intense precipitating events occurring during the period of interest (blue shaded areas in Figure 2.2). All dendrites captured were at least lightly rimed (i.e., riming degree=1), which provides direct evidence for the co-existence of supercooled droplets and ice in clouds. Except the indirect evidence of the presence of MPCs over WFJ, Figure 2.5 provides an overview of the direct microphysical measurements carried out by the HoloBalloon at WOP (Section 2.3.1.3). Three cloud events are sampled during 7 and 8 March, a more detailed description of which can be found in Ramelli et al. (2021a, b). The observed low-level clouds are likely produced by orographic lifting when the low-level flow is forced to ascent over the local topography from Klosters to WOP producing local updrafts and thus water supersaturated conditions. The cloud LWC measurements from the holographic imager display significant temporal variability that is also related to variations in the altitude of the tethered balloon system, as it tends to follow an adiabatic profile (Figure 2.5a, b). Deviations from the adiabatic LWC profile are likely caused by entrainment of dry air within the low-level clouds. During the mixed-phase conditions recorded on 8 March (Figure 2.5b), such deviations could also be attributed to the depletion of N_d through riming and depositional growth. These two processes are frequently found to enhance orographic precipitation in feeder clouds. Indeed, a large fraction of rimed ice particles and graupel were observed that day with HOLIMO between 17:00 and 17:40 UTC (Ramelli et al., 2021b). Throughout the two-day dataset presented in Figure 2.5, the HoloBalloon system samples at altitudes lower than 300 m AGL, providing observations that are representative of BL conditions.

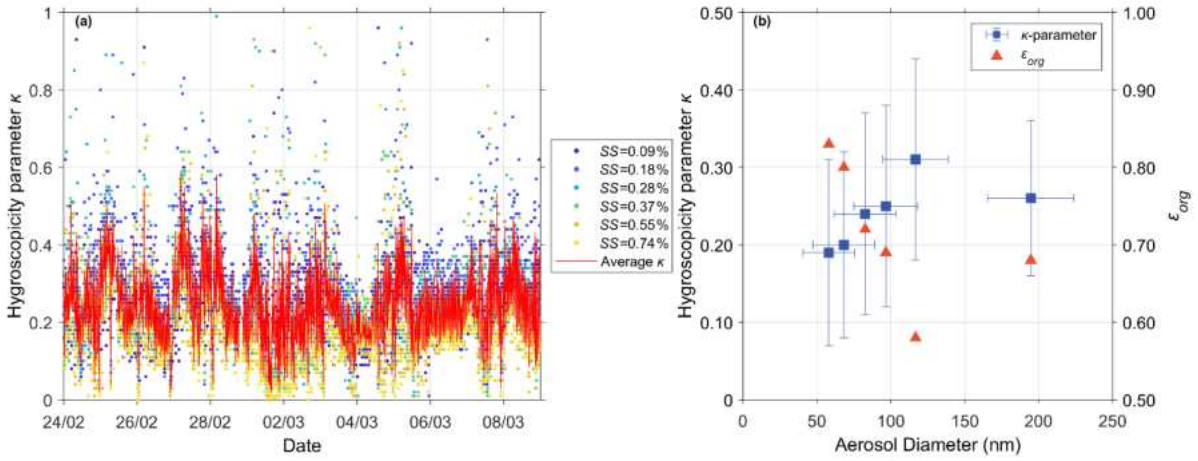

Figure 2.4 (a) Time series of the hygroscopicity parameter κ at WFJ at different levels of SS (0.09 %–0.74 %) throughout the period of interest. The red solid line indicates the hourly averaged κ time series over a complete SS cycle. (b) Size-resolved aerosol hygroscopicity (blue squares) and the respective ε_{org} (orange triangles) calculated for the WFJ site.

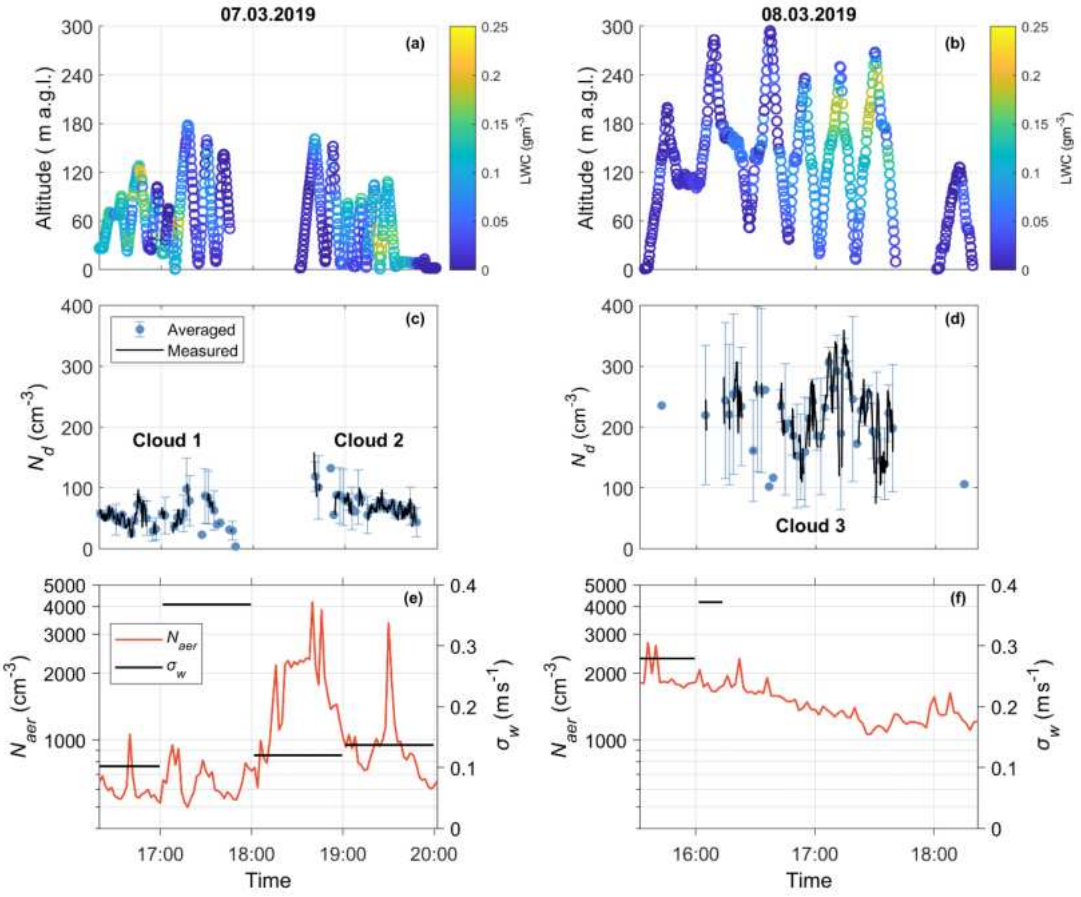

Figure 2.5 Time series of 7 March (a, c, e) and 8 March (b, d, f) showing the vertical profiles of the LWC (g m^{-3}) in panels (a) and (b), the filtered (black lines) and the 2 min averaged (cyan circles) Nd (cm^{-3}) measured at WOP with the HoloBalloon platform in panels (c) and (d), and the corresponding SMPS aerosol concentrations (cm^{-3}) (orange line) and the hourly wind lidar derived σ_w values (m s^{-1}) (black line) in panels (e) and (f). Error bars represent the standard deviation of N_d during the averaging period.

The observed N_d time series collected at WOP are illustrated in Figure 2.5c and d. The measurements corresponding to LWC < 0.05 gm^{-3} are filtered out from the analysis, assuming that they do not effectively capture in-cloud conditions. A similar criterion for LWC was also applied in Lloyd et al. (2015) to determine the periods when clouds were present over the alpine station of Jungfraujoch. Since the measured cloud properties have finer resolution (10–20 s) than the predicted ones, the observed dataset is averaged every 2 min. On 7 March, the balloon-borne measurements were taken in a post-frontal air mass (i.e., passage of a cold front in the morning) and indicated the formation of two low-level liquid layers (Figure 2.5c) over WOP, which is attributed to low-level flow blocking (Ramelli et al., 2021a). Note that small droplets (< 6 µm) cannot be detected by HOLIMO (Section 2.3.1.3) and therefore the reported Nd should be considered a lower estimate. However, the influence of small cloud droplets on the reported LWC is minor, since the contribution of the larger cloud droplets dominates. During the first cloud event, an N_d of up to ∼100 cm^{-3} was recorded, while slightly increased Nd in the range of ∼50–120 cm^{-3} is visible during the second cloud event. On 8 March, a small-scale disturbance passed the measurement location Davos, which brought precipitation (Ramelli et al., 2021b). During the passage of the cloud system, the in situ measurements collected at WOP revealed the presence of a persistent low-level feeder cloud confined to the lowest 300 m of the cloud. The mixed-phase low-level cloud that is shown in Figure 2.5d turned into an ice-dominated low-level cloud after 18:00 UTC (not shown). Throughout this event, N_d seems to range between ∼100– 350 cm^{-3} (Figure 2.5d), while the observed ICNC was in the range of ∼1–4 L^{-1} (see Figure 2.6b in Ramelli et al., 2021b).

According to Figure 2.5e and f, low N_{aer} (<10^3 cm^{-3}) and highly variable σ_w values (∼4 times higher σ_w after 17:00 UTC) are representative of the period throughout which the first cloud formed, while up to 4 times higher N_{aer} is observed during the following two cloud events, with relatively low σ_w values characterizing the second cloud compared to the third one. On 8 March, the disdrometer recorded rainfall over WOP, starting a few minutes after the development of the observed cloud system, which is reflected in the removal of updraft velocity measurements after 16:15 UTC (Figure 2.5f). Note that the concentration measurements presented in Figure 2.5 correspond to ambient temperature and pressure conditions. The contrasted aerosol and vertical velocity regimes, in which the observed clouds are formed, offer a great opportunity to test how the proposed methodology performs under a wide range of aerosol and velocity conditions. Indeed, the mean cloud droplet diameters exhibit a wide range of values, which for WOP range between 10 and 17 µm on 7 March and 8 to 12µm on 8 March (not shown).

The N_d closure performed for the three cloud events observed over WOP during the last two days of the period of interest is presented in Figure 2.6. Note that the predicted N_d is evaluated using the updraft velocity PDF calculated for each cloud period, rather than the hourly σ_w data shown in Figure 2.5e and 5f (Section 2.3.3). Owing to the precipitation occurrence during 8 March, we focused on the 15 min time period between 16:00 and 16:15 UTC to determine a relevant updraft velocity from the wind lidar measurements representative of Cloud 3. The Gaussian fit to the updraft velocities gave a distribution with σ_w = 0.24 and 0.16 m s^{-1} for the first two clouds present on 7 March and σ_w = 0.37 ms^{-1} for the cloud system observed on 8 March. The $w*$ values used to apply the droplet parameterization are therefore between 0.1–0.4ms^{-1} (Section 2.3.3). Figure 2.6 indicates that the parameterization predictions agree to within 25% with the in situ cloud droplet number concentrations. A similar degree of closure is frequently obtained for other in situ studies (Fountoukis et al., 2007; Kacarab et al., 2020; Meskhidze et al., 2005; Morales Betancourt et al., 2011); however, these focused on liquid-phase clouds. Here we show that the methodology can also work for MPCs (i.e., Cloud 3 in Figure 2.6). It is important to note here that part of the discrepancy between prediction and measurement could also be related to the underestimation of the measured N_d (Section 2.3.1.3).

Hence, an even better degree of closure is likely. Also, the derived σ_w value used to calculate the predicted N_d for Cloud 1 might be biased low by the lower σ_w values recorded before 17:00 UTC (Figure 2.5e). Nevertheless, the updraft averaging used in the droplet closure study corresponds to the measured Nd averaging time period and, therefore, we do not expect the degree of closure to be affected.

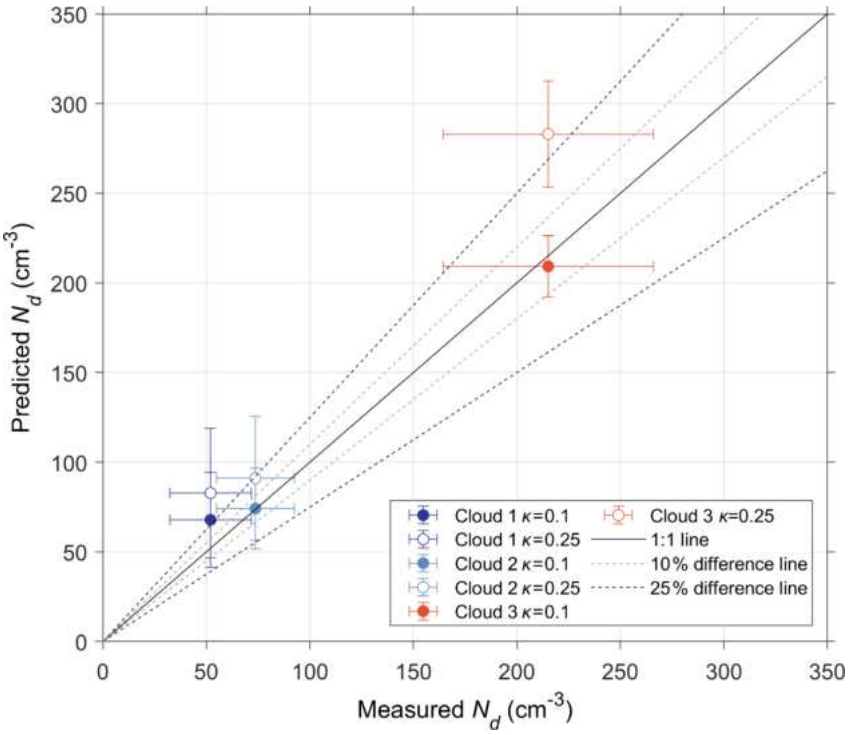

Figure 2.6 Comparison between average predicted N_d (cm^{-3}) with the droplet activation parameterization and observed N_d (cm^{-3}) during the three cloud events on 7 March (blue and cyan circles) and 8 March (orange circles) 2019. For all three cloud events, droplet closure is performed assuming a κ parameter of 0.1 (filled circles) and 0.25 (empty circles). The error bars represent the standard deviation of Nd during each cloud event.

The good agreement between measurements and predictions – even under mixed-phase conditions – reveals that processes like condensation freezing and the removal of cloud droplets through riming and collision coalescence do not disturb the S_{max} and hence the N_d predicted by the parameterization, at least for the given clouds. That said, it is known that pre-existing liquid and ice hydrometeors falling to the activation region of clouds can deplete the supersaturation affecting the number of the activated droplets; such supersaturation depletion effects can be included in the droplet activation parameterization (Barahona et al., 2014; Sud et al., 2013) if needed. Furthermore, the parameterization predictions indicate that the best fit is achieved using a κ of ~0.1 (Figure 2.6). N_{aer} at WOP is likely dominated by lower κ values, indicating that the particles are getting richer in organic material, compared to WFJ, which supports the aerosol analysis carried out in Section 2.4.1. These results are robust, indicating that for non-precipitating BL clouds the proposed calculation method captures cloud droplet formation at WOP and WFJ.

2.4.2.2 Potential droplet formation at WOP and WFJ

According to the methodology proposed in Section 2.3.3, using the in situ measured N_{aer}, the estimated chemical composition, and the observed updraft velocity range, we determine the potential N_d and S_{max} that would form over both measurement sites. At WOP, clouds are formed locally due to the local topography (Ramelli et al., 2021a, b), supporting the use of surface measured aerosol to estimate the potential N_d over this site. This is further supported by the good agreement between predicted and measured N_d (Section 2.4.2.1). A similar closure study could not be repeated for WFJ owing to a lack of in situ data; however, the air masses sampled (i.e., those given as input to the parameterization) are often in the FT, so they should contain the same aerosol as the one used to form the clouds. This does not apply under perturbed FT conditions, which are, however, accompanied by the presence of less hygroscopic particles over the mountain-top site and are less likely related to cloud formation (Section 3.4.1). Here we assume a κ of 0.25 to calculate the potential droplets for WFJ according to our CCN-derived hygroscopicity values (Table 2.2) and given that S_{max} usually ranges between ~0.1%– 0.3%. In estimating the potential droplets for WOP, we use a κ of 0.1 given that the aerosol is likely strongly enriched in organics; the good degree of closure supports its selection (Section 2.4.2.1). Figure 2.7 depicts the potential N_d and the corresponding S_{max} time series calculated at ambient conditions for WOP (orange dots) and WFJ (blue dots) using cloud updraft velocities that are indicative of the observed σ_w range (Section 2.4.2.4), namely 0.1, 0.3, 0.6, and 0.9 m s^{-1}. The same behavior is seen for all four σ_w values selected while, as expected, larger values of N_d and S_{max} are achieved at higher σ_w. During the first days of the period of interest, the calculated N_d at WOP (Figure 2.7a, c, e, g) is up to 10 times larger than at WFJ, despite the lower κ values characterizing its aerosol population. WFJ tends to have lower N_d due to the lower N_{aer} recorded. It is also important to highlight the anticorrelation between S_{max} and N_d values arising from the nonlinear response of droplet number and maximum cloud parcel supersaturation to fluctuations in the available aerosol and CCN concentrations (Bougiatioti et al., 2016; Kalkavouras et al., 2019; Reutter et al., 2009). Higher N_{aer} elevates the potential N_d values. The available condensable water is then shared among more growing droplets, depleting the supersaturation. Even more interesting is the fact that until 28 February the calculated N_d time series at WOP show a pronounced diurnal cycle, similar to the total N_{aer} time series (Section 2.4.1). Lower N_d values are visible after midnight, presumably due to a paucity of BB activities in the valley. Droplet concentrations at WFJ do not follow a diurnal pattern in contrast to the aerosol data (Figure 2.1a). However, the activation fraction (i.e., N_d/N_{aer}) at WFJ displays a clear diurnal variability until the end of February (Figure A5).

Through comparison with the MeteoSwiss precipitation measurements at WFJ (Figure 2.2), it should be emphasized again that during the second sub-period of interest the occurrence of precipitation is followed by a depression in N_d (Figure 2.7a, c, e, g) and a concurrent increase in S_{max} reaching up to ~1% (Figure 2.7b, d, f, h). Especially at WFJ, N_d drops almost to zero on 1, 4, and 7 March, when precipitation is most intense (blue shaded areas in Figures 2.2 and 2.7). These trends are related to the washout of hygroscopic material observed at WFJ (Figure 2.2) leading to the extremely low CCN concentrations (~10 cm^{-3}) measured during these 3d (Figure 2.3). During the first two intense precipitation events, the N_{aer} is relatively high compared to the third event, with concentrations reaching up to ~300 cm^{-3} at both stations (Figure 2.2). The small activation fraction (Figure A5) combined with the high S_{max} values indicate once more that small particles that activate into cloud droplets only above 0.3% to 0.5% of supersaturation are present at both stations. However, this behavior is not seen on 7 March at WFJ.

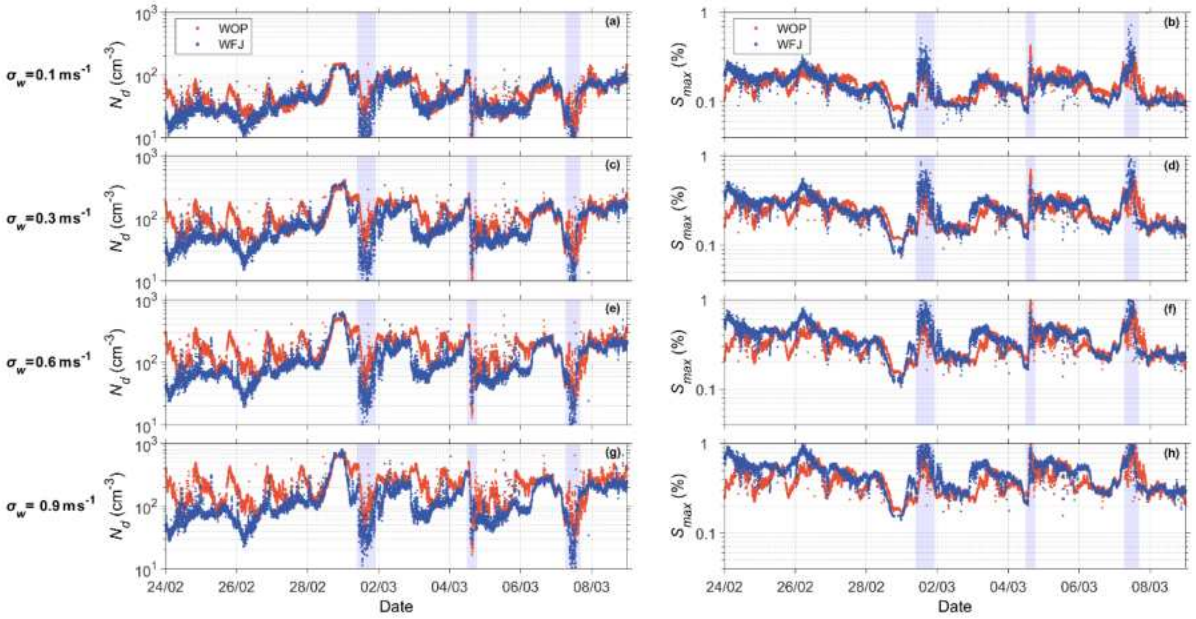

Figure 2.7 Calculated time series of N_d (cm^{-3}) (left panels) and S_{max} (%) (right panels) for updraft velocities of σ_w=0.1 m s^{-1} in panels (a) and (b), 0.3 m s^{-1} in panels (c) and (d), 0.6 m s^{-1} in panels (e) and (f), and 0.9 m s^{-1} in panels (g) and (h) during the period of interest at WOP (orange dots) and WFJ (blue dots). The blue shaded areas represent the intense precipitating periods shown in Figure 2.2.

2.4.2.3 Droplet behavior under velocity-limited conditions

Combining the potential N_d and the corresponding S_{max} with the N_{aer} data yields important information on whether clouds are sensitive to vertical velocity or aerosol changes. Cloud studies (e.g., Ghan et al., 1998; Jensen & Charlson, 1984; Nenes et al., 2001; Reutter et al., 2009; Twomey, 1993) have long recognized the role of water vapor competition on droplet formation, while the success of mechanistic parameterizations for climate models relies on the ability to capture this effect accurately (e.g., Ghan et al., 2011; Morales Betancourt & Nenes, 2014). Twomey (1993) discusses this conceptually and states that competition may be fierce enough to reduce N_d with increasing N_{aer}, which was later demonstrated by Ghan et al. (1998) to occur for mixtures of sulfate aerosol and sea spray. Reutter et al. (2009) did not focus on such extreme conditions of water vapor competition, but rather situations that are consistent with dominance of anthropogenic pollution in clouds. Indeed, for high N_{aer}, droplets in clouds become insensitive to aerosol perturbations, giving rise to the so-called "velocity-limited cloud formation". Figure 2.8 displays this by presenting the response of the calculated Nd to changes in N_{aer} for a representative range of updraft velocities prevailing over WOP (top panels) and WFJ (bottom panels). The data are colored by the respective S_{max} achieved in cloudy updrafts. For low σ_w values (Figure 2.8a, d) we can identify that above an N_{aer} of ~300 cm^{-3}, the N_d at both stations reaches a plateau where it becomes insensitive to further aerosol changes. At WFJ, the same behavior is seen for intermediate σ_w values and N_{aer} 1000 cm^{-3} (Figure 2.8f). Kacarab et al. (2020) and Bougiatioti et al. (2020) examined a wide range of ambient size distributions and proposed that clouds became velocity limited when S_{max} dropped below 0.1%. This reflects the increasingly fierce competition for water vapor during droplet formation, which allows only a few particles to activate into cloud droplets.

Building upon these findings, we used the calculated S_{max} as an indicator for aerosol- or velocity-limited conditions prevailing over the Alps. The horizontal dashed lines plotted in Figure 2.8a, e, and f illustrate a plateau, where S_{max} <0.1% and the modulation of the N_d is driven mostly by the cloud dynamics,

hence the updraft velocity variability, rather than aerosol variations. This plateau is termed the limiting droplet number (N_d^{lim}), following Kacarab et al. (2020), and is essentially the maximum N_d that can be formed under these vertical velocity conditions. The vertical-velocity regime is therefore strictly defined as whenever S_{max} drops below 0.1% and N_d approaches N_d^{lim}. Conversely, when S_{max} in clouds exceeds 0.1%, droplet formation in the BL of both measurement sites is in the aerosol-limited regime, as the S_{max} is high enough for clouds to be responsive to aerosol changes.

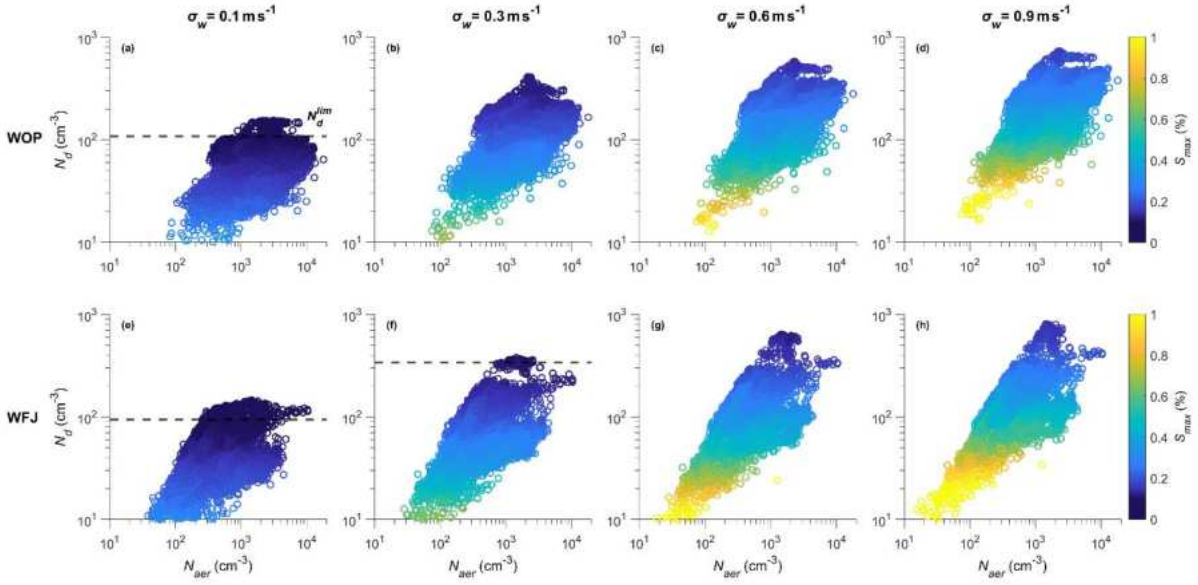

Figure 2.8 In situ N_d (cm^{-3}) vs. N_{aer} (cm^{-3}) for updraft velocities of σ_w=0.1 m s^{-1} in panels (a) and (e), 0.3 m s^{-1} in panels (b) and (f), 0.6 m s^{-1} in panels (c) and (g), and 0.9 m s^{-1} in panels (d) and (h) during the period of interest at WOP (top panels) and WFJ (bottom panels). Data are colored by S_{max} (%).

An alternative way of examining the N_d^{lim} response to changes in σ_w is shown in Figure 2.9. It should be noted that the N_d^{lim} values shown on this figure are determined by calculating the averaged N_d achieved whenever S_{max} <0.1% for each examined σ_w value. At WOP, droplet formation is in the velocity-limited regime only for low σ_w values, namely 0.1 and 0.2 m s^{-1}, when the activated particles have more time to deplete the gas phase and the S_{max} reached is that required to activate only the largest particles. At WFJ the prevailing dynamics create velocity-limited conditions even for more turbulent boundary layers when σ_w reaches up to 0.5 m s^{-1}. N_d^{lim} (cm^{-3}) is linearly correlated with σ_w (m s^{-1}), which can be described as $N_d^{lim} = 1137.9\,\sigma_w - 17.1$ (Figure 2.9). As a result, doubling σw from 0.1 to 0.2 m s^{-1} increases N_d^{lim} by ~60% for both sites, while transitioning from 0.2 to 0.4 m s^{-1} further increases N_d^{lim} by ~45% and finally an additional ~20% increase in N_d^{lim} occurs for WFJ for the 0.4–0.5 m s^{-1} velocity range. Remarkable agreement is seen for corresponding trends between N_d^{lim} and σ_w calculated for marine Stratocumulus clouds formed under extensive BB aerosol plumes over the Southeast Atlantic (SEA) Ocean (Kacarab et al., 2020), along with BL clouds formed in the Southeast United States (SEUS) (Bougiatioti et al., 2020). Both studies have followed the same probabilistic approach for computing N_d as the one followed here. This realization is important as it implies that for regions where velocitylimited conditions are expected (i.e., under particularly high particle loads), $N_d \sim N_d^{lim}$ and the N_d^{lim}– σ_w relationship can be used to diagnose σ_w from retrievals of

droplet number for virtually any type of BL cloud using a number of established methods (e.g., Grosvenor et al., 2018; Snider et al., 2017).

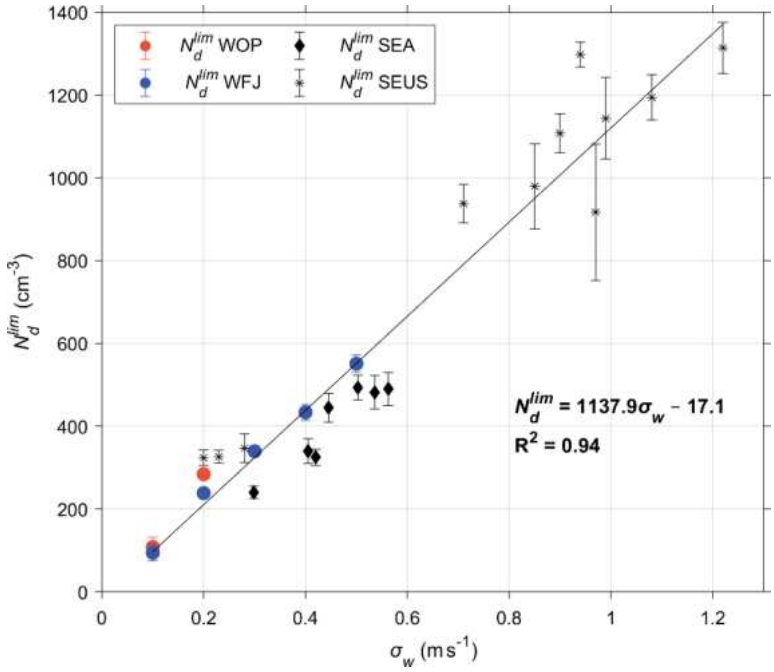

Figure 2.9 N_d^{lim}(cm^{-3}) against σ_w (m s^{-1}) calculated when velocity-limited conditions are met at WOP (orange circles) and WFJ (blue circles) throughout the period of interest. Superimposed are the corresponding values calculated for clouds forming over the SEA Ocean (rhombuses) and over the SEUS (asterisks).

2.4.2.4 σw and observed Nd determine if droplet formation is aerosol or velocity limited

Observations of N_d when compared against N_d^{lim} can potentially be used to deduce if droplet formation is velocity or aerosol limited. This is important because it indicates whether aerosol fluctuations are expected to result in substantial N_d responses in clouds. The strong correlation between σ_w and N_d^{lim} enables this comparison. From the σ_w time series together with the linear N_d^{lim}–σ_w relationship (Section 2.4.2.3; Figure 2.9) we obtain estimates of N_d^{lim} for both measurement stations (black dashed line in Figure 2.10a, b) and the ratio N_d/N_d^{lim} (magenta dotted lines in Figure 2.10a, b). The N_d time series calculated for WOP tend to be approximately one third of N_d^{lim} for most of the observational period (colored circles in Figure 2.10a, b), while for WFJ the same ratio is even lower (~1/4). Focusing on the relatively short periods when S_{max} values drop below 0.1%, we estimate that droplet formation over both measurement sites enters a velocity-limited regime when the ratio N_d/N_d^{lim} exceeds a critical value of 0.65, with the most prevalent value being at ~0.9 (Figure A6).

Throughout the period of interest, velocity-limited conditions are met at WOP (WFJ) with a frequency of ~0.5% (~2.5%) of the total time, again reflecting the sensitivity of droplet formation to aerosol fluctuations. During nighttime, however, when lower σ_w values (~0.1 m s^{-1}) are recorded at WOP (Figure 2.10c), we can observe some short periods characterized by intermediate to high N_{aer} (>1000 cm^{-3}) when the ratio N_d/N_d^{lim} exceeds ~0.65, indicating that droplet variability is driven by updraft velocity. The σ_w values calculated at WFJ do not display a clear temporal pattern (Figure 2.10d) but

are generally higher than those recorded at the valley site. This is expected considering the steepness of the topography than can cause updraft velocities to be higher, especially for air masses approaching the site from the northeasterly directions. Over the high mountain-top site, cloud formation is in the velocity-limited regime (i.e., 0.65) under high N_{aer} (~1500 cm^{-3}) and higher σ_w conditions (~0.8 ms^{-1}). These conditions can be created when polluted air masses from the valley site are vertically transported to WFJ.

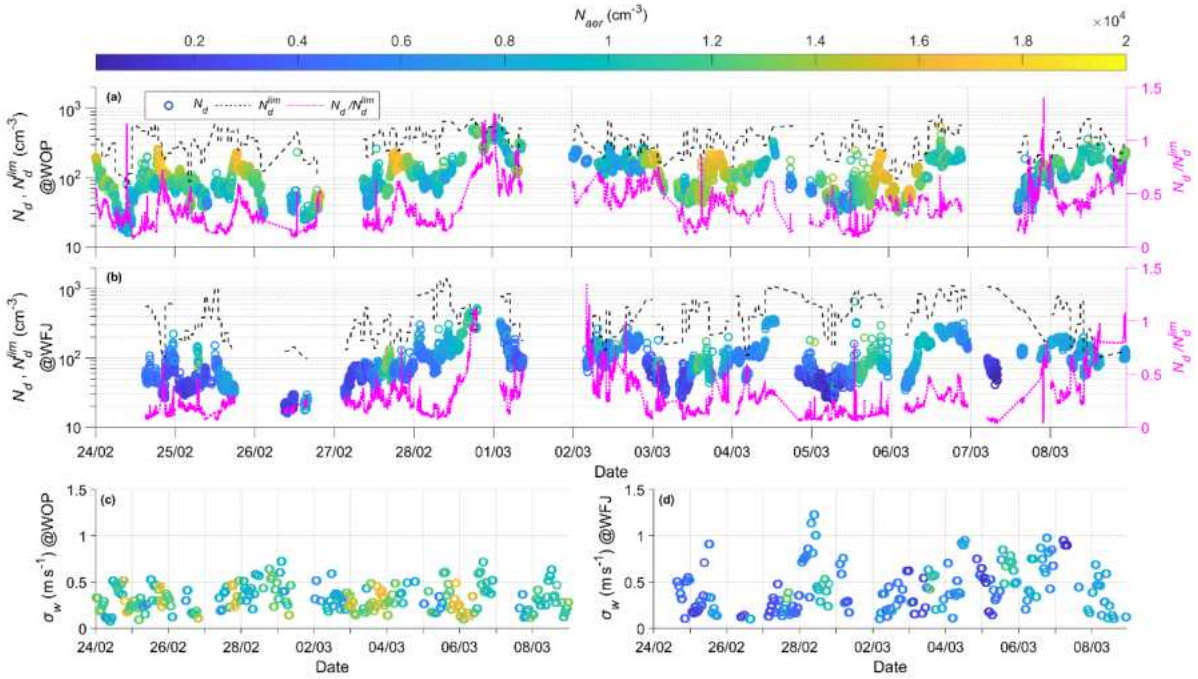

Figure 2.10 Time series of potential N_d (cm^{-3}) (circles colored by N_{aer}) along with N_d^{lim} (cm^{-3}) (black dashed line) and the ratio between those two (i.e., N_d/N_d^{lim}) (magenta dotted line), together with the timeseries of the calculated σ_w (m s^{-1}) (circles colored by N_{aer}), as estimated for WOP (a, c) and WFJ (b, d).

2.5 Summary and conclusions

The current study focuses on the aerosol–CCN–cloud droplet interplay in alpine clouds sampled during the RACLETS field campaign over a two-week period of measurements conducted in the valley (WOP) and at the mountain-top station (WFJ). Our main objective was to investigate the drivers of droplet formation in MPCs formed in the region and understand in which situations N_d is sensitive to aerosol perturbations.

Overall, lower N_{aer} was systematically recorded at WFJ, indicating that the site is influenced by FT conditions. Deviations from this behavior are observed during fair weather conditions, when injections from the BL of lower altitudes can cause up to an order of magnitude elevation in the N_{aer} measured at WFJ. Combining the particle size distribution and CCN number concentration measured at WFJ, the average hygroscopicity parameter κ is about 0.25, consistent with expectations for continental aerosol. The size-dependent κ reveals that accumulation mode particles are more hygroscopic than the smaller ones, which we attribute to an enrichment in organic material associated with primary emissions in the valley. The hygroscopicity of the particles at WFJ exhibit variations until February 28,

which could reflect BL injections from the valley. Precipitation events occurring between 1 and 8 March efficiently decrease N_{aer}, sometimes leaving some less hygroscopic particles.

Wind lidar products collected at WOP constrain the PDF of updraft velocities, which combined with observed size distributions and hygroscopicity can be used to calculate the N_d in clouds. We show predictions to agree within 25% with the limited observations of N_d available. While this degree of closure has been achieved in past studies for liquid-phase clouds, it has not been done at temperatures below freezing and with clouds containing ice, as has been done here.

Combining the potential N_d and the corresponding S_{max} with the aerosol size distribution data we sought to identify regimes where the clouds formed are aerosol or velocity limited. We found that when sufficient aerosol is present to decrease S_{max} below 0.1%, alpine clouds become velocity limited with the N_d reaching an upper limit, N_d^{lim}~150–550cm^{-3}, that depends on σ_w. Velocity-limited conditions occur when N_d/N_d^{lim} is above 0.65. Based on this understanding, we deduce that droplet formation throughout the period of interest appears most of the time to be aerosol limited. More specifically, at the WOP valley site, clouds become sensitive to updraft velocity variations only during nighttime, when the BL turbulence is low. Conversely, velocity-limited conditions are encountered at WFJ during periods characterized by elevated aerosol and CCN concentrations (> 10^3 cm^{-3}) and higher σ_w values (~0.8 m s^{-1}). Although variations in vertical velocity have not always been found to be the strongest factor influencing the cloud microphysical characteristics, correct consideration of updraft velocity fluctuations is crucial to fully understand the drivers of droplet formation and the role of aerosols as a driver of N_d variability.

Interestingly, we find that the same linear relationship between N_d^{lim} and σ_w that describes the droplet formation during RACLETS holds for warm boundary layer clouds formed in the SEUS (Bougiatioti et al., 2020) and in the SEA Ocean (Kacarab et al., 2020). This implies that the N_d^{lim}– σ_w relationship may be universal, given the wide range of cloud formation conditions it represents. If so, measurements (or remote sensing) of N_d and vertical velocity distribution alone may be used to determine if cloud droplet formation is susceptible to aerosol variations or solely driven by vertical velocity – without any additional aerosol information.

Approaching velocity-limited conditions also carries important implications for ice-formation processes in MPCs, as high N_d means that droplet size and the probability of riming becomes minimum. Indeed, Lance et al. (2011) saw that the concentration of large droplets exceeding 30 μm diameter – critical for rime splintering or droplet shattering to occur – drops considerably for polluted arctic MPCs with LWC ~ 0.2 g m^{-3} and N_d ~ 300–400 cm^{-3}. Assuming that these levels of N_d reflects N_d^{lim}, the corresponding σ_w is 0.3–0.35 ms^{-1} (Figure 2.9), which is characteristic for arctic stratus. The same phenomenon can also occur in the alpine clouds studied here, given that velocity-limited conditions (N_d/N_d^{lim} > 0.65) occur especially during nighttime (Figure 2.10). Therefore, observations of N_d and vertical velocity distribution (i.e., N_d^{lim}) may possibly be used to determine if SIP from rime splintering and droplet shattering is impeded and, if they occur frequently enough, may help explain the existence of persistent MPCs.

3. Secondary ice production processes in wintertime alpine mixed-phase clouds

In this chapter, the focus is on examining the role of secondary ice production in orographic mixed-phase clouds, as observed during the CLACE2014 campaign at the high-altitude station of Jungfraujoch in Switzerland. The analysis primarily involves numerical modeling, evaluated against in-situ ground-based observations. The text is derived from the postprint version of the article:

- **Georgakaki, P.,** Sotiropoulou, G., Vignon, É., Billault-Roux, A.-C., Berne, A., and Nenes, A. (2022): Secondary ice production processes in wintertime alpine mixed-phase clouds, *Atmospheric Chemistry and Physics*, 22, 1965–1988, doi: 10.5194/acp-22-1965-2022.

Paraskevi Georgakaki implemented the droplet-shattering parameterizations with input from Georgia Sotiropoulou, conducted the numerical simulations, analyzed the results, and together with Athanasios Nenes wrote the main paper. Georgia Sotiropoulou provided the updated microphysics scheme with the detailed collisional break-up parameterizations. Étienne Vignon helped with the WRF configuration and set-up. Alexis Berne and Anne-Claire Billault-Roux provided the processed radar data and created Figure B6. Athanasios Nenes organized the research project and supervised the progress. All authors contributed to the scientific interpretation and writing of the paper.

3.1 Summary

Observations of orographic mixed-phase clouds (MPCs) have long shown that measured ice crystal number concentrations (ICNCs) can exceed the concentration of ice nucleating particles by orders of magnitude. Additionally, model simulations of alpine clouds are frequently found to underestimate the amount of ice compared with observations. Surface-based blowing snow, hoar frost, and secondary ice production processes have been suggested as potential causes, but their relative importance and persistence remains highly uncertain. Here we study ice production mechanisms in wintertime orographic MPCs observed during the Cloud and Aerosol Characterization Experiment (CLACE) 2014 campaign at the Jungfraujoch site in the Swiss Alps with the Weather Research and Forecasting model (WRF). Simulations suggest that droplet shattering is not a significant source of ice crystals at this specific location, but breakups upon collisions between ice particles are quite active, elevating the predicted ICNCs by up to 3 orders of magnitude, which is consistent with observations. The initiation of the ice–ice collisional breakup mechanism is primarily associated with the occurrence of seeder–feeder events from higher precipitating cloud layers. The enhanced aggregation of snowflakes is found to drive secondary ice formation in the simulated clouds, the role of which is strengthened when the large hydrometeors interact with the primary ice crystals formed in the feeder cloud. Including a constant source of cloud ice crystals from blowing snow, through the action of the breakup mechanism, can episodically enhance ICNCs. Increases in secondary ice fragment generation can be

counterbalanced by enhanced orographic precipitation, which seems to prevent explosive multiplication and cloud dissipation. These findings highlight the importance of secondary ice and seeding mechanisms – primarily falling ice from above and, to a lesser degree, blowing ice from the surface – which frequently enhance primary ice and determine the phase state and properties of MPCs.

3.2 Introduction

Understanding orographic precipitation is one of the most critical aspects of weather forecasting in mountainous regions (Chow et al., 2013; Roe, 2005; Rotunno & Houze, 2007). Orographic clouds are often mixed-phase clouds (MPCs), containing simultaneously supercooled liquid water droplets and ice crystals (Henneberg et al., 2017; Lloyd et al., 2015; Lohmann et al., 2016). MPCs are persistent in complex mountainous terrain, because the high updraft velocity conditions generate supercooled liquid droplets faster than can be depleted by ice production mechanisms (Korolev et al., 2003; Lohmann et al., 2016). In mid- and high-latitude environments almost all precipitation originates from the ice phase (Field & Heymsfield, 2015; Mülmenstädt et al., 2015), emphasizing the necessity of correctly simulating the amount and distribution of both liquid water and ice (i.e., the liquid-ice phase partitioning) in MPCs (Korolev et al., 2017).

Our understanding of MPCs remains incomplete, owing to the numerous and highly nonlinear cloud microphysical pathways driving their properties and evolution evolution (Morrison et al., 2012). MPCs tend to glaciate over time through the Wegener–Bergeron–Findeisen (WBF) process, which is the rapid ice crystal growth at the expense of the surrounding evaporating cloud droplets (Bergeron, 1935; Findeisen, 1938). Ice crystals falling from a high-level seeder cloud into a lower-level cloud (external seeder–feeder event) or a lower lying part of the same cloud (in-cloud seeder–feeder event) can trigger cloud glaciation and enhance precipitation over mountains (e.g., Mott et al., 2014; Purdy et al., 2005; Ramelli et al., 2021a; Reinking et al., 2000; Roe, 2005). Analysis of satellite remote sensing over the 11-year period, between April 2006 and October 2017, suggests that seeding events are widespread over Switzerland, occurring with a frequency of 31% of the total observations in which cirrus clouds seed lower mixed-phase cloud layers (Proske et al., 2021).

Primary ice formation in MPCs is catalyzed by the action of ice nucleating particles (INPs) (e.g., Hoose & Möhler, 2012; Kanji et al., 2017). However, in-situ observations of MPCs in orographic environments regularly reveal that measured ice crystal number concentrations (ICNCs) are several orders of magnitude more abundant than INPs (Beck et al., 2018; Geerts et al., 2015; Lloyd, et al., 2015; Lowenthal et al., 2019; Mignani et al., 2019; Rogers & Vali, 1987). Model simulations of alpine MPCs frequently fail to reproduce the elevated ICNCs dictated by observations (Dedekind et al., 2021; Farrington et al., 2016; Henneberg et al., 2017).

The inability of primary ice to reproduce the observed ICNCs in orographic MPCs has often been attributed to the influence of surface processes including lofting of snowflakes (i.e., “blowing snow”; (Geerts et al., 2015; Rogers & Vali, 1987), detachment of surface hoar frost (Lloyd et al., 2015), turbulence near the mountain surface or convergence of ice particles due to orographic lifting (Beck et al., 2018) and riming on snow-covered surfaces (Rogers & Vali, 1987). The impact of blowing snow ice particles (BIPs) has been studied thoroughly, either using observations collected in mountainous regions (e.g., Beck et al., 2018; Lloyd et al., 2015; Lowenthal et al., 2019), remote sensing (e.g., Geerts et al., 2015; Rogers & Vali, 1987; Vali et al., 2012) or detailed snow-cover models (e.g., Krinner et al., 2018; Lehning et al., 2006) coupled with atmospheric models (e.g., Sharma et al., 2023; Vionnet et al., 2014). The extent to which BIPS can affect ICNCs in MPCs remains poorly understood.

In-cloud secondary ice production (SIP) – or ice multiplication – processes may also enhance ice production above the concentration of INPs (Field et al., 2017; Korolev & Leisner, 2020). A total of three mechanisms are thought to be responsible for most of the SIP. The first, known as the Hallett–Mossop (HM) process (Hallett & Mossop, 1974), refers to the ejection of small secondary ice splinters after a supercooled droplet with a diameter larger than ∼25μm rimes onto a large ice particle at temperatures between −8 and −3 °C (Choularton et al., 1980; Heymsfield & Mossop, 1984). This SIP mechanism is widely implemented in atmospheric models (Beheng, 1987; Morrison et al., 2005; Phillips et al., 2001) but cannot, on its own, explain the enhanced ICNCs in remote environments (Sotiropoulou et al., 2020; Sotiropoulou, Vignon, et al., 2021; Young et al., 2019), especially for when the conditions required for HM initiation are not fulfilled (e.g., Korolev et al., 2020).

Collisional fracturing and breakup (BR) of delicate ice particles with other ice particles (Griggs & Choularton, 1986; Takahashi et al., 1995; Vardiman, 1978) is another important SIP mechanism. Several field studies in the Arctic (Rangno & Hobbs, 2001; Schwarzenboeck et al., 2009), the Alps (Mignani et al., 2019; Ramelli et al., 2021a) and laboratory investigations (Takahashi et al., 1995; Vardiman, 1978) all show the importance of BR. The latter two studies created the basis for a mechanistic description of BR (Phillips et al., 2017a; Sotiropoulou et al., 2020; Sullivan, Hoose, et al., 2018). Parameterizations of BR have recently been implemented in small-scale (Fridlind et al., 2007; Phillips et al., 2017a; Sotiropoulou et al., 2020; Sotiropoulou, Ickes, et al., 2021; Sullivan, Hoose, et al., 2018; Yano & Phillips, 2011; Yano et al., 2016), mesoscale (Dedekind et al., 2021; Hoarau et al., 2018; Qu et al., 2020; Sotiropoulou, Vignon, et al., 2021; Sullivan, Barthlott, et al., 2018) and global climate models (Zhao & Liu, 2021), each with their own approach towards BR description.

Droplet freezing and shattering (DS) is a third SIP mechanism that can produce significant amounts of ice crystals. It occurs when drizzle-sized drops (diameter exceeding 50 μm) come in contact with an ice particle or INP. A solid ice shell is initially formed around the droplet (e.g., Griggs & Choularton, 1983), and as it thickens, it begins building up pressure that leads to a breakup in two halves, cracking, bubble burst, or jetting (Keinert et al., 2020). The ejection of small ice fragments may occur, the number of which varies considerably (James et al., 2021; Keinert et al., 2020; Kleinheins et al., 2021; Lauber et al., 2018). Experimentally, the fragmentation rate maximizes at temperatures between ∼ −10 and −15 °C (Keinert et al., 2020; Lauber et al., 2018; Leisner et al., 2014). DS can dominate in convective updrafts (Korolev et al., 2020; Lawson et al., 2015; Phillips et al., 2018; Qu et al., 2020). Remote sensing of warm Arctic MPCs suggests DS can be much more conducive to SIP than the HM process (Luke et al., 2021). Single-column simulations by Zhao et al. (2021) support this but are in contrast with small-scale modeling studies (Fu et al., 2019; Sotiropoulou et al., 2020). Mesoscale model simulations of winter alpine clouds formed at temperatures lower than −8 ◦C indicate that DS is not active (Dedekind et al., 2021), while field observations suggest the increasing efficiency of the mechanism at temperatures warmer than −3 °C (Lauber et al., 2021).

Orographic ICNCs in MPCs exceeded the predicted INPs by 3 orders of magnitude, reaching up to ∼1000 L^{-1} at –15 °C during the Cloud and Aerosol Characterization Experiment (CLACE) 2014 campaign at the Jungfraujoch (JFJ) station in the Swiss Alps (Lloyd et al. 2015). Although the efficiency of BR and DS peaks at around the same temperature, Lloyd et al. (2015) did not find evidence for their occurrence. Instead, at periods when there was a strong correlation between horizontal wind speed and observed ICNC they suggested that BIPS is contributing to the latter, but could not get ICNCs to exceed ∼100 L^{-1}. In the absence of such correlation, a flux of hoar frost crystals was considered responsible for the very high ice concentration events (ICNCs > 100 L^{-1}), albeit without any direct evidence. Farrington et al. (2016) showed that the inclusion of the HM process upwind of JFJ could not explain the measured concentrations of ice, while the addition of a surface flux of hoar crystals provided the best agreement with observations.

Although surface-originated processes have been frequently invoked to explain the disparity between ICNCs and INPs, the role of SIP processes – especially the BR and the DS mechanism – has received far less attention and is addressed in this study. We utilize the Weather Research and Forecasting model (WRF) to conduct simulations of two case studies observed in winter during the CLACE 2014 campaign. Our primary objective is to investigate if the implementation of two SIP parameterizations that account for the effect of BR and DS can reduce the discrepancies between observed and simulated ICNCs. Additionally, we aim to identify the conditions favoring the initiation of SIP in the orographic terrain and explore the synergistic influence of SIP with windblown ice.

3.3 Methods

3.3.1 CLACE instrumentation

CLACE is a long-established series of campaigns taking place for over two decades at the mountain-top station of JFJ, located in the Bernese Alps, in Switzerland, at an altitude of ∼3580 m above sea level (a.s.l.) (e.g., Choularton et al., 2008). The measurement area is very complex and heterogeneous with distinct mountain peaks (Figure 3.1), while JFJ is covered by clouds approximately 40% of the time, offering an ideal location for microphysical observations (Baltensperger et al., 1998). Owing to the local orography surrounding the site, the wind flow is constrained to two directions (Ketterer et al., 2014). Under southeasterly (SE) wind conditions, air masses are lifted along the moderate slope of the Aletsch Glacier, whereas under northwesterly (NW) wind conditions the air is forced to rise faster along the steep north face of the Alps, which is associated with persistent MPCs (Lohmann et al., 2016). A detailed description of the in-situ and remote sensing measurements taken during January and February 2014 as part of the CLACE 2014 campaign is provided by Lloyd et al. (2015) and Grazioli et al. (2015). Here we only offer a brief presentation of the datasets used in this study.

Shadowgraphs of cloud particles were produced by the two-dimensional stereo hydrometeor spectrometer (2D-S; Lawson et al., 2006), part of a three-view cloud particle imager (3V-CPI) instrument. The 2D-S products have been used to provide information on the number concentration and size distribution of particles in the size range of 10-1280 µm. Following Crosier et al. (2011), the raw data were processed to distinguish ice crystals from droplets. Removal of artefacts from shattering events was also considered (Korolev et al., 2011), however analysis of the probe imagery (Crosier et al., 2011) along with inter-arrival time histograms did not reveal the presence of shattered particles, presumably because of the much lower velocity at which the 2D-S probe was aspirated (∼15 m s^{-1}) compared to those during aircraft deployments (Lloyd et al., 2015). An approximation of the ice water content (IWC) at JFJ could also be derived by the 2D-S data using the Brown and Francis (1995) mass-diameter relationship with an uncertainty of up to 5 times (Heymsfield et al., 2010). Additionally, the quantification of the liquid water content (LWC) is based on the liquid droplet size distribution data derived from a DMT cloud droplet probe (CDP; Lance et al., 2010) over the size range between 2 and 50 µm. Meteorological parameters (e.g., temperature, relative humidity, wind speed and wind direction), were provided by MeteoSwiss and used to evaluate the model.

3.3.2 WRF simulations

WRF version 4.0.1, with augmented cloud microphysics to include the effects of additional SIP mechanisms (Sotiropoulou, Vignon, et al., 2021) is used for non-hydrostatic cloud-resolving simulations. The model has been run with three two-way nested domains (Figure 3.1), with a respective horizontal resolution of 12, 3, and 1km. A two-way grid nesting is generally found to improve the model performance in the inner domain (e.g., Harris & Durran, 2010), although the

sensitivity of the results to the applied nesting technique has been shown to be negligible (not shown). The parent domain consists of 148×148 grid points centered over the JFJ station (46.55°N, 7.98°E; shown as a black dot in Figure 3.1), while the second and the third domain include 241×241 and 304×304 grids, respectively. The Lambert conformal projection is applied to all three domains, as it is well suited to mid-latitudes. Here we adapted the so-called refined vertical grid spacing proposed by Vignon et al. (2021), using 100 vertical eta levels up to a model top of 50hPa (i.e., ~20km). This setup provides a refined vertical resolution of ~100m up to mid-troposphere at the expense of the coarsely resolved stratosphere. To investigate the dynamical influence on the development of MPCs under the two distinct wind regimes prevailing at JFJ (Section 3.3.1), we simulate two case studies, starting on 25 and 29 January 2014, 00:00UTC, respectively. Both case studies are associated with the passage of frontal systems over the region of interest, approaching the alpine slopes either from the NW (cold front) or the SE (warm front) direction, as shown by the vertically integrated condensed water content (ICWC; sum of cloud droplets, rain, cloud ice, snow, and graupel) in Figure 3.1. For both cases, the simulation covers a 3d period, with the first 24h being considered sufficient time for the spin-up. A 27s time step was used in the parent domain and goes down to 9s in the second domain and 3s in the third domain. Note that achieving such small time steps in the innermost domain is essential to ensure numerical stability in non-hydrostatic simulations over a region with complex orography such as around JFJ.

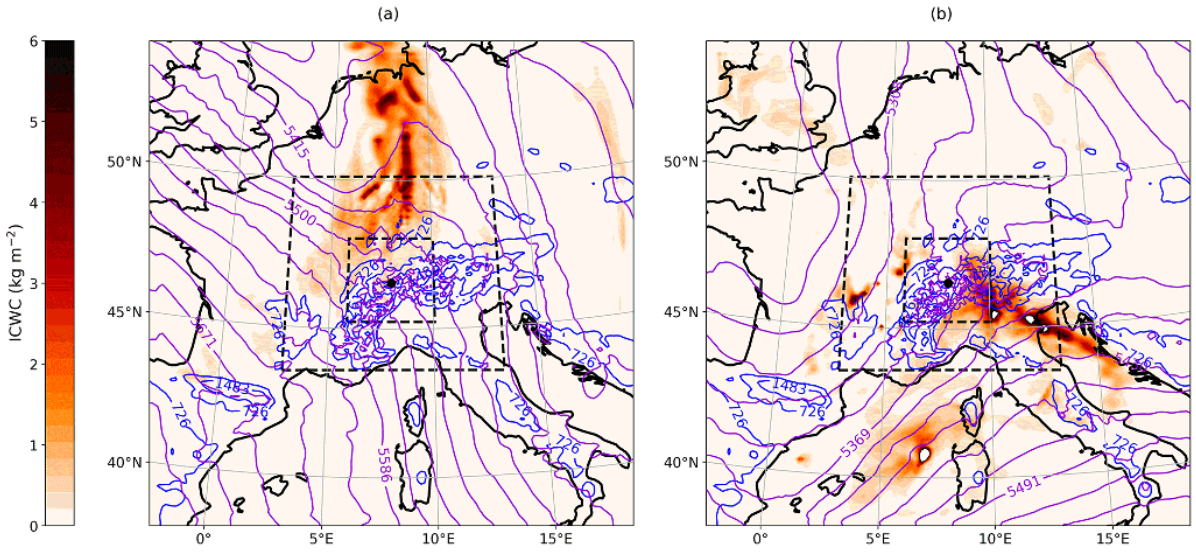

Figure 3.1 Map of synoptic conditions around JFJ station at (a) 00:00 UTC, 26 January 2014, and (b) 00:00 UTC, 30 January 2014, from the control simulation (12 km resolution domain). The purple (blue) contours show the 500 hPa geopotential height in meters (the terrain heights in meters). The color shading shows the vertically integrated condensed water content (in kilograms per square meter; hereafter kg m^{-2}). The black dashed lines delimit the 3 and 1 km resolution domains, while the black dot indicates the location of the JFJ station.

The fifth generation of the European Centre for Medium Range Weather Forecasts (ECMWF) atmospheric reanalyses dataset (ERA5; Hersbach et al., 2020) is used to initialize the model and provide the lateral forcing at the edge of the 12km resolution domain every 6h. Static fields at each model grid point come from default WRF pre-processing system datasets, with a resolution of 3000 for both the topography and the land use fields. Land use categories are based on the Moderate

Resolution Imaging Spectroradiometer (MODIS) land cover classification. Regarding the physics options chosen to run WRF simulations, the Rapid Radiative Transfer Model for General Circulation Models (RRTMG) radiation scheme is applied to parameterize both the shortwave and long-wave radiative transfer. The vertical turbulent mixing is treated with the Mellor–Yamada–Janjic (MYJ; Janjić, 2002) 1.5 order scheme, while surface options are modeled by the Noah land surface model (Noah LSM; Chen and Dudhia, 2001). The Kain–Fritsch cumulus parameterization has been activated only in the outermost domain, as the resolution of the two nested domains is sufficient to reasonably resolve cumulus-type clouds at grid scale.

3.3.2.1 Microphysics scheme and primary ice production

The Morrison two-moment scheme (Morrison et al., 2005; hereafter M05) is used to parameterize the cloud microphysics, following the alpine cloud study of Farrington et al. (2016). The scheme includes double-moment representations of rain, cloud ice, snow, and graupel species, while cloud droplets are treated with a single-moment approach, and therefore, the cloud droplet number concentration (N_d) must be prescribed. Here N_d is set to 100cm^{-3}, based on the mean N_d observed within the simulated temperature range (Lloyd et al., 2015).

In total, three primary ice production mechanisms through heterogeneous nucleation are described in the default version of the M05 scheme, namely immersion freezing, contact freezing, and deposition/condensation freezing nucleation. Immersion freezing of cloud droplets and raindrops is described by the probabilistic approach of Bigg (1953). Contact freezing is parameterized following Meyers et al. (1992). Finally, deposition and condensation freezing is represented by the temperature-dependent equation derived by Rasmussen et al. (2002), based on the in situ measurements of Cooper (1986) collected from different locations at different temperatures. Following Thompson et al. (2004), this parameterization is activated either when there is saturation with respect to liquid water and the simulated temperatures are below −8 °C or when the saturation ratio with respect to ice exceeds a value of 1.08. The accuracy of these parameterizations in representing atmospheric INPs is debatable, as they are derived from very localized measurements over a limited temperature range. Nevertheless, Farrington et al. (2016) argued that the deposition/condensation freezing parameterization of Cooper (1986) can effectively explain INPs between the range 0.01 and 10L^{-1}, which is frequently observed during field campaigns at JFJ (Chou et al., 2011; Conen et al., 2015).

3.3.2.2 Ice multiplication through rime splintering in the M05 scheme

Apart from primary ice production, the HM process is the only SIP mechanism included in the default version of the M05 scheme. This parameterization adapted from Reisner et al. (1998), based on the laboratory findings of Hallett and Mossop (1974), allows for splinter production after cloud- or raindrops are collected by rimed snow particles or graupel. The efficiency of this process is zero outside the temperature range between −8 and −3 °C, while it follows a linear temperature-dependent relationship in between. HM is not activated unless the rimed ice particles have masses larger than 0.1 g kg^{-1} and cloud or rain mass mixing ratio exceeds the value of 0.5 or 0.1 g kg^{-1}, respectively. Since these conditions are rarely met in natural MPCs, previous modeling studies had to artificially remove any thresholds to achieve an enhanced efficiency of this process (Atlas et al., 2020; Young et al., 2019). In the current study, however, the HM process is not effective, as the simulated temperatures at JFJ altitude are below −8 °C (see Section 3.3.3).

3.3.2.3 Ice multiplication through ice–ice collisions in the M05 scheme

In addition to the HM process, we have also included two parameterizations to represent the BR mechanism. An extensive description of the implementation method is provided in Sotiropoulou, Vignon, et al. (2021; see their Appendix B). Among the three ice particle types included in the M05 scheme (i.e., cloud ice, snow, and graupel), we assume that only the collisions between cloud ice–snow, cloud ice–graupel, graupel–snow, snow–snow, and graupel–graupel can result in ice multiplication. The first parameterization tested here follows the simplified methodology proposed by Sullivan, Hoose, et al. (2018), which is based on the laboratory work of Takahashi et al. (1995). Their findings revealed a strong temperature dependence of the fragment numbers generated per collision (N_{BR}), as follows:

$$N_{BR} = 280\ (T - T_{min})^{1.2} e^{-(T-T_{min})/5}\ , \tag{3.3}$$

where $\mathrm{T_{min}} = 252\ \mathrm{K}$, is the minimum temperature for which BR occurs. Yet their experimental set-up was rather simplified involving only collisions between large hail-sized ice spheres with diameters of ~2 cm. Taking this into account, (Sotiropoulou, Vignon, et al., 2021) further scaled the temperature-dependent formulation for size:

$$N_{BR} = 280\ (T - T_{min})^{1.2} e^{-(T-T_{min})/5}\ \frac{D}{D_0}\ , \tag{3.2}$$

where D is the size in meters of the particle that undergoes break-up and D_0=0.02 m is the size of the hail-sized balls used in the experiments of Takahashi et al. (1995).

Phillips et al. (2017a) proposed a more physically based formulation, developing an energy-based interpretation of the experimental results conducted by Vardiman (1978) and Takahashi et al. (1995). The initial collisional kinetic energy is considered as being the governing constraint driving the BR process. Moreover, the predicted NBR depends on the ice particle type and morphological habit and is a function of the temperature, particle size, and rimed fraction. Here the generated fragments per collision are described as follows:

$$N_{BR} = aA\left(1 - exp\left\{-\left[\frac{CK_0}{aA}\right]^{\gamma}\right\}\right), \tag{3.3}$$

where $K_0 = \frac{1}{2}\frac{m_1\, m_2}{m_1+m_2}\ (\Delta u_{n12})^2$ is the initial kinetic energy, in which m_1 and m_2 are the masses of the colliding particles and $|\Delta u_{n12}| = \{(1.7\ u_{n1} - u_{n2})^2 + 0.3\ u_{n1}\ u_{n2}\}^{1/2}$ is the difference in their terminal velocities. The correction term is proposed by Mizuno (1990) and Reisner et al. (1998) to account for underestimates when $u_{n1} \approx u_{n2}$. The parameter a in Equation (3.3) is the surface area of the smaller ice particle (or the one with the lower density), defined as $a = \pi D^2$, with D as in Equation (3.2). A in Equation (3.3) represents the number density of breakable asperities on the colliding surfaces. For collisions that involve cloud ice and snow particles A is described as $A = 1.58 \times 10^7(1 + 100\Psi^2)(1 + \frac{1.33\times10^{-4}}{D^{1.5}})$, where Ψ < 0.5 is the rimed fraction of the most fragile ice particle. For graupel-graupel collisions A is given by a temperature-dependent equation as $A = \frac{a_0}{3} + \max(\frac{2a_0}{3} - \frac{a_0}{9}|T - 258|, 0)$, in which $a_0 = 3.78 \times 10^4\left(1 + \frac{0.0079}{D^{1.5}}\right)$. C is the asperity-fragility coefficient, which is empirically derived to account for different collision types, while the exponent γ is equal to 0.3 for collisions between graupel-graupel and is calculated as a function of the rimed fraction for collisions including cloud ice and snow. The parameterization was developed based on particles with diameters 500 μm < D < 5 mm, however Phillips et al. (2017a) suggest that it can be used for particle sizes outside

the recommended range as long as the input variables to the scheme are set to the nearest limit of the range. Finally, since N_{BR} was never observed to exceed 100 in the experiments of Vardiman (1978), here we also use this value as an upper limit for all collision types (Phillips et al., 2017a). All predicted fragments emitted through BR are added to the cloud ice category.

3.3.2.4 Ice multiplication through droplet shattering in the M05 scheme

In the M05 scheme, two different parameterizations are implemented to investigate the potential efficiency of the DS mechanism in producing secondary ice splinters (N_{DS}). Phillips et al. (2018) proposed two possible modes of raindrop–ice collisions that can initiate the freezing process. In the first mode, the freezing of the drop occurs either by collecting a small ice particle or through heterogeneous freezing. In the default M05 scheme, the product of collisions between raindrops and cloud ice is considered to be graupel (snow) if the rain mixing ratio is greater (lower) than 0.1gkg−1, following Reisner et al. (1998). Additionally, the heterogeneous freezing of big raindrops in the immersion mode follows Bigg's (1953) parameterization (Section 3.3.2.1). Here we consider that the product of these two processes can undergo shattering and generate numerous ice fragments, the number of which is parameterized after Phillips et al. (2018). The formulation is derived by fitting multiple laboratory datasets to a Lorentzian function of temperature and a polynomial expression of the drop size. More precisely, the total number of fragments (N) generated per frozen drop are given by the following:

$$N = \Xi(D_r)\Omega(T)\left[\frac{\zeta\eta^2}{(T-T_0)^2+\eta^2} + \beta T\right], \tag{3.4}$$

where T is the temperature (in K) and D_r is the size of the freezing raindrop (in mm). Note that N is defined as the sum of the big fragments (N_B) and tiny splinters (N_T). Equation (3.4) applies only to drop diameters less than 1.6 mm, which is the maximum observed experimentally. For droplet sizes beyond this maximum value, N can be inferred by linear extrapolation. N_B is described by another Lorentzian:

$$N_B = min\left\{\Xi(D_r)\Omega(T)\left[\frac{\zeta_B{\eta_B}^2}{\left(T-T_{B,0}\right)^2+{\eta_B}^2}\right], N\right\}. \tag{3.5}$$

The factors $\Xi(D_r)$ and $\Omega(T)$ in Equation (3.4) and (3.5) are cubic interpolation functions, impeding DS for D_r < 0.05 mm and T > –3 °C. Furthermore, the parameters ζ, η, T_0, β, ζ_B, η_B, $T_{B,0}$, are analytically described in Phillips et al. (2018). That the big fragments emitted (i.e., N_B) will be initiated in the model as graupel, snow or frozen drops, while only the splinters ($N_T = N - N_B$) are considered secondary ice (i.e., $N_{DS} = N_T$) and are passed to the cloud ice category.

The second mode of raindrop–ice collisions includes the accretion of raindrops on impact with more massive ice particles, such as snow or graupel, the description of which in the M05 scheme is adapted from (Ikawa & Saito, 1991)i. While there is only one dedicated laboratory study of this SIP mode (James et al., 2021), it was also indirectly investigated in the experimental study of Latham and Warwicker (1980), who reported that the collision of supercooled raindrops with hailstones can generate secondary ice. Phillips et al. (2018) proposed an empirical, energy-based formulation to account for the tiny splinters ejected after collisions between raindrops and large ice particles as follows:

$$N_{DS} = 3\Phi(T) \times [1 - f(T)] \times max(DE - DE_{crit}, 0)\ , \tag{3.6}$$

where $DE = \frac{K_0}{S_e}$, is the dimensionless energy given as the ratio of the initial kinetic energy (K_0; described in 2.2.3) over the surface energy, which is expressed by the product $S_e = \gamma_{liq}\pi {\mathrm{D_r}}^2$, in which

γ_{liq}=0.073 J m^{-2}, is the surface tension of liquid water. The critical value of DE used in Equation (3.6) for the onset of splashing upon impact is set to DE_{crit} = 0.2. The parameter $f(T) = -c_w T/L_f$, represents the initial frozen fraction of a supercooled drop during the first stage of the freezing process, where C_w = 4200 J kg^{-1} K^{-1}, is the specific heat capacity of liquid water, L_f = 3.3 × 10^5 J kg^{-1}, is the specific latent heat of freezing, while T is the initial freezing temperature (°C) of the raindrop. Finally, $\Phi(T)$ = min[4$f(T)$,1] is an empirical fraction, which represents the probability of any new drop in the splash products to contain a frost secondary ice particle. At temperatures ∼ –10 °C this formulation yields Φ = 0.5, meaning that the probability of a secondary drop to contain ice is 50%. James et al. (2021) provided the first laboratory study to constrain this parameter. Further details regarding the derivation of the empirical parameters and the uncertainties underlying the mathematical formulations are discussed in Phillips et al. (2018).

The second DS parameterization tested in this study was developed by Sullivan, Hoose, et al. (2018) and is a function of the freezing droplet diameter (D_r in µm), a shattering probability (p_{sh}) and a freezing probability (p_{fr}) as follows:

$$N_{DS} = 2.5 \times 10^{-11}\, {D_r}^4\, p_{sh}\, p_{fr} \ . \tag{3.7}$$

The diameter dependence describing the fragment numbers generated per fractured frozen droplet is derived by nudging the liquid water and ice particle size distributions in one-dimensional cloud model simulations towards aircraft observations collected in tropical cumulus clouds (Lawson et al., 2015). The p_{sh} is based upon droplet levitation experiments shown in Leisner et al. (2014) and is represented by a temperature-dependent Gaussian distribution, centered at ∼ –15 °C. Note that p_{sh} is non-zero only for droplets with sizes greater than 50 µm. The p_{fr} is 0 for temperatures warmer than –3 °C and 1 if temperatures fall below –6 °C, following the cubic interpolation function, $\Omega(T)$, adapted from Phillips et al. (2018).

3.3.3 Model evaluation

The control simulation (CNTRL), performed with the standard M05 scheme, sets the basis for assessing the validity of the model against available meteorological observations. Temperature, relative humidity, wind speed, and wind direction are obtained from the MeteoSwiss weather station at JFJ. The comparison of each meteorological variable with the results from the nearest model grid point of the CNTRL simulation is shown in Figure 3.2. Note that the outputs are from the first atmospheric level of the innermost domain at ∼10m above ground level (AGL; Figure 3.1), while the first 24h of each simulation period are considered spin-up time and are, therefore, excluded from the present analysis. The mean modeled values and standard deviations (SDs), along with the root mean square error (RMSE), and the index of agreement (IoA) between model predictions and observational data are summarized in Table 3.1. IoA is both a relative and a bounded measure (i.e., 0≤IoA≤1) that describes phase errors between predicted (Pi) and observed (Oi) time series (Willmott et al., 2012) as follows:

$$IoA = 1 - \left[\frac{\sum_{i=1}^{N}(P_i - O_i)^2}{\sum_{i=1}^{N}(|P_i'| + |O_i'|)^2}\right] , \tag{3.8}$$

where $\mathrm{P_i'} = P_i - \bar{O}$ and $\mathrm{O_i'} = O_i - \bar{O}$, in which $\bar{O}$ is the mean of the observed variable.

Throughout the two case studies, the WRF simulations seem to closely follow the observed temperatures (Figure 3.2a), which is also indicated by the high IoA in Table 3.1. The synoptic situation occurring on 26 January, with a deep trough extending to western Europe (Figure 3.1), has been associated with intense snowfall in the alpine regions (Panziera & Hoskins, 2008). The passage of the cold front was followed by a sharp temperature decrease, with the simulated temperatures

fluctuating between −10 and ∼−20 °C throughout the NW case (Figure 3.2a). Under the influence of the warm front during the SE case, the modeled temperatures rose from ∼−18 to ∼−14 °C and remained less variable until 30 January at 12:00 UTC, with mean values of ∼−15.5 °C (Table 3.1).

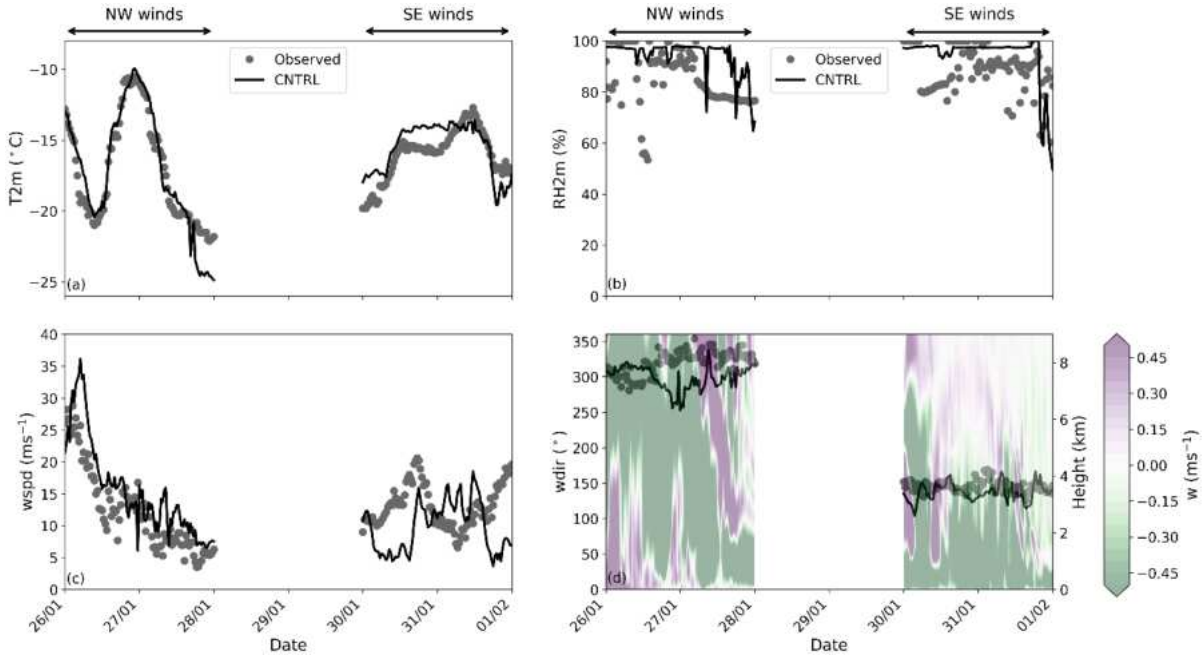

Figure 3.2 Time series of (a) temperature (T2m), (b) relative humidity with respect to liquid phase at 2 m height (RH2m), (c) wind speed (wspd), and (d) wind direction (wdir). Gray circles indicate measurements collected between 26 January and 1 February 2014 at JFJ station, while modeled values from the CNTRL simulation are shown with a black line. The semi-transparent contour plot represents the vertical velocity (w) profile predicted by the CNTRL simulation. Each day starts at 00:00 UTC.

The 1 km resolution domain can sufficiently capture the local wind systems to a certain extent (Figure 3.2c, d). During the NW flow, the horizontal wind speeds are reproduced better by the CNTRL simulation (IoA=88%), whereas during the SE winds, the simulated wind speed is frequently underestimated compared with observations (Figure 3.2c). Such deviations in the horizontal wind speed might be caused by the relatively coarse horizontal resolution of the model, which prevents some small-scale and very local orographic structures from being resolved. As discussed in Section 3.3.2, the observed winds at JFJ are channeled by the orography to either NW or SE directions. The CNTRL simulation of WRF can satisfactorily reproduce the wind direction in both cases, although the simulated values exhibit larger fluctuations than the measured ones (Figure 3.2d), presumably because of the surrounding orography being less accurately represented in the model. This is particularly evident during NW winds, when the simulated wind directions shift slightly to west directions compared to observations. The positive vertical velocities, illustrated in the contour plot in Figure 3.2d, result from the orographically forced lifting of the air masses over the local topography and are not related to convective instability in the lower atmospheric levels. The stronger updrafts prevailing until the end of 26 January are associated with the steep ascent of the air parcels, which can also contribute to the enhanced relative humidity (Figure 3.2b). After the frontal passage, the vertical velocities at the lower levels are downward directed, with the vertical profile of potential temperature revealing that the atmosphere at JFJ is stabilized (not shown). The same vertical velocity pattern, with mainly downward motions, characterizes the stably stratified atmosphere after 30

January. Overall, Figure 3.2 suggests that local meteorological conditions at JFJ are reasonably well represented by the model.

Table 3.1 Mean modeled values (± SDs), RMSE, and IoA between the CNTRL simulation of WRF and measurements carried out by the MeteoSwiss station at JFJ.

Variable	Mean ± std		RMSE		IoA	
	NW winds	SE winds	NW winds	SE winds	NW winds	SE winds
T2m (˚C)	-17.10 ± 4.36	-15.48 ± 1.75	1.40	1.33	0.97	0.84
RH2m (%)	94.07 ± 7.02	94.24 ± 10.31	14.01	11.61	0.55	0.64
wspd (ms^{-1})	15.57 ± 7.45	9.78 ± 3.94	4.85	6.75	0.88	0.22

3.3.4 Model simulations

Given the good representation of the atmospheric conditions at JFJ, the CNTRL simulation of WRF is further accompanied by five sensitivity simulations aiming to investigate the contribution of BR and DS mechanisms. Here we also perform three additional sensitivity experiments to explore the potential impact of blowing ice and the synergistic interaction with SIP on the development of the simulated MPCs. A detailed list of the sensitivity experiments is provided in Table 3.2.

The contribution of the DS mechanism is addressed in two sensitivity experiments, DS_PHILL and DS_SULL, where the parameterizations of Phillips et al. (2018) and Sullivan, Hoose, et al. (2018) were applied, respectively (Section 3.3.2.4). Both sensitivity simulations yield predictions that coincide with the CNTRL simulation (supplement Figure B1) suggesting that the DS mechanism is hardly ever activated, and fail to produce realistic total ice number concentrations (N_{isg}; cloud ice + snow + graupel). The absence of correlation between LWC and N_{isg} fluctuations might also suggest the ineffectiveness of this mechanism under the examined conditions. Note that the parameterized expressions used to describe the DS mechanism involve a number of empirical and rather uncertain parameters, the value of which could potentially influence the efficiency of the process in producing secondary ice fragments. However, the sensitivity of our results to the choice of these parameters would be negligible, as the low concentrations ($\lesssim 10^{-2}$ cm^{-3}) of relatively small raindrops with mode diameters below the threshold size of 50 μm seem to completely prevent the onset of the DS process (supplement Figure B2). The DS mechanism is therefore excluded from the following discussion. This result is in line with the modeling study of Dedekind et al. (2021), who also reported the inefficiency of this mechanism in wintertime alpine clouds.

The effect of secondarily formed ice particles through BR is then examined in the following three sensitivity simulations. First, the TAKAH simulation adopts the temperature dependent formula of Takahashi et al. (1995) scaled with the size of particles that undergo fragmentation (Sotiropoulou, Vignon, et al., 2021). Applying Equation (3.2) to collisions between all ice categories considered in the M05 scheme (except collisions between cloud ice particles; Section 3.3.2.3) inserts a caveat to our approach. The laboratory results of Takahashi et al. (1995) suggest that it is mostly the collisions between rimed particles and graupel that are more conducive to SIP through BR. Vardiman (1978) also reported that ice crystal growth through riming is essential to boost fragmentation. Applying the Takahashi breakup scheme for unrimed ice particles might, therefore, overestimate the number of secondary ice fragments. To test this hypothesis, we performed the TAKAHrim sensitivity simulation,

where we enabled ice multiplication through BR only after collisions between rimed cloud ice/snow and graupel particles. To diagnose the presence of rime on ice particles, we used the amount of cloud droplets or raindrops accreted by snow and cloud ice, which is predicted in the M05 scheme.

Finally, the performance of the more advanced Phillips et al. (2017a) parameterization is tested in the PHILL simulation. Parameters involved in the Phillips parameterization that are not explicitly resolved in the M05 microphysics scheme are the rimed fraction and the ice habit of colliding ice particles. The choice of ice habit is based on particle images collected during the CLACE 2014 campaign, showing the presence of non-dendritic sectored plates and oblate particles at temperatures ∼−15 °C (Lloyd et al., 2015). Grazioli et al. (2015) also presented some examples of particle imagery produced by a 2D-S imaging probe, revealing the presence of heavily rimed hydrometeors and highly oblate particles (probably columns or needles). The rimed fraction is prescribed to a value of 0.4 (0.3) to account, respectively, for heavily and moderately rimed ice particles present under NW (SE) wind conditions. A high degree of riming is expected in the simulated cases, as they both occur under ice seeding situations (Section 3.4.1.1), where large precipitating ice particles from the seeder clouds effectively gain mass in the mixed-phase zone through riming. Direct observations with balloon-borne measurements carried out within ice-seeding events in the region around Davos in the Swiss Alps support the presence of a large fraction of rimed particles and graupel (Ramelli et al., 2021a). The higher riming degree is prescribed under NW winds because the orographic forcing (i.e., vertical velocity) is stronger and helps with maintaining mixed-phase conditions in the feeder clouds – which, in turn, promotes ice crystal growth through riming. However, our results were not very sensitive to the choice of the rimed fraction.

Table 3.2 List of sensitivity simulations conducted with WRF. Note: NBIPs is the number concentrations of BIPs.

Simulation	BR process	DS process	NBIPS (L^{-1})
CNTRL	off	off	0
DS_PHILL	off	Phillips et al., 2018	0
DS_SULL	off	Sullivan et al., 2018a	0
TAKAH	Takahashi et al., 1995	off	0
TAKAHrim	Takahashi et al., 1995 activated only after collisions between rimed ice particles	off	0
PHILL	Phillips et al., 2017a	off	0
BIPS10	off	off	10
BIPS100	off	off	100
BIPS100_PHILL	Phillips et al., 2017a	off	100

The remaining sensitivity simulations focus on the potential impact of BIPs. A recently developed blowing snow scheme, used to simulate alpine snowpacks, reported significant mass and number mixing ratios of BIPs that can be found up to ∼1km above the surface under high wind speed conditions (see Figure 17 in Sharma et al., 2023), with the potential to trigger cloud microphysical processes. Given that in the default M05 scheme there is no parameterization of a flux of ice particles

from the surface, we parameterize the effect of BIPs lofting into the simulated orographic clouds by applying a constant ice crystal source to the first atmospheric level of WRF over the whole model domain. Although the source of BIPs at the first model level remained constant, their number will be affected by processes such as advection, sublimation, and sedimentation that are described in the M05 scheme. Note that the relatively coarse horizontal resolution in the innermost domain of our simulations (i.e., 1 km) does not allow the accurate representation of the small-scale turbulent flow over the orographic terrain. This is considered a limitation of our methodology, since turbulent diffusion is a key process affecting the amount of BIPs that will be resuspended from the surface.

The applied concentrations of BIPS varied between 10^{-2} and 100 L^{-1}, which is the upper limit proposed by Lloyd et al. (2015) and observed within in-cloud conditions by Beck et al. (2018). Number concentrations of BIPS (i.e., NBIPS) lower than 10 L^{-1} were found incapable of affecting the simulated cloud properties and are, therefore, not included in the following discussion. Two sensitivity simulations are finally performed, BIPS10 and BIPS100 (Table 3.2), in which the number indicates the NBIPS in L^{-1}. In our approach we assume BIPS are spherical with diameters of 100 µm, based on typical sizes that are frequently reported in the literature (Geerts et al., 2015; Schlenczek et al., 2014; Schmidt, 1984; Sharma et al., 2023). The relatively small fall speed of these particles (e.g., Pruppacher and Klett, 1997) will allow them to remain suspended in the atmosphere. As a sensitivity we also considered smaller particles with sizes of 10 µm, but our results did not change significantly (supplement Figure B3). Nevertheless, such small ice particles are not expected to substantially contribute to the simulated IWC, as shown by Farrington et al. (2016).

As SIP through BR and blowing snow are both important when trying to explain the high ICNCs observed in alpine environments, their combined effect is addressed in our last simulation, BIPS100_PHILL (Table 3.2). In this sensitivity simulation the effect of BR is parameterized after Phillips et al. (2017a), while a constant ice crystal concentration of 100 L^{-1} is applied to the first atmospheric level of WRF to represent the effect of BIPS.

3.4 Results and discussion

3.4.1 Impact of SIP through BR on simulated microphysical properties

The temporal evolution of N_{isg}, IWC, and LWC, at the first model level (~ 10 m AGL) from the nearest to JFJ model grid point of the CNTRL, TAKAH, and PHILL simulations is presented in Figure 3.3. Instead of focusing on a single grid point, we also averaged the results from the 9 km^2 area surrounding the point of interest. However, the produced time series showed only little difference when compared to the nearest grid point time series (not shown), ensuring that our analysis is robust. Besides, the region in the vicinity of JFJ is very heterogeneous, supporting the single point comparison presented in the following discussion. The gray dots shown in Figure 3.3 represent the measurements taken by the 2D-S and CDP instruments at JFJ throughout the two periods of interest. The displayed time frequency of the observations is 30min to match the output frequency of the model. Note that the simulated LWC includes liquid water from cloud droplets and rain, while the simulated IWC includes cloud ice, snow, and graupel. The contribution of rain in our simulations is, however, negligible (Figure B2). Several statistical metrics for N_{isg}, IWC, and LWC are summarized in Tables 3.3, 3.4, and 3.5, respectively. Periods with missing data in the measurement time series are excluded from the statistical analysis.

During the NW flow, between 26 and 28 January, the measured ICNCs exceed 100 L^{-1} for >50% of the time, whereas during the SE flow, the ICNCs usually fluctuate between 10 and 100 L^{-1} (Figure 3.3a). The highest ICNCs are generally observed at temperatures higher than ~ −15 °C, where SIP processes are thought to be dominant and primary ice nucleation in the absence of bioaerosols is limited (e.g., Hoose and Möhler, 2012; Kanji et al., 2017). The CNTRL simulation fails to reproduce N_{isg} higher than 10 L^{-1}, with the mean simulated values being ~2–2.5 L^{-1} during both periods. At the same time, the

mean observed ICNC values are ~200 (70) L^{-1} during the NW (SE) case. Thus, CNTRL systematically underestimates the amount of ice by up to 2 orders of magnitude, which is also consistent with the interquartile statistics presented in Table 3.3. With the HM process being totally ineffective in the prevailing temperatures, this discrepancy suggests that ice crystals produced by heterogeneous ice nucleation in CNTRL are not high enough to match the observations. A similar discrepancy between predicted INPs and measured ICNCs was also documented in Lloyd et al. (2015).

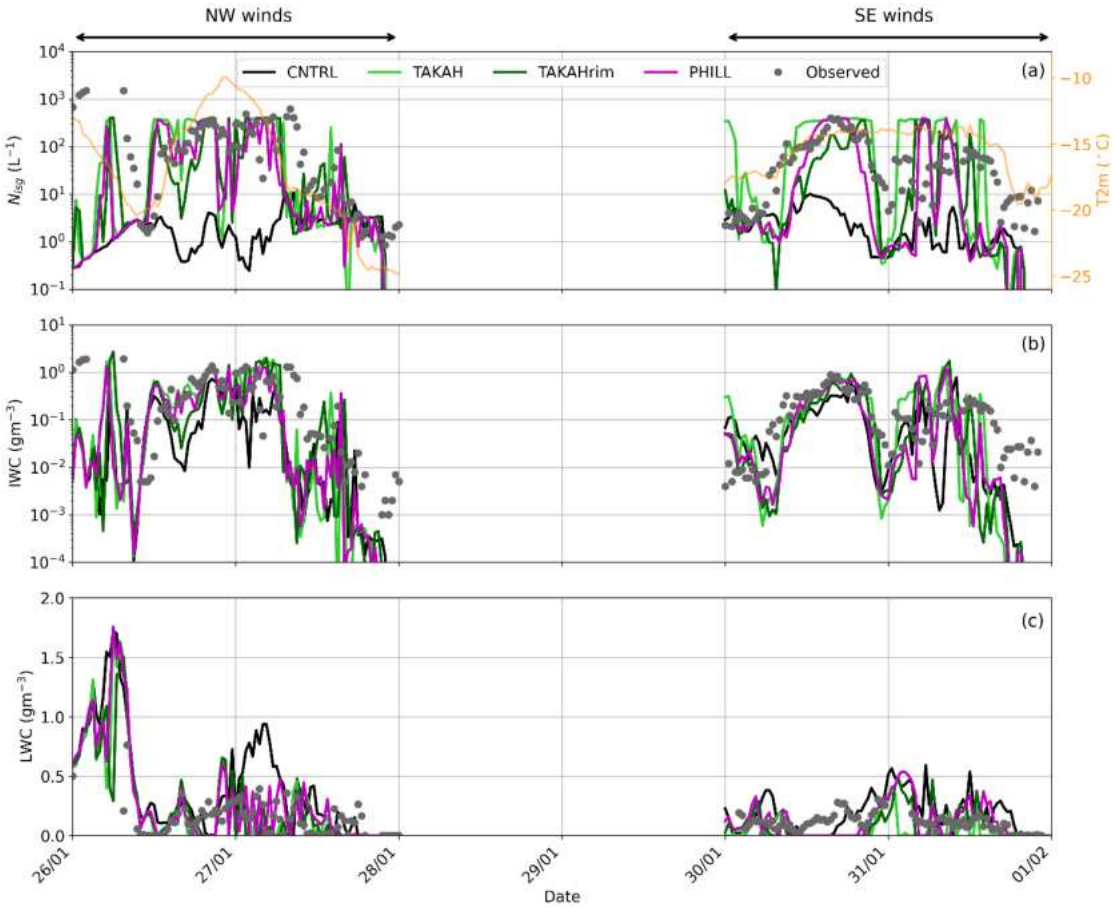

Figure 3.3 Time series of (a) total N_{isg} and temperature at 2 m height (orange line), (b) IWC, and (c) LWC, predicted by the CNTRL (black line), TAKAH (light green line), TAKAHrim (dark green), and PHILL (magenta line) simulations between 26 January and 1 February 2014. The gray dots in all three panels represent the 2D-S ICNCs, the inferred IWC, and the CDP LWC measured at the JFJ station, respectively. Note the logarithmic y axes in panels (a) and (b).

Activating the BR process in TAKAH, TAKAHrim, and PHILL simulations is found to produce N_{isg} as high as 400 L^{-1} during both case studies (Figure 3.3a), resulting in a substantially better agreement with observations. At times when the simulated temperatures drop below ~ −18 °C, the N_{isg} modeled by all three simulations coincide with the CNTRL simulation. At relatively warmer subzero temperatures, though, the significant contribution of the BR process is evident, elevating the predicted N_{isg} by up to 3 orders of magnitude during the NW case and by more than 2 orders of magnitude during the SE case. Although the median N_{isg} in all three sensitivity simulations with active breakup remains underestimated compared to observations during the NW flow, TAKAH seems to produce unrealistically high median and 75th percentile values during the SE flow (Table 3.3). Indeed, focusing on the N_{isg} time series (Figure 3.3a), TAKAH is, ~25% of the time, shown to overestimate the observed

ICNCs by a factor of ∼3, reaching up to a factor of 10 on 30 January at 00:00UTC. TAKAHrim and PHILL, on the other hand, produce more reasonable concentrations of ice particles throughout both case studies, with the N_{isg} values in the 75th percentile exceeding 100 (50) L^{-1} during the NW (SE) case study (Table 3.3), which is found to reduce the gap between observations and model predictions.

Table 3.3 The 25th, 50th (median), and 75th percentiles of ICNC (per liter) time series.

Simulation	25th perc.		Median		75th perc.	
	NW winds	SE winds	NW winds	SE winds	NW winds	SE winds
OBSERVED	8.69	6.64	80.47	34.53	261.25	88.69
CNTRL	0.76	0.84	2.02	1.68	2.80	3.60
TAKAH	2.27	1.08	9.85	122.56	362.51	358.38
TAKAHrim	2.56	0.75	12.30	4.17	101.46	82.16
PHILL	2.49	0.76	6.27	2.09	118.21	59.23
BIPS10	1.60	1.90	2.42	2.72	3.30	4.78
BIPS100	6.17	10.74	10.36	13.88	12.32	17.39
BIPS100_PHILL	8.95	11.51	15.87	16.30	138.92	98.43

It is worth noting that, despite the fact that the Takahashi parameterization (Equation 3.2) is applied to both TAKAH and TAKAHrim simulations, the former seems to systematically overestimate the number of secondary ice fragments, while the latter produces ICNCs that are more consistent with the observations. Hence, the Takahashi parameterization predicts reasonable results if it is allowed to generate fragments from collisions between rimed ice particles only (Section 3.3.4).

Table 3.4 The 25th, 50th (median), and 75th percentiles of IWC (in grams per cubic meter; hereafter gm^{-3}) time series.

Simulation	25th perc.		Median		75th perc.	
	NW winds	SE winds	NW winds	SE winds	NW winds	SE winds
OBSERVED	0.03	0.02	0.19	0.11	0.66	0.26
CNTRL	4.3×10^{-3}	5.0×10^{-3}	0.03	0.04	0.15	0.12
TAKAH	1.3×10^{-3}	2.0×10^{-3}	0.10	0.09	0.52	0.34
TAKAHrim	4.7×10^{-3}	3.1×10^{-3}	0.08	0.04	0.33	0.27
PHILL	3.8×10^{-3}	3.7×10^{-3}	0.10	0.02	0.38	0.30
BIPS100_PHILL	3.9×10^{-3}	9.1×10^{-3}	0.09	0.03	0.40	0.30

The observed IWC time series (Figure 3.3b) are frequently reaching ∼1 g m^{-3} during the NW case, with the median values being a factor of 2.5 higher than those observed during the SE case (Table 3.4). This indicates the presence of more massive ice particles when higher updraft velocities prevail. The CNTRL

simulation cannot produce IWC values > 0.8 g m^{-3} and is, most of the time, below the observed range. Adding a description of the BR process (i.e., in TAKAH, TAKAHrim, and PHILL) sufficiently increases the modeled IWC by up to ∼1 order of magnitude between 26 January 12:00UTC and 27 January 06:00UTC, when the modeled N_{isg} exceeds 100 L^{-1}, and the temperature remains higher than −16 °C. The same conditions are observed in the SE case, between 12:00 and 18:00 UTC on 30 January, when IWC shows a ∼3 fold enhancement reaching the observed levels. The IWC values in the third quartile predicted by TAKAH, TAKAHrim, and PHILL are more than a factor of 2 higher than the ones predicted by CNTRL (Table 3.4). This increase improves the model performance, although the modeled IWC remains slightly underestimated (overestimated) during the NW (SE) case. The size distribution of the three ice species considered in the M05 scheme (Figure B4) reveals that the implementation of the BR mechanism leads to elevated concentrations of relatively smaller cloud ice crystals but, at the same time, increases the concentrations of snow particles. This is the reason why the modeled total ice mass is also increased compared with the CNTRL simulation.

The comparison of the simulated cloud LWC with the concurrent CDP observations at JFJ is presented in Figure 3.3c. The LWC values recorded during the NW case are highly variant, reaching up to 0.75 gm^{-3}, which is substantially higher than the respective maximum LWC observed during the SE case (0.30 gm^{-3}). On 26 January before 12:00 UTC, all sensitivity simulations predict LWC > 1gm^{-3}, which, however, cannot be validated against measurements due to missing data in the CDP time series. Note that this period is excluded from the statistics derived in Table 3.5. The CNTRL simulation is found to overestimate the cloud LWC, predicting 0.42 (0.25) gm^{-3} in the third quartile, which is a factor of ∼2 higher than the observed values during the NW (SE) case (Table 3.5).

Table 3.5 The 25th, 50th (median), and 75th percentiles of LWC (in gm^{-3}) time series.

Simulation	25th perc.		Median		75th perc.	
	NW winds	SE winds	NW winds	SE winds	NW winds	SE winds
OBSERVED	8.5×10^{-3}	70.0×10^{-3}	0.12	0.11	0.21	0.14
CNTRL	87.7×10^{-3}	26.0×10^{-3}	0.19	0.17	0.42	0.25
TAKAH	1.3×10^{-10}	0.0	0.01	6.7×10^{-10}	0.16	0.05
TAKAHrim	1.2×10^{-7}	0.0	0.06	2.8×10^{-6}	0.23	0.09
PHILL	6.3×10^{-8}	0.0	0.09	0.03	0.26	0.18
BIPS10	82.0×10^{-3}	4.6×10^{-3}	0.18	0.12	0.33	0.24
BIPS100	67.1×10^{-3}	13.1×10^{-3}	0.18	0.13	0.36	0.23
BIPS100_PHILL	6.3×10^{-10}	0.0	0.09	0.06	0.27	0.10

The modeled LWC in the 75th percentile is decreased by a factor of 1.5–5 in the simulations that account for the BR process (Table 3.5), improving the agreement with observations (Figure 3.3c). The reduction in LWC is expected, considering that the higher N_{isg} produced when BR is activated can readily deplete the surrounding droplets under liquid water subsaturated conditions through the WBF process. This introduces a challenging environment to simulate, as the model is sometimes seen to convert water to ice too rapidly, leading to cloud glaciation (e.g., on 30 January after 12:00 UTC). Despite all sinks of cloud water (i.e., condensation freezing, WBF, or riming), observations at JFJ suggest that mixed-phase regions are generally sustained (Lloyd et al., 2015). This is particularly true for the NW case, when the sufficiently large updrafts caused by the steep ascent of the air masses help maintain the supersaturation with respect to liquid water (Lohmann et al., 2016). PHILL and TAKAHrim

can more efficiently sustain the observed mixed-phase conditions compared to TAKAH, which frequently results in explosive ice multiplication – especially during the SE case – leading to an underestimation of the LWC (see Figure 3.3c and Table 3.5). TAKAH is, therefore, excluded from the following discussion, as it fails to reproduce an accurate liquid-ice phase partitioning.

The time-averaged vertical profiles of cloud ice (N_i), graupel (N_g), snow (N_s), and total N_{isg} number concentrations are illustrated in Figure 3.4 for the CNTRL, TAKAHrim, and PHILL simulations. The mean N_i (Figure 3.4a) and N_{isg} profiles (Figure 3.4d) are enhanced by up to 2 orders of magnitude in TAKAHrim and PHILL compared to CNTRL. During the NW flow, both simulations, including the BR process, produce a similar vertical distribution of the ice hydrometeors in the lowest 1–1.5 km in the atmosphere. This is not the case for the SE case, where TAKAHrim seems to predict a rapid decrease in N_i and N_s and, thus, in total N_{isg} with altitude. The main difference between these two simulations lies in the fact that the total LWC and, hence, the probability of riming, decreases with height, limiting the efficiency of BR in TAKAHrim. This become more evident during the SE case, where mixed-phase conditions are exclusively confined below 1.5 km in the atmosphere (Section 3.4.1.1). However, we cannot estimate which vertical distribution better represents reality, due to the lack of corresponding measured profiles. TAKAHrim coincides with PHILL only when there is sufficient liquid water in the atmosphere, allowing for the riming of the ice hydrometeors. Moreover, at heights above ∼2.5 km, where the simulated temperatures drop well below −20 °C (Figure B5), all three simulations are seen to produce similar results. This implies the greater importance of SIP through BR at heights below 2–3 km in the atmosphere (i.e., in the temperature range between ∼−18 °C and ∼−10 °C).

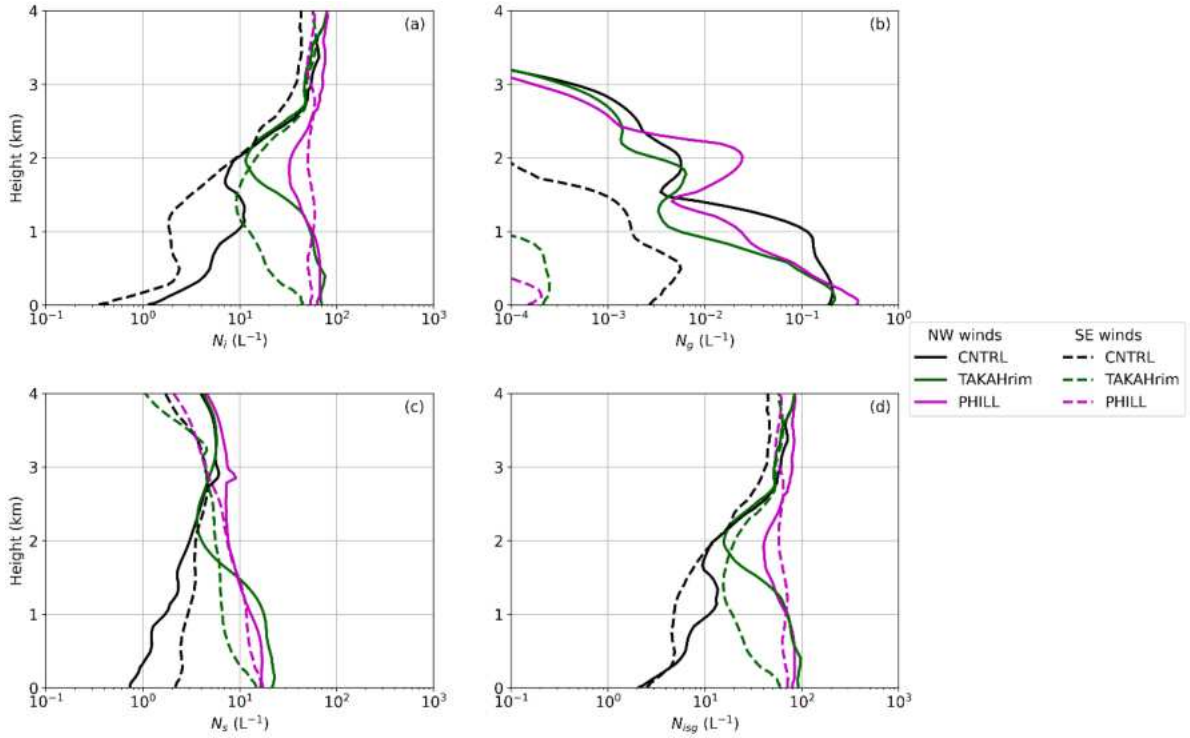

Figure 3.4 Mean vertical profiles of (a) N_i, (b) N_g, (c) N_s, and (d) total N_{isg} predicted by the CNTRL (black), TAKAHrim (dark green), and PHILL (magenta) simulations for the NW (solid lines) and SE (dashed lines) cases. Note the different scale on the x axis of the Ng vertical distribution. The height is given in kilometers above ground level (hereafter km AGL).

Graupel number concentrations (Figure 3.4b) do not contribute much to the modeled ice phase, especially during the SE case when the simulated N_g is negligible compared with the N_i and N_s (Figure 3.4c). In the M05 scheme, a portion of the rimed cloud or rain water onto snow is allowed to convert into graupel (Reisner et al. 1998), provided that snow, cloud liquid, and rain water mixing ratios exceed a threshold of 0.1, 0.5, and 0.1 g kg^{-1}, respectively. These mixing ratio thresholds for graupel formation are arbitrary and might not be suitable for the examined conditions, preventing the formation of graupel from rimed snowflakes (Morrison & Grabowski, 2008). During the NW case, however, we can identify substantially higher Ng than the SE case, owing to the presence of sufficient supercooled liquid water especially during the first half of 26 January. Activating the BR mechanism in TAKAHrim and PHILL generally decreases the simulated N_g in both cases (Figure 3.4c), suggesting that the breakup of graupel contributes to ice multiplication.

The mean vertical profile of N_s (Figure 3.4c) seems to follow the respective profile of N_i (Figure 3.4a). Unlike the graupel concentrations, including the BR mechanism is found to enhance N_s up to 1 order of magnitude compared to the CNTRL simulation. Focusing on a single model time step when the BR mechanism is activated, the size distribution of snow particles shown in the Figure B4 reveals that the increase in snow number concentrations can reach up to 2 orders of magnitude during the NW case. This is a logical consequence of the increase in the number concentration of ice crystals, which are converting to snow particles after ice crystal growth (i.e., cloud-ice-to-snow autoconversion) when surpassing a characteristic mean diameter of 250 μm. This will be discussed in detail in the following section. Since TAKAHrim and PHILL provide comparable results in terms of the in-cloud phase partitioning, we focus the subsequent discussion on the PHILL simulation because it offers the opportunity to explore the sensitivity of simulation results to parameters not considered by the Takahashi formulation.

3.4.1.1 Conditions favoring BR in the two considered events

The temporal evolution of the vertical profiles of N_{isg}, IWC, and LWC can provide valuable insight on the drivers of enhanced ice formation in the wintertime alpine MPCs. The presence of a seeder–feeder cloud system with sustained mixed-phase conditions confined to levels below ∼3 km (∼1.5 km) in the NW (SE) case and a pure ice cloud aloft is revealed in Figure 3.5. Such configurations are a well-known type of orographic multi-layer cloud that enhances precipitation over mountains (e.g., Browning et al., 1974, 1975; Roe, 2005). Cloud condensation is promoted by the synergy between a mid-latitude frontal system and its orographically induced ascent over the mountain range (Figure 3.1). The separation between the seeder and feeder clouds is often nonexistent, meaning that ice seeding can occur either in layered clouds or internally within one cloud (Proske et al., 2021; Roe, 2005). In the first case, which seems to occur here as well, there can be a vertical continuum of cloud condensates between the seeder and the feeder cloud due to precipitation of ice crystals from the higher-level cloud (Figure 3.5a). This means that the seeding ice crystals fall through subsaturated cloud-free air before reaching the feeder region of the cloud and might sublimate. The remote sensing analysis over Switzerland presented by Proske et al. (2021), showed that in-cloud seeding occurs in 18% of the observations, while the external seeder–feeder mechanism is present 15% of the time when the seeder is a cirrus cloud.

To illustrate the processes taking place during the two cases of interest, Figure 3.6 displays the tendency of primary and secondary ice production, as well as the growth of ice particles through deposition, riming, and aggregation from the CNTRL and PHILL simulations at 17:00 (19:00) UTC on 26 (30) January. The vertical profiles on 26 January are taken within the seeder–feeder event, while those on 30 January are taken when the high-level cloud associated with the warm front has already passed the region of interest. Upon arrival of the frontal system on 26 January, CNTRL indicates a rapid increase in the total N_{isg} near the cloud top (Figure 3.5a), which is not shown in the vertical profile of primary ice production rates taken at 17:00 UTC (Figure 3.6a). The ice particles consisting the seeder

cloud are, therefore, formed far from the JFJ station and seem to be advected over the domain of interest. Primary ice crystals are formed in both cases below 2km in the feeder cloud at temperatures lower than −30 °C through heterogeneous freezing (Figure 3.6a). At these heights, supercooled liquid water is also present (Figure 3.5c), and the newly formed ice particles start growing initially by vapor deposition due to supersaturation with respect to ice, followed by riming (Figure 3.6b). This is also indicated by the increased IWC values closer to the ground (Figure 3.5b).

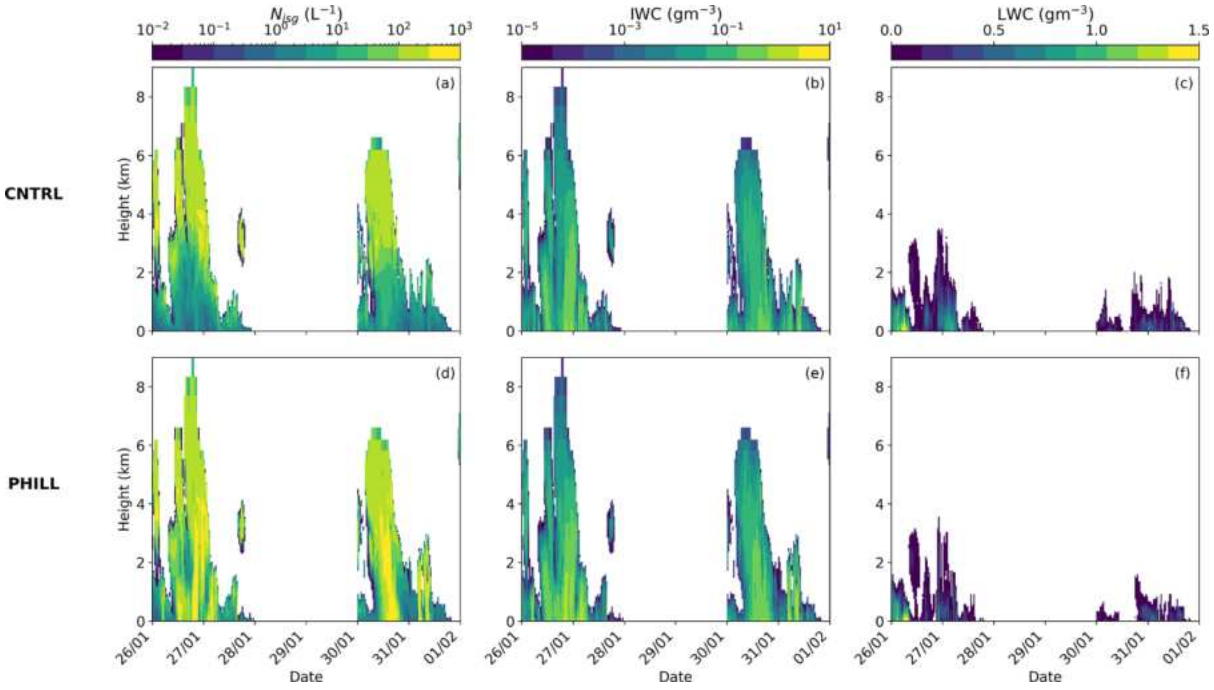

Figure 3.5 Time–height plots of total N_{isg} (a, d), IWC (b, e), and LWC (c, f) produced by CNTRL (a–c) and PHILL (d–f) simulations between 26 January and 1 February 2014. The height is given in km AGL.

Focusing on the ice-seeding event of 26 January, the enhanced aggregation rate observed at heights above ∼2.5 km in the atmosphere indicates the enhanced collision efficiencies of precipitating ice particles while falling from the seeder cloud (Figure 3.6c). Note that a portion of the sedimented ice particles sublimates before reaching the feeder cloud at heights ∼3–5 km, indicating the prevailing unsaturated conditions in this layer (Figure 3.6b). Within this layer, the aggregation of snowflakes weakens, while it is enhanced again when the falling hydrometeors enter the feeder cloud. The bottom line is that, even under the simulated seeder–feeder events, the concentrations of ice particles reaching the ground in CNTRL remain severely underestimated (Section 3.4.1). Despite the low concentrations of ice crystals simulated by the CNTRL simulation, the low-level cloud is glaciated more frequently during the SE than during the NW winds case (Figure 3.5c). This is probably because of the higher updraft velocities prevailing until 28 January (Figure 3.2d), preventing ice crystals from falling through the lower parts of the cloud (Lohmann et al., 2016).

Activating the BR mechanism along with the seeding of precipitating hydrometeors in PHILL shifts the simulated N_{isg} towards higher concentrations that are found to exceed 300 L^{-1} in the lower-level part of the cloud (Figure 3.5d). On 26 January, the mode of the cloud ice distribution shifts to slightly bigger sizes, while on 30 January the modal sizes become almost an order of magnitude smaller compared with the CNTRL simulation (Figure B4). The enhanced concentrations of bigger ice particles simulated in the first case experience rapid growth through vapor deposition and riming (Figure 3.6e), causing a slight increase in the simulated IWC (Figure 3.5e) at the expense of the surrounding cloud droplets in

the low-level feeder cloud (Figure 3.5f). Nevertheless, the smaller ice particles simulated in the second case grow less efficiently through vapor deposition, while the explosive multiplication of ice through BR seems to fully glaciate the low-level cloud below ~1 km, resulting in an almost zero riming rate (Figure 3.6e). The reduced primary ice production rate observed during both case studies is a consequence of the depletion of liquid water when BR is considered (Figure 3.6d). A suppression of heterogeneous ice nucleation following the introduction of SIP into models has already been reported in previous studies (Dedekind et al., 2021; Phillips et al., 2017b; Zhao & Liu, 2022).

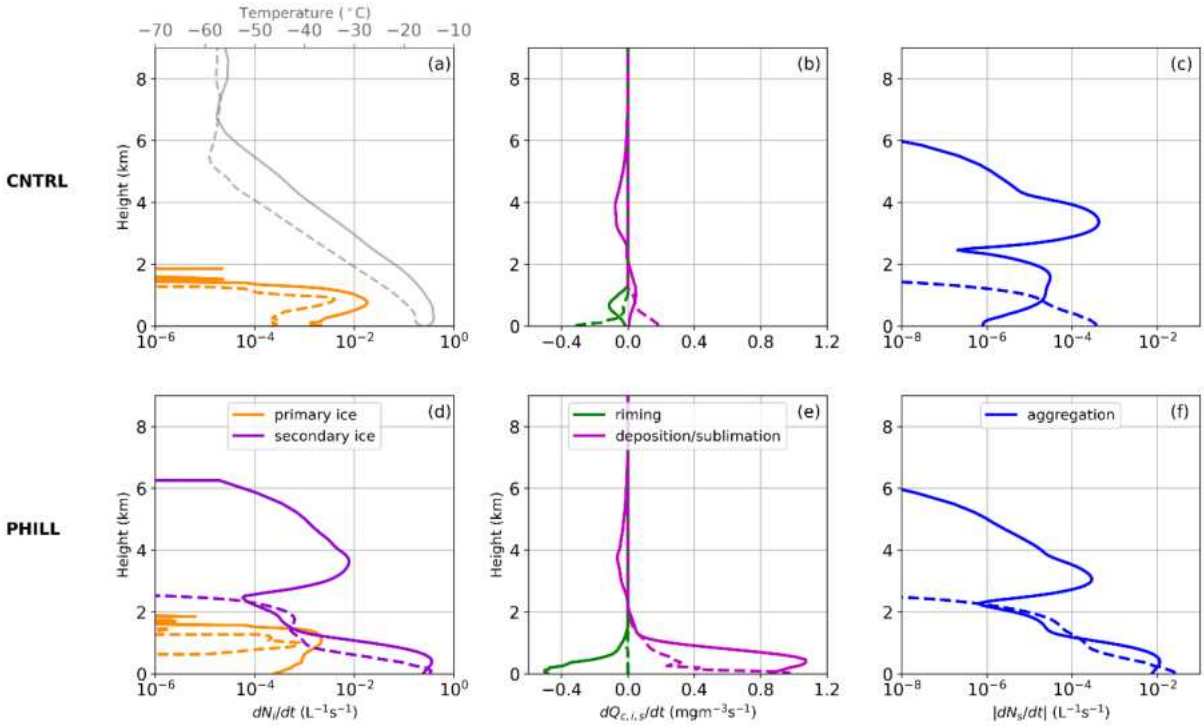

Figure 3.6 Vertical profiles of (a, d) primary and secondary ice production, (b, e) riming and vapor deposition or sublimation, and (c, f) snow aggregation produced by the CNTRL (a–c) and PHILL (d–f) simulations at 17:00 UTC on 26 January (solid line) and at 19:00 UTC on 30 January (dashed line). The vertical profile of simulated temperature is also superimposed in panel (a). The cloud liquid water content (Q_c) is shown in panels (b) and (e) to represent the tendency due to riming, while the mass mixing ratio of the ice and snow species (Q_i+Q_s), represents the relative tendencies due to vapor deposition or sublimation. Note that the tendencies due to snow aggregation in panels (c) and (f) are presented in absolute values. The height is given in km AGL.

The key difference between CNTRL and PHILL simulations is that the latter takes advantage of the enhanced ice particle growth through aggregation, while falling to the feeder cloud below ~2 km where large snowflakes coexist with smaller ice crystals (Figures 3.4a, 3.6a, 3.6d). This allows for differential settling, which enhances collision efficiency facilitating ice multiplication through BR. This is the reason why the vertical profile of secondary ice formation agrees with the corresponding profile of aggregation during both case studies (Figure 3.6d, f). On 26 January, the first secondary ice particles start forming already within the seeder cloud, with the contribution of SIP increasing considerably when reaching the feeder cloud, where the tendency, due to SIP, is more than 3 orders of magnitude higher than primary ice production (Figure 3.6d). The significant role of SIP stands out also on 30 January at altitudes below 2km. It is, therefore, essential to consider SIP though BR in the feeder cloud, in order to achieve the enhanced levels of ICNCs frequently observed within seeder–feeder events in the alpine region. This is in agreement with the observational study of Ramelli et al. (2021a) on an ice-

seeding case occurring in the region around Davos in the Swiss Alps. In this study, they proposed that SIP though HM and BR were necessary to explain the elevated ICNCs in feeder clouds.

A classification of the dominant type of precipitation was applied to the polarimetric data collected by a weather radar deployed at the Kleine Scheidegg station (2061 m a.s.l) during the SE case between 30 and 31 January (Figure B6). In the derived time series, we can identify periods when individual ice crystals (not aggregated and not significantly rimed) dominate over the entire precipitation column, followed by periods when a clear stratification is present with ice crystals aloft and mostly aggregates and rimed ice particles below. This stratification is observed on 30 January at 19:00 UTC when the model tendencies are extracted (dashed lines in Figure 3.6). Allowing for the BR process in PHILL results in an enhancement of 2 orders of magnitude in the aggregation rates close to the ground, which can better reproduce the signatures observed in the hydrometeor classification at that time. An increase in the simulated aggregates and rimed particles is expected to increase orographic precipitation, which is important given that these low-level feeder clouds are incapable of producing significant amounts of precipitation. Indeed, the mean surface precipitation produced by PHILL is increased by 30% (10%) during the NW (SE) case compared with CNTRL (Figure B7), which is in contrast to Dedekind et al. (2021), where the activation of the BR process is found to suppress the regions of strong surface precipitation. This was attributed to the limited efficiency of the small secondary ice particles to grow sufficiently to precipitation sizes when the local updrafts lift them to the upper parts of the cloud that were glaciated. The radar-based hydrometeor classification reveals also the predominance of ice crystals at the beginning and the end of the precipitating periods (e.g., on 30 January at 15:00–17:30 UTC or 31 January at 04:30–06:00 UTC), which is again more consistent with the vertical profile of Ni produced by PHILL rather than the CNTRL simulation (Figure B6, B8).

3.4.2 Sensitivity to the injection of ice crystals from the surface

In this section, we examine if the surface-originating small ice particles could have the potential to initiate and enhance ice particle growth in the near-surface MPCs present in our case studies. Figure 3.7 illustrates two additional WRF simulations – BIPs10 and BIPs100 – where the ice crystal source applied to the first model level is equal to 10 and 100 L^{-1}, respectively (Table 3.2). Note that these two sensitivity tests do not consider any SIP process to analyze the influence of BIPs only. The total N_{isg} values produced in BIPs10 are only slightly increased compared to the CNTRL simulation and generally remain outside the observed range at JFJ (Figure 3.7a). An order of magnitude increase in the applied NBIPs is seen to enhance the modeled N_{isg} during both case studies; however, our simulations are still lacking ice particles. This is particularly evident during the NW winds case, where the simulated N_{isg} varies most of the time around 10 L^{-1}, remaining an order of magnitude lower than the observations. During the SE case, the model performance is slightly improved, with the N_{isg} reaching up to ∼25 L^{-1} in BIPs100, which occasionally falls within the lower limit of the observed ICNC values (e.g., in the evening of 31 January). At times when the detected ICNCs remain quite low (i.e., of the order of 10 L^{-1}), the contribution of blowing snow particles probably from the Aletsch Glacier is sufficient to explain the observations at JFJ.

As indicated in Figure 3.7b, during the NW flow the simulated LWC at the first model level in BIPs10 and BIPs100 almost coincides with the CNTRL simulation of WRF. The three sensitivity simulations are producing comparable median and quartile LWC values (Table 3.5), with BIPs10 and BIPs100 producing median LWC values closer to the observed ones during the SE flow. When comparing against the LWC values in the third quartile though, the two simulations lead to an overestimation up to a factor of ∼1.5 during both case studies. Given that there is approximately a factor of >20 (5) difference between the modeled and observed ICNCs during the NW (SE) winds case (Table 3.3), overall Figure 3.7 reveals that the addition of a source of ice crystals from the effect of blowing snow cannot account for the observed liquid-ice phase partitioning in the simulated orographic MPCs.

Our findings are in contrast with the modeling study of Farrington et al. (2016), where a different approach was proposed to include the surface effect on the ICNCs simulated with WRF. In this study, a single model domain was used with a horizontal resolution of 1 km. To account for the flux of hoar crystals being detached from the surface by mechanical fracturing, Farrington et al. (2016) included a wind-dependent surface flux of frost flowers adapted from Xu et al. (2013). Despite the improved performance of WRF in terms of predicted ICNCs and LWC, the wind-dependent formulation of the surface flux caused the modeled ICNCs to become strongly correlated with the simulated horizontal wind speed – a behavior that was not confirmed by the observations of Lloyd et al. (2015). Nonetheless, the highest observed ICNCs at the beginning of the NW case correspond to the time when both the observed and modeled wind speed is the strongest (Figure 3.2c), implying that a wind-dependent surface flux of BIPs could potentially elevate the simulated N_{isg} to the observed levels at this time.

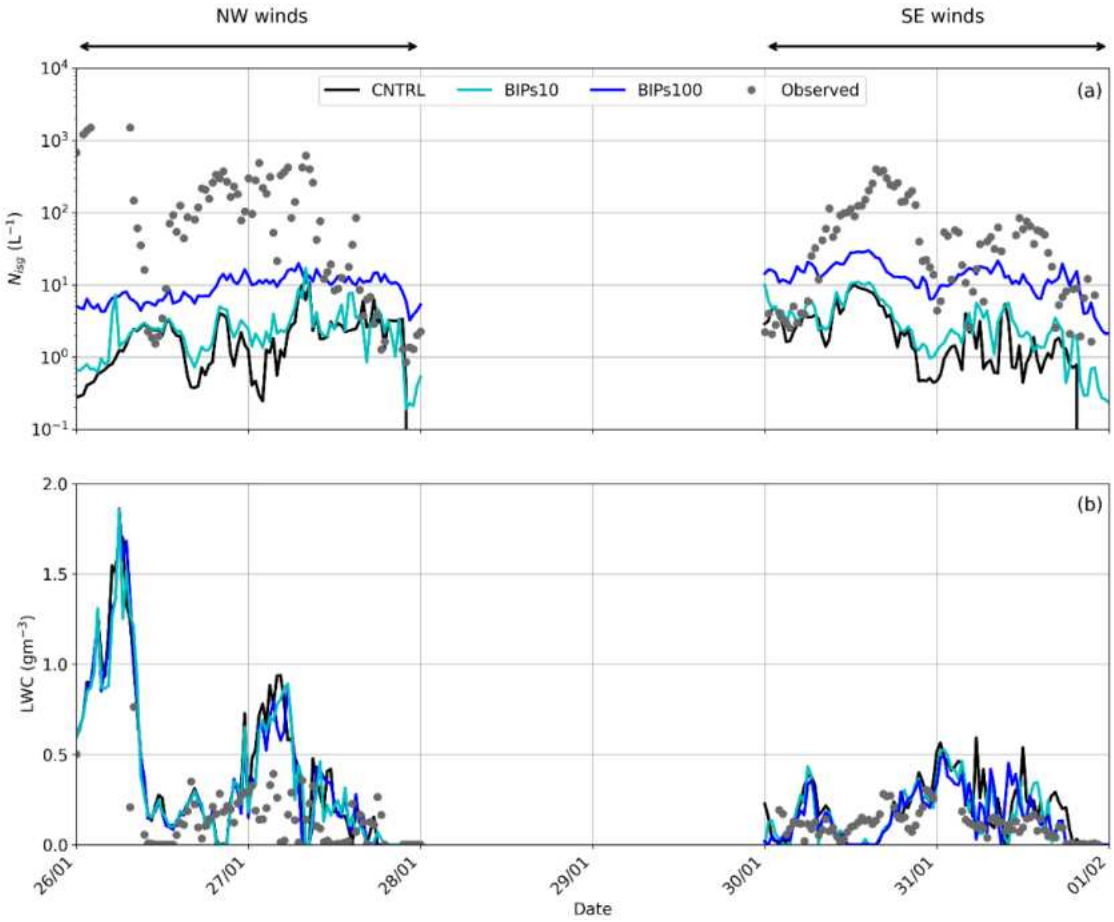

Figure 3.7 Time series of (a) total N_{isg} and (b) LWC predicted between 26 January and 1 February 2014 by the two sensitivity simulations accounting for the effect of blowing snow, i.e., BIPs10 (cyan line) and BIPs100 (blue line).

3.4.3 The synergistic impact of BR and surface-induced ice crystals

It is deducible from the above discussion that the sole inclusion of a constant source of BIPs in our simulations cannot efficiently bridge the gap between modeled and measured ICNCs. Our aim in this section is to explore the combined effect of SIP through BR and blowing snow on the simulated orographic MPCs, since both processes are deemed to be important when trying to explain the high

ICNCs observed in alpine environments. This is addressed in the final sensitivity simulation, BIPs100_PHILL, the results of which are compared with the CNTRL and PHILL simulations in Figure 3.8.

In terms of the modeled ice particle concentrations, the combination of the simplified blowing snow treatment and BR parameterization can account for most of the discrepancy between modeled and observed ICNCs, particularly during the SE case (Figure 3.8a), when the simulation leads to a best agreement with the observed interquartile values (Table 3.3). BIPs100_PHILL and CNTRL generally differ by an average factor of ∼100 (40) during the NW (SE) case, with the former producing N_{isg} values that are sometimes elevated by up to ∼3 (2) orders of magnitude (Figure 3.8a). Compared to the PHILL setup, including a source of BIPs is found to improve the modeled ICNCs close to the surface episodically – for instance, in the evenings of 30 and 31 January, with the N_{isg} in BIPs100_PHILL efficiently reaching the observed levels (Figure 3.8a). Note that BIPs can contribute to the modeled N_{isg} even without the presence of a near-surface orographic cloud (e.g., Geerts et al., 2015; Beck et al., 2018). For instance, BIPs100_PHILL is the only sensitivity simulation producing high N_{isg} values in the evenings of 27 and 31 January when the low-level cloud is dissipated (Figure 3.5c, f). In the former case, however, the model results in an overestimate of the ICNCs, which is also observed during the early hours of 30 January, suggesting that the applied source of ice crystals is unrealistically high at this time.

As the mixed-phase conditions are sustained throughout both case studies (Figure 3.8c), the plume of ice crystals is mixed into an ice-supersaturated environment and, thus, BIPs are expected to promote ice growth through their interaction with the surrounding supercooled liquid droplets and (ice) supersaturated air. The number of BIPs reaching the cloud base might not be large, but their presence is expected to further facilitate the action of the BR mechanism, considering the depositional growth they will undergo within the supercooled boundary layer cloud. This is illustrated, for example, with the concurrent increase in N_{isg} and IWC observed on 30 January at approximately 21:00UTC (Figure 3.8a, b) in the presence of the low-level cloud (Figure 3.8c). Note that the elevated N_{isg} caused by the addition of BIPs is not always followed by an efficient increase in the simulated IWC. This can be observed, for instance, on 27 January at 12:00UTC or in the evening of 31 January (Figure 3.8b).

A discrepancy between modeled and observed IWC was also highlighted in the study of Farrington et al. (2016) and was attributed to the small sizes of the hoar frost particles assumed (i.e., 10 μm). Although here BIPs are assumed to have sizes of 100 μm, the underestimation in the cloud IWC has still not been overcome. This suggests that the applied source of BIPs combined with the effect of SIP through BR shifts the ice particle spectra to smaller sizes, which are not very efficient at riming and the WBF process and, thus, do not always contribute to significant increases in IWC values. Overall, the interquartile values presented in Table 3.4 reveal that BIPs100_PHILL and PHILL yield almost identical IWC values, suggesting that the implementation of a constant source of BIPs does not further improve the representation of the total ice mass, despite the improvements in the simulated N_{isg}. Focusing on the LWC values in the third quartile, though, including a source of BIPs results in better agreement with the CLACE observations during the SE case, while it is shown to have little effect on the cloud liquid phase during the NW case (Table 3.5). Despite the increase in the modeled N_{isg} observed in BIPs100_PHILL, especially during the SE case, the liquid water in the low-level orographic cloud is not further depleted (Figure 3.8c). This is presumably because the mean surface precipitation produced is also enhanced by almost ∼20% compared to PHILL (Figure B7), which seems to balance the excessive ice production.

One final point that is worth noting here is that there are still certain periods when BIPs100_PHILL fails to reproduce the observed range of ICNCs. This could imply the potential contribution of additional ice multiplication processes to the observed ice particle concentrations. Indeed, the seeder– feeder configuration observed in the examined case studies could favor the fragmentation of sublimating hydrometeors while falling through an subsaturated environment before entering the feeder cloud (Bacon et al., 1998; Deshmukh et al., 2022). The so-called sublimational breakup is an overlooked SIP

process which is not yet described in the M05 scheme. Also, note that the periods when the modeled ICNCs remain below the observed ice number levels are mainly identified when the simulated temperature drops below −15 °C and the wind speed exceeds 10 ms^{-1} or even 20 ms^{-1} (e.g., in the morning of 26 or 27 January at around 12:00UTC). This is when the incorporation of surface-based processes becomes of primary importance. The simplified methodology we followed here, although instructive, faces several limitations. For instance, the constant source of BIPs is sometimes found to overestimate the modeled N_{isg} and IWC. In order to accurately assess the potential role of the snow-covered surfaces in elevating the simulated ICNCs, an improved spatiotemporal description of the concentration and distribution of BIPs is required. Furthermore, the applied ice crystal source is independent of some key parameters controlling its resuspension, such as the horizontal wind speed, the updrafts, or the friction velocity (e.g., Vionnet et al., 2013, 2014). For example, in the early morning hours of 26 January, the high simulated horizontal and vertical velocities (Figure 3.2c, d) are expected to loft significant NBIPs into the cloud layer, owing to enhanced mechanical mixing and momentum flux close to the surface. Nonetheless, the contribution of the induced plume of BIPs remains constant throughout the NW case study (Figure 3.7a), which seems to lead to an underestimation of the total ice particle concentration and mass. A more realistic parameterization of the BIPs flux or the coupling with a detailed snowpack model (e.g., Sharma et al., 2023) would, therefore, be essential for a more accurate representation of the effect of blowing snow.

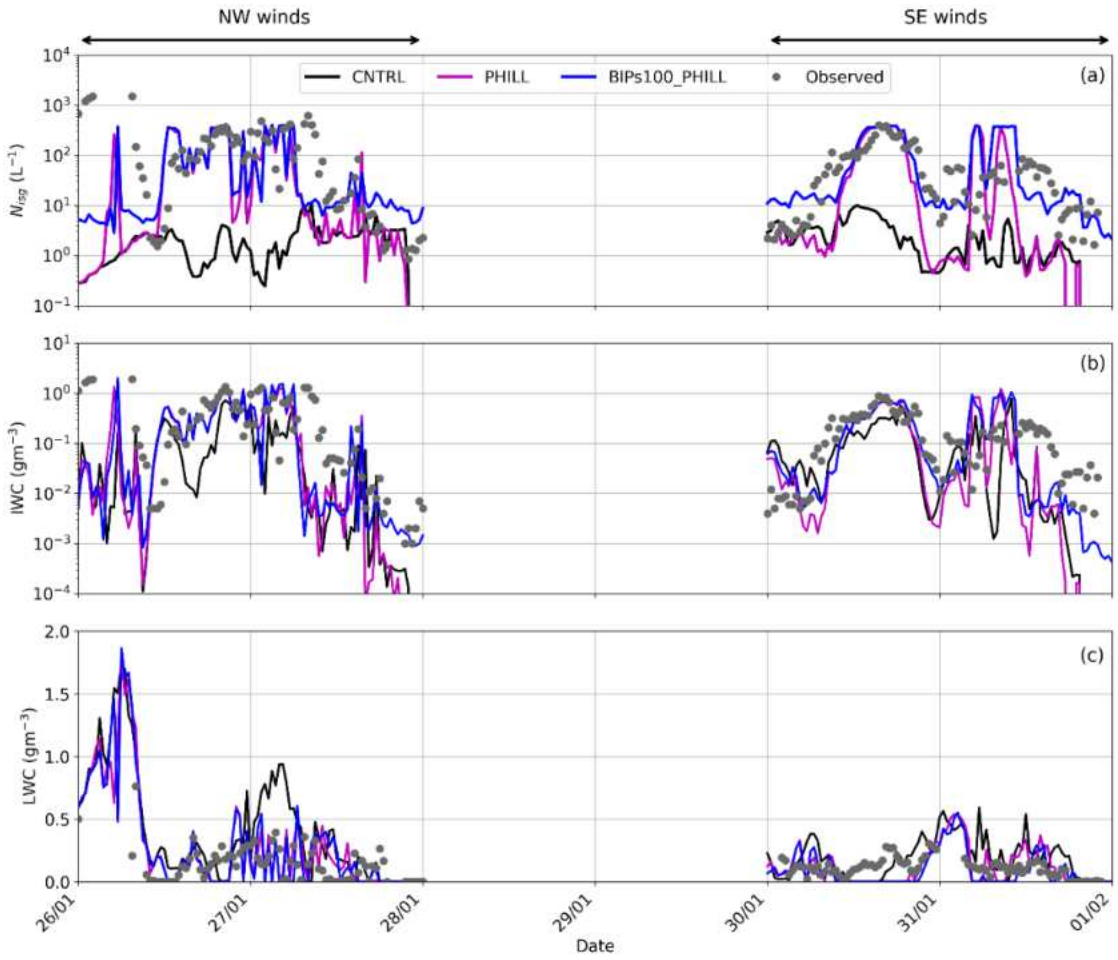

Figure 3.8 Time series of (a) total N_{isg}, (b) IWC, and (c) LWC predicted between 26 January and 1 February 2014 by the sensitivity simulation BIPs100_PHILL (blue line), which examines the combined effect of ice multiplication through BR and blowing snow.

3.5 Summary and conclusions

This study employs the mesoscale model WRF to explore the potential impact of ice multiplication processes on the liquid ice-phase partitioning in the orographic MPCs observed during the CLACE 2014 campaign at the mountain-top site of JFJ in the Swiss Alps. The orography surrounding JFJ channels the direction of the horizontal wind speed, giving us the opportunity to analyze two frontal cases occurring under NW and SE conditions.

DS and BR mechanisms were implemented in the default M05 scheme in WRF, in addition to the HM parameterization, which, however, remained inactive in the simulated temperature range (−10 to −24 ^{o}C). The DS process is parameterized following either the latest theoretical formulation developed by Phillips et al. (2018) or the more simplified parameterization proposed by (Sullivan, Hoose, et al., 2018). Our sensitivity simulations revealed that the DS mechanism is ineffective in the two considered alpine MPCs, even under the higher updraft velocity conditions associated with the NW winds case study, owing to the lack of large drops required for the process.

To parameterize the number of fragments generated per ice–ice collision, we followed again two different approaches. We used either the simplified temperature dependent formulation of Takahashi et al. (1995) scaled for the size of the particle that undergo fragmentation (Sotiropoulou, Vignon, et al., 2021) or the more advanced physically based Phillips et al. (2017a) parameterization. It is important to apply the Takahashi parameterization only to consider collisions between rimed ice particles, otherwise the number of generated fragments is significantly overestimated. Including a description of the BR mechanism is essential for reproducing the ICNCs observed in the simulated orographic clouds, especially at temperatures higher than ∼−15 ^{o}C, where INPs are generally sparse. SIP through BR is found to enhance the modeled ICNCs by up to 3 (2) orders of magnitude during the NW (SE) case, improving the model agreement with observations. This ice enhancement can cause up to an order of magnitude increase in the mean simulated IWC values compared with the CNTRL simulation, which is attributed to the enhanced ice crystal growth and cloud-ice-to-snow autoconversion. The increase in the simulated ICNCs also depletes the cloud LWC by at least a factor of 2 during both cases, which is more consistent with the measured LWC values.

One of the most interesting outcomes of this study is the association of the enhanced BR efficiency with the occurrence of in-cloud seeder–feeder events, which are commonly found in Switzerland (Proske et al., 2021). While ice-seeding situations are associated with enhanced orographic precipitation in the alpine region, the CNTRL simulation fails to reproduce the elevated ICNCs reaching the ground. The falling ice hydrometeors experience efficient growth through aggregation in the seeder part of the cloud, which is enhanced when reaching the feeder cloud at altitudes below 2km, where primary ice crystals form and grow through vapor deposition and riming. Aggregation of snowflakes seems to be the major driver of secondary ice formation in the examined seeder–feeder events. SIP through BR is initiated already within the seeder cloud, while it becomes immensely important in the feeder cloud, where its production rate exceeds the one of primary ice formation. The increased generation of secondary ice fragments does not always lead to ice explosion and cloud glaciation, as it is followed by an enhancement in the precipitation sink owing to a shift in the ice particle spectrum. Including a description of the BR mechanism is, therefore, crucial for explaining the ice particle concentration and mass observed in the low-level feeder clouds.

To assess the potential role of blowing snow in the simulated orographic clouds, a constant source of ice crystals was introduced in the first atmospheric level of WRF. Our results indicate that blowing snow alone cannot explain the high ICNCs observed at JFJ, but when this source is combined with the BR mechanism then the gap between modeled and measured ICNCs is sufficiently bridged. The biggest influence of blowing snow is mainly detected at times when the simulated temperatures are low enough (<−15 ^{o}C), while the presence of a low-level cloud is required for SIP to manifest. The concentrations of BIPs reaching the cloud base are not high, but when they are mixed among

supercooled liquid droplets then they are expected to grow, facilitating ice multiplication through BR. Nonetheless, including a wind dependence or a spatiotemporal variability in the applied ice crystal source would be essential to provide a more precise description of the effect of blowing snow on the simulated clouds.

Overall, our findings indicate that, outside the HM temperature range, a correct representation of both secondary ice (through BR) and an external ice-seeding mechanism, which is primarily precipitating ice particles formed aloft and, to a lesser degree, windblown ice from the surface, is fundamentally important for accurately predicting the liquid-ice-phase partitioning and properties of MPCs. Given the high frequency of seeder–feeder events in orographic environments, including the new physics of BR may address a large source of predictive bias in atmospheric models.

4. Unraveling secondary ice production in winter orographic clouds through a synergy of in-situ observations, remote sensing and modeling

In this chapter we aim to identify potential indicators of secondary ice production in ground-based radar observations of orographic mixed-phase clouds obtained during the CALISHTO campaign at Mount Helmos, Greece. The research involves numerical modeling, analysis of full Doppler spectra and radar moments, as well as forward radar simulations. The text is based on the submitted manuscript:

- **Georgakaki, P.,** Billault-Roux, A.-C., Foskinis, R., Gao, K., Sotiropoulou, S., Gini, M., Takahama, S., Eleftheriadis, K., Papayannis, A., Berne, A., Nenes, A. (2023): Unraveling secondary ice production in winter orographic clouds through a synergy of in-situ observations, remote sensing and modeling. *Under review for npj Climate and Atmospheric Science.*

The modeling experiments, set-up of the radar simulator and analyses were performed by Paraskevi Georgakaki. Anne-Claire Billault-Roux performed post-processing on the radar observations collected from Romanos Foskinis, and together with Alexis Berne provided valuable insights into their analysis. Georgia Sotiropoulou contributed to the implementation of the sublimational break-up mechanism parameterization. Athanasios Nenes organized the research project and supervised the progress. All authors contributed to the scientific interpretation and writing of the manuscript.

4.1 Summary

Recent years have shown that secondary ice production (SIP) is ubiquitous, affecting all clouds from polar to tropical regions. SIP is not described well in models and for this may vastly underpredict ice crystal number concentrations in warm mixed-phase clouds. Through a synergy of modeling, remote sensing and in-situ measurements carried out in an orographic environment during the Cloud-AerosoL InteractionS in the Helmos background TropOsphere (CALISHTO) campaign, we show that SIP can have a profound impact on the vertical distribution of hydrometeors and precipitation, especially in seeder-feeder configurations which are encountered in multi-layered cloud systems. The mesoscale model simulations coupled with a radar simulator strongly support a unique signature that is characteristic of SIP; because of this, our study opens the possibility of using the vast global archive of cloud radar data for systematically inferring SIP signatures and frequency of occurrence.

4.2 Introduction

The distribution of the ice and liquid phases of water within mixed-phase clouds (MPCs) significantly affects surface cloud radiative forcing (Tan & Storelvmo, 2019; Vergara-Temprado et al., 2018) and the hydrological cycle (Heymsfield et al., 2020; Mülmenstädt et al., 2015). MPCs exhibit spatial heterogeneity at spatial scales lower than 100 m, with spatially separated ice- and liquid-phase clusters (Field et al., 2004; Korolev & Milbrandt, 2022; Korolev et al., 2003). This heterogeneity impacts the efficiency of the Wegener-Bergeron-Findeisen (WBF) process (Bergeron, 1935; Findeisen, 1938; Wegener, 1911) (where ice crystals grow at the expense of cloud droplets) and the rate of cloud glaciation. Accurately representing these processes in numerical weather prediction (NWP) and climate models remains a major challenge and a source of model bias(Matus & L'Ecuyer, 2017; McCoy et al., 2016; Zelinka et al., 2020).

Ice crystal number concentration (ICNC) in mixed phase clouds is expected to be modulated by the availability of ice nucleating particles (INPs) (Hoose & Möhler, 2012; Murray et al., 2012). The sparsity of INPs (Kanji et al., 2017; Wex et al., 2019) at temperatures above -20°C cannot account for ICNCs observed in MPCs. Secondary ice production (SIP) following the initial primary ice nucleation events must be considered to bridge the gap between the limited availability of INPs and the abundance of ICNCs (Field et al., 2017; Korolev & Leisner, 2020). Atmospheric models neglecting the effect of SIP are therefore prone to underestimate simulated ICNCs at warm subzero temperatures with important implications for the radiative properties and microphysical evolution of this type of clouds (Huang et al., 2022; Young et al., 2019; Zhao et al., 2023).

The importance of SIP has been widely acknowledged in laboratory (Grzegorczyk et al., 2023; James et al., 2021; Keinert et al., 2020; Vardiman, 1978), field (Järvinen et al., 2022; Lasher-Trapp et al., 2016; Lawson et al., 2015), remote sensing (Billault-Roux et al., 2023; Grazioli et al., 2015; Li, Möhler, et al., 2021; Luke et al., 2021), and modeling studies (Atlas et al., 2020; Sotiropoulou, Vignon, et al., 2021; Zhao & Liu, 2021) worldwide (Hoose, 2022). The most commonly invoked SIP processes include the Hallett-Mossop (HM) or rime-splintering process (Hallett & Mossop, 1974; A. J. Heymsfield & Mossop, 1984), ice-ice collisional break-up (BR) (Phillips et al., 2017a; Takahashi et al., 1995), and droplet-shattering during freezing (DS) (Griggs & Choularton, 1983; Lauber et al., 2018). While HM is extensively incorporated in atmospheric models, its efficiency is limited to a narrow temperature range of -8°C to -3°C and specific cloud microphysical configurations. Recent experimental studies even suggest potential overestimation of the efficiency of this process (Hartmann et al., 2023). Vigorous convective downdrafts (Patade et al., 2022; Waman et al., 2022) and associated subsaturated regions may also foster the break-up of graupel and dendritic snow particles from sublimation (SUBBR) (Bacon et al., 1998; Deshmukh et al., 2022).

A major challenge is the ability to detect the presence of SIP in global MPCs, ideally with insights on its intensity and mechanisms. Without such information, models lack a key microphysical constraint that impedes progress in the description of MPCs. Ground-based remote sensing observations of cloud and precipitation can provide key information for constraining SIP (Li, Korolev, et al., 2021; Li, Möhler, et al., 2021; Luke et al., 2021; Oue et al., 2018). One approach is to use lidar and radar retrievals to extract ice multiplication factors (i.e., ICNCs/INPs); application of such a method in wintertime orographic MPCs indicated the widespread occurrence of SIP, with a frequency exceeding 85% (Wieder et al., 2022). Doppler spectra from vertically-pointing radars provide another powerful approach, as they often exhibit multimodal distributions within the temperature range associated with SIP or within the dendritic growth layer (DGL), typically between -20 and -10°C (von Terzi et al., 2022). These distributions suggest interactions between fast-falling and slower-falling particles within

the radar volume from riming (Kalesse et al., 2016) or new ice formation (Billault-Roux et al., 2023; Luke et al., 2021; Oue et al., 2015, 2018). Significant ambiguity however remains on the interpretation of these signals, as downdrafts, horizontal winds, turbulence or other measurement uncertainties can affect their interpretation.

Here, we show – by coupling an updated version of the mesoscale Weather Research and Forecasting (WRF) model with a forward radar simulator (Oue et al., 2020; Vignon et al., 2019, 2021) – that characteristic signatures in observed cloud radar data can indeed be attributed to the presence of SIP, as inclusion of the latter significantly improves the agreement with the radar observations, including the vertical distribution of precipitation and the timing thereof, and thus opening the possibility to leverage the abundant cloud remote sensing observations for SIP signatures.

4.3 Data and Methods

The observational data presented in this study were collected as part of the as part of the Cloud-AerosoL InteractionS in the Helmos background TropOsphere (CALISHTO) campaign (https://calishto.panacea-ri.gr/). CALISHTO took place between October 2021 and March 2022 at Mount Helmos, Greece, with the primary objective of enhancing our understanding of the processes involved in orographic MPC formation and evolution. In this campaign, extensive in-situ and remote sensing observations were carried out at three different altitudes. Meteorological, aerosol, and cloud measurements were taken at the mountain-top station, Helmos Hellenic Atmospheric Aerosol and Climate Change $(HAC)^2$ (Figure 4.1), located at 2314 m above mean sea level (AMSL) (37°N 59' 2.4'', 22°E 11' 45.6'') (Coen et al., 2018). On the lee side of the $(HAC)^2$ station, a region called "Vathia Lakka" (VL) at approximately 1850 m AMSL, aerosol and cloud measurements were conducted using remote sensing techniques. At the lower altitude site, ~1700 m AMSL, a multi-wavelength depolarization lidar was used to sample vertical profiles of aerosol and cloud properties. Figure 4.1b illustrates the complex orography surrounding $(HAC)^2$ and VL. Here, we provide a brief summary of the instrumentation employed in this study.

4.3.1 In-situ observations

Cloud in-situ measurements were conducted at $(HAC)^2$ using the Gerber Particulate Volume Monitor (PVM-100, Gerber Scientific Instruments Inc.) (Gerber, 1991). This instrument is designed to measure the cloud liquid water content (LWC), particle surface area (PSA), and derive the droplet effective radius (r_{eff}) for ambient clouds. To obtain these measurements, a diode-emitted laser beam is directed along a 40-cm path, and the scattered light in the open air along the path is converted into a signal after passing two spatial filters. The first filter converts scattered light to a signal proportional to the particle volume density (or LWC), while the second filter produces a signal proportional to the PSA. By analyzing the ratio of these two quantities, r_{eff} can be derived for droplet diameter from 3 to 45 µm. The uncertainty of LWC is 10 % for this diameter range. The PVM-100 instrument has undergone testing and inter-comparison with other instruments during ACTRIS (Aerosol Cloud and Trace gases Research Infrastructure) activities (Guyot et al., 2015). For the purposes of this study, LWC and r_{eff} data collected by the PVM-100 were utilized to derive the cloud droplet number concentration (N_{d}) based on the formulation presented in Brazda et al. (2013) (see their Equation 4).

Aerosol size distributions over the size range between 0.25 and 32 µm were measured at $(HAC)^2$ by an Optical Particle Counter (OPC; GRIMM Technologies Inc., Model 1.109), which provides real-time

aerosol characterization including 32 channels. In this study, OPC diameter (d_{opc}) was converted into aerodynamic diameter (d_{aer}) using the formula: $d_{aer} = d_{opc}\left(\frac{\rho}{\chi}\right)^{0.5}$, assuming a shape factor of χ=1.1 and a particle density of ρ=2.0 g cm^{-3} (Hu et al., 2012; Peters et al., 2006).

4.3.2 Remote sensing observations

At the VL station, a frequency-modulated continuous wave (FMCW) W-band Doppler spectral zenith profiler (WProf) (Küchler et al., 2017) was deployed. Operating at a frequency of 94 GHz, WProf allows for measurements up to approximately 10 km above ground level. Vertically, WProf employs three chirps, each with a respective range resolution of 7.5 m, 16 m, and 32 m. WProf settings are summarized in Table C1 in Appendix C. For this study, we utilized full Doppler reflectivity spectra and corresponding moments. These moments include the radar equivalent reflectivity factor (Ze_w), MDV and skewness. An attenuation correction has been applied to the W-band radar reflectivities, to facilitate their comparison against the forward simulation products. To do so, the radiative transfer model PAMTRA (Mech et al., 2020) was used to simulate both gaseous and cloud liquid water attenuation at 94 GHz. The vertical profiles of the necessary atmospheric and liquid water profiles were obtained from the WRF model set-up, which includes the most advanced description of both primary and secondary sources of ice crystals (see ALLSIP simulation described below).

In addition to the radar variables, WProf offers the capability to estimate the cloud liquid water path (LWP) using a retrieval algorithm presented by Billault-Roux and Berne (2021). This algorithm uses the brightness temperature measured by a joint 89-GHz radiometer, in combination with available meteorological data such as temperature, pressure, and reanalysis data as well as geographical information (i.e., latitude, longitude). The relative error in the retrieved LWP values was determined to be 18% for cloudy cases (i.e., LWP > 30 g m^{-2}).

4.3.3 WRF simulations

4.3.3.1 Model set-up

We utilized WRF version 4.0.1, incorporating augmented cloud microphysics to account for additional SIP mechanisms (Georgakaki et al., 2022; Karalis et al., 2022; Sotiropoulou, Vignon, et al., 2021), to model the current case study. Our model configuration consisted of three two-way nested domains (Figure 4.1) with horizontal resolutions of 12 km, 3 km, and 1 km, respectively. The parent domain encompassed a 148x148 grid centered over the (HAC)^2 station. The second and third domains consisted of 241x241 and 304x304 grids, respectively. All domains employed the Lambert conformal projection, suitable for mid-latitudes. We implemented a refined vertical grid spacing, following the approach proposed by Vignon et al. (2021), employing 97 vertical eta levels up to a model top of 50 hPa (∼20 km). Note that the employed model setup was consistent with the one utilized for wintertime orographic clouds in the Swiss Alps (Georgakaki et al., 2022).

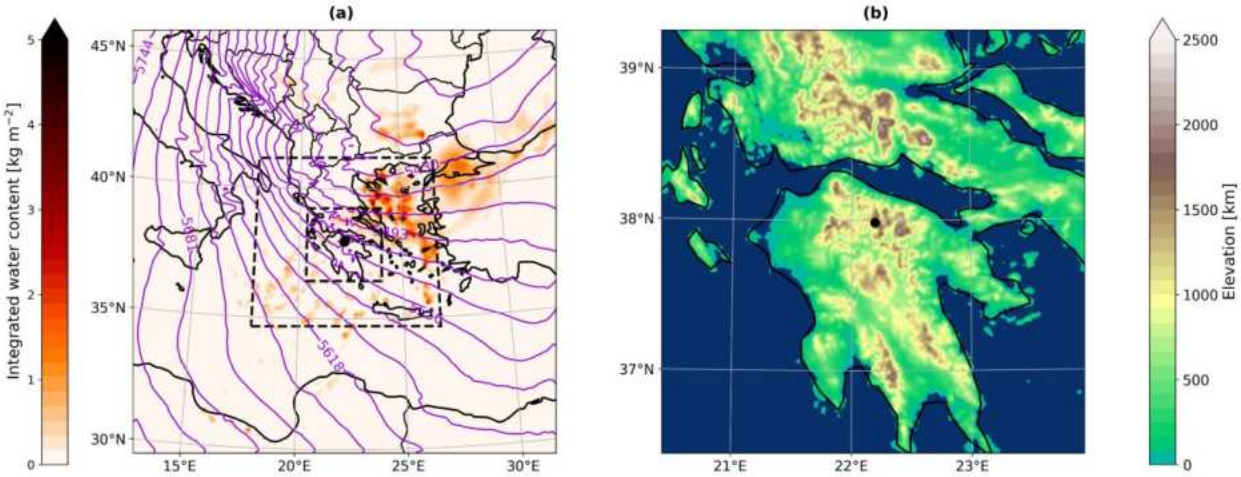

Figure 4.1 (a) Vertically integrated water content obtained from the 12-km resolution domain of the CONTROL simulation of WRF on December 17 (22:00 UTC), 2021. The purple contours represent the 500 hPa geopotential height in meters. The black dashed lines outline the boundaries of the two nested domains of WRF. (b) Model orography from the 1-km resolution domain. The black dot in both panels marks the location of the $(HAC)^2$ station.

The WRF simulations started on December 17, 2021, at 00:00 UTC, providing 22 hours of spin-up time before the passage of a low-pressure system over the region of interest. This system, named storm Carmel, was associated with polar airmasses originating from northern Europe (Figure C1 in Appendix C), bringing a significant temperature decrease, stormy winds, and heavy snowfall to most parts of Central and Southern Greece. The temperature drop and the prevailing strong-wind conditions are illustrated in Figure C2, where they are compared against surface meteorological variables obtained from the weather station at $(HAC)^2$ to evaluate the performance of the model. Our analysis covers the period until December 19, 2021, at 12:00 UTC. We employed a time step of 36 s in the parent domain, which decreased to 9 s in the second domain and 3 s in the third domain. The output frequency was set at every 5 minutes.

WRF is forced with initial and 6-hourly boundary conditions from the fifth generation of the European Centre for Medium-Range Weather Forecasts (ECMWF) atmospheric reanalyses dataset (ERA5) (Hersbach et al., 2020). The use of high-resolution ERA5 data (0.36°) for initializing WRF has been found to outperform the near real-time Global Forecasting System (GFS) data from the National Centers for Environmental Protection (NCEP), which has a spatial resolution of 1° (not shown). The static fields at each model grid point, including topography and land use fields, were sourced from default WRF pre-processing system datasets with a resolution of 30''. The land use categories were based on the Moderate Resolution Imaging Spectroradiometer (MODIS) land cover classification. In terms of physics options, we employed the Rapid Radiative Transfer Model for General Circulation Models (RRTMG) radiation scheme to parameterize both shortwave and long-wave radiative transfer. The planetary boundary layer (PBL) physics were represented using the non-local, first-order closure YSU (Yonsei University) scheme (Hong et al., 2006), coupled with its associated surface layer scheme. A sensitivity simulation revealed that YSU outperformed the local Mellor-Yamada-Janjić (MYJ) (Janjić, 2002) 1.5 order scheme (not shown) in terms of meteorological observations. Surface processes were modeled using the Noah land surface model (Noah LSM) (Chen & Dudhia, 2001). The Kain-Fritsch cumulus parameterization was only activated in the 12-km resolution domain, as the resolution of the

two nested domains was deemed sufficient to reasonably resolve cumulus cloud processes at the grid scale.

4.3.3.2 Microphysics scheme and sensitivity simulations

Cloud microphysics is parameterized using the Morrison et al. (2005) (M05) scheme of WRF. This scheme utilizes a double-moment approach to represent the characteristics of raindrops, cloud ice, snow, and graupel particles by predicting both their mass and number concentrations. However, for cloud droplets, a single-moment approach is employed, necessitating the specification of a constant N_d. During the passage of storm Carmel, a power outage caused by severe weather conditions disrupted the PVM-100 measurements. In our study, we opted for an N_d value of 100 cm^{-3}. This choice aligns with the temperature-dependent median N_d spectrum observed by PVM-100 throughout the CALISHTO campaign and is also consistent with observations at the high-altitude station of Jungfraujoch in the Swiss Alps (Lloyd et al., 2015).

The M05 scheme incorporates different ice formation processes. Homogeneous freezing is considered for temperatures below -40°C, while heterogeneous ice nucleation is initiated below -4°C. The latter accounts for various temperature-dependent mechanisms, including immersion freezing of cloud droplets and raindrops (Bigg, 1953), contact freezing (Meyers et al., 1992), and condensation/deposition freezing nucleation (Cooper, 1986). The default PIP scheme of WRF was used to perform the CONTROL sensitivity simulation. However, when comparing the predicted INPs derived offline using the simplified temperature-dependent formulations of WRF with two-month INP measurements taken between -28°C and -23°C at $(HAC)^2$, a significant overestimation of up to three orders of magnitude was observed (Figure C3b, c, Appendix Text C1). As a more advanced alternative, DeMott et al. (2010) (DM10) developed an aerosol-aware scheme that accounts for the concentration of aerosols with sizes larger than 0.5 µm aerodynamic diameter ($n_{aer,0.5}$) and temperature. The DM10 parameterization yielded more realistic offline INP concentrations, with predictions that agree with observations within a factor of three (Figure C3a) for more than 70% observed data points. Therefore, in the DEMOTT sensitivity simulation, we replaced the default PIP scheme of WRF with the DM10 parameterization. In our case an $n_{aer,0.5}$ of 0.30 scm^{-3} was prescribed, as dictated by the mean OPC measurements taken during the simulation period. Note that in DEMOTT, the Bigg parameterization was still kept active to account for the freezing of big raindrops.

The final sensitivity simulation analyzed in this study, referred to as ALLSIP, incorporates both PIP and SIP processes, with the former following the advanced DM10 parameterization. The M05 scheme, similar to other microphysics schemes in NWP models, includes the representation of only one SIP process: HM. This process is parameterized following Reisner et al. (1998), which accounts for the production of ice splinters within the HM temperature range ($-8 \leq T \leq -3$°C). It occurs when supercooled droplets or raindrops collide and freeze onto snow or graupel particles. Provided that a certain threshold in the mixing ratios of the involved ice and liquid hydrometeors is exceeded, the efficiency of this process is regulated by a temperature-dependent scaling factor which allows for a maximum production rate of 350 splinters per milligram of accreted liquid, at around -5°C (Reisner et al., 1998). The splinter production rate decreases linearly towards the edges of the HM zone and becomes zero outside this range.

The BR mechanism is an additional SIP process considered in ALLSIP. In the M05 scheme, BR follows the parameterization by Phillips et al. (2017a), which has been shown to provide realistic representation of ICNCs in orographic MPCs (Georgakaki et al., 2022). A detailed implementation of

the BR mechanism in M05 is described in Sotiropoulou, Vignon, et al. (2021). The number of ice fragments generated from collisions among the three ice hydrometeor species is determined by factors such as collisional kinetic energy, size, rimed fraction, and ice habit of the particles involved. While M05 does not explicitly resolve the rimed fraction and ice habit, assumptions are made to account for their influence. The impact of the prescribed rimed fraction has been previously investigated (Sotiropoulou, Ickes, et al., 2021; Sotiropoulou, Vignon, et al., 2021), and a sensitivity experiment in the current case study revealed that a rimed fraction of 0.2 aligns better with observed cloud systems (not shown). Higher degrees of riming led to unrealistically high ICNCs, particularly within the lower cloud layers. Activation of BR requires a nonzero mass of raindrop or cloud droplet to be rimed onto the ice particle, leading to fragmentation. It is important to note that the original BR scheme was designed for ice particles larger than 500 μm. According to Phillips et al. (2017a), when dealing with smaller sizes, it is advisable to set them to the nearest limit within the specified range. Consequently, we limit the efficiency of BR to particles with a characteristic size exceeding 100 μm. Regarding the ice habit, the Phillips parameterization provides two formulations depending on the prevailing temperature range. Dendritic particles are considered between -17 and -12°C, while non-dendritic planar ice particles are assumed outside this temperature range. (Sotiropoulou, Ickes, et al., 2021) found minimal sensitivity to the prescribed ice habit, and thus we adopt planar ice particles, which capture a wider temperature range and are valid for a broader range of particle shapes. All secondary ice fragments resulting from the BR mechanism are classified as cloud ice.

Another SIP process accounted for in ALLSIP is the DS mechanism. A detailed description of how M05 scheme was updated to include this process is provided in Georgakaki et al. (2022). DS involves two collision modes, as outlined by Phillips et al. (2018). In the first mode, freezing and subsequent shattering occur when a supercooled raindrop collides with a less massive cloud ice particle or when an INP triggers freezing in immersion mode. The number of fragments generated in this mode are multiplied by the product of droplet freezing and shattering probabilities, being described by the cubic interpolation functions found in Phillips (Phillips et al., 2018). The former is set to unity for temperatures below -6°C and zero for temperatures above -3°C, while the latter depends on the size of the raindrop, being 0 for sizes smaller than 50 μm, 1 for sizes larger than 60 μm. The second mode, involves collisions between raindrops and larger ice particles such as snow or graupel (James et al., 2021). These collisions produce tiny ice fragments, which are introduced as cloud ice in the number conservation equations. Larger fragments are classified depending on the specific collision that triggered the freezing process of raindrops, which will in turn determine whether they will be treated as graupel, snow, or frozen drops.

The last SIP process included in ALLSIP is SUBBR, which occurs when dendritic or heavily rimed particles sublimate under subsaturated conditions within downdrafts, resulting in the detachment of ice parts (e.g., branches from dendrites) from the parent ice particle (Bacon et al., 1998). A recent study by Deshmukh et al. (2022) introduced two empirical formulations for the SUBBR of graupel and dendritic snow. When implemented into the M05 scheme, the former parameterization is valid throughout all temperatures provided that the RH_i is less than 100%. The latter is enabled at temperatures between -20≤T≤-10 °C, where the dendritic ice habit of snow particles is favored (Libbrecht, 2017). The number of fragments generated after SUBBR (N_{SUBBR}) is determined by the product: $N_{SUBBR} = K \cdot M^{0.5702}$, where *K* is a function of the initial size of the particle, ambient RH_i, and a ventilation factor associated with the fall speed of the particle, while *M* is the sublimated mass described by the M05 scheme. More details about this empirical parameterization can be found in Deshmukh et al. (2022).

4.3.4 The CR-SIM forward radar simulator

Forward simulators are valuable tools for converting model output into quantities that can be directly compared with observations from remote sensing instruments. This enables a more accurate assessment of the agreement between model predictions and real-world data. In our study, we utilized the outputs from the 3 WRF sensitivity simulations (i.e., CONTROL, DEMOTT, and ALLSIP) as input for the Cloud Resolving Model Radar Simulator (CR-SIM) version 3.32 (Oue et al., 2020). CR-SIM is compatible with various microphysics schemes of WRF and has previously been employed to evaluate the performance of polar WRF in representing Southern Ocean MPCs and snowfall microphysics (Vignon et al., 2019, 2021). The T-matrix method is used in CR-SIM to calculate the scattering properties of simulated frozen and liquid hydrometeors, which are then organized into look-up tables. In our study, CR-SIM was configured as a vertically profiling radar operating at 94 GHz, matching the frequency of the WProf deployed at VL. The radar beamwidth and range resolution were also adjusted to align with the characteristics of the actual instrument. The CR-SIM was run using a specific model grid point located closer to the VL station. The idealized simulated radar variables (i.e., after correction for the total hydrometeor attenuation) are then provided at each vertical model grid cell, facilitating straightforward comparisons with real observations.

4.4 Results and discussion

The updated WRF model, which incorporates detailed descriptions of SIP processes, was used to investigate the microphysics driving the intense snowfall event observed on December 18, 2021 in mainland Greece. Doppler spectrograms along with timeseries of radar moments were captured by the WProf radar (Section 4.3.2). The radar observations provided valuable insights into the microphysics of snowfall and served as a basis for evaluating the performance of the WRF model and investigating potential SIP signatures.

4.4.1 Comparing radar observations with radar observables

Figure 4.2 shows time-height contours of two standardized moments of the Doppler spectra measured by WProf: reflectivity (Figure 4.2a) and skewness (Figure 4.2e). The measured Ze_w primarily reflects variations in hydrometeor size and total concentration, while skewness provides insight into the spectral asymmetry. A low-pressure system associated with the passage of storm Carmel reached the CALISHTO measurement sites on the evening of December 17, 2021. The radar timeseries reveals three distinct cloud periods indicated by the turquoise boxes shown in Figure 4.2a. The distinction between these three cloud periods in both measurements and simulations is based on the presence of seeding ice particles falling either from higher levels within the same cloud (internal seeding) or from an overlying cloud (external seeder-feeder), as summarized in Figure C4.

The first cloud system exhibits a characteristic nimbostratus cloud structure, while the second one appears in a distinctive seeder-feeder cloud configuration, which is frequently observed in orographic environments (Proske et al., 2021). Upon advection of the seeder cloud, a low-level orographic cloud persisted for almost one day. The skewness timeseries reveal the presence of extended regions with positive or negative signs especially during the first two cloud periods (Figure 4.2e). Changes in the sign of skewness imply changes in the balance of the different hydrometeor populations within the radar volume. With the sign convention employed here, negative skewness means that the Doppler spectra are skewed towards the more massive, faster-falling side.

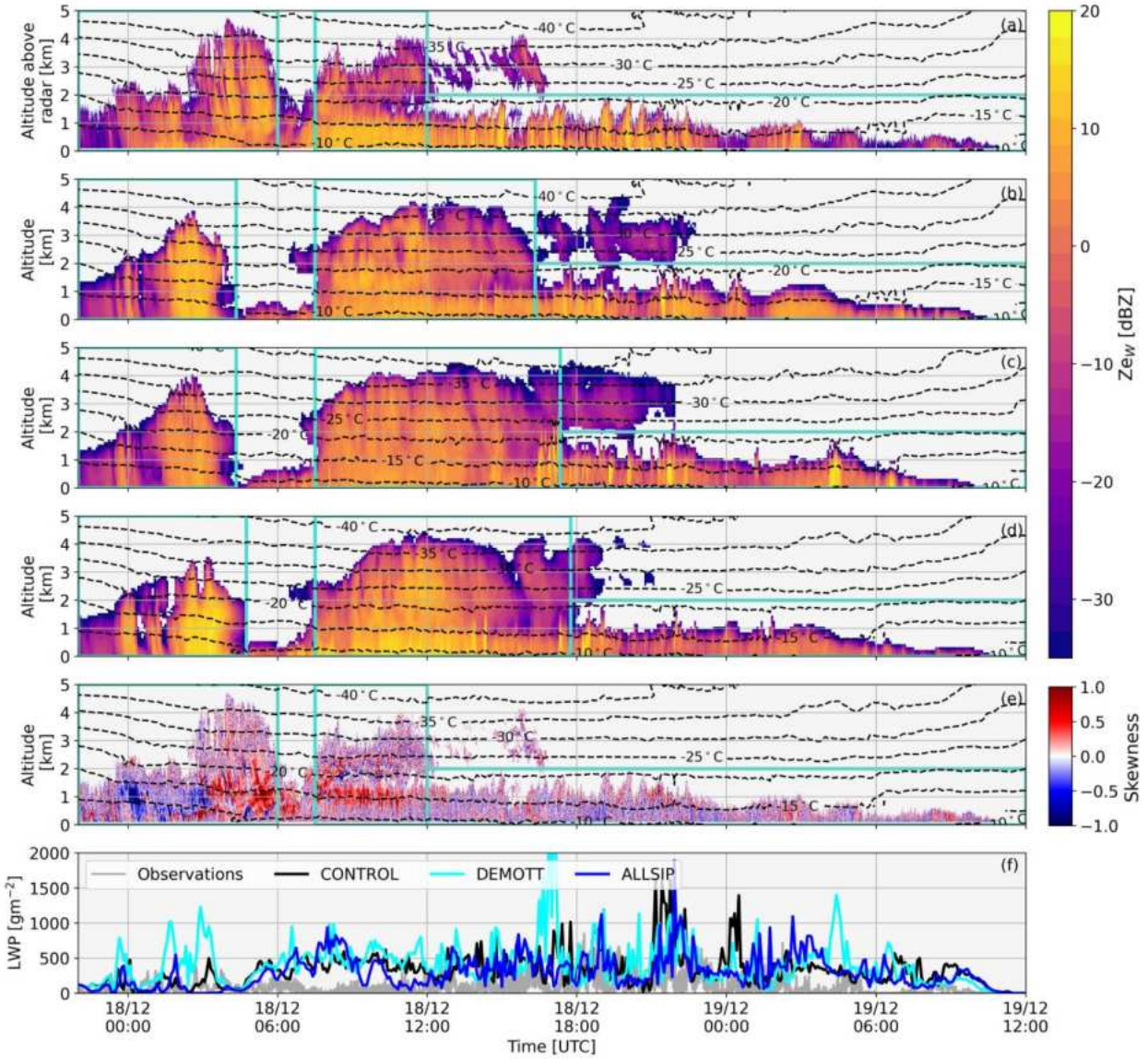

Figure 4.2 Time-height plots of radar reflectivity Ze_w from December 17 (22:00 UTC) to December 19 (12:00 UTC), 2021, displaying (a) measurements by the WProf radar deployed at VL, and simulations coupling the CR-SIM radar simulator with the (b) CONTROL, (c) DEMOTT, and (d) ALLSIP WRF model set-ups. The observed Doppler spectral skewness is also superimposed in panel (e). The LWP timeseries at VL, measured by the joint radiometer and simulated by WRF, is shown in the last panel (f). Note that the simulated LWP takes into account both cloud droplets and raindrops. The turquoise boxes indicate the three distinct cloud periods used to extract statistics. Temperature contours (in °C) are from the CONTROL simulation of WRF in (a, b, e), and from the DEMOTT and ALLSIP simulations in (c) and (d), respectively.

To evaluate the simulations and understand the cloud microphysical processes occurring in the radar volume, we coupled the CR-SIM radar simulator with the outputs from the WRF grid cell nearest to the VL station. The comparison between radar measurements and WRF simulations focuses solely on Ze_w (Figure 4.2a-d), since the other radar observables were less accurately simulated by CR-SIM (not shown). Replacing the default PIP scheme of WRF used in CONTROL (Figure 4.2b) with the aerosol-

aware DM10 scheme (Figure 4.2c), leads to a notable reduction in predicted Ze_w values across all altitudes, especially at temperatures below -20°C. The activation of SIP mechanisms within the model induces a distinct shift in simulated Ze_w towards higher values, primarily within the DGL temperature zone (Figure 4.2d), which becomes more pronounced during the initial two cloud periods. Evaluation of the simulations against the radiometer-derived LWP is also provided in Figure 4.2f. Over the simulation period, there is a substantial but highly variable amount of LWP present. Although the simulations tend to overestimate the radiometer-derived LWP measured at VL, they capture the timing of the peaks in the LWP timeseries, with ALLSIP more effectively reducing the simulated LWP, bringing it closer to observations.

Despite the good performance of WRF, the timing of the first two cloud events does not perfectly align with the remote sensing observations (Figures 4.2a-d). Coupling CR-SIM with the grid cells surrounding the one closer to VL, or substituting the ERA5 reanalysis forcing dataset with the National Centers for Environmental Prediction (NCEP) dataset did not improve the simulated timing of either cloud events (not shown). The most plausible explanation for this discrepancy may be errors in predicted wind fields and relative humidity with respect to ice (RH_i; Figure C2b). Further evaluation of the model at higher altitudes is impeded by the intense snowfall during storm Carmel, which prevented the derivation of the wind profile from the wind lidar deployed at VL. Despite these model-observation discrepancies, WRF coupled with CR-SIM can sufficiently capture the presence of the three consecutive cloud systems measured at VL, which is remarkable given the complex microphysics and small-scale turbulent flow over such complex orographic terrain (Figure 4.1b). A statistical summary of Ze_w for each cloud period is provided in Figures 4.5b, 4.6b and Figure C5, that will help us uncover which WRF model configuration results in predictions that align most closely with the WProf measurements. Before delving into this comparison, it is essential to gain a better understanding of the microphysical processes that shape the simulated ice- and liquid-phase partitioning, and subsequently, the Ze_w values generated by the three WRF sensitivity simulations.

4.4.2 Microphysical process insights

Figure 4.3 illustrates the temporal evolution of vertical profiles for the total ICNC (cloud ice + snow + graupel), while Figure 4.4 presents the corresponding profiles for the total LWC, as predicted by the three sensitivity simulations of WRF. These profiles – extracted from the WRF grid point nearest to the VL station (i.e., the same location used for running the CR-SIM simulator) – provide insights into the sources and sinks of ice and liquid hydrometeors driving the vertical distribution of Ze_w.

The hatched region in Figure 4.3a delineates where water vapor is supersaturated with respect to ice (according to the CONTROL simulation). During the first cloud period, frozen hydrometeors precipitate from the higher-level parts of the cloud, without experiencing ice subsaturation before entering the low-level MPC below ∼1 km. In contrast, during the external seeder-feeder period, subsaturated air separates the orographic cloud from the synoptic cloud above. Accurate representation of the microphysical processes underlying such multi-layered cloud systems in NWP models is found to be crucial for correctly simulating the cloud glaciation fraction as well as the amount of orographic precipitation (Georgakaki et al., 2022; Thomas et al., 2023).

Within the first two seeding cloud periods, falling ice particles undergo effective mass gain, initially through vapor deposition, in the ice supersaturated cloud regions (Figure 4.4) at temperatures below -20°C. As a result, these particles vary in size and experience different terminal velocities, enhancing their collision efficiencies and facilitating further growth through aggregation (Figure 4.3). Ice crystal growth through riming is also prevalent in the lower atmospheric levels of CONTROL (Figure 4.4a), but

is found to contribute even at colder temperatures in DEMOTT and ALLSIP, where higher-level clouds are not entirely glaciated (Figures 4.4b, c).

The role of INP description between simulations also carries important implications for the LWC and ICNCs at cold temperatures. The default temperature-dependent scheme of the WRF model shows a gradual increase in simulated ICNCs, reaching peak concentrations exceeding 100 L^{-1} at temperatures below -30°C (Figure 4.3a). However, when replacing the default primary ice production parameterizations with the aerosol-aware scheme utilized in the DEMOTT simulation, the colder-temperature ICNCs are reduced, with predicted values consistently remaining below 50 L^{-1} (Figure 4.3b). It is worth noting here that the aerosol information used to constrain the DM10 parameterization was derived from the altitude of $(HAC)^2$, which is ∼500 m higher than the VL station. Although this may lead to slight underestimations of the INPs at lower altitudes and, conversely, an INP overestimation at altitudes above $(HAC)^2$, DEMOTT still predicts much lower ICNCs than CONTROL at cold temperatures and provides a more realistic representation of the upper-level INPs. Reducing the predicted ICNCs increases the LWC present at temperatures below -20°C (Figure 4.4b), which is non-existent for CONTROL (Figure 4.4a). Analysis of the 2D temperature histograms reveals that in CONTROL, ice production rates are primarily dominated by the deposition/condensation freezing scheme, particularly at temperatures below −15°C where PIP rates range between 10^{-2} and 1 L^{-1} s^{-1}, while contact freezing dominates at temperatures warmer than about −10°C (Figure C6). In contrast, DEMOTT exhibits PIP rates that never exceed 10^{-1} L^{-1} s^{-1}, even at the colder temperatures down to -40°C (Figure C6d). Reducing the predicted ICNCs allows for more LWC to be present at temperatures below -20°C (Figure 4.4b), which is not possible in CONTROL (Figure 4.4a). During the 3rd cloud period, in the absence of seeding ice particles from above, higher ICNCs predicted by CONTROL lead to effective growth through riming and WBF, allowing for differential settling and justifying the enhanced aggregation rates compared to DEMOTT (Figures 4.3a, b).

Activation of SIP in the ALLSIP simulation shifts the yellowish shades (indicative of higher ICNCs) that were observed predominantly at temperatures below -20°C in CONTROL, towards the warmer temperature range between -20 and -10°C (Figure 4.3c). This leads to a reduction in the vertical availability of LWC, which is noticeable especially during the nimbostratus period. The colored contours in Figure 4.3c delineate the regions where significant ice particle production occurs due to various SIP processes included in WRF. It is evident that SIP is particularly efficient during the first two seeding events, with limited and localized contributions from DS during the third cloud period. By examining the characteristic sizes of raindrops in M05, we find that they rarely exceed the threshold of 50 µm required for DS activation (Figure C7b). This explains the occurrence of spikes in the contours of DS production rates in the timeseries presented in Figure 4.3c. SUBBR also shows highly localized effects when precipitating ice particles fall through subsaturated air layers (Figure C8). The HM process remains completely inactive during the simulation period, partially due to the colder temperatures at which the simulated clouds are formed, and also because the imposed ice and liquid thresholds are not met.

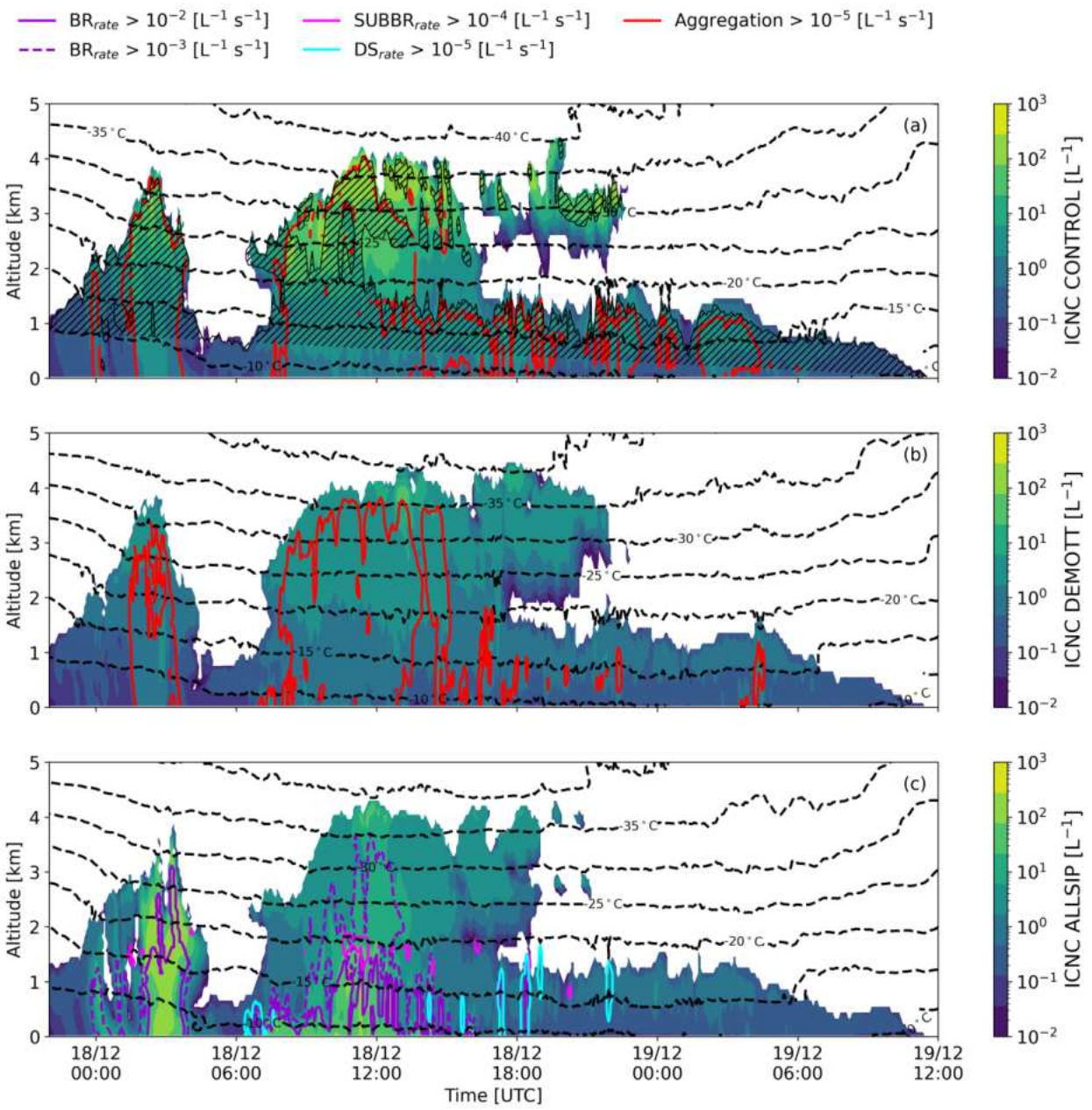

Figure 4.3 Time-height plots of total ICNCs produced by the (a) CONTROL, (b) DEMOTT, and (c) ALLSIP simulations for the period December 17 (22:00 UTC) to December 19 (12:00 UTC), 2021. The black contours in all panels represent temperature isotherms, while the red contours in (a) and (b) show areas where snowflake aggregation rates exceed 10^{-5} $L^{-1}s^{-1}$. Note that the tendencies due to snow aggregation are presented in absolute values. The black hatched lines in (a) indicate regions that are supersaturated with respect to ice. In panel (c), the contours represent each active SIP rate: purple solid (dashed) contours indicate regions where BR rates exceed 10^{-2} (10^{-3}) $L^{-1}s^{-1}$, while cyan (magenta) contours show regions where DS (SUBBR) rates exceed 10^{-5} (10^{-4}) $L^{-1}s^{-1}$. Note that the tendencies of snowflake aggregation predicted by ALLSIP are presented in Figure C8 in Appendix C.

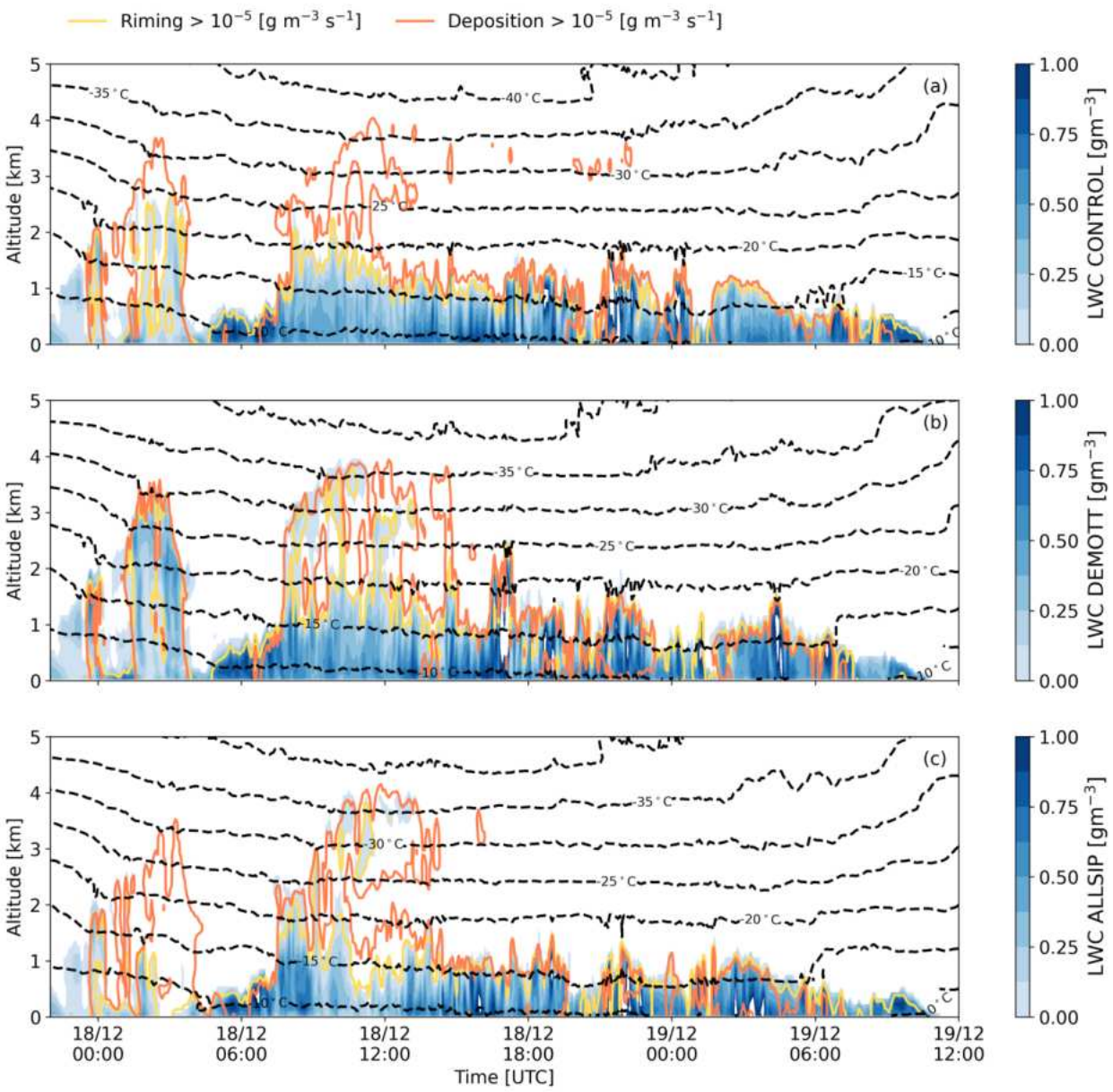

Figure 4.4 Same as in Figure 4.3, but now the color shading represents the total LWC predicted by (a) CONTROL, (b) DEMOTT, and (c) ALLSIP simulations for the period December 17 (22:00 UTC) to December 19 (12:00 UTC), 2021. The black contour lines represent again the temperature isotherms, while in all three panels the yellow (orange) contours indicate the regions, where riming (vapor deposition) rates exceeds 10^{-5} g m^{-3} s^{-1}.

BR demonstrates significant particle production rates, exceeding 10^{-3} particles L^{-1} s^{-1} at temperatures below the DGL, with a tenfold increase in efficiency within this temperature range (Figure 4.3c). This substantial enhancement in BR rates, by two to three orders of magnitude compared to SUBBR and DS, suggests the predominance of the BR mechanism in the simulated cloud systems. Another noteworthy observation is that the snowflake aggregation contours (Figure C8) consistently envelop the BR contours (Figure 4.3c). In particular, inside the DGL, collisions of aggregated dendrites can trigger SIP through BR. Although the ice habit is not explicitly resolved in M05, the number of

fragments described by the employed Phillips BR parameterization shows a triangular relationship with temperature, peaking at around -15°C, which justifies the peak in its efficiency inside the DGL.

The simultaneous enhancement of aggregation and new ice particle formation through BR is consistently highlighted in several modeling (Dedekind et al., 2023; Georgakaki et al., 2022) and remote sensing studies (von Terzi et al., 2022). Images of fragmented dendritic crystals captured during aircraft flights within nimbostratus clouds over China revealed the predominance of SIP via BR, particularly between -10°C and -15°C (Yang et al., 2014). Importantly, during the 3rd cloud period, when aggregation is not favored in ALLSIP (Figure C8), SIP through BR is entirely inefficient.

4.4.3 SIP indications in Doppler spectra

Integrating information from the high-resolution modeling framework and radar Doppler spectra, allows for attributing distinct radar signals to SIP or other microphysical processes. This is done by comparing the simulated Ze_w for all three sensitivity simulations of WRF examined in this study. The unavailability of polarimetric radar observables during the CALISHTO campaign restricts our ability to identify specific ice hydrometeor habits (i.e., columnar crystals), which have proven valuable in previous research (Billault-Roux et al., 2023; Oue et al., 2015). Nonetheless, we will focus on two specific moments of the timeseries – one from the nimbostratus and the other from the seeder-feeder cloud periods, as these periods were identified to create favorable conditions for SIP.

Starting from the nimbostratus cloud period, Figure 4.5a presents an example Doppler spectrogram measured by the WProf on December 18 at 03:55:10 UTC. Analyzing radar Doppler spectra, particularly in the presence of multimodes/peaks, helps reveal distinct hydrometeor populations within the same radar volume. The chosen spectrogram highlights a turbulent region between 2-2.5 km altitude, below which a clear bimodal distribution appears at around 1.6 km, signifying two hydrometeor populations – the origin of which will be discussed below.

Median statistics derived for this cloud period are summarized in Figure 4b. The gray shaded regions in this plot indicate the observed interquartile range (IQR). CONTROL overestimates Ze_w at temperatures ranging from roughly -25°C to -17°C, while underestimates Ze_w at warmer subzero temperatures. The updated PIP scheme in DEMOTT agrees better with observations at temperatures colder than ∼-18°C, but still fails to achieve the higher Ze_w values observed at warmer temperatures. In contrast, ALLSIP enhances the simulated Ze_w by over 10 dBZ at these temperatures, reducing the discrepancy with the WProf measurements. Analysis of simulated ice particle size distributions (Figure C9) reveals that, closer to the ground (∼700 m AGL), ALLSIP predicts more than two (one) orders of magnitude elevated ICNCs compared to CONTROL (DEMOTT). In terms of large particles dominating the radar reflectivity, ALLSIP predicts tenfold higher snow particle concentrations compared to the other two sensitivity simulations (Figure C9e), likely from increased cloud-ice-to-snow autoconversion. However, at colder temperatures, particularly below -20°C, ALLSIP simulates lower snow and graupel concentrations relative to the WRF simulations disregarding SIP, resulting in Ze_w values below the observed IQR. Despite uncertainties and simplifications in the modeling approaches (some further discussed in Text C2), it becomes evident that, inside the DGL, inclusion of SIP mechanisms within ice seeding configurations is necessary for refining the vertical distribution of Ze_w, particularly the Ze_w enhancement near the ground. This implies that the ALLSIP simulation of WRF can be used to assess when characteristic radar signatures can be used to identify SIP processes.

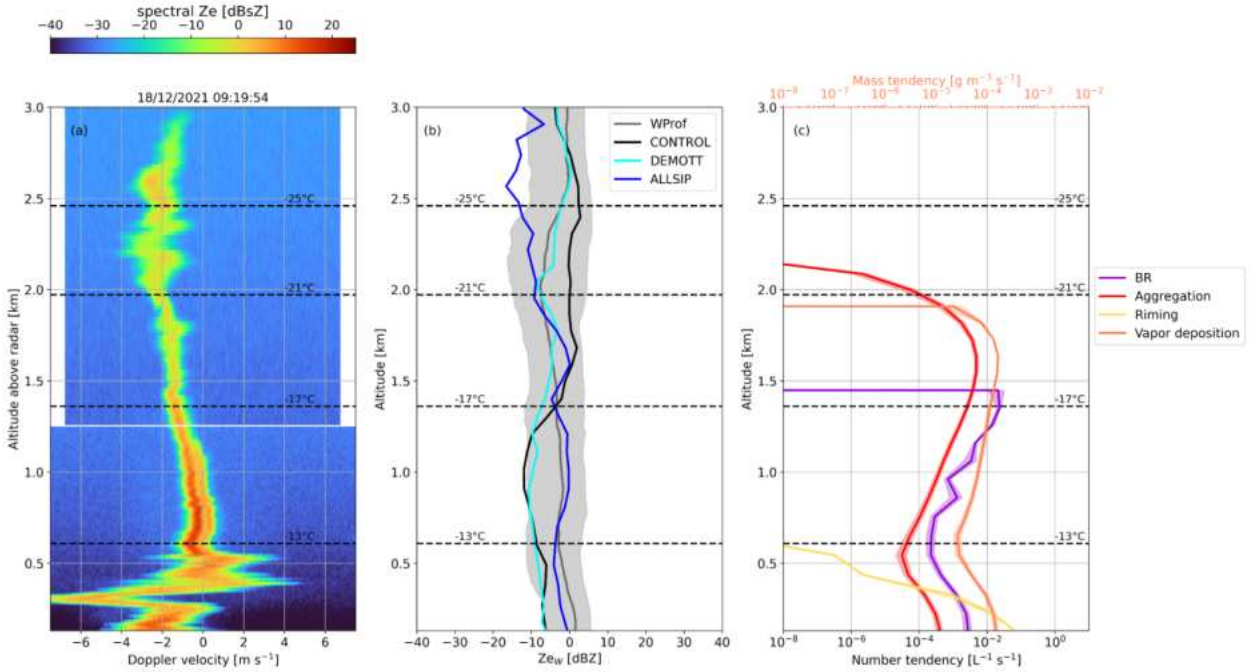

Figure 4.5 Synergistic insights from WProf radar Doppler spectra and WRF predictions: (a) Example of the WProf reflectivity spectrogram collected on December 18 at 03:55:10 UTC, during the nimbostratus cloud period. A horizontal white line around 1.2 km marks a sampling gap in a small radar volume between the first and second chirp. Note that 1dBsZ = $10\log_{10}(1\text{mm}^6\text{m}^{-3}\ (\text{ms}^{-1})^{-1})$; (b) Median vertical profiles of observed and simulated radar reflectivity extracted during the nimbostratus cloud period. The grey line represents the median WProf observations, while the black, cyan, and blue lines denote the results from the CONTROL, DEMOTT, and ALLSIP simulations, respectively; (c) Median vertical profiles (extracted from the ALLSIP simulation over a 10-min time window centered around the chosen spectrogram) of the number tendency due to BR (purple line) and snow aggregation (red line) shown in the lower x-axis, while the mass tendencies due to riming (yellow) and vapor deposition (orange) are shown in the upper x-axis. The shaded regions correspond to the IQR, while the temperature contours superimposed in these panels are from the ALLSIP simulation. Note that the tendency due to snow aggregation in panel (c) is presented in absolute values.

Figure 4.5c illustrates the median tendency profiles for several microphysical processes simulated by ALLSIP within a 10-min timeframe of the observed WProf spectrogram (Figure 4.5a). Ice particles grow through vapor deposition and aggregation while falling through the atmosphere. The primary mode detected by the cloud radar could therefore be attributed to dendritic and/or aggregated ice particles. Here it is worth noting that a single Doppler spectrogram at a specific timestep does not necessarily reflect the microphysical trajectory of a particle population (Kalesse et al., 2016). Indeed, the fast-falling spectral mode in Figure 4.5a may result from overlapping particle trajectories as they are advected toward the measurement site. Furthermore, the mean Doppler velocity (MDV) of the primary peak reaches up to ~ -2.5 m s^{-1} at 1 km altitude (Figure 4.5a), which is significantly higher than the typical terminal velocities of aggregates at around 1 ms^{-1} (Kneifel & Moisseev, 2020). Although large MDV could be caused by heavily rimed ice structures – WRF simulations do not suggest the presence of SLW (Figure 4.4c). The high MDV is likely from the influence of downdrafts, and the effects of prevailing high horizontal winds (Figure 4.2c) and potential deviations in the vertical radar setup alignment (Orr & Kropfli, 1999).

A secondary mode emerges in the radar Doppler spectrogram just above the -18°C isotherm, with a reflectivity of -0.4 dBZ (Figure 4.5a). The pronounced reflectivity of the peak, alongside its broad spectral range, rules out the possibility of its origin being supercooled liquid droplets, as such droplets typically exhibit lower values below -15 dBZ (Kalesse et al., 2016). To understand the origin of the secondary mode, we refer to the ALLSIP predictions (Figure 4.5c). Simulated microphysical tendencies suggest that interactions between particles of the primary mode entering the DGL may fuel SIP below 1.5 km altitude. Indeed, the emergence of the secondary mode in the Doppler spectrogram almost coincides with enhanced aggregation and BR in the model, the former peaking below -18°C. Efficient growth of sedimenting ice particles inside the DGL promotes differential settling, increasing the likelihood of collisions, which in turn drives both aggregation and BR. These two processes exhibit consistent alignment across all altitudes in the atmosphere. While snowflake aggregation can be an efficient ICNC sink in MPCs, Figure 4.5c reveals that aggregation drives SIP through BR, which in turn compensates for the depletion of ice crystals and may even enhance them. Below ∼600 m, the source of ice particles due to BR can be up to one order of magnitude enhanced compared to the loss due to aggregation. At this altitude, interaction with supercooled droplets further augments ice crystal mass via riming (Figure 4.5c). Riming and possibly WBF deplete cloud liquid water in lower atmospheric levels, improving agreement with radiometer-derived LWP compared to CONTROL and DEMOTT (Figure 4.2f). The distinct spectral modes broaden and converge below ∼1 km, indicating an "advection-type" effect (although this could also relate to atmospheric turbulence or the imperfect vertical beam alignment during this instance).

Another important realization comes from reexamining the skewness timeseries, depicted in Figure 4.2e. We observe that the emergence of the slower spectral mode coincides precisely with a region in the radar data showing persistent positive skewness, both temporally and spatially extended. This pattern bears similarity to findings in von Terzi et al. (2022), where a winter frontal case study unveiled spectral asymmetry associated with the rapid increase in Doppler spectral skewness at temperatures above -18°C. This was attributed to the formation of new small ice particles, likely due to SIP processes within the DGL. Giangrande et al. (2016) also linked bimodal spectra skewing toward slower falling particles with the formation and growth of ice needles. In our study, during the nimbostratus cloud period, persistent small ice particle formation is evident, represented by the red shading, at altitudes ranging from the -10 to -20°C isotherms after approximately 03:00 UTC on December 18 (Figure 4.2e). This confirms that the observed bimodal spectrogram (Figure 4.5a), although representing a single timestep, is not an isolated feature. The model with advanced SIP descriptions predicts enhanced BR (Figure 4.3c) and aggregation (Figure C8) that aligns remarkably spatially and temporally with the increase in the observed spectral skewness (Figure 4.2e). This one-to-one comparison allowed us to infer the presence of SIP through BR, resulting from collisions between delicate dendritic and/or aggregated ice structures inside the DGL, leading to a skewing of the Doppler spectra towards slower falling particles.

Moving to the seeder-feeder cloud period, Figure 4.6 presents a WProf spectrogram juxtaposed with the corresponding vertical profiles of the WRF simulations. We discern the primary spectral mode corresponding to the aggregate population falling from the seeder cloud. A clear secondary mode becomes evident in the feeder cloud below the -16°C isotherm (Figure 4.6a) – a region where the ALLSIP simulation suggests again the presence of SIP-generated particles (Figure 4.6c). A high reflectivity of -1.0 dBZ together with its quite wide spectral signature indicate that the slow-falling spectral subpeak corresponds to cloud ice particles rather than supercooled liquid droplets.

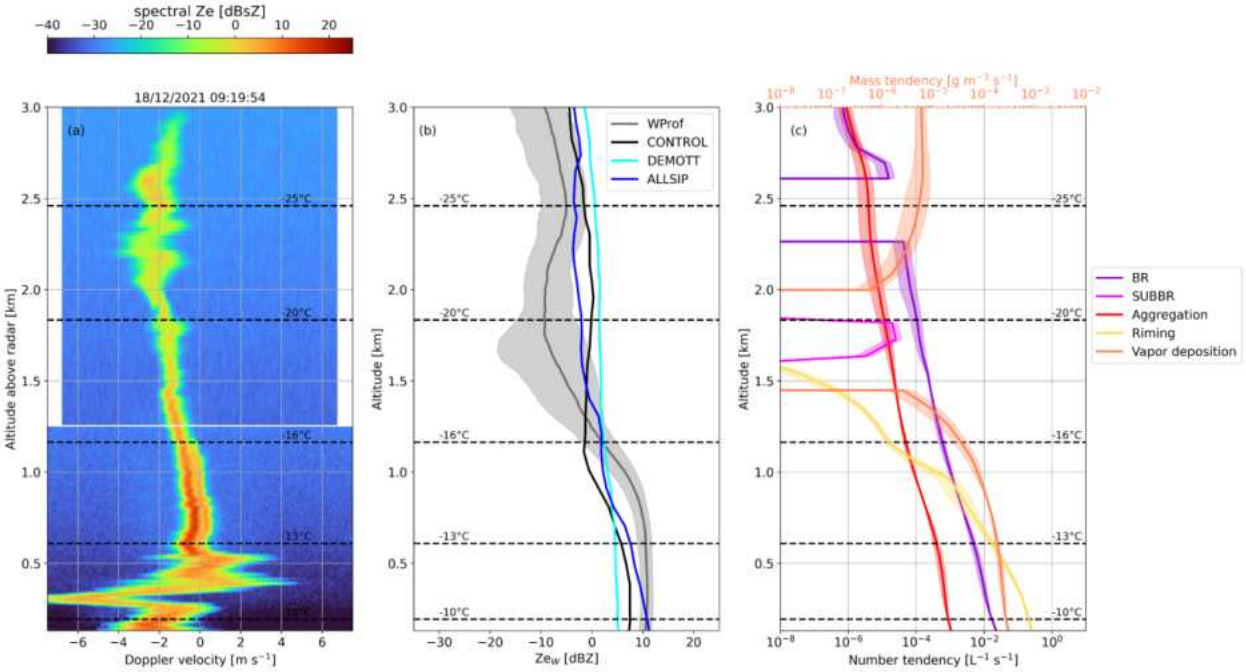

Figure 4.6 Same as in Figure 4.5, but the information is extracted from December 18 at 09:19:54 UTC, during the seeder-feeder cloud period. In panel (c) the magenta line indicates the median vertical profile of the number tendency due to SUBBR shown in the lower x-axis.

The median profiles extracted from this cloud period reveal two distinct Ze_w profile characteristics (Figure 4.6b). In the feeder part of the cloud, the measured Ze_w saturates likely from non-Rayleigh scattering by large ice particles with sizes comparable to the WProf wavelength. Indeed, the simulated size distribution of snow particles, supports the presence of large particles exceeding 1 mm at altitudes below 1 km above ground level (AGL) (Figure C7a). From the modeling perspective, at these altitudes, BR aligns with aggregation, but consistently generates an order of magnitude more particles per liter than aggregation depletes from snowflake number loss (Figure 4.6c). The efficiency of BR maximizes closer to the surface, yielding almost $2 \cdot 10^{-2}$ small ice fragments per liter. Even though CONTROL and ALLSIP produce comparable snow number concentrations, yet the latter yields almost 2 orders of magnitude elevated cloud ice particle concentrations (Figure C10). The subsequent growth of these particles via vapor deposition and riming (Figure 4.6c) boosts the simulated Ze_w values leading to better agreement not only with the WProf reflectivity profile (Figure 4.6b) but also with the LWP measurements during this period (Figure 4.2f).

At higher altitudes and temperatures between approximately -16 and -25°C, WProf measured reduced Ze_w that is not reproduced by any WRF simulation (Figure 4.6b). This discrepancy is likely from the presence of a dry layer separating the two clouds (Figures 4.3a and Figure C8) that does not backscatter much signal to the radar. The timing and microphysics inside this cloud free region is likely more challenging to be captured by all model set-ups examined, but this does not appear to have a significant impact on ground precipitation and SIP. CONTROL generates cloud ice (Figure C10a) and snow particle (Figure C10b) concentrations one order of magnitude higher than DEMOTT at an altitude of ~2.2 km, which is nearly one (two) orders of magnitude elevated cloud ice (snow) concentrations compared to ALLSIP. The elevated concentrations of larger ice particles are probably causing the overestimated Ze_w values in CONTROL and DEMOTT. At these temperatures, initiation of BR in the ALLSIP simulation is found to shift the particle distributions towards smaller sizes, effectively moving

the simulated Ze_w values closer to the observed IQR at the appropriate altitude and timing. Additionally, it is worth noting the contribution of SUBBR within the subsaturated air layer that separates the seeder from the feeder cloud regions, generating up to 10^{-5} particles per liter. This observation aligns with findings presented in Deshmukh et al. (2022) (see their Figure 14).

When reviewing the skewness timeseries in Figure 4.2e, we consistently notice positively skewed distributions, between mostly the -15°C and -20°C isotherms, persisting throughout the entire seeder-feeder cloud period. This reaffirms our earlier hypothesis regarding the connection between positive skewness, spectral bimodality, and processes such as BR and aggregation, as previously highlighted during the nimbostratus cloud period. Altogether, this underscores once more the significance of incorporating SIP descriptions within the microphysics scheme of the WRF model, and the usefulness of the coupled model-radar simulator approach to reliably interpret the radar reflectivity signals.

4.5 Conclusions

In this study, we delved into the microphysical mechanisms of snowfall during the passage of storm Carmel in mainland Greece. During this event a complex wintertime mixed-phase cloud system was recorded by the W-band cloud radar deployed at a high-altitude station as part of the CALISHTO field campaign. Radar observations unveiled three sequential cloud structures: a nimbostratus cloud, succeeded by a multi-layered seeder-feeder system, eventually leading to a low-level orographic MPC. Our analysis combined remote sensing, aerosol in-situ data, modeling, and forward-simulation tools. This integrated approach aimed to pinpoint ice crystal growth and multiplication processes within the DGL, recognizing the need to improve our understanding – particularly of SIP – at such cold temperatures outside the HM zone. By coupling WRF with the CR-SIM radar simulator, we successfully replicated all three observed cloud systems, which is noteworthy given the complexity of the terrain surrounding the measurement site.

Three sensitivity simulations were performed using WRF to assess the sensitivity of the model to the chosen PIP and SIP schemes. Refining the default PIP scheme in WRF, incorporating a more sophisticated aerosol-aware parameterization, reduced simulated ICNCs at all altitudes. Our WRF simulations highlight the crucial role of incorporating advanced SIP descriptions within the microphysics scheme of models to capture the underlying mechanisms affecting ice particle growth, multiplication, and consequent precipitation production. SIP significantly amplifies simulated cloud ice and snow concentrations by 1-2 orders of magnitude; BR-driven SIP initiates near the upper edge of the DGL (colder temperatures), with substantial snow and graupel particles colliding and generating small ice fragments. As these ice particles encounter warmer temperatures within mixed-phase conditions, they efficiently grow through vapor deposition and riming, fostering differential settling and enabling further aggregation-driven growth. This cascade effect ultimately contributes to increased snowfall near the ground, resulting in elevated reflectivities, that can be replicated solely through WRF simulations considering SIP. Rapid aggregation and vapor deposition of dendritic ice particles enhances differential settling, which increases collision probabilities and BR. The competition between BR and aggregation determines the modelled ICNCs. Upon entering low-level mixed-phase cloud regions, BR produces approximately tenfold more ice crystals than those depleted through aggregation. Among the three cloud types studied, SIP showed significant activity solely in cases involving ice particle seeding, whether internally within the same cloud or externally in a seeder-feeder arrangement.

Integration of modeling and remote sensing tools helps decipher microphysical signatures in observed full Doppler spectra. Using WRF with all SIP mechanisms active, we interpret observed spectral bimodalities for internal and external seeding cases. The faster-falling spectral mode was associated with the aggregate population, while distinct secondary modes emerged at temperatures around -18°C to -16°C coincided with enhanced BR and aggregation in WRF with remarkably good temporal and spatial alignment with an increase in the observed skewness timeseries. Persistent positive skewness arose within the DGL due to the spectra shift toward the slower-falling peak after SIP initiation. These findings propose strong connections between positive skewness, Doppler spectral bimodalities, aggregation, and SIP through BR within the DGL in the SIP temperature regime. Correct prediction of the vertical distribution of INPs is also key for getting the right balance of primary and secondary ice production, as well as the microphysical evolution of MPCs.

Overall, the presence of multi-modalities in the radar Doppler spectra, particularly within the DGL, has long underlined the need to improve our understanding of the intricate microphysical interactions taking place. This is important for more accurate modeling of surface precipitation. In this research, we suggest that SIP-aware models coupled with forward simulators have the potential to unveil concealed microphysical processes in radar observations. Beyond model evaluation, this approach provides fresh avenues to derive prolonged statistics regarding the significance and frequency of SIP. This applies even in remote polar regions where ground-based remote sensing instruments are widely available.

5. RaFSIP: Parameterizing ice multiplication in models using a machine learning approach

In this chapter, we introduce a new machine learning parameterization to represent the effect of all important secondary ice processes within large-scale models. The content of this chapter is drawn from the submitted manuscript:

- **Georgakaki, P.,** and Nenes, A. (2023): RaFSIP: Parameterizing ice multiplication in models using a machine learning approach. *Under review for Journal of Advances in Modeling Earth Systems.*

The machine learning algorithm was designed and evaluated by Paraskevi Georgakaki. Athanasios Nenes organized the research project, offered valuable insights into the online integration of the developed scheme, and supervised the progress.

5.1 Summary

Representing single or multilayer mixed-phase clouds (MPCs) accurately in global climate models (GCMs) is critical for capturing climate sensitivity and Arctic amplification. Ice multiplication, or secondary ice production (SIP), can increase the ice crystal number concentration (ICNC) in MPCs by several orders of magnitude, affecting cloud properties and processes. Here, we propose a machine-learning approach, called Random Forest SIP (RaFSIP), to parameterize the effect of SIP on stratiform MPCs. The RaFSIP scheme uses few input variables available in models and considers rime splintering, ice-ice collisional break-up, and droplet-shattering, operating at temperatures between 0 and -25˚C. The training dataset for RaFSIP was derived from two-year pan-Arctic simulations with the Weather Research and Forecasting (WRF) model with explicit representations of SIP processes. The RaFSIP scheme was evaluated offline against WRF simulation outputs, then integrated within WRF. The parameterization exhibits stable performance over a simulation year, and reproduced predictions of ICNC with explicit microphysics to within a factor of 3. The coupled WRF-RaFSIP scheme can replicate regions of enhanced SIP and accurately map ICNCs and liquid water content, particularly at temperatures above -10˚C. Uncertainties related to the RaFSIP representation of MPCs marginally affected surface cloud radiative forcing in the Arctic, with radiative biases of lower than 3 Wm-2 compared to simulations with explicit SIP microphysics. Training from a few high-resolution model grid points did not limit the predictive skill of RaFSIP, with the approach opening up new avenues for model simplification and process description in GCMs by physics-guided machine learning algorithms.

5.2 Introduction

In the big data and machine learning era, general circulation models (GCMs) remain an indispensable tool for predicting how the Earth system will respond to rising greenhouse gas concentrations (Balaji et al., 2022; Irrgang et al., 2021). GCMs typically represent

atmospheric processes with a horizontal grid spacing of about 50-100 km. However, at this coarse resolution, small-scale processes, such as those associated with clouds, cannot often be explicitly resolved. These complex subgrid scale processes interact with the resolved model scales only through parameterizations tuned in a way to improve the agreement with theory or observations (Hourdin et al., 2017). Parameterization schemes are a necessary but non-trivial part of climate modeling, introducing uncertainties in future climate projections. These uncertainties frequently result in persistent model biases, especially over climatically sensitive regions of the world, such as the Arctic (Sledd & L'Ecuyer, 2021; Tan & Storelvmo, 2019) and the Southern Ocean (Schuddeboom & McDonald, 2021; Vergara-Temprado et al., 2018).

Machine learning (ML)-based parameterizations are a promising and computationally efficient approach increasingly used in climate science to replace, supplement or speed up conventional parameterizations (e.g., Brenowitz & Bretherton, 2019; Gentine et al., 2018; Grundner et al., 2022; Han et al., 2020; Mooers et al., 2021). ML parameterizations are sometimes developed based on high-resolution three-dimensional (3D) simulations, in which subgrid processes are either explicitly resolved (Brenowitz & Bretherton, 2018; Yuval et al., 2021; Yuval & O'Gorman, 2020) or parameterized using conventional schemes (Grundner et al., 2022; O'Gorman & Dwyer, 2018). In this approach, high-resolution data is often coarse-grained to match the lower spatial resolution of the GCM grid (e.g., Brenowitz & Bretherton, 2019). Advances in both computational tools and data assimilation methods have now allowed for global observations to be integrated into ML training datasets (Schneider et al., 2017), yet limitations concerning the limited spatiotemporal coverage of observational data still need to be addressed (Irrgang et al., 2021).

Neural networks (NNs) and random forests (RFs) are two ML methods that have been used for developing parameterizations for GCMs. RF – an ensemble learning algorithm consisting of multiple decision trees – ensures the preservation of physical properties by taking the average predictions of subsets of the training samples (Breiman, 2001). This conservative behavior leads to more stable simulations when coupled with GCMs compared to NNs (Han et al., 2020; O'Gorman & Dwyer, 2018), which can deviate from the training data pool. Notably, RF parameterizations have demonstrated successful emulation of conventional convective schemes in GCMs (O'Gorman & Dwyer, 2018). Yuval and O'Gorman (2020) applied RF parameterization using coarse-grained, high-resolution outputs from an idealized simulation, achieving effective replication of climate patterns across different grid spacings. In contrast, NN parameterizations, although requiring less memory in GCMs, can introduce numerical instabilities and result in model runaway or climate drift (Rasp et al., 2018; Brenowitz & Bretherton, 2018, 2019). To ensure stable long-term simulations, post-prediction adjustments and accurate processing of the training dataset are necessary (Rasp, 2020; Yuval et al., 2021). While offline comparisons favored NN parameterizations, both RF and NN algorithms satisfied physical constraints (energy conservation and non-negative surface precipitation) and demonstrated comparable performance when coupled with the dynamical core of a coarse-resolution aqua-planet GCM (Yuval et al., 2021). Additionally, RFs and NNs showed similar performance in predicting the probability density function of surface solar irradiance under 3D cumulus clouds (Gristey et al., 2020).

Parameterizations of cloud microphysical processes and aerosol-cloud interactions are perhaps one of the most challenging aspects of climate simulations (e.g., Liu et al., 2023; Hugh Morrison et al., 2020). They are also computationally expensive because they require a large amount of information to be carried around in simulations (e.g., cloud microphysical and aerosol quantities and their interactions) and the parameterizations themselves also may require considerable computational effort. Few studies to date try to simplify cloud microphysical processes using ML-based approaches, focusing on warm cloud microphysical processes. For instance, Seifert & Rasp (2020) employed a Monte Carlo superdroplet simulation to train neural network (NN) models for parameterizing autoconversion, accretion, and self-collection rates in two-moment schemes. Chiu et al. (2021) developed NN-based parameterizations for autoconversion and accretion rates, incorporating in-situ observations of droplet size distributions and employing the stochastic collection equation with bin

microphysics to separately account for cloud and drizzle water contents. Although these ML approaches were evaluated offline, Gettelman et al. (2021) successfully replaced the computationally expensive bin microphysical scheme used in a GCM with ML emulators to predict autoconversion and accretion tendencies, achieving comparable accuracy with reduced computational costs. However, there remains a research gap regarding ML parameterizations specifically tailored to represent cold cloud microphysics.

This study focuses on developing an RF-based approach for parameterizing secondary ice production (SIP) in stratiform mixed-phase clouds (MPCs) which are prevalent in polar regions (de Boer et al., 2009; Shupe et al., 2006), sustained by a complex interplay of microphysics, dynamics, radiatively-driven turbulence, as well as surface heat and moisture fluxes (Morrison et al., 2012). Misrepresentation of the mid- and high-latitude MPCs in GCMs has been shown to increase the spread of predicted cloud feedbacks in the recent Climate Model Intercomparison Project (phase 6 – CMIP6; Murray et al., 2021; Zelinka et al., 2020). Furthermore, the ice and liquid phase partitioning in GCMs can significantly impact Arctic amplification, highlighting the necessity of revisiting the microphysical parameterizations associated with Arctic MPCs (Tan & Storelvmo, 2019).

Ice multiplication, also known as SIP, can be an important source of ice particles in MPCs, as it can rapidly increase the pre-existing ice crystal number concentrations (ICNCs) through a number of collisional processes (Field et al., 2017; Korolev & Leisner, 2020). The most frequently acknowledged SIP mechanism is the Hallett-Mossop (HM; Choularton et al., 1980; Hallett & Mossop, 1974), ice-ice collisional break-up (BR; Takahashi et al., 1995; Vardiman, 1978) and droplet-shattering (DS; Choularton et al., 1980; James et al., 2021; Kleinheins et al., 2021). Observations of MPCs in the Arctic region have shown high concentration of ICNCs that greatly surpass ice nucleating particle (INP) concentrations (Wex et al., 2019), particularly at temperatures above -25˚C (Luke et al., 2021; Julie Thérèse Pasquier et al., 2022; Rangno & Hobbs, 2001; Schwarzenboeck et al., 2009). This suggests that SIP must be a prevalent process in the moderately cold polar conditions.

Along with observations, modeling studies across scales have also emphasized the significance of incorporating SIP parameterizations in regional and global climate model simulations for an accurate representation of the phase partitioning and radiative properties of Arctic MPCs (e.g., Fridlind & Ackerman, 2019; Sotiropoulou et al. 2020; Sotiropoulou, Vignon, et al., 2021; Zhao et al. 2021; Zhao and Liu 2021; 2022). Recent physically-based SIP parameterizations tested in GCMs were developed by pooling experimental observations and further considering the physics of collisions or applying correction factors to account for the simplified laboratory setups (Phillips et al., 2017a; 2018). These advanced SIP formulations require that the host model explicitly describes a number of ice (cloud ice, snow and graupel) and liquid species (cloud droplets and raindrops) as well as interactions among them (i.e., aggregation, collection and riming). Zhao et al. (2021) and Zhao & Liu (2022) developed a hybrid-bin framework for improved representation of SIP, but this approach can be computationally expensive (Sotiropoulou et al., 2022).

Here we propose a new approach towards parameterizing SIP in stratiform MPCs, which we call the RaFSIP (Random Forest SIP) parameterization. RaFSIP is derived from comprehensive model output from mesoscale model simulations that account for all three SIP processes: HM, BR and DS. Following this, the effect of SIP is expressed either directly by predicting the corresponding SIP rates or through the use of the ice-enhancement factor (IEF), which is a multiplication factor applied to primary ice crystals. To account for the effects of SIP for a wide range of stratiform conditions, the RaFSIP parameterization is trained using key thermodynamic and microphysical variables to facilitate its implementation in most models with double-moment representations of ice hydrometeors.

5.3 Data and Methods

The reference simulation used to develop the RF framework is derived from the mesoscale Weather Research and Forecasting (WRF) model. The WRF outputs from the target simulation were used to train two different versions of the RaFSIP parameterization: the first version of the parameterization predicts the effect of SIP through the use of a multiplication factor applied to the primary ice production rates (hereafter denoted as RaFSIPv1), while the second version is trained to predict directly the production rates of secondarily formed ice particles (hereafter referred to as RaFSIPv2). The workflow followed to develop each parameterization is summarized in Figure 5.1.

5.3.1 WRF regional climate simulations

The target simulation was generated using WRF version 4.0.1, including augmented cloud microphysics that considers the effects of BR and DS mechanisms introduced by Sotiropoulou, Vignon, et al. (2021) and Georgakaki et al. (2022), in addition to the default HM parameterization. A regional climate configuration was employed (Abdelwares et al., 2018), where a 50-km resolution parent domain covering the Arctic region contains a single-way nested domain of 10-km resolution. Figure 5.1 shows the map of the two domains centered over Ny-Ålesund using a polar-stereographic projection, that is suitable for high-latitude WRF domains. The outermost domain consists of 148×148 grid points, while the innermost one contains 301×301 grids. In the hybrid terrain-following mass coordinate system adopted by WRF, we used 40 vertical levels up to a model top of 50 hPa (i.e., ∼20 km), with the standard grid spacing generated automatically by WRF.

The initial and lateral boundary conditions are taken from the fifth generation of the European Centre for Medium-Range Weather Forecasts (ECMWF) atmospheric reanalyses dataset (ERA5; Hersbach et al., 2020), with a 31-km horizontal grid spacing. The lateral forcing at the edge of the parent domain was updated every 6 h. To ensure realistic synoptic dynamics in the model and allow for a comparison between in situ observations and simulations, the outer domain of WRF has been nudged toward ERA5 reanalysis for zonal and meridional wind speed, with a relaxation time scale of 6 h. Static fields come from default WRF pre-processing system datasets with a resolution of 30'' for both the topography and land use fields. The WRF physics options include the Rapid Radiative Transfer Model for General Circulation Models (RRTMG) radiation scheme to parameterize both the shortwave and longwave spectra, the local Mellor-Yamada-Nakanishi-Niino Level 2.5 (MYNN; Nakanishi & Niino, 2006) scheme with its associated surface layer scheme for the planetary boundary layer (PBL) processes representation, the Noah land surface model (Noah LSM; Chen & Dudhia, 2001) for surface options, and the Kain–Fritsch cumulus parameterization, which was activated in both domains.

Cloud microphysics is treated using the scheme of Morrison et al. (2005) (hereafter M05), which represents raindrops, cloud ice, snow and graupel particles with a double-moment approach. However, a single-moment approach is used for cloud droplets, which requires predefining a constant number concentration. For this study, we assumed that an average cloud droplet number concentration of 100 cm^{-3} is suitable for Arctic clouds (e.g., McCoy et al., 2020; Young et al., 2016). Regarding ice formation processes, M05 includes parameterizations for homogeneous freezing at temperatures below -40˚C, as well as heterogeneous ice nucleation initiated below -4˚C. The latter accounts for immersion freezing of cloud droplets and raindrops (Bigg, 1953), contact freezing (Meyers et al., 1992) and condensation/deposition freezing nucleation (Cooper, 1986), all of which are dependent only on temperature.

In the standard M05 code there is only one SIP mechanism described – the HM process – which is activated after cloud droplets or raindrops rime onto snow or graupel particles within a specific temperature range between -8 and -3˚C (Cotton et al., 1986). The activation of this process depends

on preset thresholds concerning the minimum mass mixing ratios of the involved ice and liquid species that are found to limit its efficiency and were removed (Atlas et al., 2020; Karalis et al., 2022; Young et al., 2019).

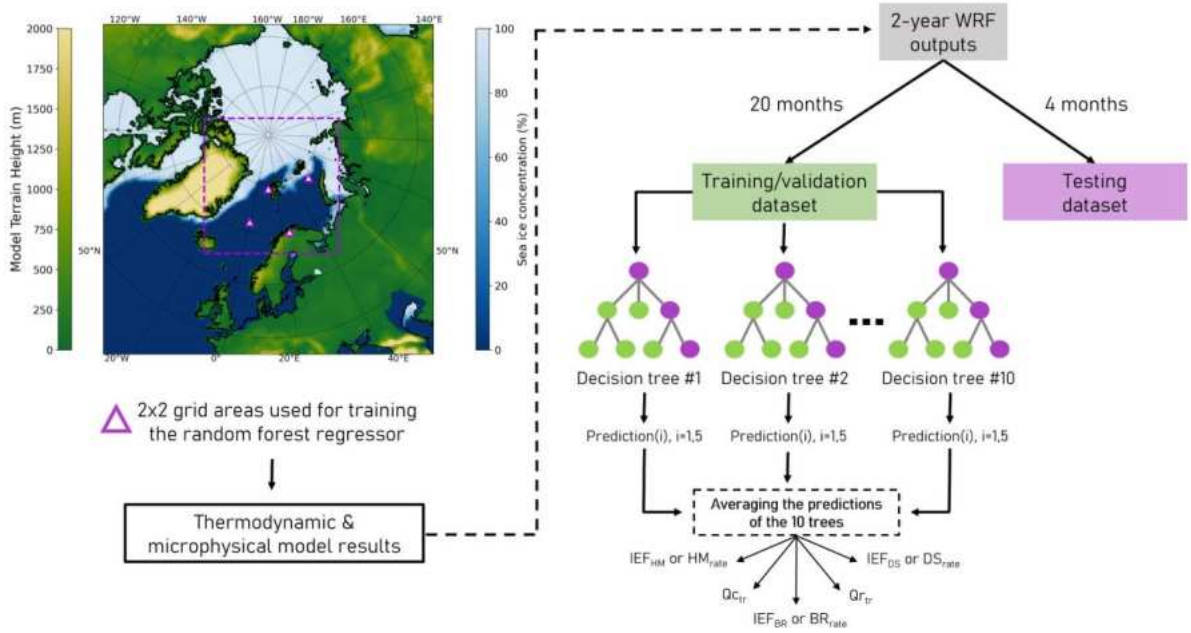

Figure 5.1 Schematic diagram of the methodology followed to develop the two versions of the RaFSIP parameterization. The map on the left shows the two WRF domains used to simulate the two-year period required for training the RaFSIP parameterization. The rectangular region marked by the purple dashed lines delimit the 10-km resolution domain, while colors indicate terrain heights (left axis) and sea ice concentration (right axis). The 4 triangles represent the regions from where the training dataset is extracted. The two-year high-resolution model output is split into ∼85% training dataset (20 months) and ∼15% testing dataset (4 months). The RaFSIPv1 (RaFSIPv2) parameterization is trained to predict the IEF (SIP_{rate}) as well as the transfer of mass from cloud droplets (Qc_{tr}) or raindrops (Qr_{tr}) to cloud ice due to SIP. The snapshot corresponds to the monthly average of January, 2016.

A detailed description of the BR implementation in M05 is provided in Sotiropoulou, Vignon, et al. (2021). The default M05 code was updated to include all possible collisional interactions among the three ice hydrometeor species (see their Appendix B). The number of fragments produced is parameterized as a function of the ice particle size, habit, degree of riming as well as the collisional kinetic energy, following Phillips et al. (2017a). Two types of collisions were considered: those involving only high-density precipitating ice particles (such as graupel), and those involving collisions of rimed snow or cloud ice particles with any ice species. The rimed fraction and ice habit were used only in the formulation describing the latter type of collisions, but they were not explicitly resolved in the M05 scheme. BR was enabled only when there was a nonzero rimed mass of either raindrop or cloud droplet onto the ice particle that would undergo fragmentation. A rimed fraction of 0.4 was prescribed, based on previous studies that showed better agreement with observations in polar clouds (Sotiropoulou et al., 2020; Sotiropoulou, Vignon, et al., 2021). Regarding the ice habit, we assumed planar ice particles, as they capture a wider range of conditions in terms of temperature and particle shapes compared to dendritic ice crystals. Sotiropoulou, Ickes, et al. (2021) suggested that the absence of a thorough handling of ice habit and rimed fraction in most bulk microphysics schemes does not

seem to significantly impact the depiction of BR in polar conditions. All secondary ice fragments produced by the BR mechanism are added to the cloud ice category.

Georgakaki et al. (2022) described the implementation of the DS mechanism in the M05 scheme of WRF. We considered two collision modes that can cause the freezing and subsequent shattering of large raindrops, as described by Phillips et al. (2018). The first mode, or 'mode 1', occurs when a supercooled raindrop collides with a less massive cloud ice particle or when an INP initiates freezing in immersion mode. Freezing probability is set to unity and zero for temperatures below -6°C and above -3°C, respectively, with intermediate values in between. The shattering probability depends on raindrop size, being 0 for sizes smaller than 50 μm, 1 for sizes larger than 60 μm, and varying for sizes in between. The second mode, or 'mode 2', involves collisions between raindrops and larger ice particles such as snow or graupel (James et al., 2021), producing only tiny ice fragments that are passed to the cloud ice category. Big fragments are treated as either graupel, snow, or frozen drop depending on the type of collision that initiated the raindrop freezing process.

The regional climate set-up (Figure 5.1) with augmented cloud microphysics was employed to run a reference WRF simulation for two years from 2016 to 2017, preceded by a 1-week spin-up period starting on December 25, 2015. This time frame was considered sufficient to capture the possible parameter space in the atmospheric state. High-resolution three-dimensional snapshots of the simulation with a 10-km resolution domain (the area bounded by the dashed lines in Figure 5.1), were saved every 3 h. These snapshots formed the basis for developing the ML parameterization, which will be described in the following section.

5.3.2 Random forest (RaFSIP) parameterization development

RaFSIP is based on a random forest regressor (RFR) algorithm, which is a supervised ML technique, consisting of an ensemble of decision trees (Breiman, 2001) trained directly from the outputs of the high-resolution WRF simulation. To minimize variance, each decision tree is trained on a random subset of the training data and a random subset of the inputs – also called as features – of that data. The RFR prediction is calculated by averaging over the individual decision trees, which reduces the risk of overfitting and improves generalization performance compared to a single decision tree. RFR can capture non-linear relationships between input features and output variables and is proficient at interpolation. However, it cannot extrapolate due to its predictions being averages over subsamples of the training dataset. This helps ensure that a RF-based parameterization will be robust when coupled with a model in an online setting, such as in our case.

5.3.2.1 Description of the two parameterization approaches

Depending on the prevailing temperature and the presence of rime onto ice particles, we expect different SIP processes to be activated. This is the reason why the two versions of the RaFSIP parameterization consist of a number of RFR models, each one of them being responsible for predicting the effect of SIP as dictated by the thermodynamic and microphysical state describing every model timestep. The RFR models consisting the RaFSIPv1 parameterization, are trained to predict the so-called IEF, which is the ratio between the production rate of secondary ice particles from each SIP process (HM_{rate}, BR_{rate} and DS_{rate}), and primary ice particles via heterogeneous freezing of cloud droplets (PIP_{rate}). Hence, RaFSIPv1 provides 3 predictions: IEF_{HM}, IEF_{BR}, and IEF_{DS}, the contribution of which can be added to yield the total IEF: $\mathrm{IEF} = SIP_{rate}/PIP_{rate}$. The notation of IEF is frequently employed in the literature as an indication of the prevalence of SIP, in both observational (e.g., Korolev et al., 2022; Wieder et al., 2022) and modeling studies (e.g., Waman et al., 2022; Zhao et al., 2023).

In RaFSIPv2, the RFR models predict directly the three SIP rates – HM_{rate}, BR_{rate} and DS_{rate} (in kg^{-1} s^{-1}), derived from the high-resolution WRF results. The three rates are combined to determine the total SIP_{rate}. As the HM and DS processes move mass from the liquid to the ice species when active (albeit from the rimed liquid particles in the former case), both versions of the RaFSIP parameterization are trained to predict Qc_{tr} and Qr_{tr} (in kg kg^{-1} s^{-1}) corresponding to the mass transferred from the cloud droplets and raindrops to the cloud ice category, respectively. Therefore, the two versions of the RaFSIP parameterization can provide up to five different predictions, given certain SIP conditions are met.

Here, we consider two main temperature regimes: -8 ≤ T< -3 °C (HM zone) and -25 ≤ T< -8 °C, which is essential as the HM mechanism can only be effective within the former one. By combining these temperature ranges with the presence or absence of mass production rate of raindrops collected by ice particles (RIMR in kg kg^{-1} s^{-1}), we obtain 4 different RFR models that are used in both versions of the RaFSIP parameterization (Table 5.1 and 5.2). Two models can be activated in the HM zone, namely "forestALL" and "forestBRHM", that are replaced by the "forestBRDS" and "forestBR" at lower temperatures (the suffix of the model name denotes the SIP processes in action). The final selection of which forest to use in the corresponding temperature range is based on the presence of a nonzero RIMR at the current timestep, which is the criterion used to identify the cases where DS might be taking place. The two forests that take into account the effect of DS are the forestALL and forestBRDS models.

Both RaFSIP parameterizations incorporate SIP through BR and DS at temperatures as low as -25°C, which is supported by recent observational findings (Korolev et al., 2022; Julie Thérèse Pasquier et al., 2022; Wieder et al., 2022). Approaching warmer subzero temperatures (T > -4 °C), RaFSIPv1 does not predict ice enhancement, since heterogeneous freezing of cloud droplets (i.e., the denominator in the IEF expression) does not occur in the M05 scheme (Section 5.3.1). In contrast, RaFSIPv2 can still account for the effect of SIP as it is not directly linked to the PIP_{rate}. An additional RFR model called "forestBRwarm" is therefore used in RaFSIPv2 (Table 5.2), to calculate the BR_{rate} at temperatures between -3 ≤ T ≤ 0 °C. At these warm subzero temperatures, DS is also proposed to contribute to SIP through recirculation (Korolev et al., 2020), but only in tropical or midlatitude frontal systems (Lauber et al., 2021) owing to strong convective turbulent updrafts that are rare in polar stratiform clouds. Therefore, RaFSIPv2 considers that only the BR mechanism initiated by collisions of seeding rimed ice particles can be efficient at temperatures above -3 °C.

5.3.2.2 Features and training dataset

Both versions of the RaFSIP parameterization share the same input features. The ambient temperature (T in K), total ice water content (IWC in kg kg^{-1}), liquid water content (LWC in kg kg^{-1}), relative humidity with respect to ice (RHi) and mass production rate of cloud droplets rimed onto ice particles (RIMC in kg kg^{-1} s^{-1}) are among the features that have been used in all RFR models of the two versions of the parameterization. Since DS requires the presence of large raindrops, RIMR is also used as input to the models accounting for its effect (i.e., forestALL and forestBRDS). With these 6 inputs we seek to effectively capture all range of cloud states that can initiate and drive ice multiplication. The training dataset was constrained to scenarios with substantial liquid water content (LWC>10^{-5} gm^{-3}), accompanied by nonzero riming tendencies, to ensure the effectiveness of SIP. The 6 inputs are chosen in a way to simplify the detailed SIP formulations (e.g., Phillips et al., 2017a; 2018), yet are expected to generate complex mappings for training the RFR models. Here we use the instantaneous predictions of the model for all individual vertical grid cells as inputs for all RFRs, rather than their vertical profiles (e.g., O'Gorman & Dwyer, 2018; Yuval & O'Gorman, 2020).

We generated the training dataset for all RFR models using the 3-hourly high-resolution WRF results (Section 5.3.1), extracted from 2×2 grid cell regions (16 grid cells in total) indicated by purple triangles in Figure 5.1. Half of these grid cells represented continental conditions, while the other half were over the sea. The absence of a latitudinal preference in SIP rates between the Northern and Southern hemispheres (Zhao & Liu, 2021) suggests that a limited number of grid points from the 2-year high-resolution simulation of WRF is adequate for capturing the thermodynamic and microphysical conditions associated with SIP events in stratiform conditions. Note that horizontal and vertical coarse-graining is frequently applied when developing ML parameterizations for GCMs based on high-resolution simulations (e.g., Brenowitz & Bretherton, 2019; Grundner et al., 2022; Yuval & O'Gorman, 2020). Indeed, the impact of SIP can vary depending on the scale considered, with higher-resolution simulations exhibiting greater SIP tendencies due to their ability to capture localized and enhanced SIP events. Our goal is to investigate whether a SIP parameterization derived from a 10-km resolution grid (innermost WRF domain) is effective at the coarser resolution of 50-km in the parent domain of WRF, which is closer to the resolutions seen in GCMs. Given that the input tendencies predicted by the coarser-resolution grids will be lower than the higher-resolution ones, we expect that the resulting SIP tendencies will also be smoothed out. An important aspect to consider also here is that the RFR models tend to underestimate extreme values and overestimate low values (Zhang & Lu, 2012). This behavior arises from the fact that RFR predictions are derived as averages of the predictions made by all decision trees within the ensemble.

To prepare for training, each feature and output variable is normalized using the natural logarithm, which is important given the range of several orders of magnitude they span (Figure 5.2). During the training process, we excluded IEF values below 10^{-1} and SIP rates below 10^{-5} $kg^{-1}s^{-1}$ (Figure 5.2). This was made because such values would not result in significant SIP, and we aimed to reduce the range of predictions. The training dataset comprises 20 months of high-resolution WRF results, representing approximately 85% of the data. The remaining 15% of the data, consisting of 4 months (January, April, July, and October 2017), were used for testing the offline performance of the RaFSIP parameterization (Section 5.4). The RandomForestRegressor class from the scikit-learn package version 1.2.0 (Pedregosa et al., 2011) was used to train each RFR model. All RFR models consisting the two RaFSIP parameterizations were stored as ASCII files.

5.3.2.3 Choice of hyperparameters

To improve the performance of the RFR models, different hyperparameters governing the learning process can be tuned. The Mean Squared Error (MSE) resulting from the RFR predictions was evaluated using 10-fold cross validation on the training dataset. We selected the number of trees in each forest, the minimum samples per leaf node, and the number of training samples as the three most important hyperparameters to tune. Figure D1 shows the validation curves for the forestALL model (used in RaFSIPv2), which illustrate how the performance of the model varies with different hyperparameter values. The final decision on hyperparameters involves a trade-off between model complexity and runtime, with the latter being crucial for optimizing online performance when coupled with the WRF model. We chose 10 trees in each RFR, a minimum of 4 samples per leaf node, and 25,000 training samples for all RFR models, as these produced comparable validation curves. Note that, for online applications of the RFR models, it is common practice to use 10 decision trees to ensure computational efficiency (O'Gorman & Dwyer, 2018; Yuval & O'Gorman, 2020). The offline performance of the RaFSIP parameterizations will be discussed in Section 5.4, followed by the online performance in Section 5.5.

5.3.3 Implementation of RaFSIP parameterization in WRF

To implement the RaFSIP parameterization in WRF, a Fortran 90 module is developed to read and store the parameters for building the RFR models. The ASCII files are only read during the first model timestep and all forest parameters are passed as public variables into the microphysics code. Within the M05 microphysics routine, the RaFSIP parameterization replaces the three detailed inline SIP parameterizations (Section 5.3.1), taking the fields of T, RHi, LWC, IWC as well as RIMC and RIMR as inputs to make predictions. Calculations for LWC and IWC, consider contributions from all liquid (cloud droplet and raindrops) and ice (cloud ice, snow and graupel) species. RIMC and RIMR encompass all possible ways in which cloud droplets or raindrops are collected by frozen particles in the M05 scheme: (i) droplet/raindrop-cloud ice, (ii) droplet/raindrop-snow, and (iii) droplet/raindrop-graupel. At each model timestep and grid cell, if certain requirements are met (discussed in Section 5.3.2.1), a different RFR model may be activated to represent the effect of single or combined SIP processes.

At the end of each model timestep, the RaFSIP parameterization calculates the total SIP_{rate} (in kg^{-1} s^{-1}) either directly or through the use of the IEF, depending on the chosen version. In RaFSIPv1, the SIP_{rate} is obtained by multiplying the number tendency of heterogeneously frozen cloud droplets (in kg^{-1} s^{-1}) by the total IEF. However, this approach has a significant caveat: SIP cannot be accounted for unless a nonzero PIP_{rate} is predicted by the model. Therefore, RaFSIPv1 can only be used at temperatures colder than -4 °C, where PIP is initiated in the model. To ensure that the final SIP_{rate} does not exceed a certain threshold, an upper limit of 100 particles kg^{-1} s^{-1} was applied, corresponding to the highest simulated value in the training dataset. Although our results were not sensitive to the choice of this upper limit, it may be an important consideration for the implementation of RaFSIPv1 in other microphysical schemes employed by different models. The SIP_{rate} predicted by RaFSIPv1 is then added to the cloud ice number concentration conservation equation. The RaFSIPv2 parameterization follows a similar approach to RaFSIPv1, but does not link SIP_{rate} to the instantaneous PIP_{rate}. This direct prediction is enabled by the RFR models, allowing for RaFSIPv2 to be applicable over a wider temperature range from 0 °C to -25 °C, without requiring a nonzero PIP_{rate}.

When HM and/or DS mechanisms are active, the transported masses Qc_{tr} and Qr_{tr} are subtracted from their respective cloud categories and added to the conservation equation for cloud ice mass mixing ratio. It is important to note that the transferred liquid masses involved in SIP were initially part of the rimed masses constituting the RIMC and RIMR quantities. Without SIP, these masses would have been transported to the mass conservation equation of the corresponding rimed ice particles. To avoid double-counting the transferred masses of liquid water, Qc_{tr} and Qr_{tr} should also be removed from the riming tendencies of the involved ice species. To account for this, we subtract the transferred masses from the term with the biggest contribution; given that the terms participating in RIMC and RIMR can vary by several orders of magnitude, this approach ensures that the simulations will not be subject to significant bias.

To evaluate the online performance of the new RaFSIP parameterizations when coupled with the WRF model, we conducted a one-year simulation using the same set-up depicted in Figure 5.1 (Section 5.3.1). This simulation covers the period between September 2019 and August 2020, which is more than 1.5 years after the training period, with one additional week of spin-up starting from August 25, 2019. The testing simulation was conducted three times. First, we carried out the ”CONTROL” simulation, which does not take into account any SIP process. Then, we performed the “ALLSIP” simulation, which includes all the detailed inline parameterizations of SIP outlined in Section 5.3.1. Finally, the “RaFSIP” simulation refers to the one where the RaFSIP parameterizations replaced the detailed SIP descriptions. By comparing the results of the ALLSIP simulation with those of the RaFSIP simulation in Section 5.5, we seek to examine the robustness of the new SIP parameterizations in terms of computational efficiency and result quality.

5.4 Offline performance of RaFSIP parameterizations and feature importance

To evaluate the performance of both RaFSIP parameterizations, each RFR model was tested on the 4-month dataset that was not used during training (Section 5.3.2.2). The performance was assessed using two metrics summarized in Tables 5.1 and 5.2: Root-Mean-Square Error (RMSE) and coefficient of determination (R^2), which were calculated based on the normalized output variables. R^2 is defined as one minus the ratio of the sum of squared errors to the true variance. The offline performance of the forestALL model, which is used by both RaFSIP parameterizations when all conditions for SIP processes are met, is shown in Figure 5.2. For the rest of the RFR models, the offline performance is displayed in Figures D2 to D5, in the Supporting Information.

All five outputs of the forestALL model present a wide range of values (Figure 5.2), making accurate prediction challenging. For instance, IEF_{BR} and IEF_{HM} vary from 10^{-1} to 10^{11}, while IEF_{DS} is confined below $\sim 10^{8}$, with predictions more spread out along the 1:1 line, especially at lower values. The RaFSIPv1 parameterization predicts an inverse relationship between IEF and PIP_{rate} (not shown), primarily due to the PIP_{rate} being in the denominator of the IEF expression. The competing relationship between SIP and PIP has also been highlighted in previous modeling studies (e.g., Georgakaki et al., 2022; Zhao & Liu, 2022), as an outcome of the enhanced ice nucleation leading to more glaciated MPCs with fewer precipitating particles such as rain or graupel. Note that the predicted IEF values are higher than those frequently reported in the literature (e.g., Waman et al., 2022; Zhao et al., 2023), as they are extracted from the ratio of tendencies rather than integrated particle concentrations. Similar trends are observed in the SIP rates predicted by RaFSIPv2 (Figure 5.2f, g, h), with the BR and HM processes again proving more efficient at producing SIP particles compared to DS.

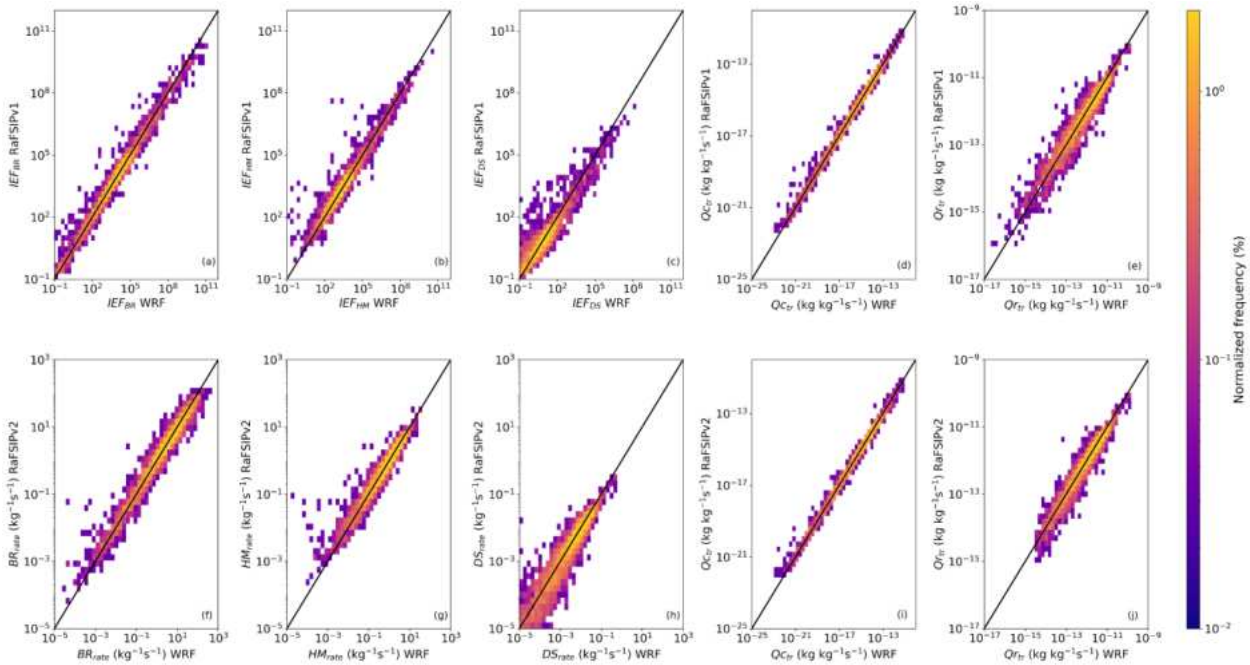

Figure 5.2 Normalized histograms (i.e., frequency is scaled by the total number of predictions) of the true WRF results versus the forestALL predictions used in (top panel) RaFSIPv1 parameterization to predict the IEF due to (a) BR, (b) HM, (c) DS, and the transferred masses from (d) cloud droplets (Qc_{tr}) and (e) raindrops (Qr_{tr}) to cloud ice, and (bottom panel) RaFSIPv2 parameterization to predict the SIP rate due to (f) BR, (g) HM, (h) DS, and the transferred masses (i) Qc_{tr} and (j) Qr_{tr}. The black line represents the one-to-one line.

Although RaFSIPv1 and RaFSIPv2 use the same predictors, the former is limited to cases where PIP_{rate} is nonzero, resulting in noticeable differences among the two approaches. To evaluate the relevance of each input feature in the predictions made by the RFR models, we employed the permutation importance metric (Figure D6 to D10) from the RandomForestRegressor class of scikit-learn. This metric estimates feature importance by randomly permuting its values and measuring the consequent decrease in model performance. This approach can capture the effect of both linear and nonlinear relationships between features and target variables, and can also help identify any potential overfitting issues in the RFR models. Note that here we used the negative RMSE as the scoring parameter and normalized the resulting variable importance by dividing by the maximum value among features.

The most significant features in the predictions made by all RFR models are the riming tendencies and the IWC. Specifically, inside the HM zone, RIMC has the highest permutation importance score for the forestALL (Figure D6) and forestBRHM (Figure D7) models employed in both RaFSIP versions. The two mass tendencies, RIMC and RIMR, are explicitly used as inputs in the detailed parameterized expression of HM in the default M05 scheme (Section 5.3.1). Outside the HM zone, where BR can lead to larger IEF or SIP_{rate} compared to DS, IWC becomes the more important feature for the predictions of the RFR models, particularly for forestBR (Figure D9) and forestBRwarm (Figure D10), with the amount of (rimed) cloud droplets becoming the second most important feature. The increase in IWC, associated with ice sedimenting from higher-level clouds, is frequently found to drive the BR process (Georgakaki et al., 2022; Järvinen et al., 2022; Pasquier et al., 2022; Ramelli et al., 2021a; Sotiropoulou, Vignon, et al., 2021).

Table 5.1. Root-Mean-Square Error (RMSE) of the output variables predicted by the RaFSIPv1 parameterization, along with the corresponding coefficient of determination (R^2) values in parentheses.

RaFSIPv1	**Conditions**		**Predictions**				
model	Temperature	RIMR	IEF_{BR}	IEF_{HM}	IEF_{DS}	Qc_{tr}	Qr_{tr}
forestALL	-8≤T<-3˚C	>0	0.32 (0.97)	0.36 (0.94)	0.46 (0.86)	0.17 (0.99)	0.26 (0.93)
forestBRHM	-8≤T<-3˚C	=0	0.37 (0.98)	0.12 (0.98)	–	0.09 (0.99)	–
forestBRDS	-25≤T<-8˚C	>0	0.31 (0.97)	–	0.38 (0.87)	–	0.39 (0.83)
forestBR	-25≤T<-8˚C	=0	0.44 (0.97)	–	–	–	–

Using the different RFR models depending on the prevailing thermodynamic and microphysical conditions allowed us to evaluate the performance of the RaFSIP parameterizations under various scenarios. The distribution of all RFR predictions against true values, as shown in Figure 5.2 and Figures D2 to D5, indicates that predictions with a higher relative frequency of occurrence are closer to the 1:1 line for both RaFSIP approaches. The statistical metrics presented in Tables 5.1 and 5.2 can differ significantly depending on the prevailing conditions and the SIP processes involved. The RMSE for RaFSIPv1 predictions varied from ∼10-45%, while for RaFSIPv2, it ranged between ∼15-40%. The

transferred masses due to SIP, Qc_{tr} and Qr_{tr}, are generally well-predicted in most of the RFR models with an RMSE of less than 30%, despite spanning more than 10 orders of magnitude.

Table 5.2. Root-Mean-Square Error (RMSE) of the output variables predicted by the RaFSIPv2 parameterization, along with the corresponding coefficient of determination (R^2) values in parentheses.

RaFSIPv2 model	Conditions		Predictions				
	Temperature	RIMR	BR_{rate}	HM_{rate}	DS_{rate}	Qc_{tr}	Qr_{tr}
forestALL	-8≤T<-3˚C	>0	0.23 (0.96)	0.22 (0.93)	0.36 (0.87)	0.16 (0.99)	0.21 (0.94)
forestBRHM	-8≤T<-3˚C	=0	0.34 (0.96)	0.36 (0.90)	–	0.18 (0.99)	–
forestBRDS	-25≤T<-8˚C	>0	0.17 (0.97)	–	0.27 (0.89)	–	0.27 (0.89)
forestBR	-25≤T<-8˚C	=0	0.28 (0.96)	–	–	–	–
forestBRwarm	0≤T≤-3˚C	=0	0.38 (0.96)	–	–	–	–

In cases where multiple SIP processes are present, the prediction error tends to be higher for DS, as shown in Figures 5.2c and 5.2h and reflected in the higher RMSE values in Tables 5.1 and 5.2. To improve the offline accuracy of the forestALL and forestBRDS models for predicting this SIP mechanism, we tested the inclusion of the size of raindrops undergoing DS as a potentially important predictor. The resulting RMSE metrics showed a ∼5% decrease in the forestBRDS model, while the forestALL model remained unaffected (not shown). However, since the total effect of SIP is cumulative and DS is the least significant mechanism compared to the other two, any errors associated with its uncertain representation are not likely to significantly impact the online performance of the RaFSIP parameterizations. Therefore, we argue that adding more predictors may not be worth the increased model complexity.

When only BR is active, either in the colder (i.e., forestBR) or warmer (i.e., forestBRwarm) temperature regime, the RMSE scores range between ∼30-45% (Tables 5.1 and 5.2). This could indicate and important input feature related to BR may be missing or that the relationship between the input features and the target variable (IEF_{BR} or BR_{rate}) is inherently difficult to model accurately due to the level of non-linearity. In the physically-based parameterization by Phillips et al. (2017a), the SIP fragments generated after BR depend on collisional kinetic energy, which is an uncertain parameter as it is a function of the difference in terminal velocities of colliding ice particles. The latter follows a fall-speed-diameter relationship, the parameters of which are highly uncertain and can directly impact both the precipitation rates and the SIP efficiency (Karalis et al., 2022). Therefore, we chose not to include collisional kinetic energy in our set of predictors, as it would increase model complexity without necessarily improving accuracy. The predictors we chose strike a good balance between model complexity and accuracy, allowing us to describe SIP occurrence as a function of simplified inputs that most GCMs can predict.

5.5 Coupling the RaFSIP parameterization with WRF

In this section, we aim to assess the performance of the parameterization when coupled back with the dynamical core of the WRF model, making fast and precise predictions at runtime. To facilitate the discussion, in the rest of the paper we will focus on the results of the RaFSIPv2 parameterization, while the corresponding RaFSIPv1 results will be available in the Supporting Information. RaFSIPv2 can predict SIP rates directly, making it less coupled with the WRF model on which it was trained. In contrast, the approach followed in RaFSIPv1 tends to be more dependent on the PIP rates predicted by each model, implying that its good online performance in WRF may not be guaranteed in other models using different PIP schemes.

When introducing the RaFSIP parameterization into the M05 scheme of WRF, two main concerns had to be addressed in order to ensure the robustness of the approach: model stability and computational efficiency. The stability of the model was tested during the one-year test simulation starting from September 2019 until August 2020 (Section 5.3.1). The coupled WRF model with the RaFSIP parameterization ran stably across a wide range of conditions. Regarding computational efficiency, the new parameterization performed comparably to the inline SIP parameterizations without increasing computational demands. This implies that the RaFSIP scheme can be easily incorporated into existing models without significant impact on runtime, being a result of carefully selecting the number of trees in the RFR models. In the following discussion all results will be divided into four groups according to season.

5.5.1 Horizontal distribution of ice crystal number concentrations

Latitude-longitude snapshots of the median ICNCs obtained from the instantaneous 3-hourly outputs of the CONTROL, ALLSIP, and RaFSIP experiments (Section 5.3.3), along with the resulting R^2 between the predictions of the latter two, provide a way to assess the quality of the WRF predictions when coupled with the RaFSIPv2 parameterization (Figure 5.3). Note that the modeled ICNCs include the contribution of all three ice species (cloud ice, snow and graupel). To calculate the median ICNCs presented in Figure 5.3 we considered only the in-cloud conditions represented by ICNCs > 10^{-5} L^{-1} and temperatures between -25 and 0 °C, which is the range where RaFSIPv2 can be active. For calculating the median values and R^2 scores, we went through each latitude and longitude reshaping the remaining two dimensions (time and height). To facilitate the identification of patches where RaFSIPv2 performs favorably in terms of R^2, we further coarse-grained the information from the coarse-resolution grid mesh by dividing the original grid into non-overlapping 3×3 sub-grids, and computing the average value of each sub-grid. Thus the R^2 map in Figure 5.3 is projected onto a 49×49 mesh.

The RaFSIPv2 parameterization coupled with WRF can skillfully predict the median horizontal distribution of ICNCs, closely following the pattern produced by the ALLSIP simulation with the detailed SIP descriptions. Darker blue shades are produced by ALLSIP and RaFSIP indicating the higher median ICNCs compared to CONTROL. The increase in median ICNCs is observed for all four seasons, even though it is more prevalent during winter and spring, particularly in the sea region between Greenland and Canada to the west and extending to the north of the Scandinavian Peninsula to the east. In these areas the median seasonal ICNCs can exceed 10 L^{-1}, suggesting the significant role of ice multiplication processes in elevating the median ICNCs by up to an order of magnitude when SIP conditions are met.

Despite being trained on a small subset of high-resolution WRF grid cells, the RaFSIPv2 parameterization can generalize and accurately predict the locations of ice enhancement in the coarser resolution domain as dictated by the ALLSIP results. The R^2 maps superimposed in Figure 5.3 reveal patches of especially high predictive skill denoted with R^2 scores exceeding 90%. The accuracy

of the predictions largely exceeds 80% of R^2 over localized areas of significant ice enhancement, shown with darker shades on Figure 5.3g and 3k. This implies the ability of RaFSIPv2 to reproduce the physical processes occurring in polar MPCs. However, the southeast part of Greenland poses a challenge for accurate model predictions, with R^2 dropping below 60%, especially in winter.

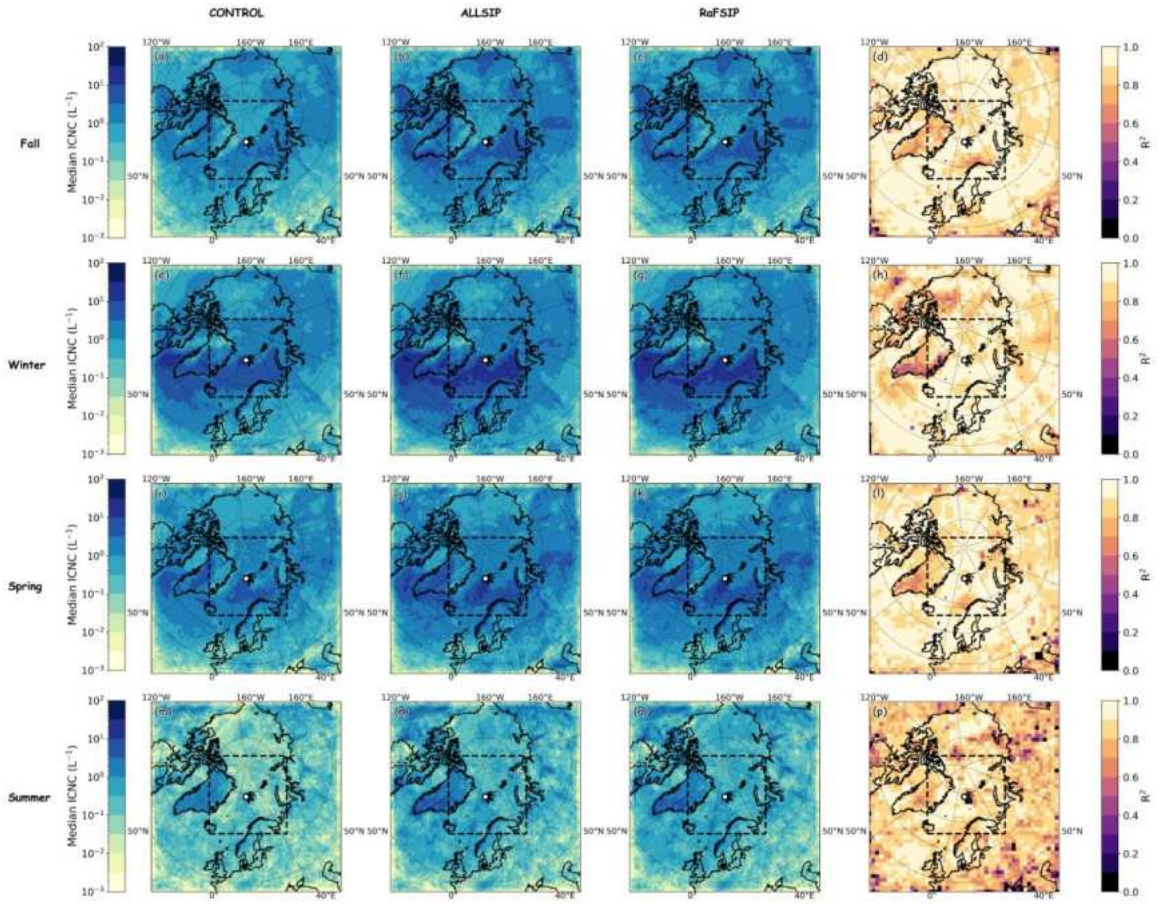

Figure 5.3 Latitude-longitude maps of the median ICNC simulated by the (a, d, g, j) CONTROL, (b, e, h, k) ALLSIP, and (c, f, i, l) RaFSIP simulations, along with the corresponding (d, h, l, p) R^2 computed between ALLSIP and RaFSIPv2 results. Statistics are calculated for the 4 simulated seasons: fall (top panel), winter (second panel), spring (third panel) and summer (bottom panel).

Compared to other seasons, the predictive skill of RaFSIPv2 is reduced during summer, with R^2 dropping below 40% in very localized regions close to the edges of the WRF domain. Higher temperatures are not likely the cause of lower R^2 values, as the RaFSIPv2 models were trained using a wide range of temperatures and temperature was not found to be among the most important input features for the predictions of the RFR models (Figures D6-D10). A possible explanation could be that during summer the expected shift towards warmer clouds may lead to increased riming tendencies, which can be associated with higher SIP rates in RaFSIPv2. Replacing the RaFSIPv2 parameterization with the RaFSIPv1 in WRF, results in a further decline in the predictive skill in all four seasons, as shown in Figure D11. The R^2 scores decrease to below 60% in most regions with significant ice enhancement, with a further drop to below 40% during the summer months. The degradation in the performance of

the model is most likely because of RaFSIPv1 requiring a nonzero value of PIP_{rate} to provide ice enhancement.

Table 5.3 presents median statistics extracted from all three sensitivity experiments during the cold (autumn and winter) and warm (spring and summer) seasons. The latitudinal zones north of 70°N are divided into three groups, and the results are grouped into two distinct temperature ranges (-10≤T≤0˚C and -20≤T<-10˚C) where SIP effects are more prevalent. During the cold season, it is observed that the CONTROL simulation leads to higher median ICNCs in the warmer temperature regions compared to the colder one at latitudes 70-80˚N, which may seem contradictory since PIP efficiency generally increases with decreasing temperatures. This unexpected finding could potentially be explained by ice seeding from colder clouds enhancing the median ICNCs in lower-level warmer clouds at temperatures above -10˚C, or by increased efficiency of ice aggregation leading to significantly lower median ICNCs in the colder temperature range (-20≤T<-10˚C) (Barrett et al., 2019; Chellini et al., 2022).

The introduction of SIP in the WRF simulations results in a substantial increase in median ICNCs, particularly in the warmer temperature bin during the cold (warm) season, where ALLSIP and RaFSIP simulations show a factor of approximately 2-3 (3-6) higher ICNCs compared to the CONTROL simulation. On the other hand, in the colder temperature bin, the ICNC enhancement in ALLSIP and RaFSIP is relatively modest, reaching only up to ∼20-25% during both examined seasons. It is worth noting that latitudes above 80°N display systematically lower ICNCs, with no significant contribution of SIP being observed at temperatures below -10°C, likely due to complete cloud glaciation. Overall, the median statistics derived from the WRF simulation coupled with the RaFSIPv2 parameterization are in good agreement with the ALLSIP simulation results during the cold and warm seasons examined here (Table 5.3).

Table 5.3. Median ICNC for different latitudinal zones, temperature ranges, and seasons, obtained from three different WRF experiments. The cold season values were extracted from September 2019 to February 2020, while the warm season values were obtained from March to August 2020. The values in all four columns represent the results from the CONTROL/ALLSIP/RaFSIP experiments. The subscript $ICNC_{si}$ indicates that the median ICNC is derived for glaciated clouds (glaciation fraction > 0.98) from model grid points over the sea-ice (sea-ice concentration > 50%).

Latitude	Temperature range (˚C)	Median ICNC cold (L^{-1})	Median ICNC warm (L^{-1})	Median $ICNC_{si}$ cold (L^{-1})	Median $ICNC_{si}$ warm (L^{-1})
70-75°N	[-10,0]	1.9/4.6/4.5	0.2/0.6/0.6	4.0/7.5/7.6	3.2/5.8/5.7
	[-20,-10)	1.5/1.9/1.7	1.2/1.4/1.3	1.4/1.5/1.7	2.5/2.7/2.8
75-80°N	[-10,0]	1.8/4.1/4.2	0.1/0.5/0.6	4.0/6.2/6.5	2.9/5.0/4.9
	[-20,-10)	1.2/1.5/1.4	0.9/1.1/1.1	1.4/1.4/1.5	2.3/2.4/2.5
> 80°N	[-10,0]	0.4/1.1/1.3	0.09/0.3/0.5	2.5/3.8/4.1	2.0/4.2/4.1
	[-20,-10)	0.8/0.9/0.8	0.8/1.0/0.9	1.0/1.1/1.2	1.5/1.6/1.7

To assess the agreement between our WRF results and satellite remote sensing data, we compare our median values from the 3 sensitivity experiments to the 10-year median values between 2006-2016 presented in (Papakonstantinou-Presvelou et al., 2022). Their study, which focused on low-level pure ice clouds, demonstrated that higher ICNCs are found over sea ice compared to open ocean, a finding

contrary to previous expectations. To ensure comparability with Figure 5.1 of Papakonstantinou-Presvelou et al. (2022), we calculated the median ICNC statistics focusing on grid points over sea ice with a glaciation fraction exceeding 98% and a sea ice concentration higher than 50%. These are annotated as $ICNC_{si}$ in Table 5.3. The glaciation fraction was determined by calculating the ratio of modeled IWC to total water content (TWC = IWC + LWC).

In the glaciated clouds simulated between -10°C and 0°C, the contribution of SIP is crucial for bringing the modeled $ICNC_{si}$ closer to the 10-year median observed values (Figure 5.1 in Papakonstantinou-Presvelou et al., 2022). At these warmer subzero temperatures, both ALLSIP and RaFSIP, enhance the median $ICNC_{si}$ by a factor of up to ∼2 compared to the CONTROL simulation of WRF during both seasons (Table 5.3). Note that glaciated conditions prevent the effect of SIP from manifesting with higher enhancement factors. This is particularly evident at temperatures below -10°C, where the efficiency of ALLSIP and RaFSIP in producing SIP particles diminishes. At these temperatures, all three experiments underestimate the observed median $ICNC_{si}$ levels (which reach up to ∼3 or 4 L^{-1}) at all latitudes. The missing ice crystal source in this temperature range may be primarily due to the representation of PIP in the model.

5.5.2 Joint probability distributions of simulated cloud properties

Figure 5.4 illustrates the bivariate joint probability density function (PDF) of the median ICNCs as a function of temperature and glaciation fraction. This figure aims to provide further insight into the conditions where the RaFSIP parameterization is expected to perform better. The statistics were derived using instantaneous 3-hourly results from the CONTROL, ALLSIP, and RaFSIP sensitivity experiments (Section 5.3.3), focusing again on the in-cloud conditions characterized by significant concentrations of ice crystals (ICNC > 10^{-5} L^{-1}), as well as ice and liquid masses (IWC, LWC > 10^{-6} gm^{-3}).

5.5.2.1 Median ice crystal number concentration

Figure 5.4 reveals that the WRF model, coupled with the RaFSIPv2 parameterization, can accurately capture the most prominent patterns of the median 2D-binned ICNCs in all four seasons compared to the ALLSIP simulation with detailed inline microphysics. This is particularly true for temperatures ranging from -8 to -3 °C and glaciation fraction below ∼25-30% or higher than ∼80%. The turquoise bands in the lower right of the 2D-binned ICNCs indicate the importance of SIP in relatively warm polar clouds. At these temperatures, supercooled liquid water prevalent in simulated MPCs enhances riming tendencies (RIMC and/or RIMR) and facilitates the action of SIP, resulting in modeled ICNCs up to an order of magnitude higher in the ALLSIP and RaFSIP simulations, compared to the CONTROL simulation. These findings align with the results of Arctic clouds presented by Sotiropoulou et al. (2020), which reported a 10-20 fold increase in ice when both HM and BR were considered, with the effectiveness of BR decreasing in moderately colder clouds (Sotiropoulou, Ickes, et al., 2021).

At higher glaciation fractions (between ∼25-80%) within the same temperature range, we observe that the RaFSIPv2 simulation tends to overestimate the median ICNCs predicted by ALLSIP. Indeed, from the normalized histograms of 2D-binned median ICNCs superimposed in Figure 5.4, we can also infer that RaFSIPv2 predictions can be up to a factor of 3 higher than the ALLSIP predictions, especially in the lower ICNC ranges (e.g., Figure 5.4d and 5h). In these temperature conditions, only the forestALL and forestBRHM can be activated, with the latter contributing presumably more due to the expected limited presence of large raindrops, which prevents the frequent activation of the forestALL model. The permutation importance of forestBRHM (Figure D7) suggests that RIMC and IWC are the two most important features for the predictions of this model. If higher SIP rates are associated with higher IWC and, hence, glaciation fraction, this could explain the slightly overestimated RaFSIPv2 predictions.

At temperatures below ~ -15 °C, where the relative contribution of PIP starts becoming more important than SIP (Zhao et al., 2023), all three sensitivity experiments produce similar ICNC patterns (Figure 5.4). The vertical zones of constant median ICNCs observed in all three sensitivity simulations originate from the PIP scheme of WRF being dependent only on temperature (Section 5.3.1). Nevertheless, reduced ICNCs are simulated during the summer months in ALLSIP (Figure 5.4n) and RaFSIP (Figure 5.4o) simulations compared to CONTROL, for clouds formed at temperatures below -18°C and glaciation fractions higher than 40% (upper left part of Figures 5.4n and 5.4o). At such low temperatures, the competition between SIP and PIP may limit the amount of water available or the distribution of ice crystals throughout the cloud, thus limiting the ice crystals produced by SIP.

Focusing on the upper right corner of Figure 5.4, where the temperatures are between -5 and 0°C and the glaciation fraction exceeds 80%, we can observe higher ICNCs simulated by the CONTROL simulation than the two experiments that include SIP parameterizations, especially during Winter and Spring. At temperatures higher than -4°C, elevated ICNCs in the CONTROL experiment can only be explained by ice sedimentation, where precipitating ice particles fall from higher model grid cells. The implementation of SIP in the model can induce numerous ice crystals – albeit with smaller sizes – in the overlying colder clouds or colder parts of the same cloud (Georgakaki et al., 2022; Sotiropoulou et al., 2022). This shift in the ice particle size distribution leads to smaller ice crystals leading to the reduced sedimentation rate of frozen hydrometeors observed in the ALLSIP and RaFSIP simulations. This is further supported by the joint PDF of the modeled IWC values (Figure D12), where both simulations accounting for SIP result in comparable or even lower IWC values compared to the CONTROL simulation. This can have important implications for the ice and liquid phase partitioning in polar MPCs, determining their microphysical evolution and radiation properties (Curry et al., 1996; Tan & Storelvmo, 2019; Shaw et al., 2022). Overall, the RaFSIP simulation adequately reproduces the most important features in the 2D-binned ICNCs (Figure 5.4) and IWC (Figure D12) modeled by the ALLSIP simulation, indicating that the newly developed ML parameterization can replicate the underlying physics of the simulation with the detailed SIP microphysics.

Despite the lower R^2 scores in the horizontally averaged ICNCs (Figure D11), replacing the RaFSIPv2 parameterization with RaFSIPv1 in the model leads to comparable results when plotted in the joint temperature-glaciation fraction spectrum (Figure D13). However, the distribution around the 1:1 line is more spread out, especially in spring and summer (Figure D13j and D11p versus Figure 5.4j and 5.4p). The main difference between the two approaches is in the very warm subzero temperatures (T>-4°C), where RaFSIPv1 disregards completely the effect of SIP due to the zero PIP rates. As a result, the upper right part of the RaFSIPv1 ICNC distribution is more comparable to the one produced by the CONTROL simulation rather than the ALLSIP simulation (Figure D13).

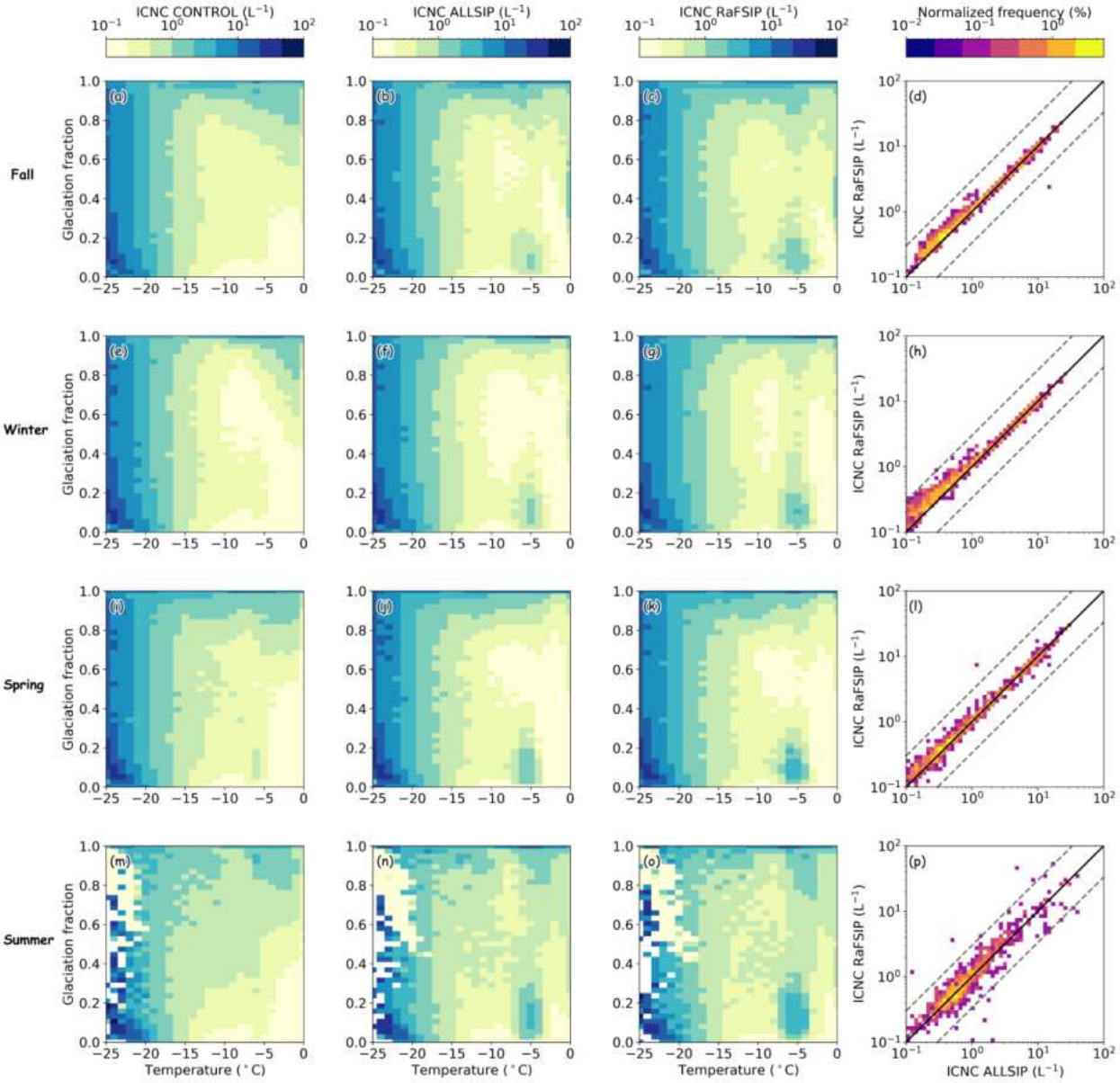

Figure 5.4 Bivariate joint PDF of median ICNC defined in terms of both temperature and glaciation fraction from the 50-km resolution domain results of the CONTROL (a, e, i, m), ALLSIP (b, f, j, n) and RaFSIPv2 (c, g, k, o) WRF simulations. The normalized histograms of the 2D-binned median ICNC results from the ALLSIP simulation are also plotted versus the RaFSIPv2 predictions (d, h, l, p). The black line represents the one-to-one line, while the grey dashed lines delimit the area where the ALLSIP values are over or under-estimated by a factor of 3. Statistics are calculated for the 4 simulated seasons: fall (top panel), winter (second panel), spring (third panel) and summer (bottom panel).

5.5.2.2 Median cloud liquid water content

SIP often causes changes in modeled liquid cloud droplets due to increased number concentrations of their frozen counterparts (e.g., Georgakaki et al., 2022; Zhao & Liu, 2021). In addition to direct liquid-to-ice mass transitions caused through the HM and/or DS mechanisms, the elevated concentrations of secondarily formed ice particles can further deplete the surrounding liquid phase hydrometeors in MPCs after their initial growth through vapor diffusion, through the action of the Wegener–Bergeron–

Findeisen (WBF) or the riming processes. It is therefore essential to investigate how SIP affects the joint PDF of LWC in the ALLSIP simulation and whether the RaFSIP simulation can reproduce the results.

From the complex patterns of LWC produced (Figure 5.5), we can infer the non-linearity of the microphysical interactions occurring in mixed-phase and ice clouds. The competition between the two cloud phases is highlighted by the decreasing cloud LWC as the glaciation fraction increases at a given temperature. The dark blue shades confined in the lower part of Figure5, indicate a persistent supercooled liquid layer present in all three sensitivity simulations at temperatures below ~ -4°C with a degree of glaciation below 20% in all seasons except summer, where in the CONTROL simulation it extends up to almost 40% (Figure 5.5m). This remark can be consistent with the typical structure of high-latitude MPCs, comprising single or multiple stratiform layers of supercooled liquid water from which ice crystals form and precipitate (e.g., Morrison et al., 2012; Shupe, 2011). Including SIP in the simulations slightly restricts the extent of this liquid layer to lower glaciation fractions in both ALLSIP and RaFSIP, most notably during the summer months.

At higher temperatures (>-4°C) and glaciation fraction (>80%), the CONTROL simulation predicts higher LWC values in the region with the elevated ICNCs caused by more frequent ice seeding events (i.e., upper right part of Figure 5.4a). The presence of more massive precipitating ice particles, indicated by higher IWC values in this region (Figure D12a, e, I, m), sediment quickly and constrains their ability to compete with supercooled liquid water for the available water vapor. In the same region, the ALLSIP and RaFSIP simulations predict lower contribution from both the liquid (Figure 5.5) and the ice hydrometeors (Figure 5.4 and S12).

By incorporating SIP into the WRF model, polar MPCs are produced with reduced LWC at temperatures above -15°C and glaciation fractions below 60%. In the CONTROL simulation, for instance, during fall and spring, a drop in the simulated LWC to $\sim 10^{-4}$ gm^{-3} requires temperatures around -8°C and glaciation fraction exceeding 60% (Figure 5.5a, i). However, in the ALLSIP (Figure 5.5b, j) and RaFSIP (Figure 5.5c, k) simulations, such low LWC values can be attained in clouds with a degree of glaciation as low as 40%. The regions of significant ice enhancement in the ALLSIP and RaFSIP simulations (i.e., turquoise bands in Figure 5.4) do not overlap with the regions of decreased LWC in Figure 5.5. This can be explained by the time needed for small secondary ice particles to grow first through vapor diffusion until the vapor pressure drops below saturation with respect to liquid water. As the glaciation fraction increases, they can gain mass more efficiently at the expense of the surrounding evaporating cloud droplets (WBF) or through their collection and subsequent freezing (i.e., riming). Both simulations accounting for SIP show remarkable agreement in the location of the most significant ice enhancement (Figure 5.4), followed by depletion of the mass of supercooled water (Figure 5.5).

At temperatures $\lesssim$-15°C, PIP can contribute significantly to the total ice crystal production rates, leading to a further decrease in LWC through heterogeneous freezing. The combination of heterogeneous freezing, WBF, riming and SIP likely controls the complex LWC patterns observed between -20°C and -4°C. Despite the complexity of the simulated system, the RaFSIP predictions align closely with the 1:1 line in the produced normalized histograms, particularly during fall and winter (Figure 5.5d and 4.5h), indicating excellent agreement with the ALLSIP simulation. These findings suggest that the RaFSIP parameterization can accurately capture the cloud phase partitioning produced by the ALLSIP simulation, with an uncertainty of up to a factor of 3. The LWC results from the RaFSIPv1 parameterization (Figure D14) demonstrate that the use of the IEF for parameterizing the effects of SIP also has sufficient predictive skill in WRF. The main difference lies again at warmer temperatures, where the RaFSIPv1 results in slightly overestimated LWC compared to the ALLSIP predictions, especially during fall and winter.

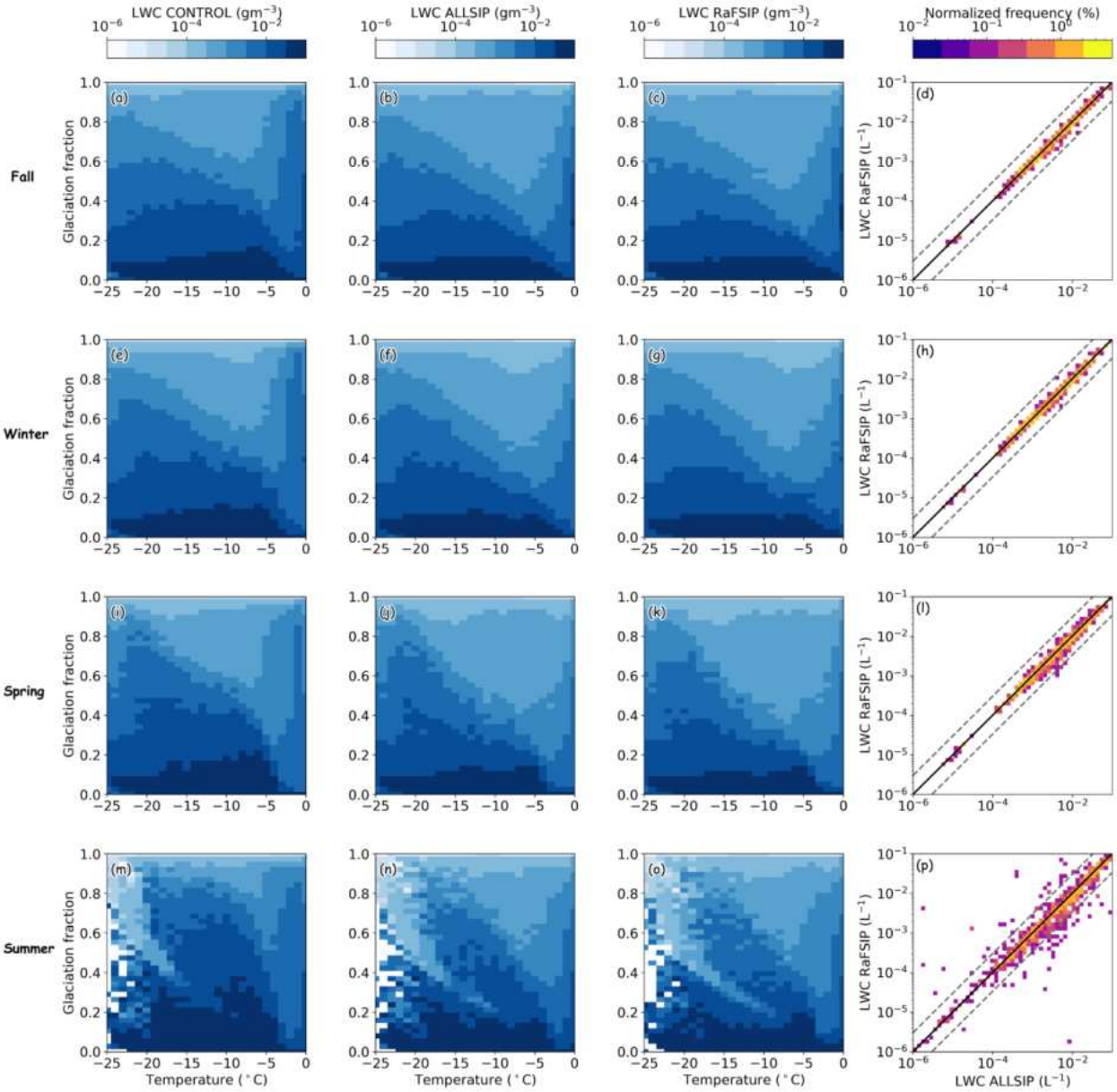

Figure 5.5 Bivariate joint PDF of median LWC defined in terms of both temperature and glaciation fraction from the 50-km resolution domain results of the CONTROL (a, e, i, m), ALLSIP (b, f, j, n) and RaFSIPv2 (c, g, k, o) WRF simulations. The normalized histograms of the 2D-binned median LWC results from the ALLSIP simulation are also plotted versus the RaFSIPv2 predictions (d, h, l, p). The black line represents the one-to-one line, while the grey dashed lines delimit the area where the ALLSIP values are over or under-estimated by a factor of 3. Statistics are calculated for the 4 simulated seasons: fall (top panel), winter (second panel), spring (third panel) and summer (bottom panel).

5.5.3 Cloud radiative forcing at the surface

The preceding discussion illustrates how SIP can significantly alter the number concentration and size distribution of ice and liquid particles in polar MPCs. Such changes in the macro- and microphysical properties of clouds are expected to impact the two most critical cloud feedbacks associated with the polar regions: the cloud optical depth and the cloud-sea-ice feedbacks (e.g., Goosse et al., 2018). For instance, changes in the albedo of MPCs resulting from an increase in the amount of small liquid

droplets contained in them can lead to enhanced shortwave radiation reflected back to space and reduced warming at the surface (Murray et al., 2021; Tan & Storelvmo, 2019). During the polar night, however, an increase in low-level cloud coverage has been found to increase the longwave radiation emitted to the surface that is trapped as heat due to the stable stratification conditions in the Arctic, ultimately resulting in surface warming (Ebell et al., 2020; Kay et al., 2016). In this section, we aim to evaluate the performance of the RaFSIP parameterization concerning the anomalies observed in the simulated cloud radiative forcing at the surface (CRF_{surf}) with respect to the ALLSIP simulation (ΔCRF_{surf}, Figure 5.6). The calculations of CRF_{surf} and ΔCRF_{surf} are elaborated in supporting information of Young et al. (2019), which also accounts for additional modifications in the shortwave fluxes to account for the highly reflective Arctic surface (Vavrus, 2006).

Figure 5.6 illustrates the annual cycle of the cloud impact on the surface radiative energy budget, with blue (red) shades indicating cloud-induced cooling (warming). The polar clouds have a strong longwave greenhouse warming effect during the non-summer months, with the maximum CRF_{surf} reaching up to ∼40 Wm^{-2} and locally up to ∼60 Wm^{-2} during fall and winter (Figure 5.6a, b). Ground-based remote sensing observations collected at Ny-Ålesund over two years (2016-2018) found positive monthly net CRF_{surf} between September and April/May, with a mean longwave warming of ∼50 Wm^{-2}, which is in line with our results (Ebell et al., 2020). In contrast, during summer, the higher occurrence of liquid in the simulated polar clouds (Figure 5.5n) combined with the lower surface albedo leads to a strong cloud-induced cooling at the surface by up to ∼-100 Wm^{-2} (Figure 5.6d), again in agreement with Ebell et al. (2020). During spring, the polar clouds have almost a neutral effect over the sea-ice and a slight cooling effect over the open ocean in the lower latitudes (Figure 5.6c).

The anomalies in longwave and shortwave radiation are calculated by the mean differences in the corresponding predictions between RaFSIP and ALLSIP, the combination of which produced the final surface anomalies, ΔCRF_{surf} (Young et al., 2019). Note that the mean ΔCRF_{surf}, is projected onto a 49 × 49 mesh by averaging over 3 × 3 sub-grids, similar to the averaged maps shown in Figure 5.3. For the interpretation of ΔCRF_{surf}, the red (blue) colors indicate that more (less) shortwave radiation is reaching the ground in the RaFSIP simulation, which in turn implies the presence of more (less) glaciated clouds than in ALLSIP. Replacing the detailed inline parameterizations of SIP in the M05 scheme with the new RaFSIP parameterization can lead to CRF_{surf} biases between -2.5 and 2.5 Wm^{-2}, with a non-uniform pattern across the model domain (Figures 5.6e-5.6h). Compared to the CRF_{surf} magnitudes illustrated in Figure 5.6, such radiative biases can be considered negligible.

During summer, when ice enhancement from SIP is the strongest (Table 5.3), the largest ΔCRF_{surf} values are largely observed over the sea-ice and ocean grid cells at latitudes higher than 70°N (Figure 5.6h). At this time, the RaFSIPv2 predictions of the ice (Figure 5p) and liquid (Figure 5.5p) cloud phase partitioning can be biased by up to a factor of 3, leading to an underestimation of the liquid-dominating clouds compared to ALLSIP, and consequently, an excess of up to ∼2.5 Wm^{-2} of shortwave radiation at the surface. However, in the continental and ocean regions of lower latitudes, mostly negative CRF_{surf} biases are observed, indicating that RaFSIPv2 is lacking some ICNCs compared to ALLSIP there. A similar ΔCRF_{surf} pattern characterizes spring (Figure 6g), with the colors shifted towards lighter tones, indicating relatively smaller radiative errors (between -1.5 and 1.5 Wm^{-2}). Fall exhibits a cooling effect (down to -1 Wm^{-2}), with some localized areas of warming (∼1 Wm^{-2}) spread around the WRF domain (Figure 6e), while winter is the season with the minimum SIP contribution and the smallest cloud radiative biases, confined mostly to the bottom part of the model domain (Figure 5.6f).

Figure D15 displays the outcome of the WRF simulations using RaFSIPv1 as a substitute for the RaFSIPv2 parameterization. The obtained ΔCRF_{surf} ranges from -3 to 3 Wm^{-2}, indicating slightly higher radiative biases in all seasons compared to the results shown in Figure 5.6. The differences between the two SIP parameterizations are most significant in the warm season (Figure D15g and h), where all the positive biases resulting from RaFSIPv2 are replaced by negative ones. The most considerable negative bias appears in the sea area to the east of Greenland (latitudes between 70-80°N), where ∼3

Wm^{-2} less shortwave radiation reaches the surface during summer (Figure D15h) compared to the ALLSIP simulation, indicating the tendency of RaFSIPv1 to overestimate the amount of liquid hydrometeors in the summer MPCs. Its reduced predictive ability to capture all the enhanced SIP events present in the ALLSIP simulation stems mainly from the fact that it is limited by the presence of PIP, and hence it cannot be activated for the whole range of conditions that would favor ice multiplication.

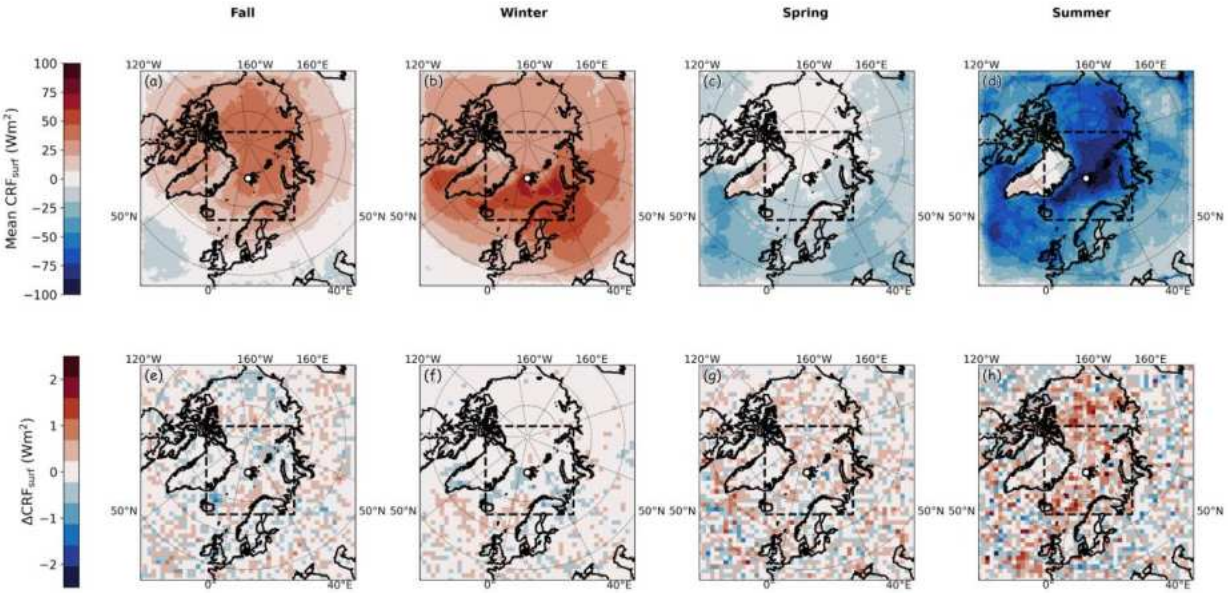

Figure 5.6 Latitude-longitude maps of (top panel): seasonally-averaged cloud radiative forcing at the surface (CRF_{surf}) simulated by the ALLSIP simulation, and (bottom panel): anomalies with respect to the ALLSIP simulation (ΔCRE_{surf}) derived from the WRF simulation coupled with the RaFSIPv2 parameterization, extracted respectively for (a, e) fall, (b, f) winter, (c, g) spring and (d, h) summer.

5.6 Outlook

This study introduces a new ML-based framework aimed at representing the impact of ice multiplication in stratiform MPCs within large-scale models. The new RF parameterization, referred to as RaFSIP, is developed using two different approaches to describe the effect of SIP at temperatures as low as -25°C. The first approach indirectly describes SIP through the use of an ice multiplication factor applied to the primary ice production rates, while the second approach directly predicts the SIP tendencies, providing a more explicit representation of the underlying physical processes. RaFSIP is trained on two years of 10-km horizontal resolution WRF simulations over the pan-Arctic region. We evaluate the parameterization both offline and online, and demonstrate that RaFSIP can accurately predict tendencies of unresolved physics in the 50-km horizontal resolution domain, comparable to the conventional SIP schemes. RaFSIP skillfully captures how SIP affects the glaciation state and evolution of polar stratiform MPCs, predicting their ice- and liquid-phase partitioning with an uncertainty of less than a factor of 3. Importantly, RaFSIP exhibits only minor radiative biases, not exceeding ±3 Wm^{-2} at the climatologically-sensitive Arctic surface. This implies that biases in the predicted SIP_{rate} or IEF (depending on the version of RaFSIP used) do not translate into significant errors in simulated cloud microphysical properties and cloud radiative forcing.

The intrinsic property of RF algorithms to make conservative predictions by averaging over the predictions of the individual decision trees allowed the coupled WRF-RaFSIP scheme to run efficiently and without instabilities for a year. The key advantage of our approach is that SIP can be represented using inputs, such as temperature, ice- and liquid water content, riming tendencies, and relative humidity with respect to ice, which are commonly predicted by most models. This facilitates its integration in host models with horizontal grid spacings comparable to or larger than the 10-km resolution grid used for training RaFSIP. This is crucial, as SIP can significantly impact cloud evolution, rapidly glaciating them, altering precipitation and eventually climate.

The incorporation of the RaFSIP framework in the microphysics scheme of 3 GCMs, namely ECHAM-HAM, NorESM2, and EC-Earth, participating in the CMIP assessments is one of the undergoing studies we are currently addressing (Ickes et al., 2023; Costa-Surós et al., 2023). The modular nature of the new SIP parameterization allows for seamless integration with the dynamical core of each GCM model, provided that the input features are well located inside the stratiform cloud microphysics routine. Preliminary results indicate that utilizing grid-box averaged atmospheric variables predicted by GCMs as inputs to the RaFSIP scheme, leads to computationally efficient simulations without numerical instabilities or explosive SIP (not shown). This model intercomparison project will evaluate the robustness of our approach as well as any potential limitations.

As the RaFSIP scheme is trained on a wide range of stratiform conditions where SIP is likely to occur, it can effectively capture the underlying mechanisms behind ice multiplication in any type of single or multilayer clouds in the polar regions. The limitations for our work stem mostly from the fact that RaFSIP is trained based on regional simulations, and it therefore may not be applicable for the entire globe (e.g., tropical marine or deep convective clouds). To address this, the training dataset can be expanded by incorporating simulation results from various locations worldwide where SIP is recognized (Hoose, 2022). Additionally, the dataset can be augmented to include the description of other SIP processes, such as fragmentation during ice particle sublimation under ice subsaturated cloudy conditions (e.g., Deshmukh et al., 2022). Our study demonstrates that by leveraging a relatively small number of grid points from the regional climate modeling framework, the training dataset can effectively encompass a broader range of cases not covered in our initial analysis.

Finally, this study highlights the significant potential of ML techniques and high-resolution data for the development of computationally efficient and accurate subgrid-scale parameterizations of cloud microphysical processes, addressing the current gaps and limitations in large-scale models. By integrating physics-guided ML algorithms and utilizing feature importance metrics, we increase the transparency of the inner workings of these algorithms, even if they are initially considered uninterpretable (Beucler et al., 2021; McGovern et al., 2019). This is a promising pathway towards model simplification and improved process representation within GCMs. Moving forward, further exploration and implementation of such techniques can contribute to advancements in GCMs, ultimately leading to more robust and comprehensive climate simulations.

6. Conclusions and perspectives

Simulating clouds and their impact on climate has been a long-standing challenge for climate models, primarily from uncertainties in representing small-scale microphysical processes. MPCs, with the numerous liquid- and solid-phase hydrometeors and their linkage through a complex web of process interactions, are especially riddled with uncertainties in process level description and lack of observational constraints. Figure 6.1 summarizes the key takeaway from each study conducted during this PhD thesis, each of which is presented as a separate chapter. While the research presented in Chapters 2-4 focused primarily in case studies, yet they collectively focus on characteristic mixed-phase cloud types for which the formation of liquid droplets and the production, growth and multiplication of ice particles require better representation in models. The modeling advancements laid out in Chapters 3 and 4 were subsequently used to generate a large dataset that served as the foundation for the development of the first ML-based parameterization designed to represent the combined effects of the most important SIP processes in stratiform MPCs, which is the most radiatively important cloud type (Chapter 5). In the following we summarize the main findings and conclusions of this thesis, contextualizing them in the broader research landscape with potential implications and avenues for future research:

Accomplishment 1: Unraveling dynamical from aerosol-related effects on cloud droplet formation

Motivation, analysis & implications

In the first study (Chapter 2), we explore the relative importance of factors influencing cloud droplet formation in orographic MPCs: cloud dynamics (i.e., updraft velocity variability) or variations in aerosol concentration. Our findings revealed that in the absence of precipitation, we could deduce cloud-scale vertical velocity distributions using ground-based remote sensing measurements, particularly wind Doppler lidar, that are useful for hydrometeor formation (i.e., droplet number) rates. When we integrated these velocity observations with ground-based aerosol measurements and aerosol hygroscopicity data, we effectively constrained the predictions generated by a state-of-the-art droplet activation parameterization. Our predictions of droplet number agreed to within ∼25% with balloon-borne measurements of Nd, which is within the uncertainty of published in-situ closure studies.

The limited availability of balloon-borne measurements for liquid- and mixed-phase clouds in this study raised questions about the applicability and accuracy of the proposed methodology under different conditions or varying degrees of cloud glaciation. In a follow-up study conducted by Motos et al. (2023), utilizing a more extensive dataset, cloud parcel activation theory was shown to predict N_d with similar accuracy in Arctic MPCs, even when the glaciation fraction (i.e., the ratio of cloud ice water content to total water content) reached levels as high as 90% (Figure 6.2). This finding suggests that warm cloud activation theory can reliably estimate N_d within 50%, irrespective of the degree of glaciation. This in turn suggests that the usage of adiabatic activation is a good approach, particularly in stratiform boundary layer MPCs with limited entrainment of dry air. It also validates the

robustness of the approach introduced in Chapter 2. Furthermore, for the Arctic MPCs studied by Motos et al. (2023), the large degree of droplet closure implies that microphysical processes such as primary ice nucleation, riming, or SIP through HM may not have contributed to the observed cloud glaciation, as they would have more effectively depleted N_d below the levels predicted by cloud parcel theory and also perhaps provide large enough surface area for condensational (depositional) loss of water vapor that in turn would decrease the maximum supersaturation and cloud droplet number. This suggests that alternative SIP mechanisms, such as ice-ice collisional break-up, could be responsible for the observed high ice fraction within the observed Arctic MPCs.

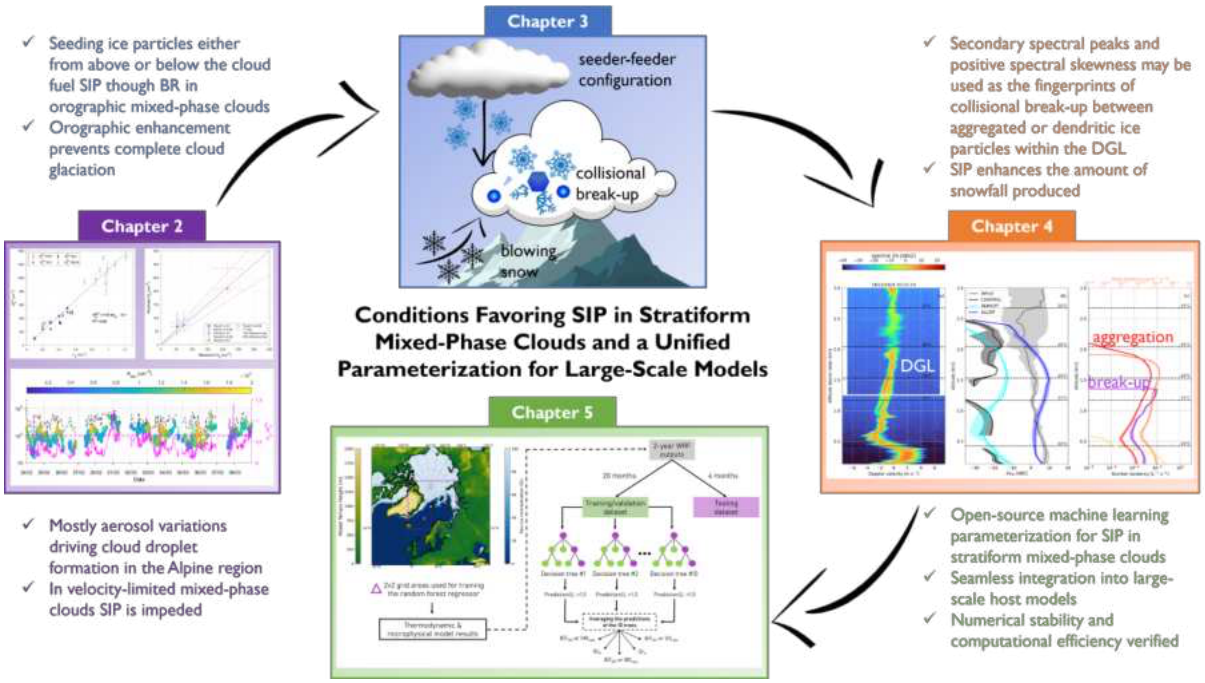

Figure 6.1 Schematic overview of the various projects undertaken within this PhD thesis. Each figure encapsulates the primary findings from its respective chapter.

Our results also highlighted the importance of water vapor competition in cloud droplet formation when understanding the sensitivity of that latter to aerosol amount. Notably, increased anthropogenic pollution reduces cloud supersaturation to below 0.1%, which simulations suggest acts as a threshold marking a transition from an aerosol-limited to a velocity-limited droplet formation regime. In fact, when aerosol concentration (for constant vertical velocity) further increases, droplet number tends to approach an asymptotic upper limit (N_d^{lim}) that seems to depend only on the value of vertical velocity. By pooling results from warm boundary layer cloud characteristics sampled in two field campaigns, we derived a linear relationship effectively describing N_d^{lim} as a function of solely the vertical velocity. Given that droplet formation in real clouds is actually a result of superposition of results for the probability distribution of updraft velocity (which in turn relates to the levels of turbulence in the PBL) we eventually express N_d^{lim} as a function of the standard deviation of updraft velocity. The findings from Motos et al. (2023) in Arctic MPCs also aligned with the linear relationship established in Chapter 2, which together with the evidence from campaigns in previous studies, supports the potential universality of this relationship. Future work involving additional case studies of liquid- and mixed-phase clouds under a broader range of conditions will further strengthen our results.

One important implication of the potential universality of the N_d^{lim}- σ_w relationship is the possibility of estimating the distribution of updraft velocities for non-precipitating boundary layer clouds through measurements or retrievals of N_d (e.g., Foskinis et al., 2022) in regions where velocity-limited conditions are expected (e.g., continental areas). Vertical velocity, especially at cloud-relevant scales, remains a poorly constrained atmospheric variable, despite it being a key driver of droplet formation in many regions globally (Morales & Nenes, 2014; Sullivan et al., 2016). Thus, having the ability to derive information about its distribution opens up additional opportunities for model evaluation, even in remote areas where in-situ measurements of vertical velocity are not feasible.

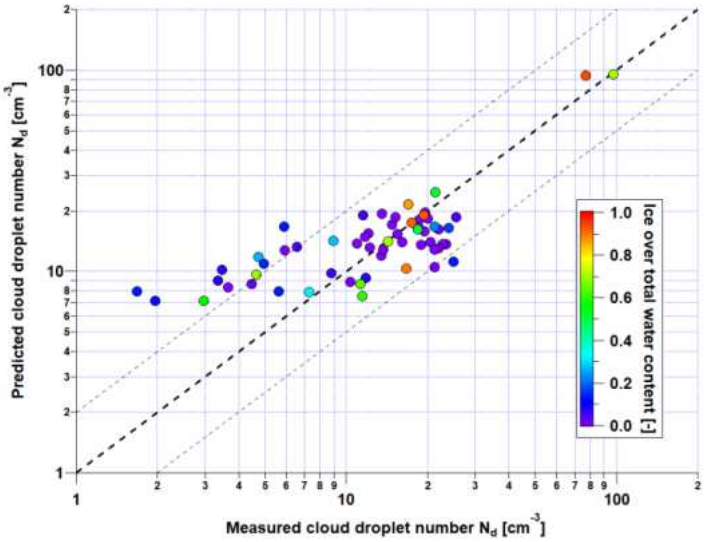

Figure 6.2 Cloud droplet closure achieved by comparing warm cloud activation theory (y-axis) with balloon-borne measurements taken in Arctic mixed-phase clouds (x-axis). The colorbar represents the degree of glaciation, with 1.0 signifying pure-ice clouds. Note that the low droplet number in the observations (below 10 cm^{-3}) are likely not representative of in-cloud conditions (i.e., the droplets sampled where below or right at cloud base), so should not be considered here. More details are provided in Motos et al. (2023), from which this figure is adapted.

The key take-home message is that knowledge of both N_d and N_d^{lim} allows us to assess cloud droplet formation susceptibility to aerosols without requiring prior aerosol concentration data. In velocity-limited MPCs, N_d reaches its maximum potential under these vertical velocity conditions. Smaller droplets hinder cloud glaciation by reducing riming and SIP efficiencies (as discussed in Section 1.2.5), favoring persistent mixed-phase conditions. In-contrast, Pasquier et al. (2022) related the low CCN concentrations observed in aerosol-limited MPCs in the Arctic with the formation of fewer but larger cloud droplets, that generate conditions conducive to SIP through DS. This, in turn, enhances cloud glaciation. While the effect of SIP was not directly addressed in our first study, being able to infer the droplet formation regime in turn carries important implications on the microphysical evolution and radiative properties of MPCs.

Accomplishment 2: Origins of high ice crystal number concentrations in orographic mixed-phase clouds

Motivation, analysis & results

In Chapters 3 and 4 of this thesis, our focus was entirely on the contribution of SIP in shaping the elevated ice crystal concentrations observed in orographically-induced MPCs. Our analysis primarily relied on numerical modeling of the observed cloud systems using the mesoscale model WRF, advancing its microphysics scheme to account for the most important SIP processes reported. The evaluation of the model was initially based on in-situ observations of the cloud ice and liquid water content in Chapter 3, but transitioned to ground-based radar remote sensing and forward simulations in Chapter 4. Both chapters investigated wintertime MPCs that formed at temperatures below the extensively studied HM mechanism, driven by the recognized need to examine SIP at such cold subzero temperatures (Korolev et al., 2022).

In mountainous regions, seeder-feeder events play a critical role in supplying low-level stratiform orographic clouds with substantial ice hydrometeors. These events initiate a sequence of ice growth processes that can significantly enhance orographic precipitation or even lead to complete cloud condensation. The extent of this effect depends on how efficiently orographic forcing can maintain supersaturation with respect to liquid water. Our NWP simulations of seeder-feeder clouds, however, provided evidence that introducing ice seeding alone is insufficient to replicate the observed ice and liquid phase distribution in MPCs. To bridge the gap between modeled and observed ICNCs, it was necessary to incorporate SIP processes into the model.

The influence of BR-induced SIP is particularly pronounced in all our model simulations of multilayer precipitating cloud systems. We showed that models missing a description of BR would underestimate the simulated ice concentrations by up to three orders of magnitude (Chapters 3 and 4). The efficiency of BR is particularly enhanced within the temperature range favoring dendritic crystal growth (i.e., DGL), which aligns perfectly with remotely-sensed fingerprints of BR (von Terzi et al., 2022). The complex plate-like branched ice structures present inside the DGL promote aggregational growth by facilitating their interlocking upon collisions. This enhances differential settling and, consequently, collision efficiencies, thereby amplifying the effectiveness of the BR mechanism. In Chapter 4, we demonstrated that BR efficiency exhibits a tenfold enhancement inside the DGL leading to a production rate of ice fragments that compensates for and even exceeds the loss of ice particles due to aggregation.

We showed that ice enhancement due to BR results in two distinct effects in the modeled MPCs. In the upper parts of the cloud, BR shifts ice particle concentrations toward smaller sizes by transferring mass from large snowflakes or graupel to small cloud ice particles during collisions. The secondary ice crystals efficiently grow through vapor deposition within the DGL (Takahashi, 2014), favoring ice-to-snow autoconversion once they exceed a threshold diameter. Interaction between these ice particles and supercooled droplets in low-level feeder clouds or the lower-lying mixed-phase levels of the same clouds further augments their growth through riming or WBF. This is expected to increase the cloud ice water path at the expense of its liquid counterpart, ultimately resulting in increased snowfall reaching the ground. The enhanced snowfall acts as an efficient ice particle sink that can effectively offset the SIP fragment generation, thereby preventing explosive ice production and complete cloud glaciation (Chapter 3).

This cascade of microphysical effects summarizes the findings from both orographic case studies presented in Chapters 3 and 4. An important takeaway is that outside the HM temperature regime,

an accurate representation of seeding snowflakes, effectively multiplied through BR, is essential for capturing the correct partitioning of ice and liquid in orographic MPCs. This realization holds significance as the effect of BR is notably absent from the microphysics schemes commonly used in most NWP models and GCMs.

Limitations & perspectives

Representation of BR in bulk microphysics schemes

When parameterizing SIP through BR using the physically-based parameterization by Phillips et al. (2017a), certain assumptions are inherent. These assumptions concern the degree of riming and the ice habit of particles undergoing fragmentation. It is important to underline that both laboratory studies conducted by Takahashi et al. (1995) and Vardiman (1978) emphasized that it is the collisions with rimed particles that promote BR. In our modeling studies, we therefore restricted BR to cases where the smallest involved ice particle is at least partly rimed. Nevertheless, we treated the rimed fraction as a tunable factor, adjusting it based on the performance of the model against available observations. For instance, a higher rimed fraction was prescribed for improved model performance in Chapter 3, albeit leading to unrealistically high ICNCs in Chapter 4. Furthermore, the ice habit was also predefined, assuming dendritic particles within the temperature range of -12°C to -17°C and spatial planar crystals for other temperature regimes. Microphysical schemes offering more degrees of freedom for representing the particle properties, such as the degree of riming (Morrison & Milbrandt, 2015) and ice habit (Jensen et al., 2017), hold promise for refining the precision of the BR parameterization, thereby mitigating the dependencies on ad hoc assumptions.

A more computationally efficient approach would involve developing a new parameterized expression for the degree of riming suitable for bulk microphysics schemes. This parameterization, for instance, could describe the rimed fraction as a function of temperature, liquid water content, and the size of the involved ice particles. The development of this parameterization could greatly benefit from ice particle imagery gathered during various field campaigns. For instance, a classification method presented in Mosimann et al. (1994), as applied in Figure A4 and Mignani et al. (2022), categorizes ice particles into six distinct rimed categories ranging from 0 (unrimed particles) to 5 (graupel). A valuable dataset, which is complemented by relevant environmental measurements, has been presented in Grazioli et al. (2022) and could potentially contribute to the development of this parameterization. This dataset encompasses over 2.5 million images of snowflakes obtained during numerous field campaigns around the globe, each categorized based on their riming degree within a spectrum ranging from 0 to 1 (with 1 signifying graupel).

What about the efficiency of additional SIP processes?

In the cold wintertime orographic clouds explored in Chapters 3 and 4 of this thesis, two additional SIP processes (besides BR) were incorporated and investigated within the Morrison microphysics scheme of WRF. The DS process was deemed inefficient in both examined cases, primarily due to the simulated raindrops not reaching the critical size threshold of 50 µm required for its activation. This observation aligns with the findings of mesoscale simulations of Alpine clouds (Dedekind et al., 2021). However, it also raises questions about whether the bulk representation of this mechanism hinders its activation. For instance, larger-scale models employing a bin-emulated framework to represent DS (Sotiropoulou et al., 2022; Zhao & Liu, 2022) have reported a more significant contribution of this mechanism, albeit at a higher computational cost. Considering this, an interesting next step would be to implement a similar approach in WRF to assess the sensitivity of DS process representation and

evaluate the potential increase in computational cost. Since DS is considered important even at warmer subzero temperatures, it would be intriguing to investigate whether the model can replicate the recirculation theory proposed by Korolev et al. (2020) and observed by Lauber et al. (2021).

We showed that SUBBR can also be activated in the case of an external seeder-feeder event when a subsaturated air layer separates the seeder from the feeder cloud (Chapter 4). The effectiveness of this process, however, depends on the depth of the subsaturated layer and the presence of fast convective downdrafts capable of swiftly transferring the small ice fragments generated into the supersaturated cloud conditions prevailing in the feeder cloud before they sublimate. While this mechanism is not expected to be as prevalent as BR in stratiform conditions, its significance may be more pronounced under deep convective downdrafts (Deshmukh et al., 2022). Evaluating its efficiency through NWP simulations of more convective cloud systems would thus be instructive.

What is the contribution of blowing snow ice particles?

Applying a constant source of ice particles to the first atmospheric level of WRF provided a simplified yet educative approach to investigate the microphysical impact of blowing snow particles in the simulated alpine clouds (Chapter 3). Our findings suggested that blowing snow has the potential to increase surface ICNCs even in the absence of a low-level cloud. However, its contribution becomes particularly notable when lofted particles mix with supersaturated cloud conditions. In these conditions, they can efficiently interact with liquid-phase particles, substantially contributing to SIP through collisions with larger precipitating ice particles.

A new blowing snow scheme, previously tested in a coupled WRF-snowpack model known as "CRYOWRF" revealed that blowing snow particle concentrations reaching up to 10^{-2} kg kg^{-1} can be induced up to ~1 km above the ground in alpine regions (Sharma et al., 2023). Since these particles can effectively trigger various microphysical processes, enhancing CRYOWRF with SIP descriptions and testing the combined effect of the two mechanisms in snow-covered regions with complex orography would offer an intriguing opportunity for a more comprehensive exploration of snow-atmosphere interactions.

Accomplishment 3: A synergistic approach to identifying secondary ice production in ground-based radar observations

Motivation, analysis & results

In Chapter 4 of this thesis, our primary goal was to detect potential SIP signatures from radar observations, including standard radar moments and full Doppler spectra. A significant body of literature has explored multi-frequency, polarimetric radar measurements within the HM temperature zone. In this temperature range, a recurring pattern associated with HM becomes evident in the Doppler spectrograms: a fast-falling rimer population falls through a supercooled liquid water layer, and upon entering the HM zone, a distinct spectral mode emerges, indicating the formation of columnar ice particles (e.g., Billault-Roux et al., 2023; Oue et al., 2015). A more systematic examination of SIP, focusing on temperatures higher than -10°C, was presented by Luke et al. (2021). They suggested that the presence of large drizzle drops was necessary for observed ice enhancements in Arctic clouds, pointing to the prevalence of DS over HM. However, identifying SIP fingerprints at colder subzero temperatures has been relatively unexplored, which motivated the Chapter 4 study.

We centered on the DGL temperature regime (between -20 and -10°C), demonstrated that even without polarimetric and multi-frequency radar observations, valuable information about SIP occurrence can be deduced through a direct comparison of single-frequency radar observations with outputs from a forward radar simulator coupled with high-resolution numerical simulations that account for SIP. Spectral bi-modalities within the DGL are frequently associated with new ice formation. From a modeling perspective, we demonstrated that these spectral signatures coincide with the initiation of aggregation and BR in the model, signifying the key role of collisions involving delicate dendritic or aggregated crystals. A competition between the two processes determines the final simulated ICNCs in this temperature regime, with ice crystal production due to BR sometimes exceeding their loss due to aggregation by up to an order of magnitude.

The emergence of a secondary spectral mode below approximately -18°C systematically coincided with an increase in observed spectral skewness, suggesting asymmetric broadening of radar spectra due to the slower-falling hydrometeor population. The link between BR, aggregation, spectral bi-modality, and positive skewness observed in the DGL was also highlighted in a 3-month radar-based study of mid-latitude winter clouds (von Terzi et al., 2022). This underscores the importance of a more systematic analysis of radar signatures within this cold subzero temperature range to establish a more robust conclusion about whether these signatures can indeed help infer the action of BR.

Perspectives

In Chapter 4, our analysis highlights the promising coupling between high-resolution numerical modeling and remote sensing through forward radar simulation tools. These tools have already proven effective in evaluating the performance of Polar WRF in capturing snowfall and mixed-phase cloud microphysics over Antarctica (Vignon et al., 2019, 2021). Our study demonstrates the potential of this synergy for identifying various microphysical processes, including SIP. The next step involves expanding our analysis beyond the limited spatial and temporal scales considered here, to establish the statistical significance of the identified signatures. For instance, confirming that extended regions of positive skewness in the DGL (as shown in Figure 4.2d) consistently indicate the presence of SIP through BR would be a significant realization. This is because timeseries of radar moments from various campaigns worldwide can be more readily available and easier to analyze compared to full Doppler spectra, especially when focusing to large-scale, statistical applications. Leveraging the wealth of ground-based remote sensing data, even in remote Arctic (e.g., Luke et al., 2021) and Antarctic regions (e.g., Ferrone & Berne, 2023), this methodology provides valuable insights that would have otherwise been challenging to obtain. The bottom line is that modeling techniques such as SIP-aware NWP models coupled with forward simulators (e.g., Trömel et al., 2021) offer a promising means to bridge the gap between remote sensing retrievals and the underlying physical mechanisms, helping to support hypotheses and pinpoint discrepancies in the representation of SIP-physics within numerical models.

Accomplishment 4: Representing secondary ice production in large-scale models using a machine-learning framework

Motivation, analysis & results

As previously discussed, implementation of sophisticated SIP parameterizations in models comes with certain assumptions that need to be made and a number of uncertain parameters that need to be

prescribed – if not explicitly resolved by the model. Having already incorporated the most detailed physically-based SIP descriptions in the model, we decided to take a step back and soke to simplify the SIP representation. With this objective in mind, a novel ML framework was introduced in Chapter 5, with the purpose to streamline the integration of SIP into large-scale models that have limited horizontal resolution and lack detailed physics for explicit SIP representation. This framework builds upon the microphysics code developed in Chapter 3 and utilizes a comprehensive training dataset derived from multi-year panarctic regional climate simulations. Employing ML techniques on this dataset, we developed a data-driven SIP parameterization called RaFSIP, which is available as open-source software.

RaFSIP can be applied in both offline and online modeling contexts. Its modular design facilitates seamless integration into the bulk microphysics schemes of models with double-moment representations of ice hydrometeors and horizontal grid spacings equal to or greater than 10 km. Using only a few predictors commonly described in most host models, RaFSIP effectively predicts the cumulative impact of the three primary SIP processes – HM, BR, and DS – in stratiform mixed-phase clouds within the temperature range of -25 to 0°C.

Limitations of the RaFSIP parameterization were already addressed in Chapter 5. Trained exclusively on polar stratiform conditions, RaFSIP may not be universally applicable to global MPCs, especially the convective ones. Nevertheless, in most large-scale models, stratiform and convective clouds are represented by distinct microphysical schemes. Therefore, the applicability of RaFSIP should be restricted to the stratiform routine. This highlights the need to expand the training dataset by incorporating simulations from diverse global locations where SIP effects are observed. The extension of the training dataset could also involve the inclusion of additional SIP processes, such as sublimational break-up, whose efficiency is expected to increase under more convective conditions. Nevertheless, one advantage of ML-driven microphysical parameterizations is the flexibility in augmenting their training dataset with diverse cases and processes. Specifically for RaFSIP, we demonstrated that only a relatively few regional climate model grid points can be sufficient for effectively capturing the complex, non-linear relationships associated with SIP.

Legacy of this thesis and concluding thoughts

The effect of ice multiplication has been acknowledged in various contexts, spanning laboratory experiments, real-world atmospheric conditions, remote sensing observations, and atmospheric modeling. Throughout this PhD, we have introduced innovative methodologies and crafted research tools with the potential to revolutionize how ice multiplication is represented in weather prediction and global climate models. The developed modeling tools, such as the updated SIP-aware microphysics scheme of WRF, have already been adopted in collaborative studies to explore the role of SIP under various conditions in different types of MPCs, including stratocumulus-to-cumulus transitions (e.g., Karalis et al., 2022).

Fusing the detailed SIP descriptions in WRF with machine learning techniques gave rise to the RaFSIP parameterization – which is probably the most novel aspect of this PhD research. This is the first application of machine learning to parameterize ice microphysical processes in cold clouds. RaFSIP has already been successfully integrated into the microphysics schemes of three leading European GCMs, including NorESM2, EC-Earth, and ECHAM-HAM, and is planned to be used in the upcoming CMIP7 assessments. Its implementation within the stratiform microphysics routines of these GCMs ensures both computational efficiency and numerical stability. Yet, for a comprehensive understanding of the global impact of SIP, it needs to be treated in other cloud types, particularly cumulus and convective clouds, which currently lack adequate microphysical representations, especially within climate modeling applications.

Furthermore, evaluation of the robustness of the RaFSIP scheme is currently underway, through a model intercomparison project encompassing the aforementioned GCMs. This collaborative effort is organized within the framework of the European Union Horizon 2020 project FORCeS (https://forces-project.eu/), as detailed by (Ickes et al., 2023). In Chapter 5 we demonstrated the performance of RaFSIP against the conventional SIP parameterizations, that it has been trained on. What remains to be assessed is how each GCM responds to the inclusion of SIP, and whether SIP can reduce predictive biases in models, leading to more accurate representations of ice- and liquid-phase partitioning in MPCs, as confirmed by satellite observations. These key questions will be addressed within the context of the model intercomparison project – an avenue underscored in the recommended future directions proposed by Field et al. (2017) to advance SIP knowledge. Quantifying the parametric uncertainties across the microphysics schemes of different models offers the most robust way to assess the performance of newly developed parameterizations.

It is important to acknowledge that ML methods come with inherent limitations. These limitations can arise from their lack of interpretability, their inability to extrapolate beyond the original training dataset, or their difficulty in satisfying physical constraints. However, recent advances have already paved the way for improving model explainability (e.g., Brenowitz et al., 2020) and post-prediction adjustments can be applied to enhance stability or physical consistency within ML frameworks (Rasp, 2020; Yuval et al., 2021). Extrapolation is likely to remain one of the most persistent limitations of ML parameterizations, which is particularly relevant for more accurate future predictions in a warming climate. However, O'Gorman and Dwyer (2018) demonstrated that, application of a random forest algorithm to parameterize moist convection and precipitation extremes can accurately capture climate change, provided that the training dataset includes samples from both the current climate and a warmer climate scenario.

Overall, the methodological approach developed in this PhD defines a new paradigm for model development. Running complex or high-resolution versions of models for limited periods of time or areas can generate extensive datasets, upon which ML algorithms can then derive data-driven parameterizations for use in simpler models. Replacing, for example, computationally expensive microphysical parameterizations with their ML counterparts can lead to simpler model versions that run a lot faster, yet behave as if they had the complex physics in them. This approach counters other model simplification methods, which may involve entirely removing or prescribing constant or climatological values for processes that the model is not sensitive to (Proske et al., 2022, 2023). The future will determine which approach, or combination thereof, would lead to the best compromise between computational efficiency and physical robustness.

Beyond its modeling applications, the adaptable nature of the ML-based perspective we propose, may be useful for diagnosing SIP contributions from field campaign measurements. Examining the input features required for RaFSIP to predict the presence of SIP, it becomes evident that with knowledge of prevailing temperature, relative humidity, ice and liquid water content, and an estimate of riming, RaFSIP can be trained and applied to data from field campaigns. Among these variables, deriving the degree of riming from field observations is the most challenging. However, recent research has demonstrated the value of ML techniques in estimating riming from ground-based, zenith-pointing cloud radar measurements (Vogl et al., 2022). Once all predictors are defined, ice enhancement factors can be derived either through concurrent measurements of ICNCs and INPs or through retrievals using collocated ground-based remote sensing data (Wieder et al., 2022). A synthesis of in-situ, remote-sensing, and ML techniques therefore holds promise for detecting SIP in field or remote sensing observations worldwide. Such an automated method for identifying SIP favorable conditions and regions could provide datasets for model evaluation, offering better observation-based SIP insights across scales. This might eventually lead to the generation of an updated "conceptual diagram", akin to those in Sullivan, Hoose, et al. (2018; see their Figures 8 and 9), which can be used to diagnose SIP presence if all necessary and sufficient criteria are met.

All modeling experiments conducted within this PhD consistently underscored the significance of seeder-feeder cloud configurations, whether internal or external, as crucial atmospheric conditions for triggering SIP. Satellite and ground-based remote sensing observations have further substantiated the prevalence of such cloud structures, occurring at an annual rate of approximately 20-30% in both the Alpine region and the Arctic (Proske et al., 2021; Vassel et al., 2019). If SIP is primarily induced by ice seeding in multilayer cloud systems, then quantifying global ice seeding frequency and patterns could offer an initial, albeit approximate, assessment of SIP-related events worldwide. This is important, as the global significance of SIP has received limited attention in existing literature. Notably, the modeling study by Zhao and Liu (2021) revealed that the distribution of SIP lacks a pronounced latitudinal preference, in stark contrast to primary ice production rates, which are two orders of magnitude higher in the Northern Hemisphere. Do the models accurately capture the distribution and frequency of occurrence of multilayer seeding clouds, and does it align with regions of enhanced SIP rates?

Another aspect requiring attention is the relative contribution between SIP and PIP, and how this may be changed in a warming climate. A number of studies have reported a minimum threshold of INPs necessary to trigger SIP under varying cloud conditions (e.g., James et al., 2023; Sullivan, Hoose, et al., 2018). At the same time there exists a competitive and non-linear interplay between SIP and PIP in MPCs (e.g., Zhao & Liu, 2022). Elevated number of INPs can cause rapid cloud glaciation via the efficient action of WBF, thereby diminishing the number of large precipitation particles that would otherwise promote SIP. Conversely, enhanced SIP has been observed to suppress PIP by depleting the cloud droplets needed for initiating heterogeneous freezing. In a warming world, reduced sea ice concentrations in high latitudes may release higher INP concentrations in the atmosphere due to increased biogenic emissions from the open ocean (Carlsen & David, 2022), eventually increasing the number of available INPs. This raises a compelling question: could this feedback mechanism dampen SIP and would this behavior be captured by GCMs – given that they still lack description of ice multiplication and the dominant INP species, particularly at low to moderate supercooling? These complexities inherent in ice-related processes within MPCs underscore the urgent necessity for the cloud physics community to join forces and improve their representation in GCMs. This is important for improving the accuracy of future climate projections. The tools developed within this PhD research, hold significant promise in contributing to this pressing scientific effort.

Appendices

A. Supplementary material for: On the drivers of droplet variability in alpine mixed-phase clouds

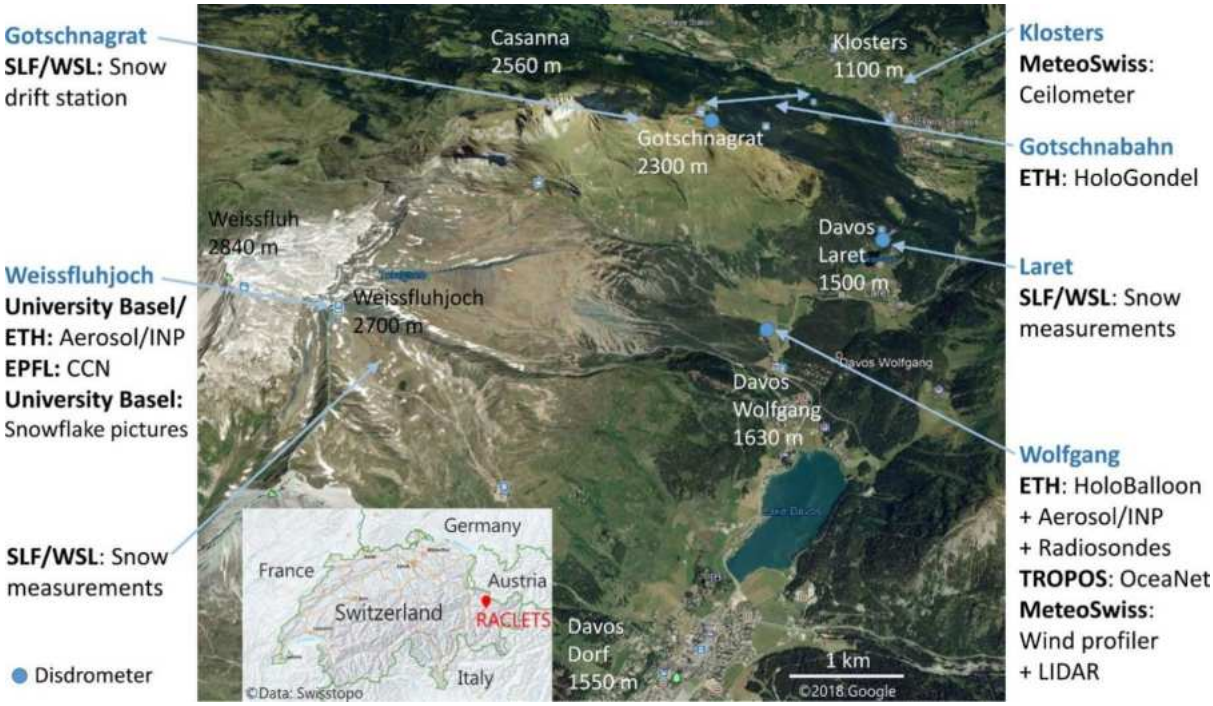

Figure A1. Location of the main measurement sites of the RACLETS 2019 campaign. The main measurement sites considered in this study are Davos Wolfgang (otherwise known as Wolfgang-Pass, WOP; 1630 m a.s.l., 46°50'08.076"N 9°51'12.939"E) and the mountain-top station of Weissfluhjoch (WFJ; 2700 m a.s.l., 46°49'58.670"N 9°48'23.309"E).

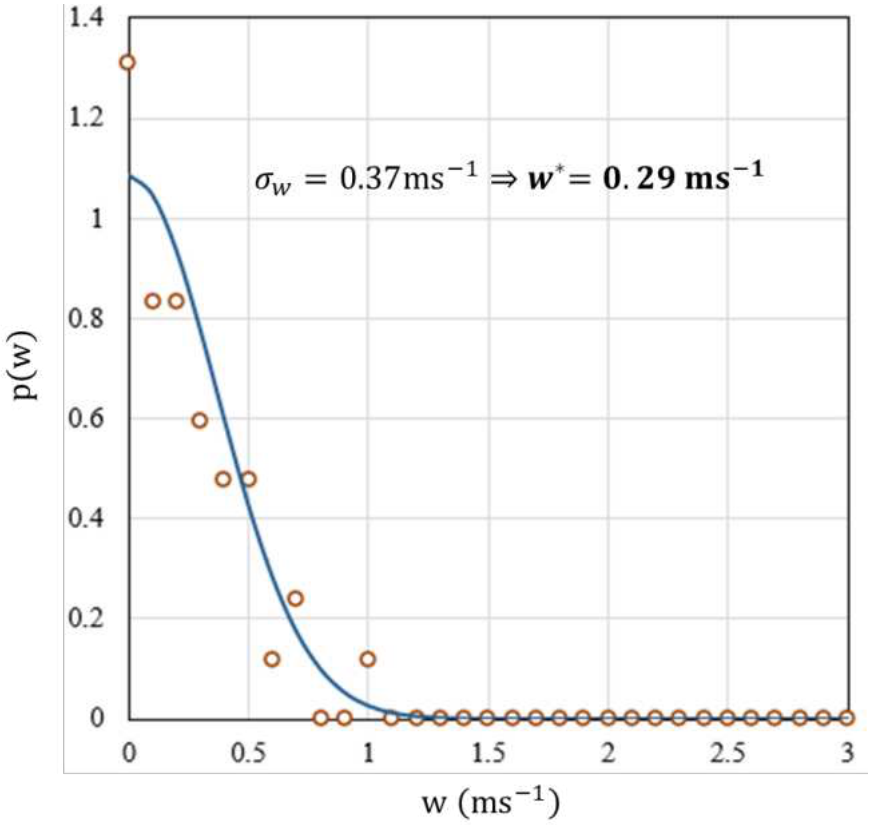

Figure A2. Example of the fitting of positive vertical velocities to a half-Gaussian probability density function, p(w). The standard deviation of the distribution, σ_w, is then used within the droplet activation parameterization to calculate the characteristic vertical velocity, $w^*=0.79\sigma_w$ (Morales and Nenes, 2010), which is employed to provide the distribution-averaged cloud droplet number (N_d). The data presented here were collected at WOP and span the hourly time period between 17:00-18:00 UTC on 24 February 2019.

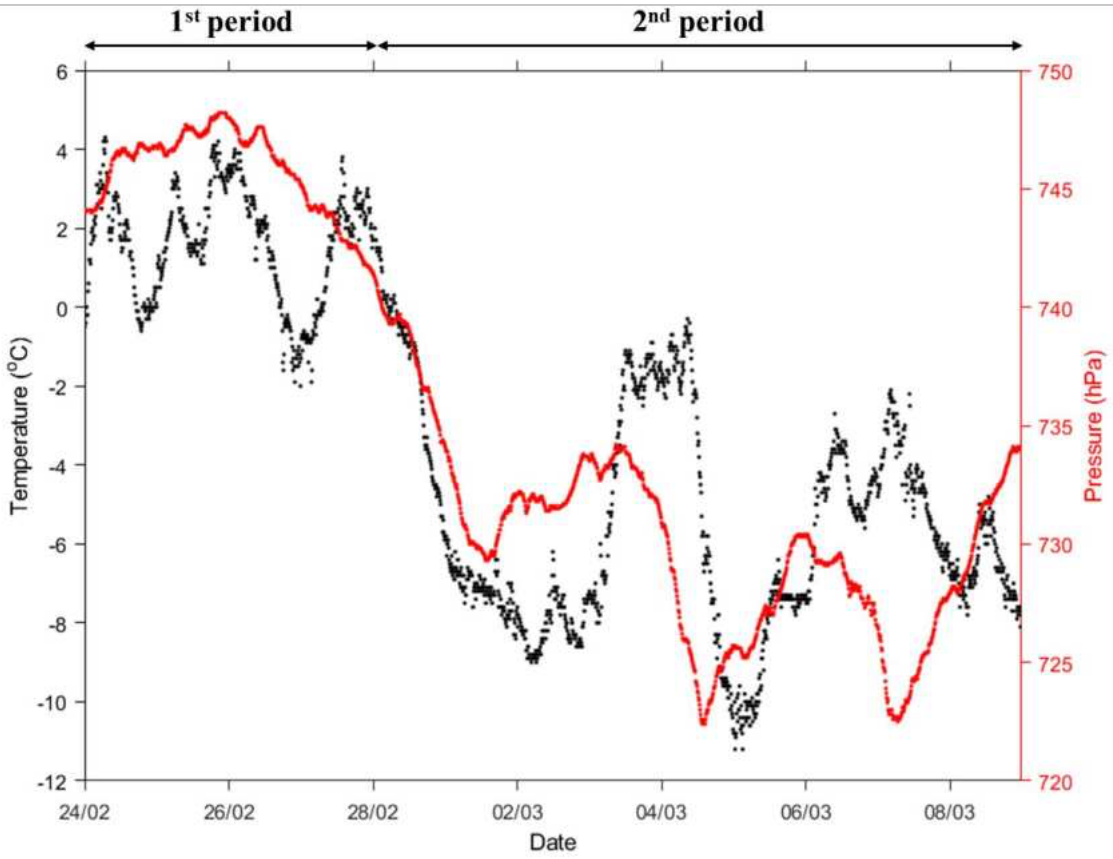

Figure A3. Air temperature 2 m above ground (˚C) (black dots) and pressure at station level (hPa) (red dots) obtained from the MeteoSwiss observation station at WFJ between 24 February and 8 March 2019.

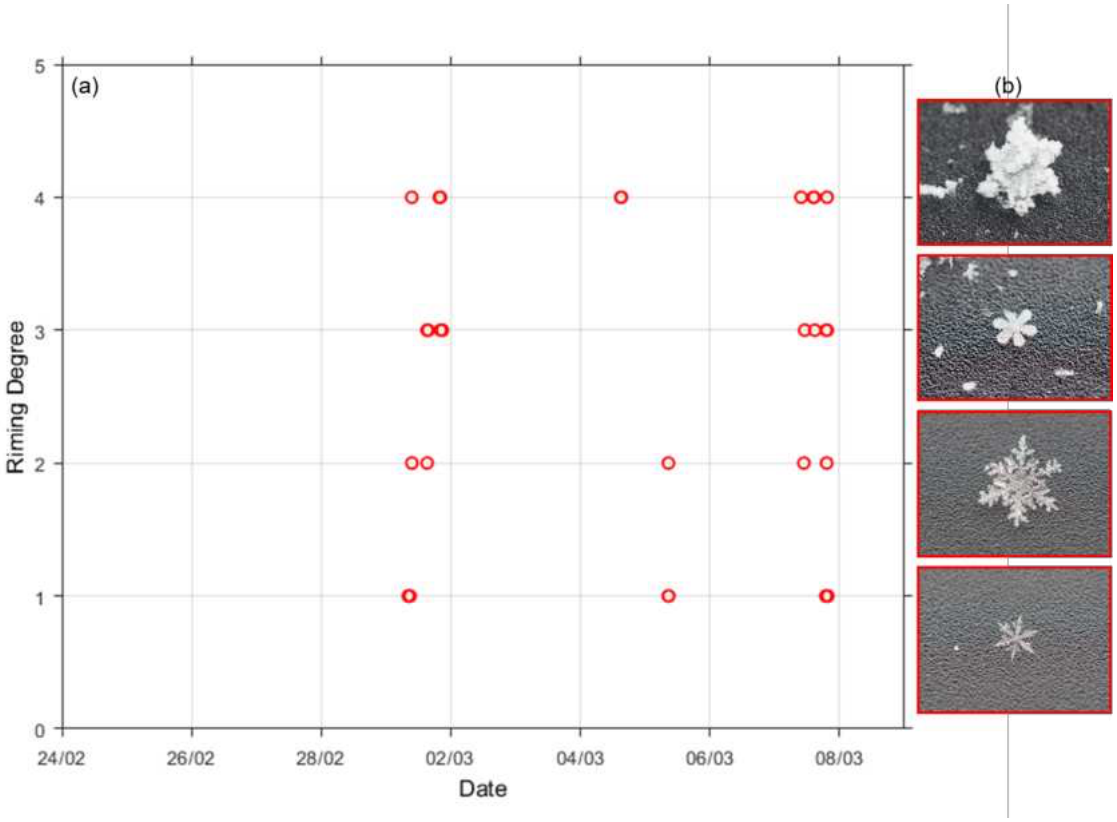

Figure A4. (a) The estimated degree of riming of the analyzed dendritic ice crystals collected at WFJ during the period of interest and (b) characteristic images of the dendrites representing the four recorded riming categories varying from 1 (bottom figure) to 4 (top figure). Following Mignani et al. (2019), dendritic crystals were collected on a plate and documented by photography. The resulting images were analyzed visually for a riming degree according to Mosimann et al. (1994). A riming degree of 1, 2, 3, 4 represents lightly, moderately, densely or heavily rimed ice particles, respectively.

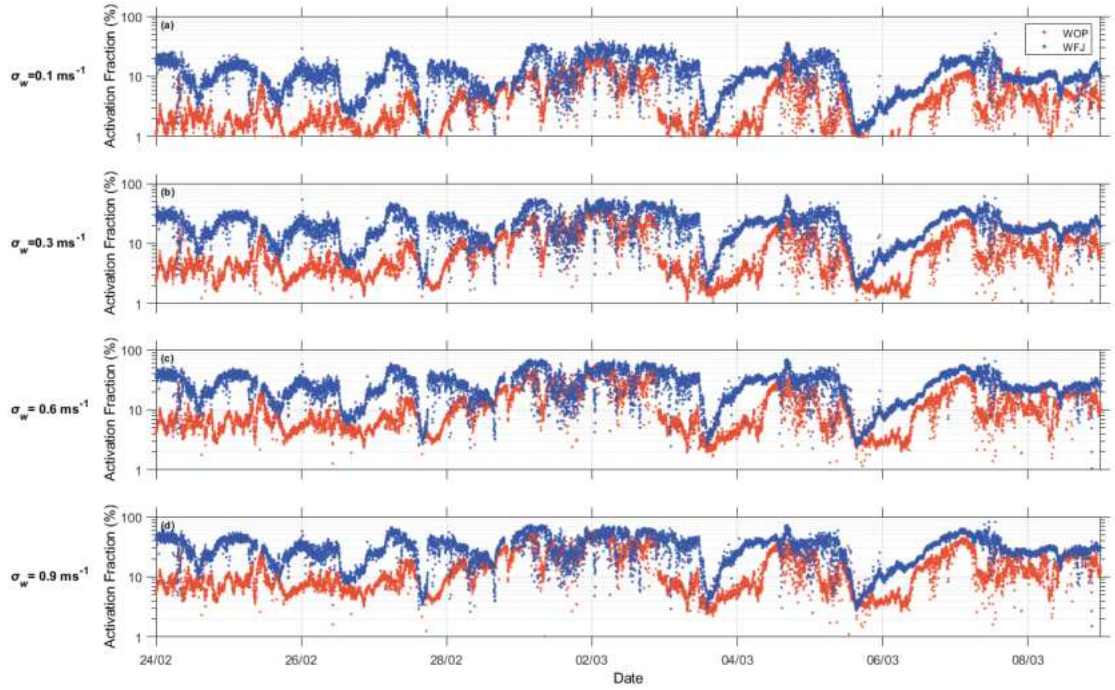

Figure A5. Calculated timeseries of the activation fraction (%) (i.e. the fraction of total aerosol particles that have been activated to form cloud droplets), for updraft velocities of σ_w = 0.1 m s^{-1} in a, 0.3 m s^{-1} in b, 0.6 m s^{-1} in c, and 0.9 m s^{-1} in d, during the period of interest at WOP (orange dots) and WFJ (blue dots).

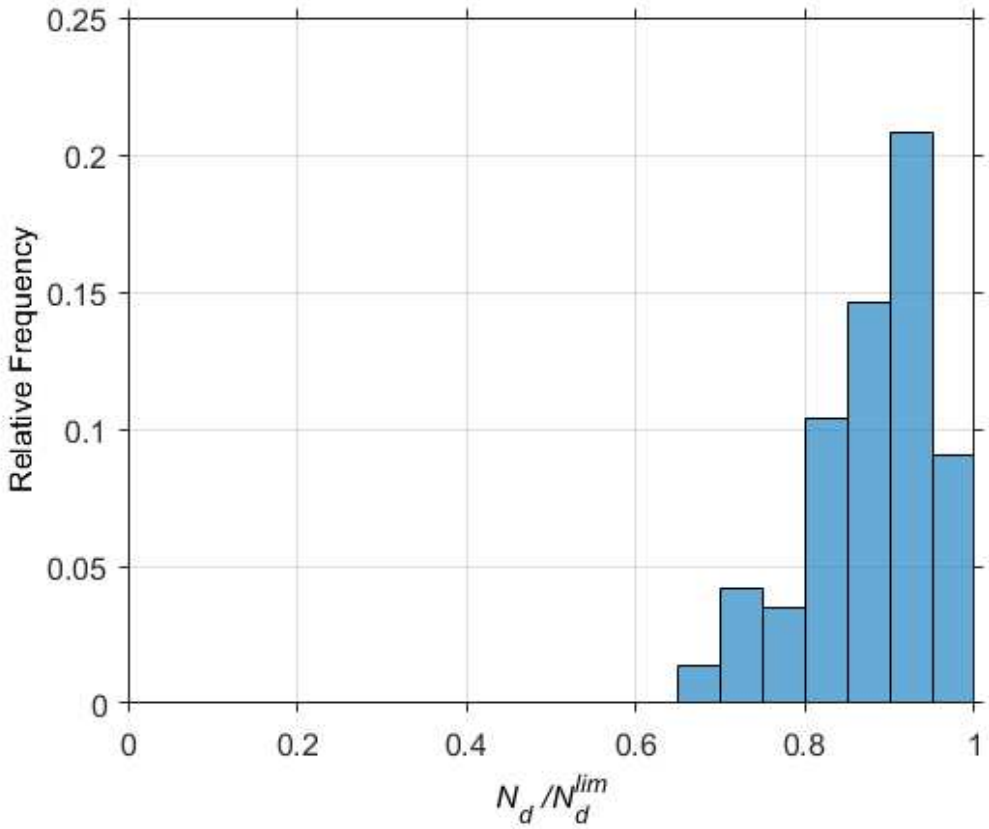

Figure A6. Relative frequency histogram of the ratio of predicted N_d to the limiting droplet number (N_d^{lim}), as calculated for both measurement sites, restricted to the periods when the predicted in-cloud maximum supersaturation (S_{max}) drops below 0.1%, indicating the transition from the aerosol- to the velocity-limited droplet activation regime.

B. Supplementary material for: Secondary ice production processes in wintertime alpine mixed-phase clouds

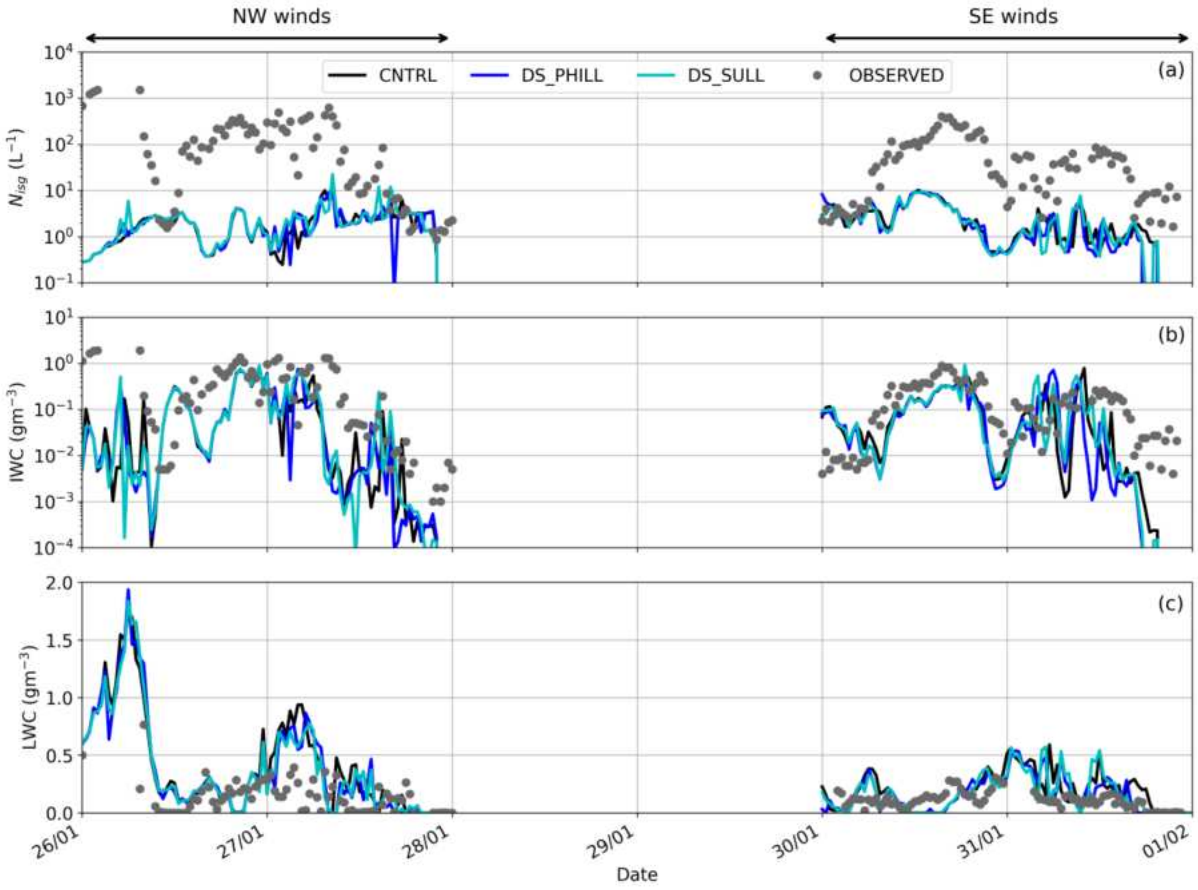

Figure B1. Timeseries of (a) total ice number concentrations (N_{isg}; cloud ice + snow + graupel), (b) ice water content (IWC) and (c) liquid water content (LWC), predicted by the control simulation of WRF (CNTRL; black line) and the two sensitivity simulations including a description of the droplet shattering (DS) process, parameterized following Phillips et al. (2018) (DS_PHILL; blue line) and (Sullivan, Hoose, et al., 2018) (DS_SULL; cyan line). The grey dots in (a), (b) and (c) represent the respective measurements of N_{isg}, IWC and LWC, taken between 26 January and 1 February 2014 at Jungfraujoch (JFJ) at an altitude of 3580 m above sea level (a.s.l.). Each day starts at 00 UTC. Note the logarithmic y-axes in panels a and b.

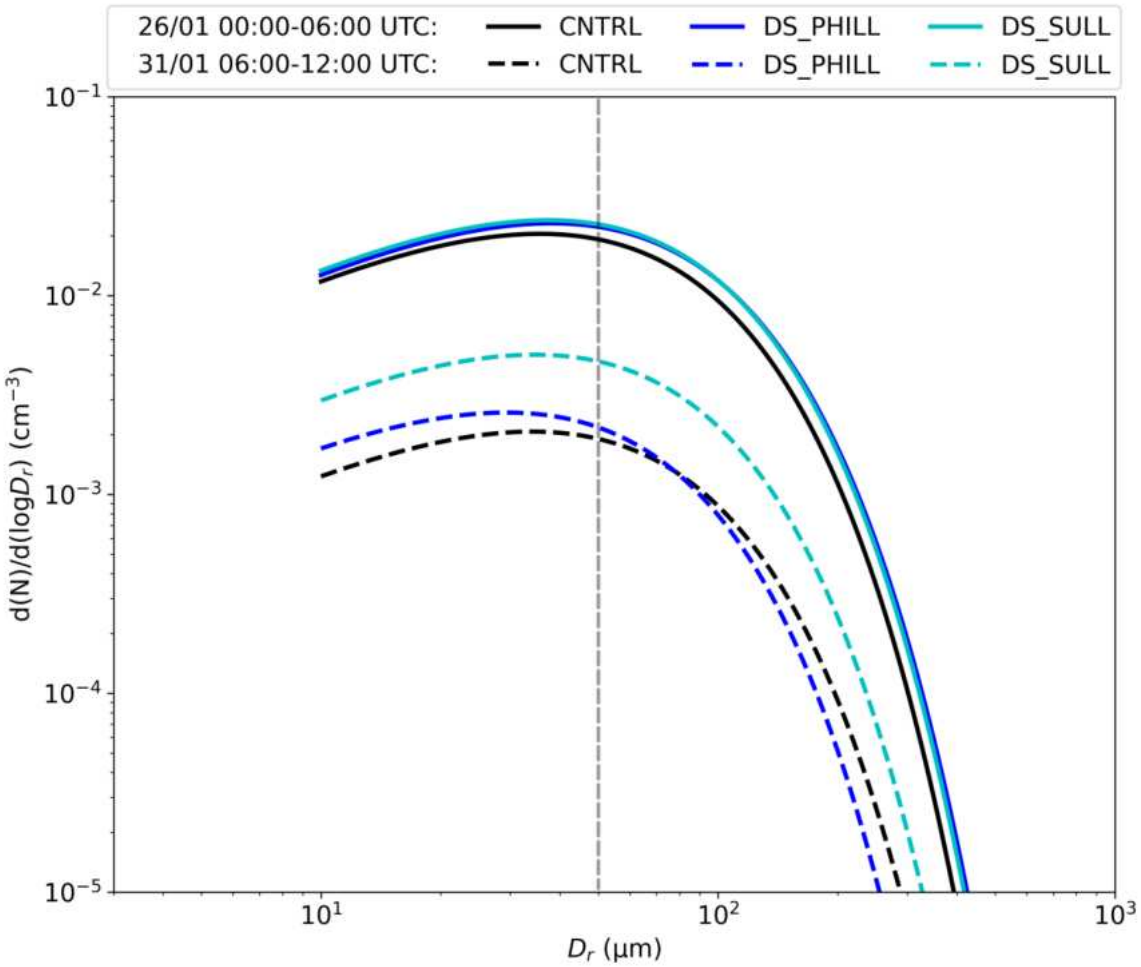

Figure B2. Size distribution of raindrops predicted by the CNTRL, DS_PHILL and DS_SULL simulations. The size distributions were averaged between 00:00 and 06:00 UTC on 26 January (solid line) and between 06:00 and 12:00 UTC on 31 January (dashed line). The vertical dashed grey line indicates the threshold size of 50 µm, which is required for DS to be activated.

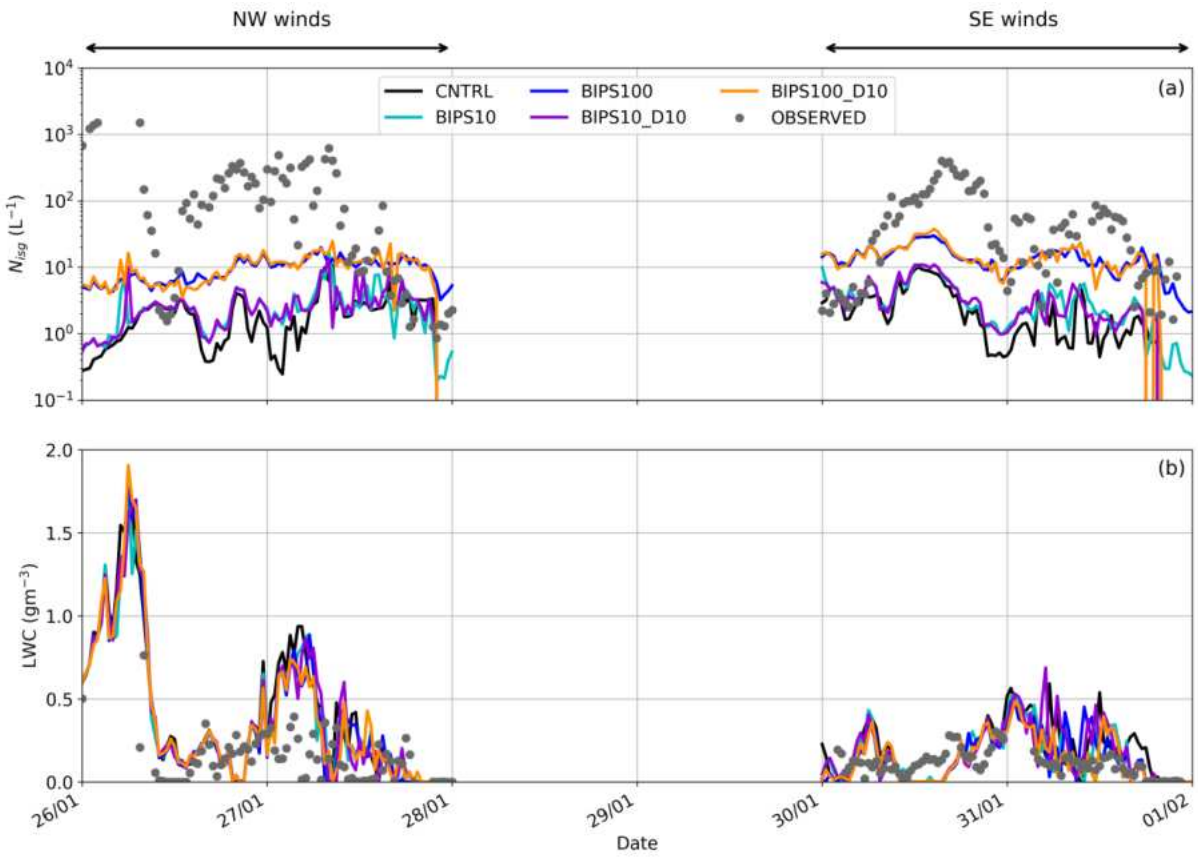

Figure B3. Time series of (a) total N_{isg} and (b) LWC, predicted between 26 January and 1 February 2014 by the sensitivity simulations including a source of ice crystals in the first atmospheric level to represent the microphysical effect of blowing snow ice particles (BIPS). We consider spherical particles with sizes of 10 µm (suffix D10) and 100 µm. The applied concentrations are equal to 10 L^{-1} in BIPS10 (cyan line) and BIPS10_D10 (purple line), and 100 L^{-1} in BIPS100 (blue line) and BIPS100_D10 (orange line).

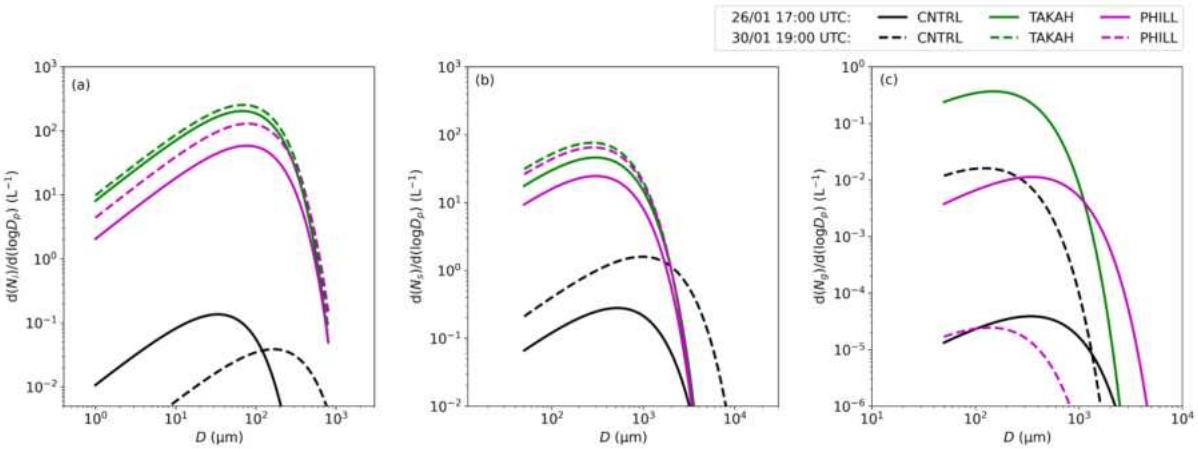

Figure B4. Size distribution of (a) cloud ice, (b) snow and (c) graupel particles, predicted by the CNTRL and the two sensitivity simulations including a description of the ice-ice collisional break-up (BR) process, parameterized following Sullivan, Hoose, et al. (2018) based on the laboratory findings of Takahashi et al. (1995) (TAKAH; green line) and Phillips et al. (2017a) (PHILLL; magenta line). The size distributions were taken at 17:00 UTC on 26 January (solid line) and at 19:00 UTC on 30 January (dashed line).

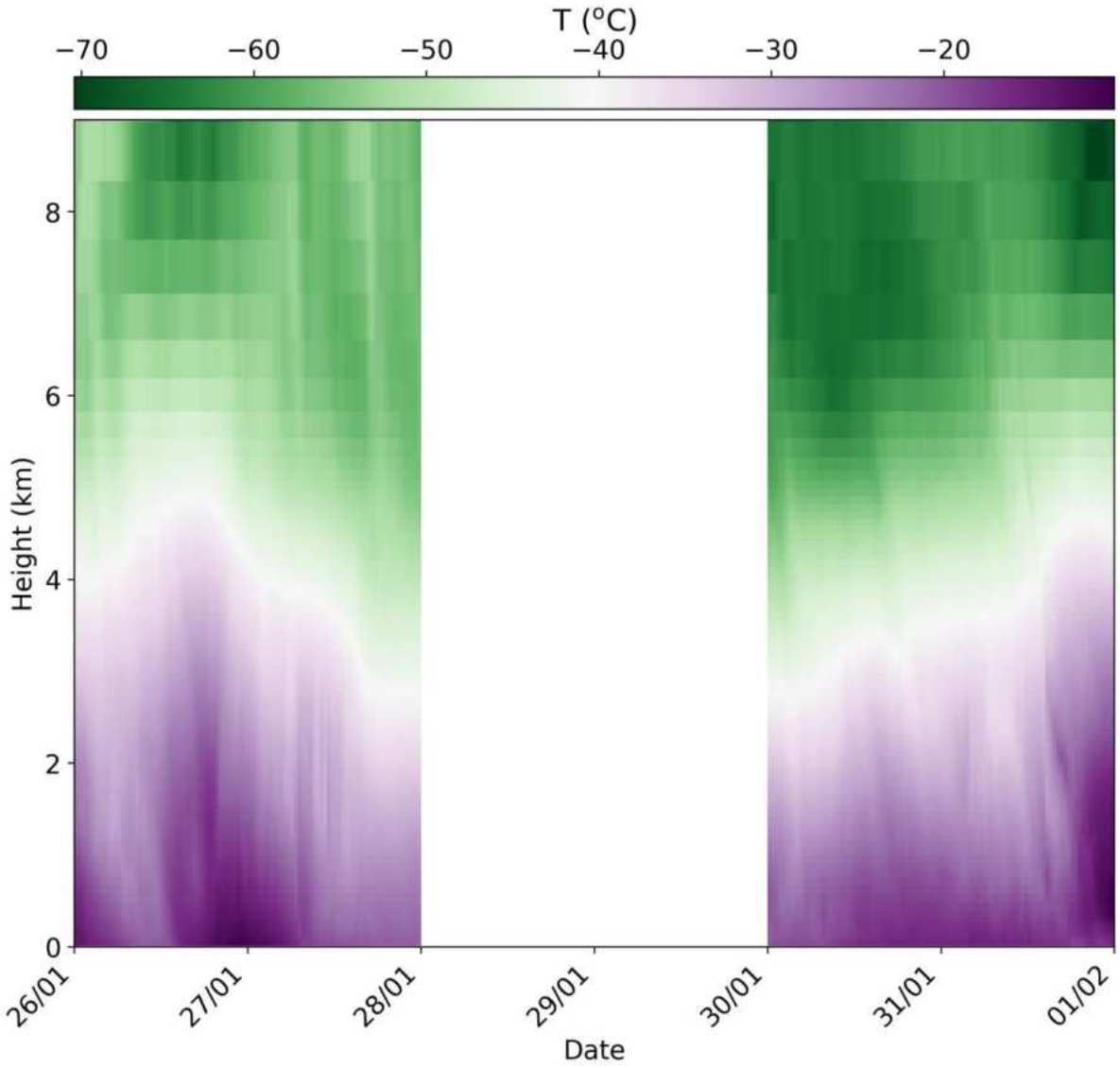

Figure B5. Height-time cross-section of temperature (T in °C) simulated from 26 January to 1 February 2014 by the CNTRL simulation at JFJ. The height is given in kilometers above ground level (hereafter km AGL).

TEXT B1:

During CLACE 2014, a polarimetric Doppler weather radar was deployed at Kleine Scheidegg (2061 m a.s.l; Grazioli et al., 2015). This compact system, operating at the X-band frequency is particularly well suited to provide high resolution data of the vertical structure of precipitation in complex terrains, including narrow Alpine valleys (Schneebeli et al., 2013). The radar was continuously operating with a scanning protocol of about 5 minutes including various types of scans in different directions. As the vertical structure of precipitation and its evolution in time is of particular interest for the present work, we used the data collected at various height levels along a transect in the direction of Grindelwad, roughly northeasterly with respect to the radar. Along this transect the quality of the data was only marginally affected by the clutter of the high mountains nearby and therefore a continuous depiction, in time and in space, of the vertical structure of precipitation (above the radar installation height) could be obtained.

Polarimetric data can be used to estimate the type of hydrometeors that dominates the signal within each radar resolution volume. We employed the hydrometeor classification method of Besic et al. (2018), which divides dry snowfall into three categories: crystals, when individual and relatively small crystals dominate; aggregates and rimed ice particles, including graupel and heavily rimed snow.

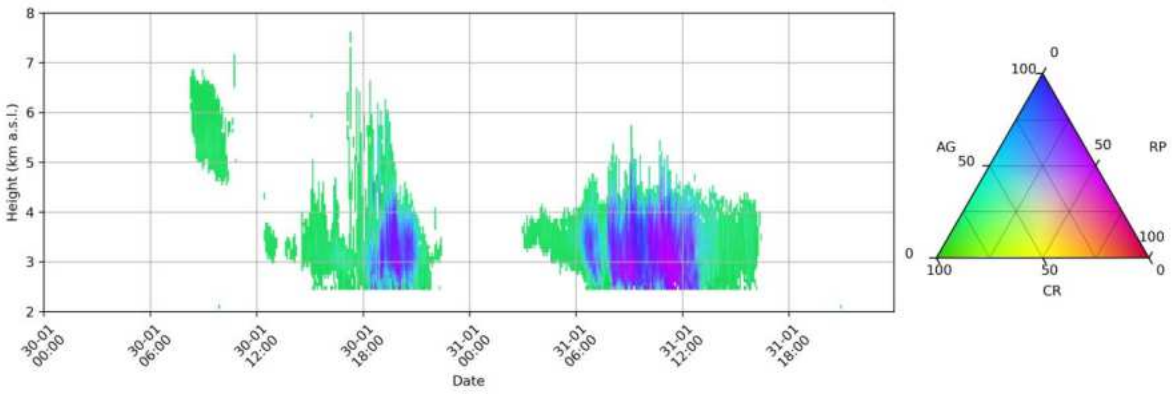

Figure B6. Radar-based hydrometeor classification between 30 and 31 January. Dry snowfall is classified into three categories: aggregates (AG), individual crystals (CR) and rimed ice particles (RI). This data should be interpreted as representative of the overall behavior along a transect of 4 km length (from 2 to 6 km distance from the radar) in the northeasterly direction. The height is given in km a.s.l.

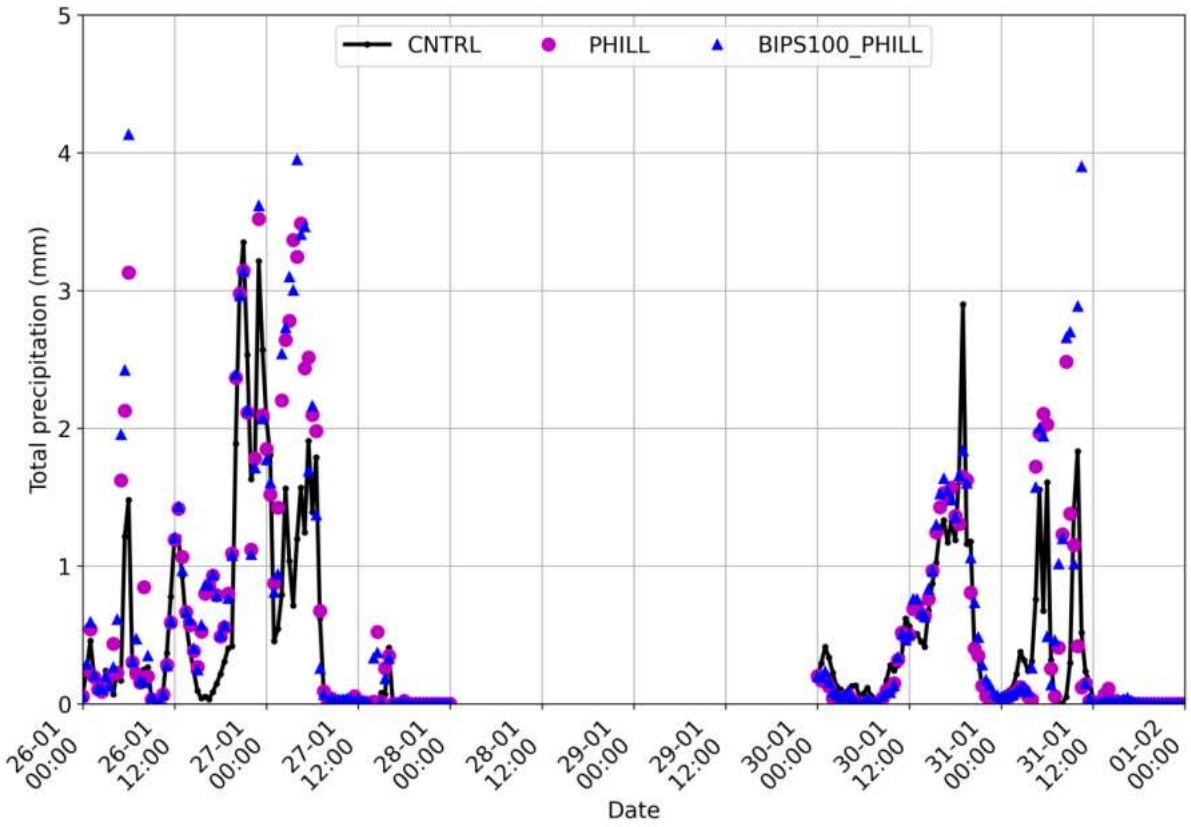

Figure B7. Total surface precipitation (rain + snow + graupel) produced by the CNTRL, PHILL and BIPS100_PHILL simulations. The latter represents the sensitivity simulation where the combined effect of blowing snow and ice-ice collisional break-up is examined.

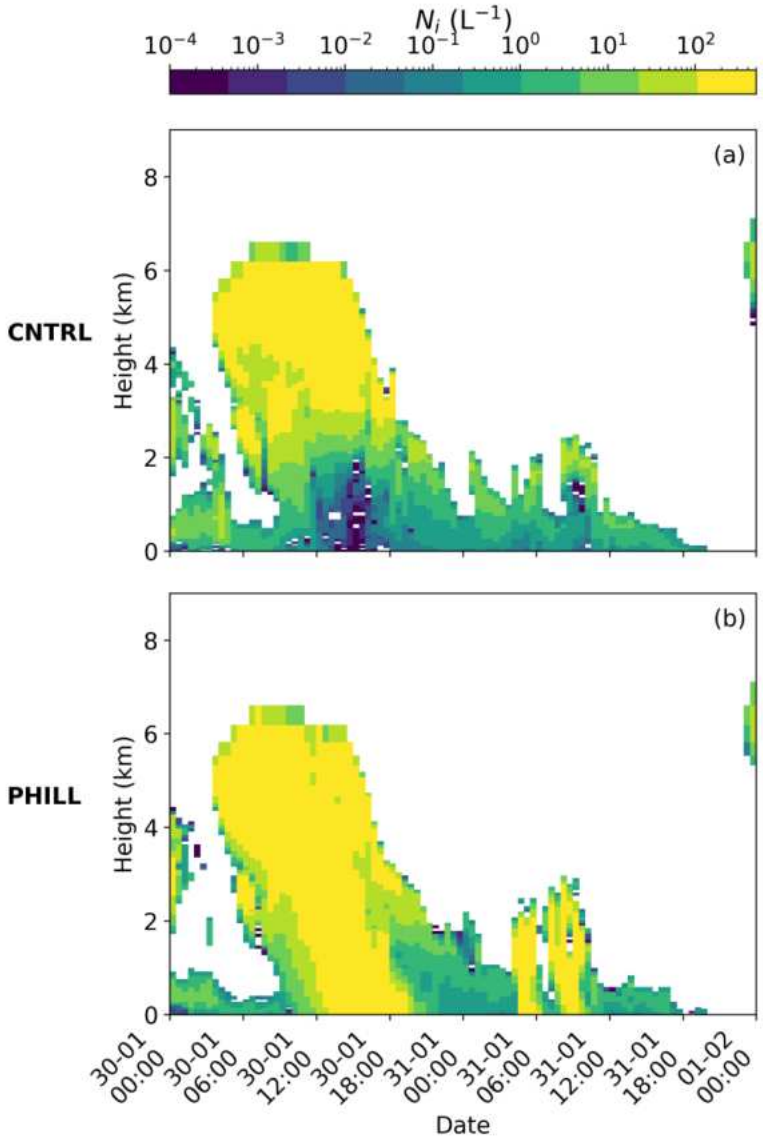

Figure B8. Time-height plots of cloud ice number concentrations (N_i) produced by (a) CNTRL and (b) PHILL simulations between 30 January and 1 February 2014. The height is given in km AGL.

C. Supplementary material for: Unraveling secondary ice production in winter orographic clouds through a synergy of in-situ observations, remote sensing and modeling

Introduction

This supplementary information provides additional figures supporting the detailed analysis included in the main manuscript.

Table C1. WProf properties and parameters. WProf uses three chirps, whose ranges are: chirp 0: 104-1,245 m, chirp 1: 1,267-4,191 m, chirp 2: 4,221-9,981 m.

Frequency (GHz)	94
Transmission	Frequency-modulated continuous wave (FMCW)
3-dB beam width (°)	0.53
Time resolution (s)	5
Range resolution (m)	7.5 / 16 / 32
Nyquist velocity (m s^{-1})	10.8 / 6.92 / 3.3

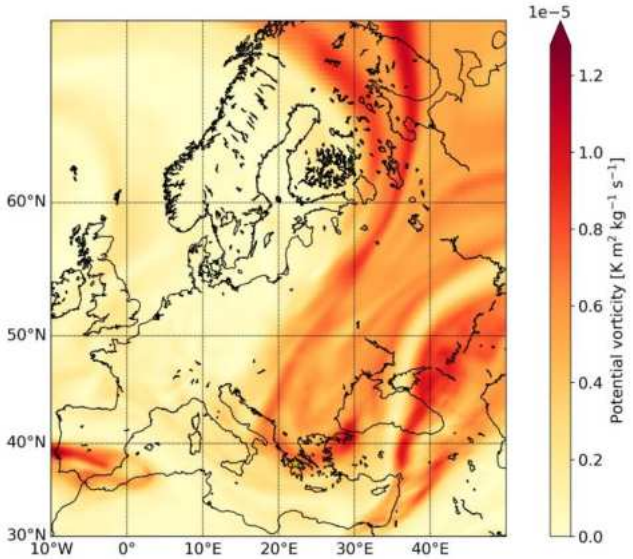

Figure C1. Synoptic situation at 22:00 UTC on 17 December 2021 from ERA5 data. The color shading represents the potential vorticity (in K m^2 kg^{-1} s^{-1}) at the 320 K isentrope. The location of Mount Helmos is indicated by the yellow star.

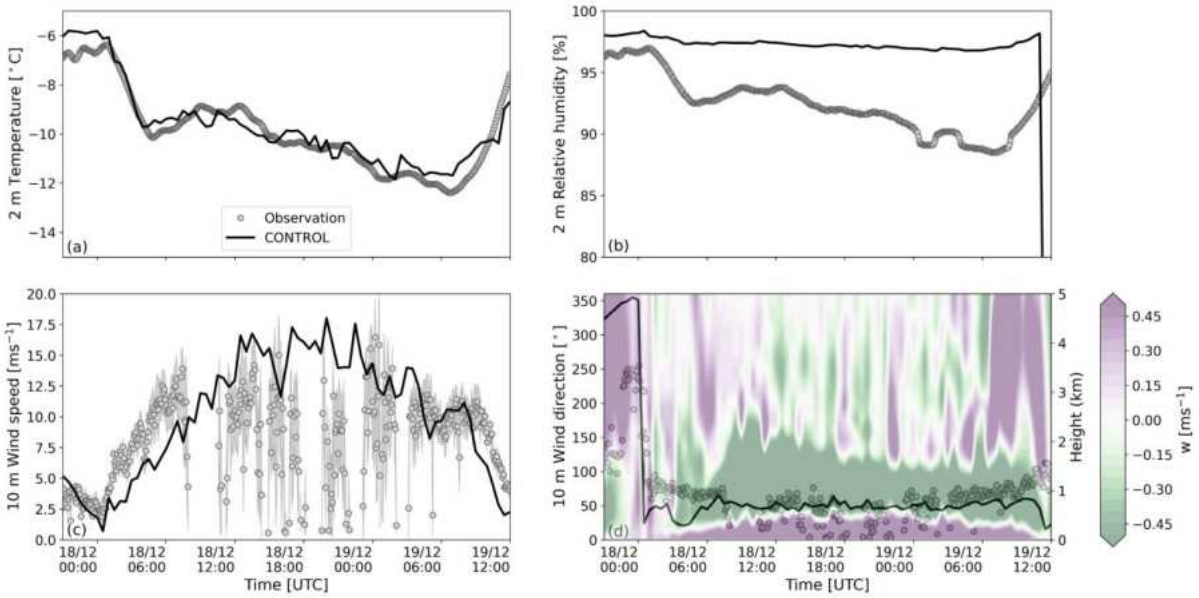

Figure C2. Time series of (a) temperature and (b) relative humidity with respect to liquid phase at 2 m height, (c) wind speed and (d) wind direction at 10 m height. Gray circles indicate measurements collected between 17 and 19 December 2021 at the Helmos Hellenic Atmospheric Aerosol and Climate Change (HAC)^2 station, while modeled values from the CONTROL simulation of WRF are shown with a black line. The semi-transparent contour plot represents the vertical velocity (w) profile predicted by CONTROL.

Text C1: INP measurements at (HAC)^2

The Portable Ice Nucleation Experiment (PINE) is an innovative instrument designed for ice nucleation studies and long-term field observations of ice nucleating particles (INPs) across a wide temperature range. During the Cloud-AerosoL InteractionS in the Helmos background TropOsphere (CALISHTO) campaign, PINE was operated at the mountain-top site of (HAC)^2. PINE employs a pumped expansion principle to generate ice and water supersaturated conditions for testing the ice nucleation ability of aerosol particles. The instrument operates in repetitive cycles, involving the sampling of aerosol into a pre-cooled cloud chamber, activation of aerosol particles as supercooled droplets and ice crystals through the expansion of air inside the chamber, and subsequent refilling of the cloud chamber with fresh aerosol for the next cycle. A more detailed description of the PINE instrument can be found in Möhler et al. (2021). The INP measurements presented in Figure C3 correspond to the period spanning one month, from the end of October to the end of November 2021.

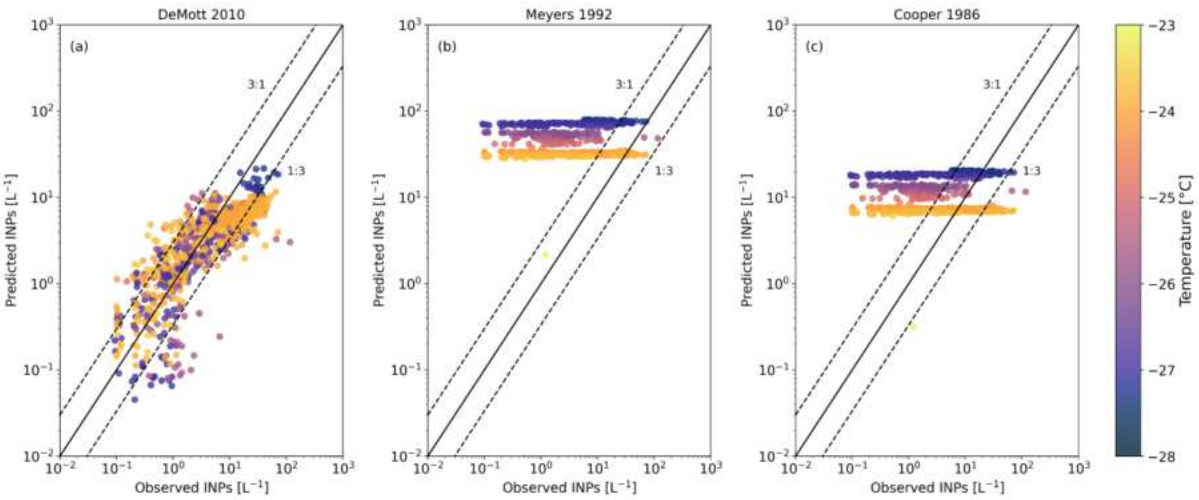

Figure C3. Scatterplot of the ice nucleating particles (INPs) predicted offline using the parameterized expressions developed by (a) DeMott et al. (2010), (b) Meyers et al. (1992), and (c) Cooper et al. (1986) vs the INPs measured at (HAC)2 station by the PINE instrument. The INP measurements are color-shaded based on the temperature (in °C).

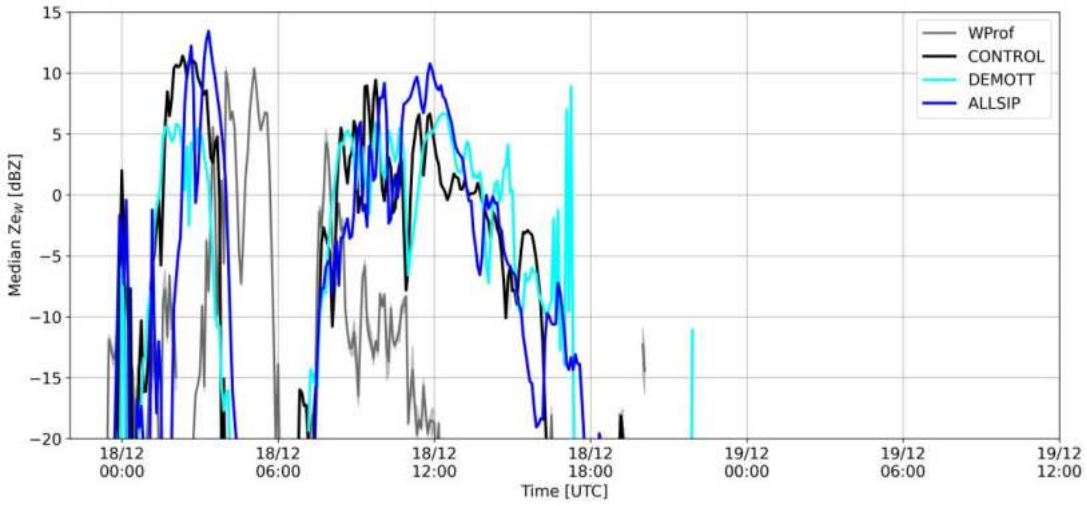

Figure C4. Median timeseries of the radar equivalent reflectivity factor (Ze_w) calculated at an altitude ranging from 1.8 to ~2 km on the atmosphere. Zew is derived from the WProf radar measurements (grey line) taken at "Vathia Lakka" (VL) station, and simulated by the CONTROL (black line), DEMOTT (cyan line) and ALLSIP (blue line) sensitivity simulations of WRF when coupled with the CR-SIM radar simulator.

Text C2: Modeling uncertainties during the low-level orographic cloud period

In the orographic cloud persisting after the passage of the seeder cloud (3rd turquoise box in Figure 4.2a), notable spikes of enhanced Ze_w are observed, which are not fully captured by the simulation that accounts for ice multiplication (Figure 4.2d), but are comparatively better reproduced by the CONTROL and DEMOTT simulations (Figures 4.2b, c). This is further supported by median profiles extracted from this period, wherein the predictions of the two simulations incorporating solely PIP parameterizations align more closely with the observations (Figure C5). The inefficiency of the ALLSIP simulation in replicating the observed Ze_w spikes might stem from uncertainties in the representation of implemented secondary ice production mechanisms within the bulk microphysics framework. For instance, Sotiropoulou et al. (2022) found that adopting an emulated bin framework for collisional break-up and droplet-shattering could enhance simulated ice multiplication rates, albeit with increased computational demand. Given the prevailing stormy conditions during the case study (Figure C2c), various surface-based processes such as blowing snow or detachment of surface hoar frost (Beck et al., 2018) could have potentially contributed to the observed instances of enhanced Ze_w close to the surface. Simplified methods to simulate such processes have been explored for orographic MPCs (Farrington et al., 2016; Georgakaki et al., 2022), yet it would be intriguing to explore more sophisticated and advanced modeling frameworks (Gerber et al., 2023; Sharma et al., 2023). To gain a deeper understanding of the microphysical processes involved, the subsequent analysis focuses on the results obtained from the WRF simulations.

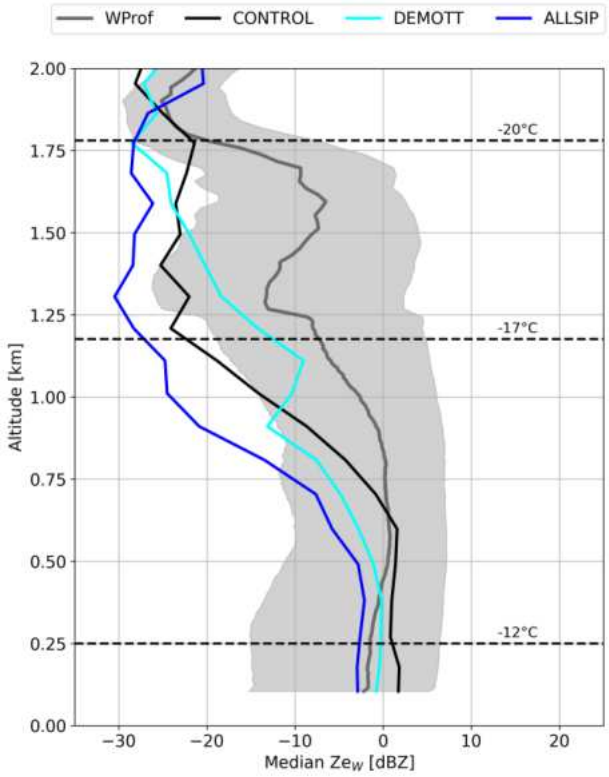

Figure C5. Median time-height vertical profiles of observed and simulated radar reflectivity extracted during the low-level orographic cloud period. The grey line represents the median WProf observations, with the shaded region indicating the IQR. The black, cyan, and blue lines denote the results from the CONTROL, DEMOTT, and ALLSIP simulations, respectively. Temperature contours superimposed in these panels are from the ALLSIP simulation.

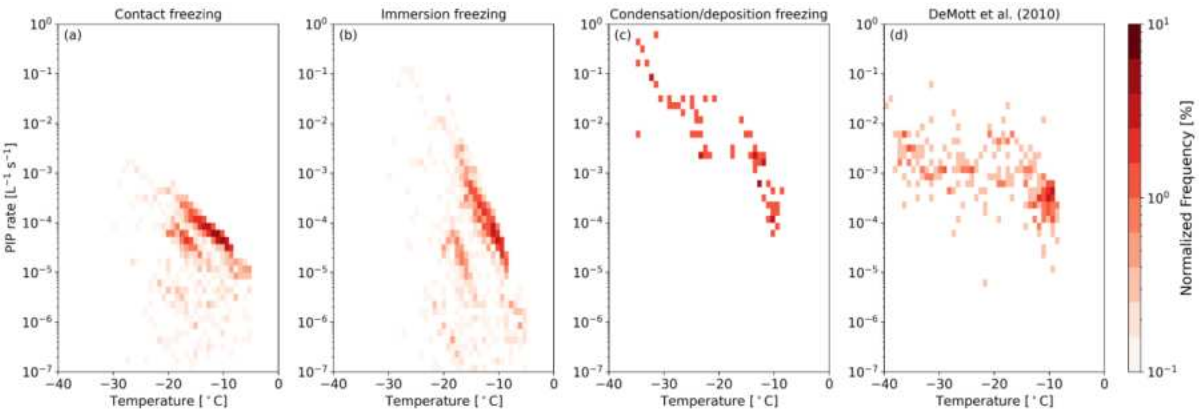

Figure C6. Histograms of the primary ice production (PIP) rates associated with the default (a) contact, (b) immersion and (c) condensation/depositions freezing used in the CONTROL simulation of WRF versus temperature. Same in (d) but replacing all default PIP parameterizations with the aerosol-aware formula from DeMott et al. (2010) and prescribing an aerosol concentration of 0.30 scm^{-3}.

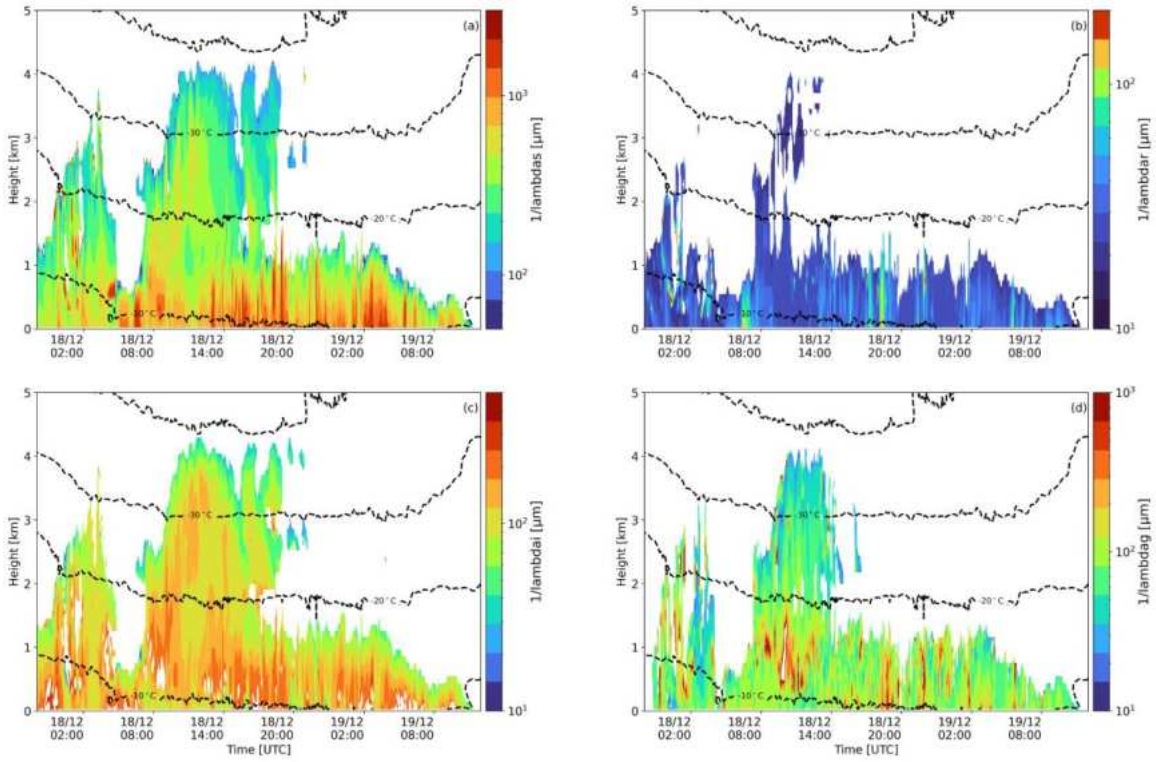

Figure C7. Timeseries of characteristic sizes (in μm) inferred by reversing the slope parameter (lambda) that describes the exponential size distributions of (a) snow (1/lambdas), (b) raindrops (1/lambdar), (c) cloud ice (1/lambdai), and (d) graupel (1/lambdag) in the Morrison microphysics scheme of WRF. These characteristic sizes are extracted from the ALLSIP sensitivity simulation of WRF, which demonstrates better agreement with radar observations.

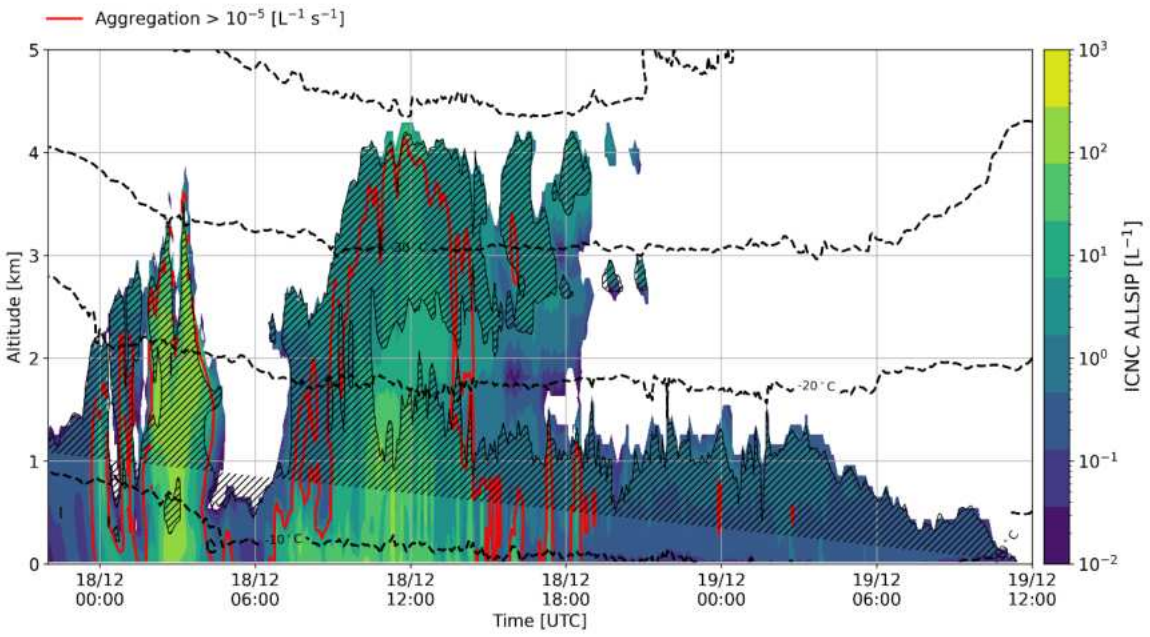

Figure C8. Time-height plots of total ICNCs produced by the ALLSIP simulation, as in Figure 5c in the main manuscript. The black contours represent temperature isotherms, while the red contours show areas where snowflake aggregation rates exceed 10^{-5} $L^{-1}s^{-1}$. The black hatched lines indicate regions that are supersaturated with respect to ice.

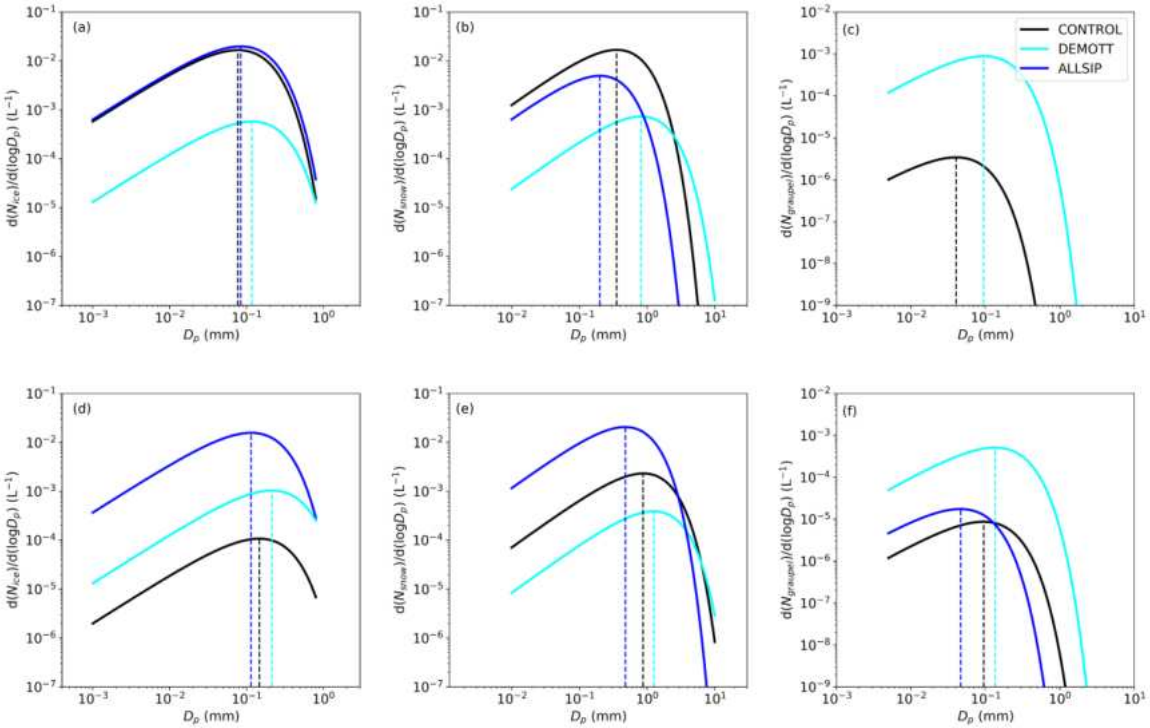

Figure C9. Size distribution of (a, d) cloud ice, (b, e) snow and (c, f) graupel particles, predicted by CONTROL (black line), DEMOTT (cyan line) and ALLSIP (blue line) simulations of WRF. The size distributions were taken at 03:55 UTC on 18 December (nimbostratus cloud period) at 2.0 km (top panel) and at 0.7 km in the atmosphere (bottom panel). The vertical dashed lines indicate the mode of each distribution.

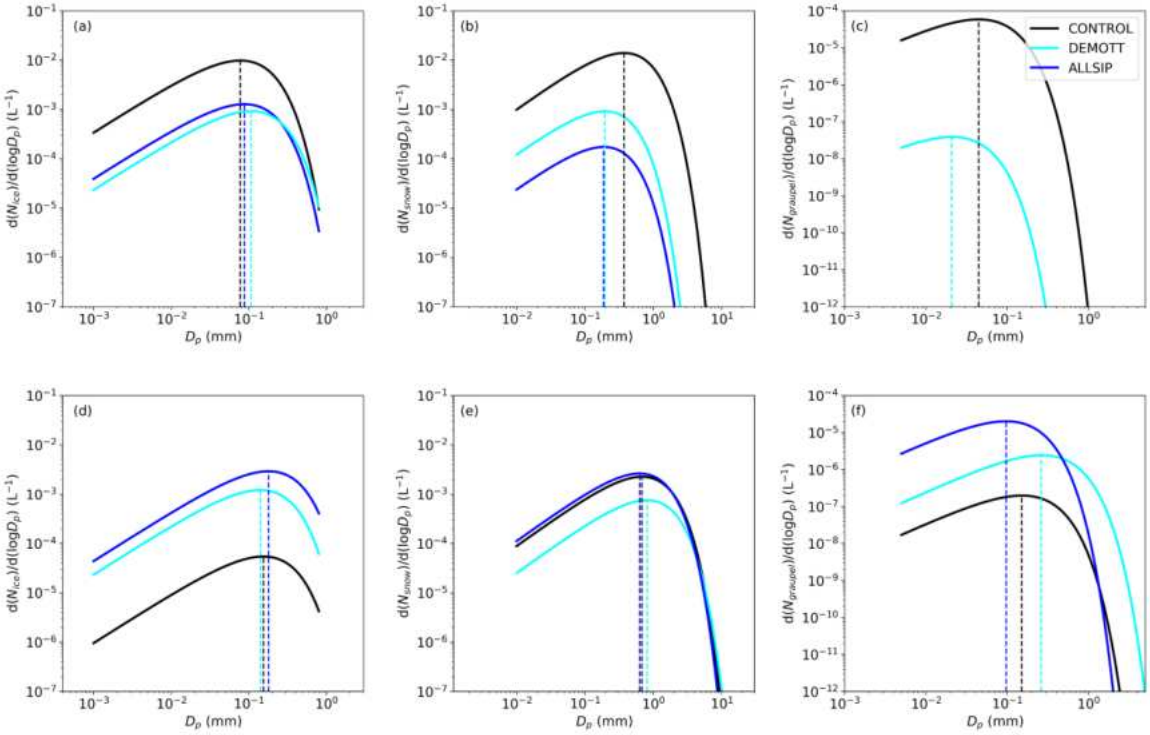

Figure C10. Size distribution of (a, d) cloud ice, (b, e) snow and (c, f) graupel particles, predicted by CONTROL (black line), DEMOTT (cyan line) and ALLSIP (blue line) simulations of WRF. The size distributions were taken at 09:20 UTC on 18 December (seeder-feeder cloud period) at 2.2 km (top panel) and at 0.5 km in the atmosphere (bottom panel). The vertical dashed lines indicate the mode of each distribution.

D. Supplementary material for: RaFSIP: Parameterizing ice multiplication in models using a machine learning approach

Introduction

This supplementary information provides additional figures supporting the detailed discussion regarding the two versions of the Random Forest Secondary Ice Production (RaFSIP) parameterization provided in the main manuscript. The information displayed in the following figures concerns the hyperparameter tuning of the Random Forest Regressor (RFR) models, the permutation importance of the RaFSIP input features, along with the offline and online performance of the RaFSIP scheme, when coupled with the mesoscale Weather Research and Forecasting (WRF) model.

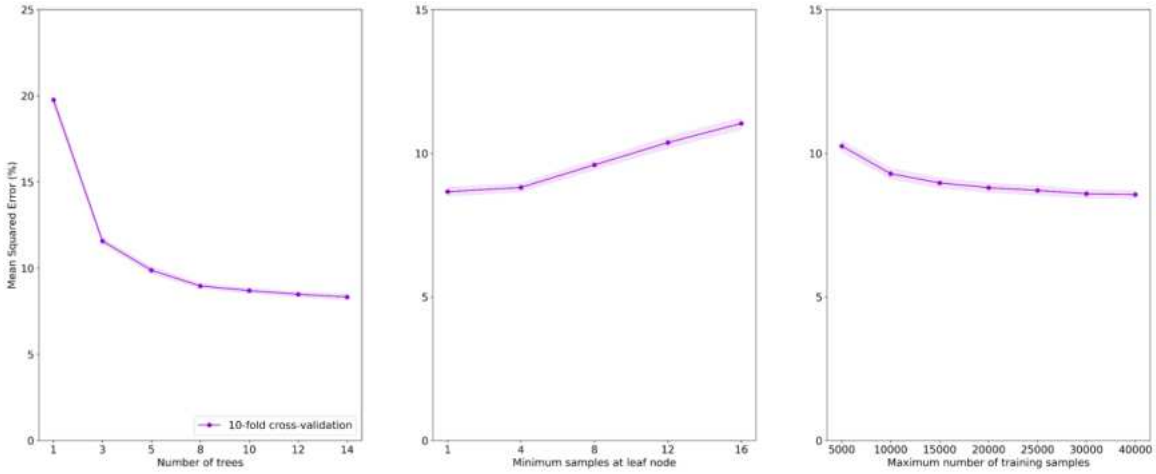

Figure D1. Hyperparameter tuning for the forestALL model used in the version 2 of the Random Forest Secondary Ice Production (RaFSIPv2) parameterization. Mean Squared Error (MSE) of the predictions was calculated using 10-fold cross validation on the training dataset. The tuning involves three hyperparameters: (a) number of decision trees in the forest, (b) minimum samples at each leaf node and (c) maximum number of training samples.

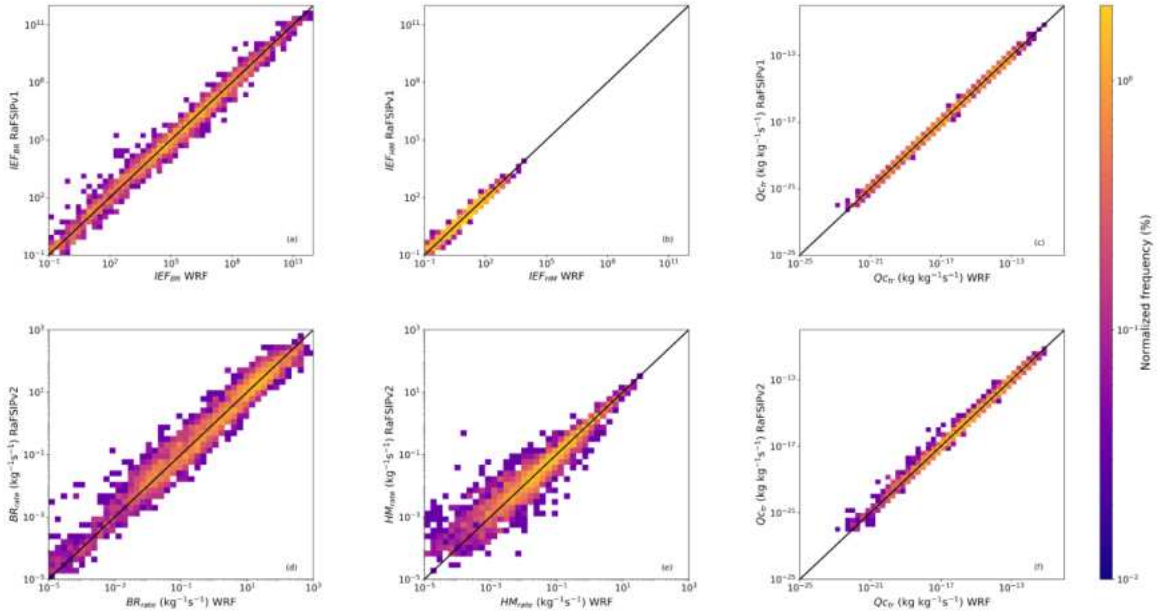

Figure D2. Normalized histogram (i.e., the frequency is scaled by the total number of predictions) of the true WRF results versus the forestBRHM predictions used in (top panel) RaFSIPv1 parameterization to predict the ice enhancement factor due to (a) ice-ice collisional break-up (IEF_{BR}), (b) Hallett-Mossop (IEF_{HM}), and (c) the transferred mass from cloud droplets to cloud ice (Qc_{tr}), and (bottom panel) RaFSIPv2 parameterization to predict the SIP rate due to (d) collisional break-up (BR_{rate}), (e) Hallett-Mossop (HM_{rate}), and (f) the transferred mass Qc_{tr}. The black line represents the one-to-one line.

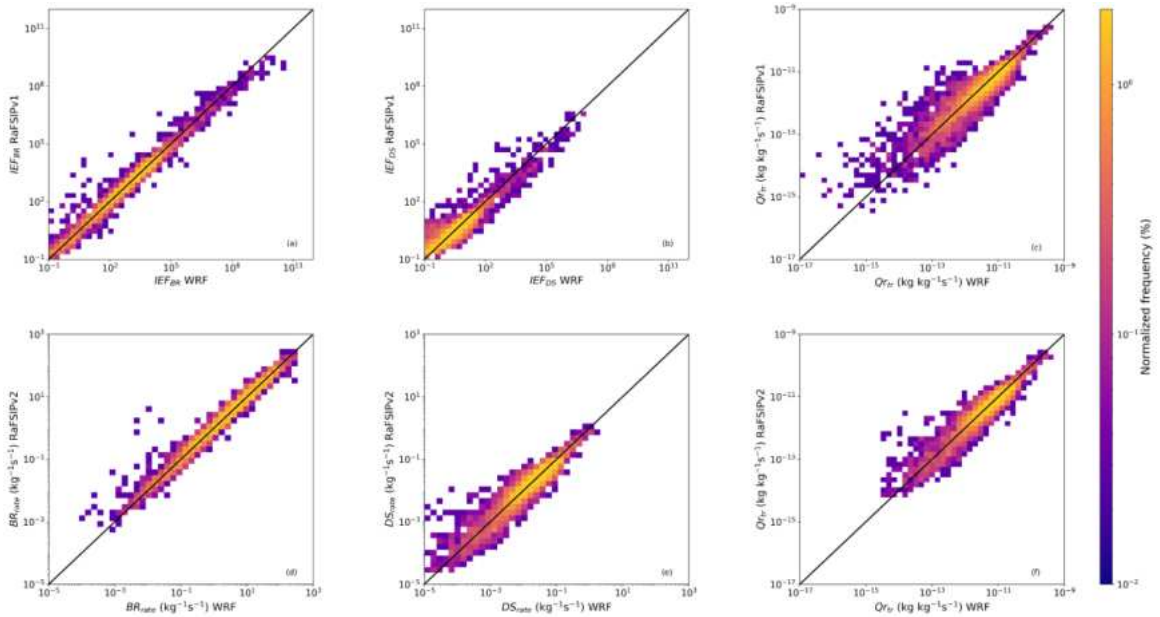

Figure D3. Normalized histogram of the true WRF results versus the forestBRDS predictions used in (top panel) RaFSIPv1 parameterization to predict the (a) IEF_{BR}, (b) ice enhancement factor due to droplet-shattering (IEF_{DS}), and (c) the transferred mass from raindrops to cloud ice (Qr_{tr}), and (bottom panel) RaFSIPv2 parameterization to predict the (d) BR_{rate}, (e) SIP rate due to droplet-shattering (DS_{rate}), and (f) the transferred mass Qr_{tr}. The black line represents the one-to-one line.

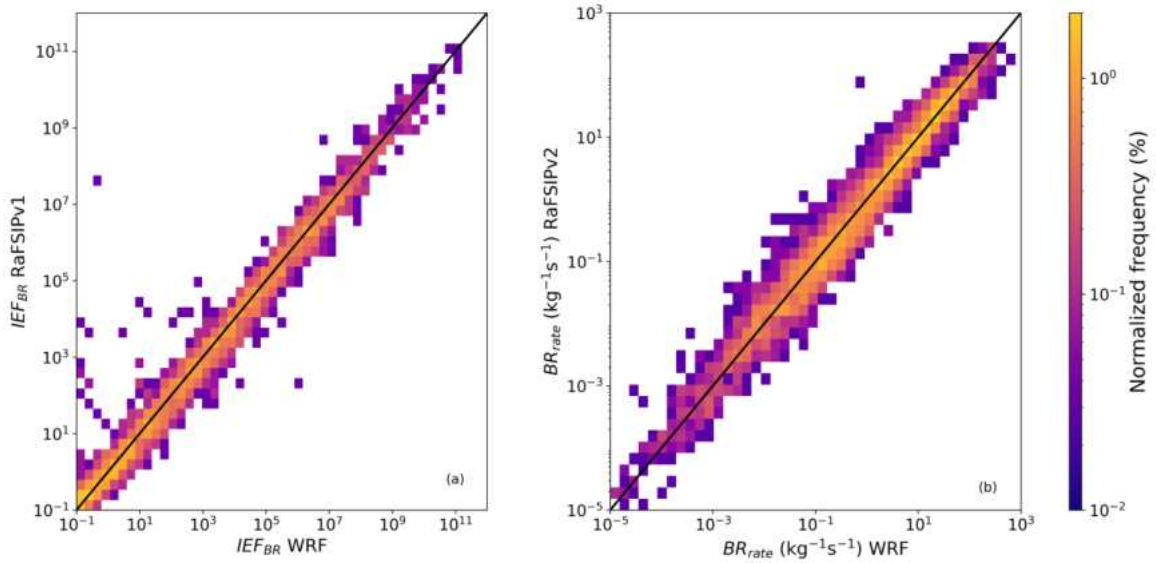

Figure D4. Normalized histogram of the true WRF results versus the forestBR predictions used in (a) RaFSIPv1 parameterization to predict the IEF_{BR}, and (b) RaFSIPv2 parameterization to predict the BR_{rate}. The black line represents the one-to-one line.

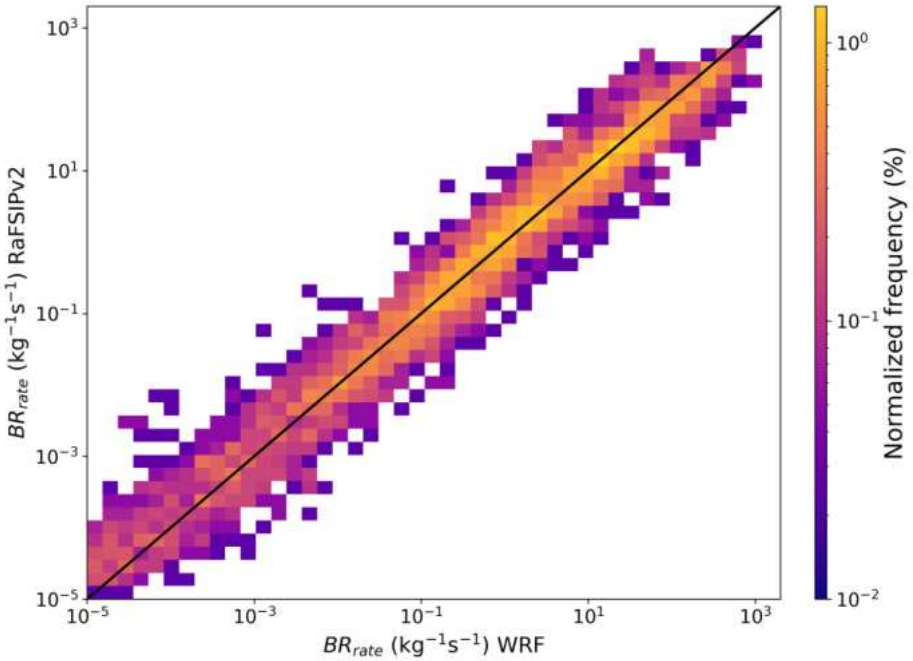

Figure D5. Normalized histogram of the true WRF results versus the forestBRwarm predictions used in RaFSIPv2 parameterization to predict the BR_{rate}. The black line represents the one-to-one line.

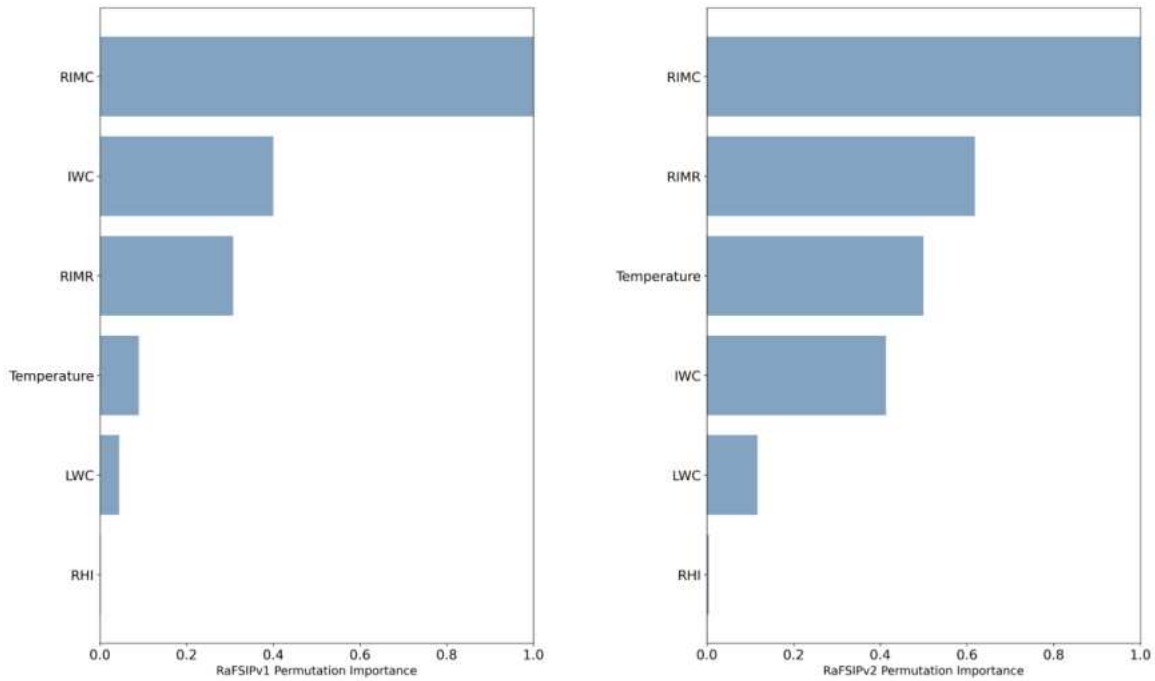

Figure D6. Permutation importance of the forestALL model of the RaFSIPv1 (left) and RaFSIPv2 (right) parameterizations. The resulting importance is normalized dividing by the maximum score achieved among the input features.

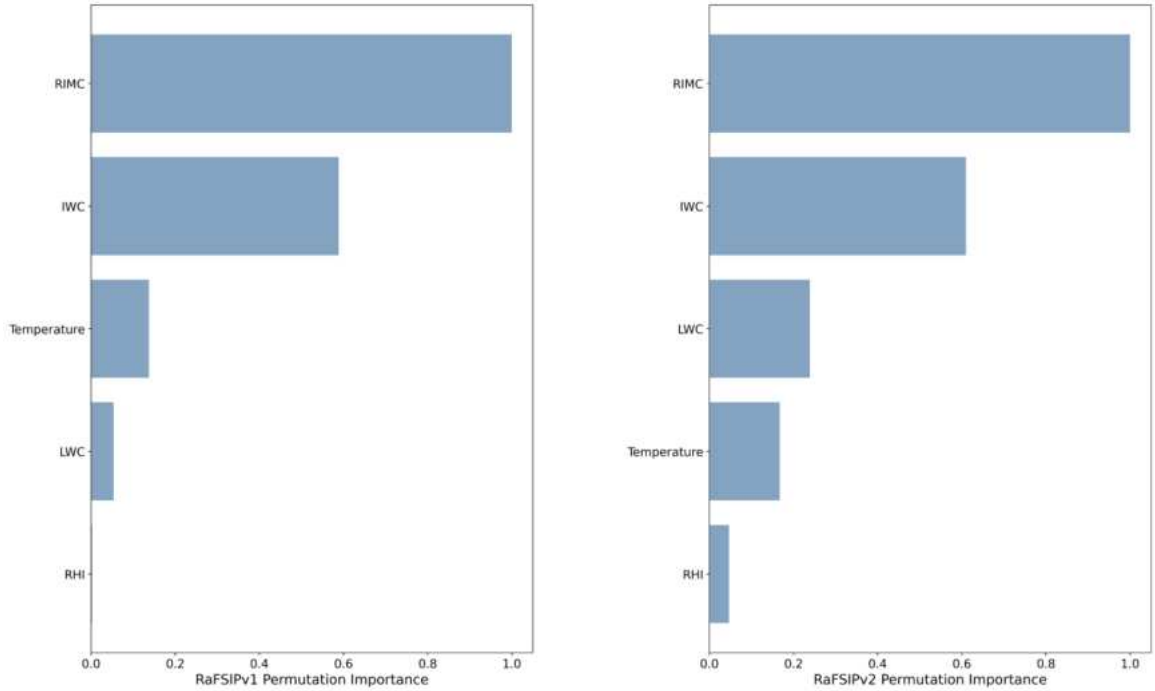

Figure D7. Permutation importance of the forestBRHM model of the RaFSIPv1 (left) and RaFSIPv2 (right) parameterizations. The resulting importance is normalized dividing by the maximum score achieved among the input features.

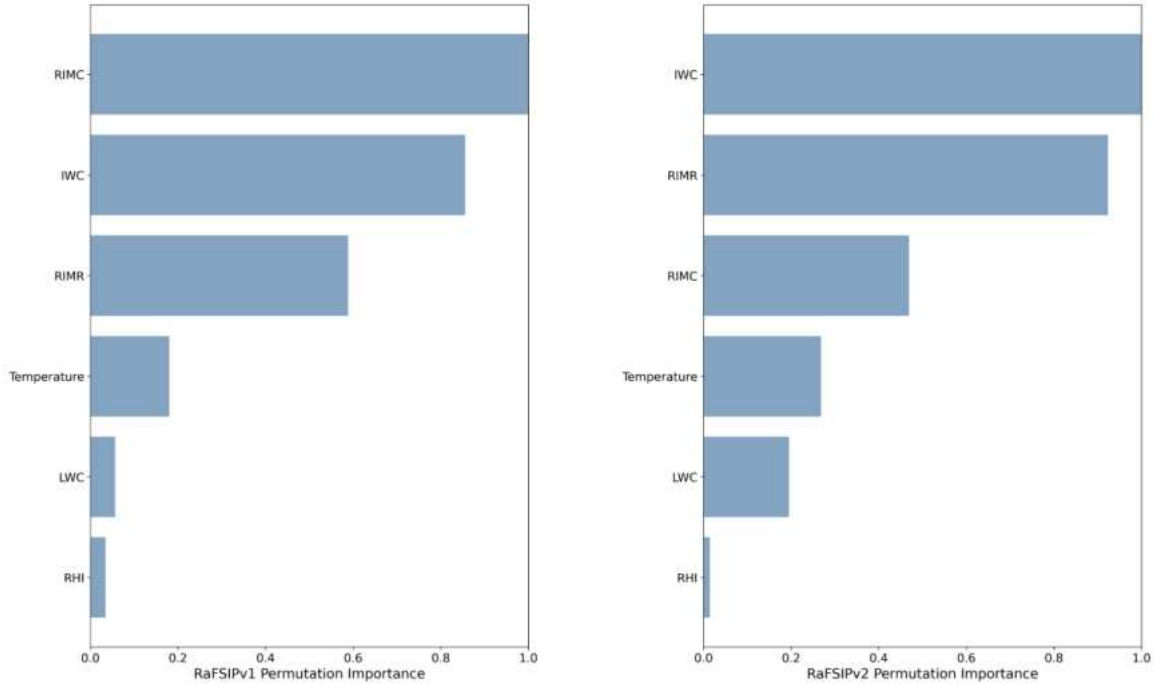

Figure D8. Permutation importance of the forestBRDS model of the RaFSIPv1 (left) and RaFSIPv2 (right) parameterizations. The resulting importance is normalized dividing by the maximum score achieved among the input features.

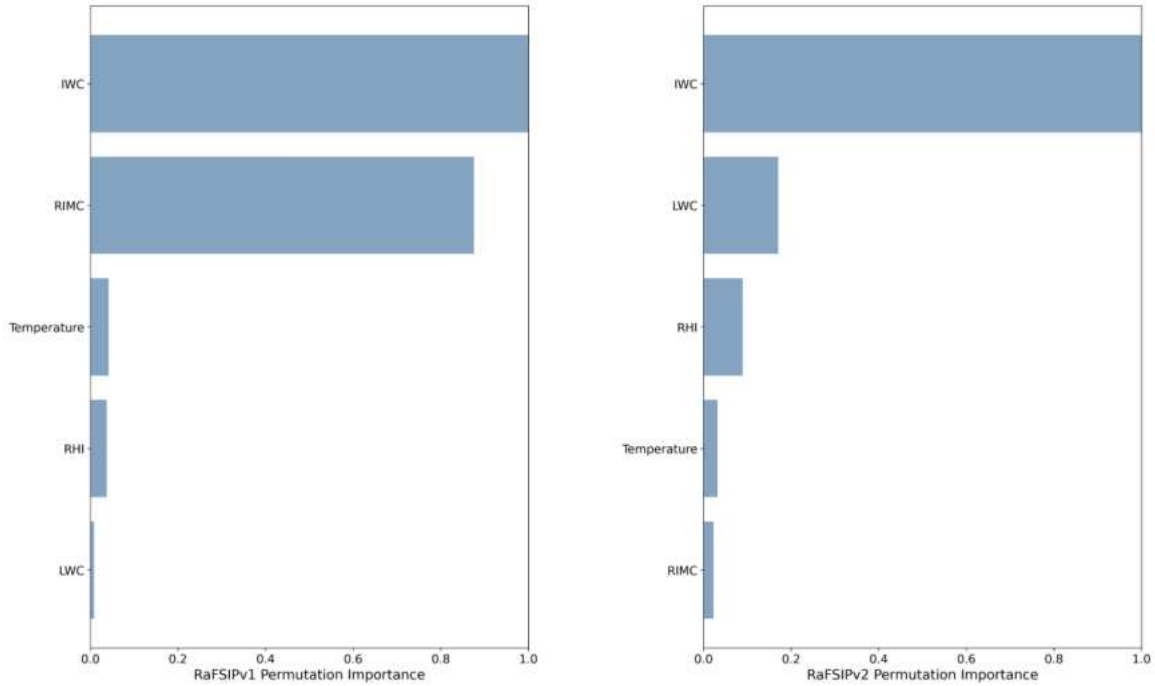

Figure D9. Permutation importance of the forestBR model of the RaFSIPv1 (left) and RaFSIPv2 (right) parameterizations. The resulting importance is normalized dividing by the maximum score achieved among the input features.

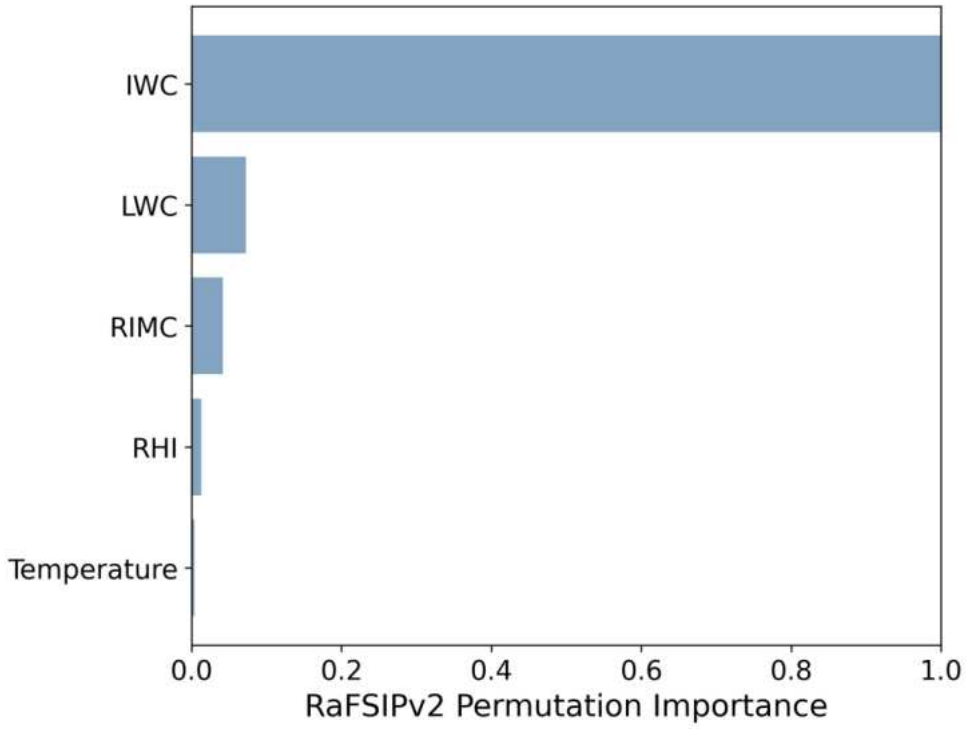

Figure D10. Permutation importance of the forestBRwarm model of the RaFSIPv2 parameterization. The resulting importance is normalized dividing by the maximum score achieved among the input features.

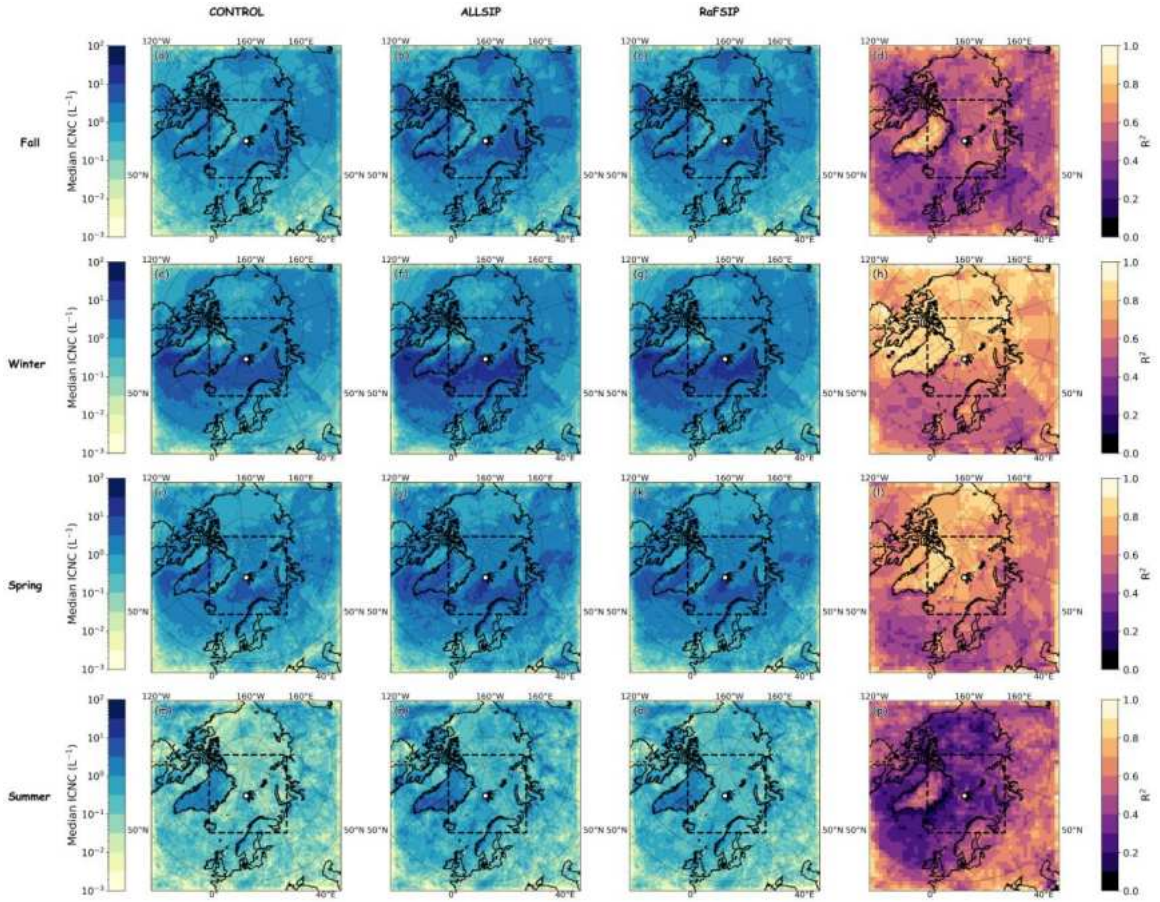

Figure D11. Latitude-longitude maps of the median ice crystal number concentration (ICNC) simulated by the (a, d, g, j) CONTROL, (b, e, h, k) ALLSIP, and (c, f, i, l) RaFSIP simulations, along with the corresponding (d, h, l, p) R^2 computed between ALLSIP and RaFSIPv1 results. Statistics are calculated for the 4 simulated seasons: fall (top panel), winter (second panel), spring (third panel) and summer (bottom panel).

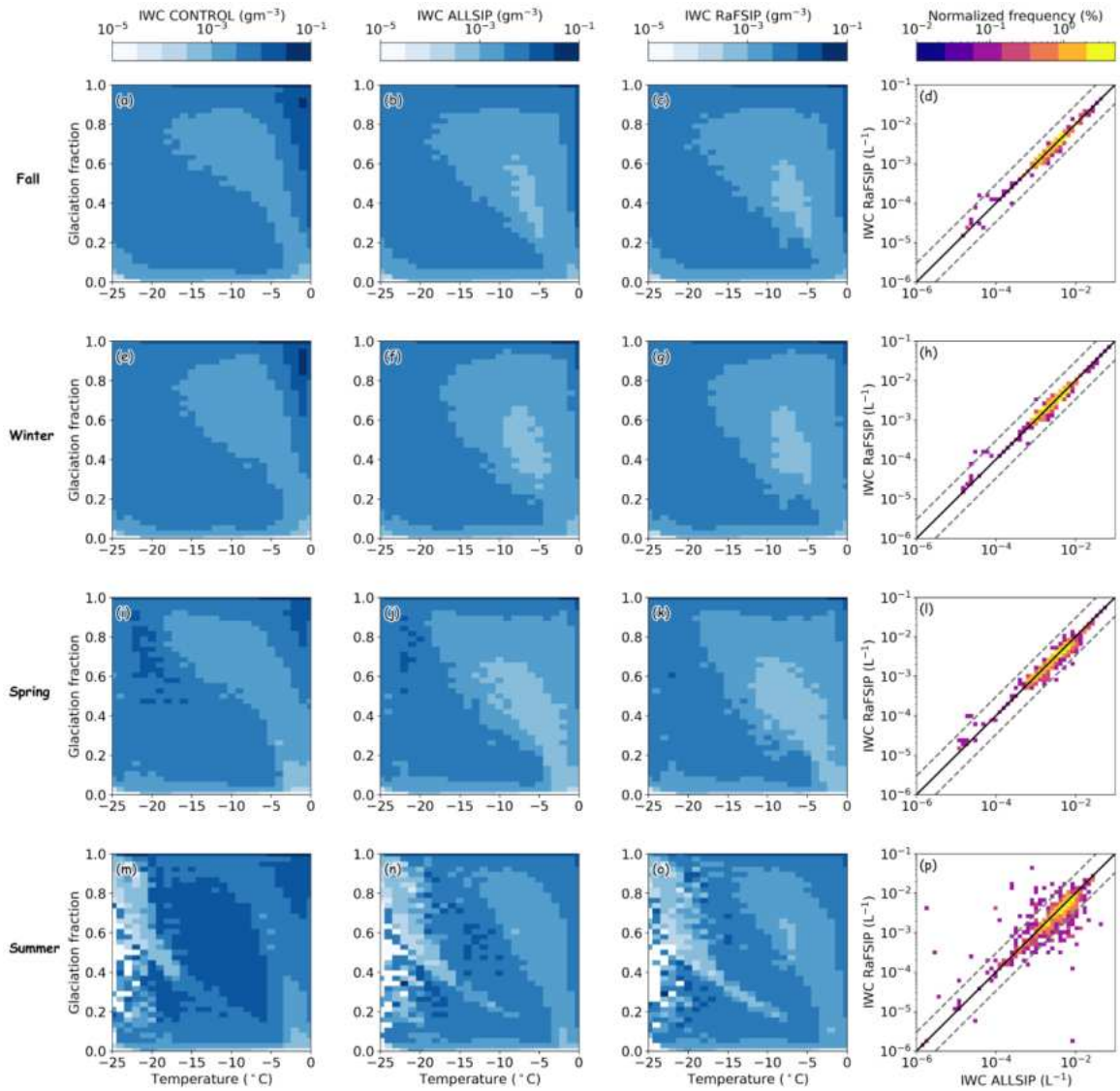

Figure D12. Bivariate joint probability density function (PDF) of median ice water content (IWC) defined in terms of both temperature and glaciation fraction from the 50-km resolution domain results of the CONTROL (a, e, i, m), ALLSIP (b, f, j, n) and RaFSIPv2 (c, g, k, o) WRF simulations. The normalized histograms of the 2D-binned median IWC results from the ALLSIP simulation are also plotted versus the RaFSIPv2 predictions (d, h, l, p). The black line represents the one-to-one line, while the grey dashed lines delimit the area where the ALLSIP values are over or under-estimated by a factor of 3. Statistics are calculated for the 4 simulated seasons: fall (top panel), winter (second panel), spring (third panel) and summer (bottom panel).

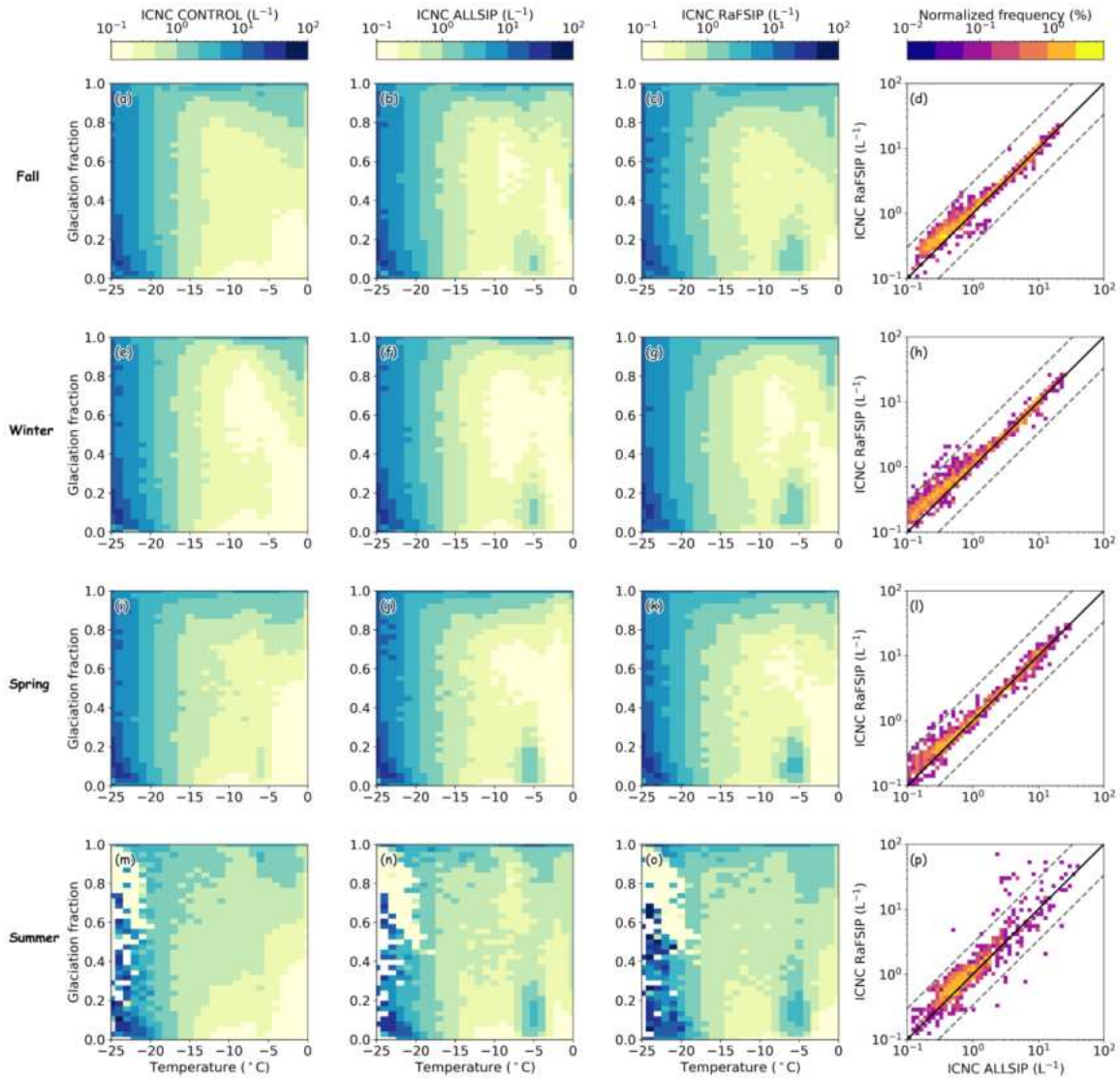

Figure D13. Bivariate joint PDF of median ICNC defined in terms of both temperature and glaciation fraction from the coarse-resolution domain results of the CONTROL (a, e, i, m), ALLSIP (b, f, j, n) and RaFSIPv1 (c, g, k, o) WRF simulations. The normalized histograms of the 2D-binned median ICNC results from the ALLSIP simulation are also plotted versus the RaFSIPv1 predictions (d, h, l, p). The black line represents the one-to-one line, while the grey dashed lines delimit the area where the ALLSIP values are over or under-estimated by a factor of 3. Statistics are calculated for the 4 simulated seasons: fall (top panel), winter (second panel), spring (third panel) and summer (bottom panel).

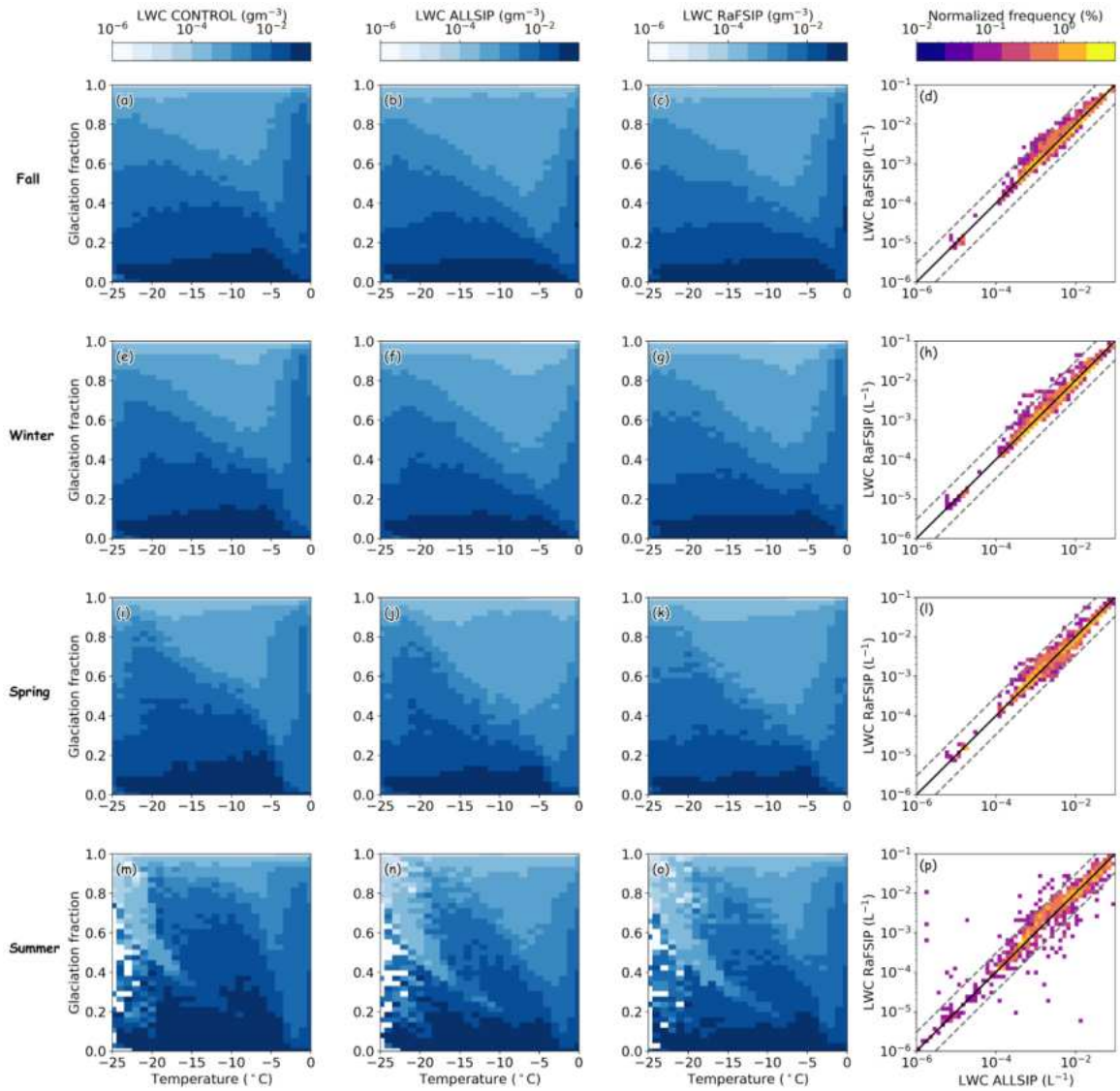

Figure D14. Bivariate joint PDF of median liquid water content (LWC) defined in terms of both temperature and glaciation fraction from the coarse-resolution domain results of the CONTROL (a, e, i, m), ALLSIP (b, f, j, n) and RaFSIPv1 (c, g, k, o) WRF simulations. The normalized histograms of the 2D-binned median LWC results from the ALLSIP simulation are also plotted versus the RaFSIPv1 predictions (d, h, l, p). The black line represents the one-to-one line, while the grey dashed lines delimit the area where the ALLSIP values are over or under-estimated by a factor of 3. Statistics are calculated for the 4 simulated seasons: fall (top panel), winter (second panel), spring (third panel) and summer (bottom panel).

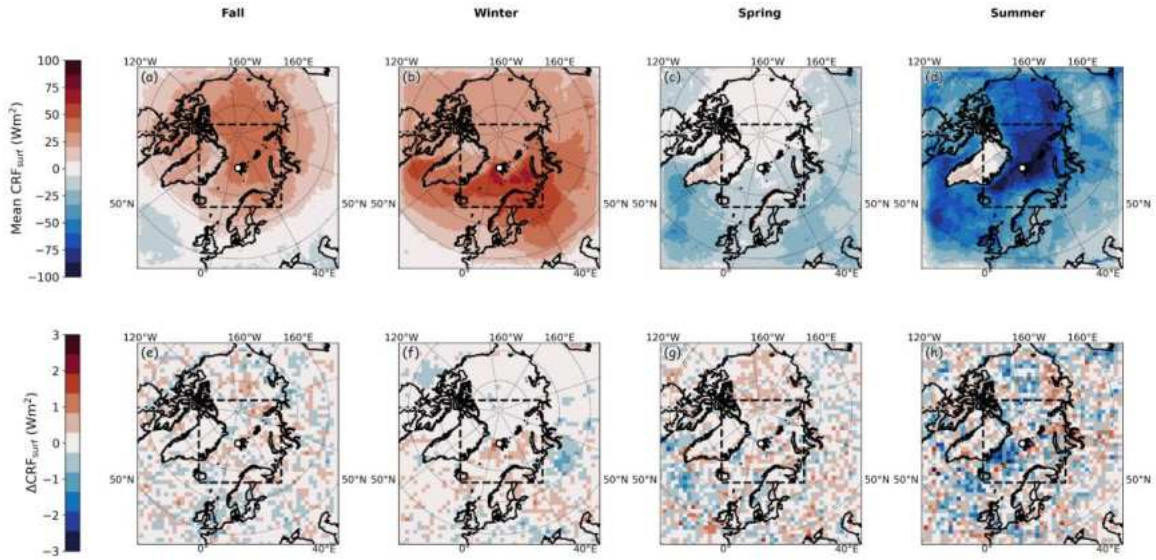

Figure D15. Latitude-longitude maps of (top panel): seasonally-averaged cloud radiative forcing at the surface (CRF_{surf}) simulated by the ALLSIP simulation, and (bottom panel): anomalies with respect to the ALLSIP simulation (ΔCRE_{surf}) derived from the WRF simulation coupled with the RaFSIPv1 parameterization, extracted respectively for (a, e) fall, (b, f) winter, (c, g) spring and (d, h) summer.

Bibliography

Abbatt, J. P. D., Leaitch, W. R., Aliabadi, A. A., Bertram, A. K., Blanchet, J., Boivin-rioux, A., et al. (2019). Overview paper : New insights into aerosol and climate in the Arctic. *Atmospheric Chemistry and Physics*, *19*, 1–34. https://doi.org/https://doi.org/10.5194/acp-19-1-2019

Abdelwares, M., Haggag, M., Wagdy, A., & Lelieveld, J. (2018). Customized framework of the WRF model for regional climate simulation over the Eastern NILE basin. *Theoretical and Applied Climatology*, *134*(3–4), 1135–1151. https://doi.org/10.1007/s00704-017-2331-2

Albrecht, B. A. (1989). Aerosols, cloud microphysics and fractional cloudiness. *Science*, *245*, 1227–1230. https://doi.org/10.1126/science.245.4923.1227

Andreae, M. O., & Rosenfeld, D. (2008). Aerosol-cloud-precipitation interactions. Part 1. The nature and sources of cloud-active aerosols. *Earth-Science Reviews*, *89*, 13–41. https://doi.org/10.1016/j.earscirev.2008.03.001

Atlas, R. L., Bretherton, C. S., Blossey, P. N., Gettelman, A., Bardeen, C., Lin, P., & Ming, Y. (2020). How Well Do Large-Eddy Simulations and Global Climate Models Represent Observed Boundary Layer Structures and Low Clouds Over the Summertime Southern Ocean? *Journal of Advances in Modeling Earth Systems*, *12*(11), 1–25. https://doi.org/10.1029/2020MS002205

Atlas, R. L., Bretherton, C. S., Khairoutdinov, M. F., & Blossey, P. N. (2022). Hallett-Mossop Rime Splintering Dims Cumulus Clouds Over the Southern Ocean: New Insight From Nudged Global Storm-Resolving Simulations. *AGU Advances*, *3*(2). https://doi.org/10.1029/2021AV000454

Bacon, N. J., Swanson, B. D., Baker, M. B., & Davis, E. J. (1998). Breakup of levitated frost particles. *Journal of Geophysical Research Atmospheres*, *103*(D12), 13763–13775. https://doi.org/10.1029/98JD01162

Balaji, V., Couvreux, F., Deshayes, J., Gautrais, J., Hourdin, F., & Rio, C. (2022). Are general circulation models obsolete? *Proceedings of the National Academy of Sciences of the United States of America*, *119*(47), 1–10. https://doi.org/10.1073/pnas.2202075119

Baltensperger, U., Gäggeler, H. W., Jost, D. T., Lugauer, M., Schwikowski, M., Weingartner, E., & Seibert, P. (1997). Aerosol climatology at the high-alpine site Jungfraujoch, Switzerland. *Journal of Geophysical Research*, *102*.

Baltensperger, U., Schwikowski, M., Jost, D. T., Nyeki, S., Gäggeler, H. W., & Poulida, O. (1998). Scavenging of atmospheric constituents in mixed phase clouds at the high-alpine site Jungfraujoch part I: Basic concept and aerosol scavenging by clouds. *Atmospheric Environment*, *32*, 3975–3983. https://doi.org/10.1016/S1352-2310(98)00051-X

Barahona, D., & Nenes, A. (2009). Parameterizing the competition between homogeneous and heterogeneous freezing in ice cloud formation - Polydisperse ice nuclei. *Atmospheric Chemistry and Physics*, *9*(16), 5933–5948. https://doi.org/10.5194/acp-9-5933-2009

Barahona, D., West, R. E. L., Stier, P., Romakkaniemi, S., Kokkola, H., & Nenes, A. (2010). Comprehensively accounting for the effect of giant CCN in cloud activation parameterizations. *Atmospheric Chemistry and Physics*, *10*, 2467–2473. https://doi.org/10.5194/acp-10-2467-2010

Barahona, D., Molod, A., Bacmeister, J., Nenes, A., Gettelman, A., Morrison, H., et al. (2014).

Development of two-moment cloud microphysics for liquid and ice within the NASA Goddard Earth Observing System Model (GEOS-5). *Geoscientific Model Development*, *7*(4), 1733–1766. https://doi.org/10.5194/gmd-7-1733-2014

Barahona, Donifan, & Nenes, A. (2007). Parameterization of cloud droplet formation in large-scale models: Including effects of entrainment. *Journal of Geophysical Research Atmospheres*, *112*(16), 1–14. https://doi.org/10.1029/2007JD008473

Barrett, A. I., Westbrook, C. D., Nicol, J. C., & Stein, T. H. M. (2019). Rapid ice aggregation process revealed through triple-wavelength Doppler spectrum radar analysis. *Atmospheric Chemistry and Physics*, *19*(8), 5753–5769. https://doi.org/10.5194/acp-19-5753-2019

Beck, A., Henneberger, J., Schöpfer, S., Fugal, J., & Lohmann, U. (2017). HoloGondel: In situ cloud observations on a cable car in the Swiss Alps using a holographic imager. *Atmospheric Measurement Techniques*, *10*, 459–476. https://doi.org/10.5194/amt-10-459-2017

Beck, A., Henneberger, J., Fugal, J. P., David, R. O., Lacher, L., & Lohmann, U. (2018). Impact of surface and near-surface processes on ice crystal concentrations measured at mountain-top research stations. *Atmospheric Chemistry and Physics*, *18*(12), 8909–8927. https://doi.org/10.5194/acp-18-8909-2018

Beheng, K. D. (1987). Microphysical Properties of Glaciating Cumulus Clouds: Comparison of Measurements With A Numerical Simulation. *Quarterly Journal of the Royal Meteorological Society*, *113*(478), 1377–1382. https://doi.org/10.1002/qj.49711347815

Bergeron, T. (1935). On the physics of clouds and precipitation. *Report, International Union of Geodesy and Geophysics.* https://doi.org/10.1038/174957a0

Beucler, T., Ebert-Uphoff, I., Rasp, S., Pritchard, M., & Gentine, P. (2021). *Machine learning for clouds and climate (invited chapter for the AGU geophysical monograph series "Clouds and Climate")*. *Clouds and Climate*. https://doi.org/https://doi.org/10.1002/essoar.10506925.1

Bigg, E. K. (1953). The supercooling of water. *Proceedings of the Physical Society. Section B*, *66*(8), 688–694. https://doi.org/10.1088/0370-1301/66/8/309

Billault-Roux, A.-C., & Berne, A. (2021). Integrated water vapor and liquid water path retrieval using a single-channel radiometer. *Atmospheric Measurement Techniques*, *14*(4), 2749–2769. https://doi.org/10.5194/amt-14-2749-2021

Billault-Roux, A.-C., Georgakaki, P., Gehring, J., Jaffeux, L., Schwarzenboeck, A., Coutris, P., Nenes, A., and Berne, A. (2023). Distinct secondary ice production processes observed in radar Doppler spectra: insights from a case study, Atmospheric Chemistry and Physics, 23, 10207–10234, https://doi.org/10.5194/acp-23-10207-2023

Bodas-Salcedo, A., Mulcahy, J. P., Andrews, T., Williams, K. D., Ringer, M. A., Field, P. R., & Elsaesser, G. S. (2019). Strong Dependence of Atmospheric Feedbacks on Mixed-Phase Microphysics and Aerosol-Cloud Interactions in HadGEM3. *Journal of Advances in Modeling Earth Systems*, *11*(6), 1735–1758. https://doi.org/10.1029/2019MS001688

de Boer, G., Eloranta, E. W., & Shupe, M. D. (2009). Arctic mixed-phase stratiform cloud properties from multiple years of surface-based measurements at two high-latitude locations. *Journal of the Atmospheric Sciences*, *66*(9), 2874–2887. https://doi.org/10.1175/2009JAS3029.1

Borys, R. D., Lowenthal, D. H., Cohn, S. A., & Brown, W. O. J. (2003). Mountaintop and radar measurements of anthropogenic aerosol effects on snow growth and snowfall rate. *Geophysical Research Letters*, *30*. https://doi.org/10.1029/2002gl016855

Bougiatioti, A., Bezantakos, S., Stavroulas, I., Kalivitis, N., Kokkalis, P., Biskos, G., et al. (2016). Biomass-burning impact on CCN number, hygroscopicity and cloud formation during summertime in the eastern Mediterranean. *Atmospheric Chemistry and Physics*, *16*, 7389–7409. https://doi.org/10.5194/acp-16-7389-2016

Brazda, V., Fiser, O., Capsoni, C., Nebuloni, R., Pesice, P., & Chladova, Z. (2013). Cloud microphysics from the free space optical link point of view - Preliminary experimental results. *Proceedings of the 2013 2nd International Workshop on Optical Wireless Communications, IWOW 2013*, 63–66. https://doi.org/10.1109/IWOW.2013.6777778

Breiman, L. (2001). Random forests. *Machine Learning*, *45*, 5–32. https://doi.org/10.1023/A:1010933404324

Brenowitz, N. D., & Bretherton, C. S. (2018). Prognostic Validation of a Neural Network Unified Physics Parameterization. *Geophysical Research Letters*, *45*(12), 6289–6298. https://doi.org/10.1029/2018GL078510

Brenowitz, N. D., & Bretherton, C. S. (2019). Spatially Extended Tests of a Neural Network Parametrization Trained by Coarse-Graining. *Journal of Advances in Modeling Earth Systems*, *11*(8), 2728–2744. https://doi.org/10.1029/2019MS001711

Brenowitz, Noah D., Beucler, T., Pritchard, M., & Bretherton, C. S. (2020). Interpreting and stabilizing machine-learning parametrizations of convection. *Journal of the Atmospheric Sciences*, *77*(12), 4357–4375. https://doi.org/10.1175/JAS-D-20-0082.1

Brewer, A. W., & Palmer, H. P. (1949). Condensation processes at low temperatures, and the production of new sublimation nuclei by the splintering of ice. *Nature*, *164*(4164), 312–313. https://doi.org/https://doi.org/10.1038/164312a0

Brown, P. R. A., & Francis, P. N. (1995). Improved Measurements of the Ice Water Content in Cirrus Using a Total-Water Probe. *Journal of Atmospheric and Oceanic Technology*, *12*, 410–414. https://doi.org/10.1175/1520- 0426(1995)012<0410:IMOTIW>2.0.CO;2

Browning, K. A., Hill, F. F., & Pardoe, C. W. (1974). Structure and mechanism of precipitation and the effect of orography in a wintertime warm sector. *Quarterly Journal of the Royal Meteorological Society*, *100*(425), 309–330. https://doi.org/10.1002/qj.49710042505

Browning, K. A., Pardoe, C. W., & Hill, F. F. (1975). The nature of orographic rain at wintertime cold fronts. *Quarterly Journal of the Royal Meteorological Society*, *101*(428), 333–352. https://doi.org/10.1002/qj.49710142815

Brunner, C., Brem, B. T., Collaud Coen, M., Conen, F., Hervo, M., Henne, S., et al. (2021). The contribution of Saharan dust to the ice-nucleating particle concentrations at the High Altitude Station Jungfraujoch (3580 m a.s.l.), Switzerland. *Atmospheric Chemistry and Physics*, *21*(23), 18029–18053. https://doi.org/10.5194/acp-21-18029-2021

Cannon, T. D., Dye, J. E., & Toutenhoofd, V. (1974). The mechanism of precipitation formation in Northeastern Colorado cumulus II. Sailplane measurements. *Journal of the Atmospheric Sciences*, *31*, 2148–2151. https://doi.org/10.1175/1520-0469(1974)031< 2152:TMOPFI> 2.0.CO;2

Carlsen, T., & David, R. O. (2022). Spaceborne Evidence That Ice-Nucleating Particles Influence High-Latitude Cloud Phase. *Geophysical Research Letters*, *49*(14), 1–11. https://doi.org/10.1029/2022GL098041

Ceppi, P., & Nowack, P. (2021). Observational evidence that cloud feedback amplifies global warming. *Proceedings of the National Academy of Sciences of the United States of America*,

118(30), 1–7. https://doi.org/10.1073/pnas.2026290118

Chellini, G., Gierens, R., & Kneifel, S. (2022). Ice Aggregation in Low-Level Mixed-Phase Clouds at a High Arctic Site: Enhanced by Dendritic Growth and Absent Close to the Melting Level. *Journal of Geophysical Research: Atmospheres*, *127*(16), 1–23. https://doi.org/10.1029/2022JD036860

Chen, F., & Dudhia, J. (2001). Coupling and advanced land surface-hydrology model with the Penn State-NCAR MM5 modeling system. Part I: Model implementation and sensitivity. *Monthly Weather Review*, *129*(4), 569–585. https://doi.org/10.1175/1520-0493(2001)129<0569:CAALSH>2.0.CO;2

Chiu, J. C., Yang, C. K., van Leeuwen, P. J., Feingold, G., Wood, R., Blanchard, Y., et al. (2021). Observational Constraints on Warm Cloud Microphysical Processes Using Machine Learning and Optimization Techniques. *Geophysical Research Letters*, *48*(2), 1–13. https://doi.org/10.1029/2020GL091236

Cho, H., Jun, S. Y., Ho, C. H., & McFarquhar, G. (2020). Simulations of Winter Arctic Clouds and Associated Radiation Fluxes Using Different Cloud Microphysics Schemes in the Polar WRF: Comparisons With CloudSat, CALIPSO, and CERES. *Journal of Geophysical Research: Atmospheres*, *125*(2), 1–21. https://doi.org/10.1029/2019JD031413

Chou, C., Stetzer, O., Weingartner, E., Jurányi, Z., Kanji, Z. A., & Lohmann, U. (2011). Ice nuclei properties within a Saharan dust event at the Jungfraujoch in the Swiss Alps. *Atmospheric Chemistry and Physics*, *11*, 4725–4738. https://doi.org/10.5194/acp-11-4725-2011

Choularton, T. W., Griggs, D. J., Humood, B. Y., & Latham, J. (1980). Laboratory studies of riming, and its relation to ice splinter production. *Quarterly Journal of the Royal Meteorological Society*, *106*(448), 367–374. https://doi.org/10.1002/qj.49710644809

Choularton, T. W., Bower, K. N., Weingartner, E., Crawford, I., Coe, H., Gallagher, M. W., et al. (2008). The influence of small aerosol particles on the properties of water and ice clouds. *Faraday Discussions*, *137*, 205–222. https://doi.org/10.1039/b702722m

Chow, F. K., De Wekker, Stephan, F. J., & Snyder, B. J. (2013). *Mountain weather research and forecasting: recent progress and current challenges. Dordrecht, Springer*.

Christensen, M. W., Carrió, G. G., Stephens, G. L., & Cotton, W. R. (2013). Radiative impacts of free-tropospheric clouds on the properties of marine stratocumulus. *Journal of the Atmospheric Sciences*, *70*(10), 3102–3118. https://doi.org/10.1175/JAS-D-12-0287.1

Coen, M. C., Andrews, E., Aliaga, D., Andrade, M., Angelov, H., Bukowiecki, N., et al. (2018). Identification of topographic features influencing aerosol observations at high altitude stations. *Atmospheric Chemistry and Physics*, *18*(16), 12289–12313. https://doi.org/10.5194/acp-18-12289-2018

Conant, W. C., VanReken, T. M., Rissman, T. A., Varutbangkul, V., Jonsson, H. H., Nenes, A., et al. (2004). Aerosol-cloud drop concentration closure in warm cumulus. *Journal of Geophysical Research D: Atmospheres*, *109*(13), 1–12. https://doi.org/10.1029/2003JD004324

Conen, F., Rodríguez, S., Hüglin, C., Henne, S., Herrmann, E., Bukowiecki, N., & Alewell, C. (2015). Atmospheric ice nuclei at the high-altitude observatory Jungfraujoch, Switzerland. *Tellus, Series B: Chemical and Physical Meteorology*, *67*(1). https://doi.org/10.3402/tellusb.v67.25014

Conen, F., Einbock, A., Mignani, C., & Hüglin, C. (2022). Measurement report: Ice-nucleating particles active ≥-15° C in free tropospheric air over western Europe. *Atmospheric Chemistry and Physics*, *22*(5), 3433–3444. https://doi.org/10.5194/acp-22-3433-2022

Cooper, W. A. (1986). Ice Initiation in Natural Clouds. *Meteorological Monographs*, *21*, 29–32. https://doi.org/10.1175/0065-9401-21.43.29

Cotton, W. R., Tripoli, G. J., Rauber, R. M., & Mulvihill, E. A. (1986). Numerical Simulation of the Effects of Varying Ice Crystal Nucleation Rates and Aggregation Processes on Orographic Snowfall. *Journal of Climate and Applied Meteorology*, *25*(11), 1658–1680. https://doi.org/10.1175/1520- 780 0450(1986)025<1658:NSOTEO>2.0.CO;2

Crawford, I., Bower, K. N., Choularton, T. W., Dearden, C., Crosier, J., Westbrook, C., et al. (2012). Ice formation and development in aged, wintertime cumulus over the UK: Observations and modelling. *Atmospheric Chemistry and Physics*, *12*(11), 4963–4985. https://doi.org/10.5194/acp-12-4963-2012

Creamean, J. M., Cross, J. N., Pickart, R., McRaven, L., Lin, P., Pacini, A., et al. (2019). Ice Nucleating Particles Carried From Below a Phytoplankton Bloom to the Arctic Atmosphere. *Geophysical Research Letters*, *46*(14), 8572–8581. https://doi.org/10.1029/2019GL083039

Crosier, J., Bower, K. N., Choularton, T. W., Westbrook, C. D., Connolly, P. J., Cui, Z. Q., et al. (2011). Observations of ice multiplication in a weakly convective cell embedded in supercooled mid-level stratus. *Atmospheric Chemistry and Physics*, *11*(1), 257–273. https://doi.org/10.5194/acp-11-257-2011

Curry, J. A., Rossow, W. B., Randall, D., & Schramm, J. L. (1996). Overview of arctic cloud and radiation characteristics. *Journal of Climate*. https://doi.org/10.1175/1520-0442(1996)009<1731:OOACAR>2.0.CO;2

D'Alessandro, J. J., McFarquhar, G. M., Stith, J. L., Diao, M., DeMott, P. J., McCluskey, C. S., et al. (2023). An Evaluation of Phase, Aerosol-Cloud Interactions and Microphysical Properties of Single- and Multi-Layer Clouds Over the Southern Ocean Using in Situ Observations From SOCRATES. *Journal of Geophysical Research: Atmospheres*, *128*(15), 1–27. https://doi.org/10.1029/2023JD038610

David, R. O., Marcolli, C., Fahrni, J., Qiu, Y., Perez Sirkin, Y. A., Molinero, V., et al. (2019). Pore condensation and freezing is responsible for ice formation below water saturation for porous particles. *Proceedings of the National Academy of Sciences of the United States of America*, *116*(17), 8184–8189. https://doi.org/10.1073/pnas.1813647116

Dedekind, Z., Lauber, A., Ferrachat, S., & Lohmann, U. (2021). Sensitivity of precipitation formation to secondary ice production in winter orographic mixed-phase clouds. *Atmospheric Chemistry and Physics Discussions*, (February), 1–27. https://doi.org/10.5194/acp-2020-1326

Dedekind, Z., Grazioli, J., Austin, P. H., & Lohmann, U. (2023). Heavy snowfall event over the Swiss Alps: did wind shear impact secondary ice production? *Atmospheric Chemistry and Physics*, *23*(4), 2345–2364. https://doi.org/10.5194/acp-23-2345-2023

DeMott, P. J., Prenni, A. J., Liu, X., Kreidenweis, S. M., Petters, M. D., Twohy, C. H., et al. (2010). Predicting global atmospheric ice nuclei distributions and their impacts on climate. *Proceedings of the National Academy of Sciences*, *107*, 11217–11222. https://doi.org/10.1073/pnas.0910818107

DeMott, Paul J., Möhler, O., Stetzer, O., Vali, G., Levin, Z., Petters, M. D., et al. (2011). Resurgence in ice nuclei measurement research. *Bulletin of the American Meteorological Society*, *92*(12), 1623–1635. https://doi.org/10.1175/2011BAMS3119.1

DeMott, Paul J., Möhler, O., Cziczo, D. J., Hiranuma, N., Petters, M. D., Petters, S. S., et al. (2018). The Fifth International Workshop on Ice Nucleation phase 2 (FIN-02): Laboratory intercomparison

of ice nucleation measurements. *Atmospheric Measurement Techniques*, *11*(11), 6231–6257. https://doi.org/10.5194/amt-11-6231-2018

Deshmukh, A., Phillips, V. T. J., Bansemer, A., Patade, S., & Waman, D. (2022). New Empirical Formulation for the Sublimational Breakup of Graupel and Dendritic Snow. *Journal of the Atmospheric Sciences*, *79*(1), 317–336. https://doi.org/10.1175/JAS-D-20-0275.1

Dong, Y., Oraltay, R. G., & Hallett, J. (1994). Ice particle generation during evaporation. *Atmospheric Research*, *32*(1–4), 45–53. https://doi.org/10.1016/0169-8095(94)90050-7

Durant, A. J., & Shaw, R. A. (2005). Evaporation freezing by contact nucleation inside-out. *Geophysical Research Letters*, *32*(20), 1–4. https://doi.org/10.1029/2005GL024175

Dusek, U., Frank, G. P., Curtius, J., Drewnick, F., Schneider, J., Krten, A., et al. (2010). Enhanced organic mass fraction and decreased hygroscopicity of cloud condensation nuclei (CCN) during new particle formation events. *Geophysical Research Letters*, *37*, *L03804*. https://doi.org/10.1029/2009GL040930

Ebell, K., Nomokonova, T., Maturilli, M., & Ritter, C. (2020). Radiative effect of clouds at ny-Ålesund, svalbard, as inferred from ground-based remote sensing observations. *Journal of Applied Meteorology and Climatology*, *59*(1), 3–22. https://doi.org/10.1175/JAMC-D-19-0080.1

Fanourgakis, G. S., Kanakidou, M., Nenes, A., Bauer, S. E., Bergman, T., Carslaw, K. S., et al. (2019). Evaluation of global simulations of aerosol particle number and cloud condensation nuclei, and implications for cloud droplet formation. *Atmospheric Chemistry and Physics Discussions*, *19*, 8591–8617. https://doi.org/10.5194/acp-19-8591-2019

Farrington, R. J., Connolly, P. J., Lloyd, G., Bower, K. N., Flynn, M. J., Gallagher, M. W., et al. (2016). Comparing model and measured ice crystal concentrations in orographic clouds during the INUPIAQ campaign. *Atmospheric Chemistry and Physics*, *16*(8), 4945–4966. https://doi.org/10.5194/acp-16-4945-2016

Ferrone, A., & Berne, A. (2023). Radar and ground-level measurements of clouds and precipitation collected during the POPE 2020 campaign at Princess Elisabeth Antarctica. *Earth System Science Data*, *15*(3), 1115–1132. https://doi.org/10.5194/essd-15-1115-2023

Field, P. R., & Heymsfield, A. J. (2015). Importance of snow to global precipitation. *Geophysical Research Letters*, *42*(21), 9512–9520. https://doi.org/10.1002/2015GL065497

Field, P. R., Hogan, R. J., Brown, P. R. A., Illingworth, A. J., Choularton, T. W., Kaye, P. H., et al. (2004). Simultaneous radar and aircraft observations of mixed-phase cloud at the 100 m scale. *Quarterly Journal of the Royal Meteorological Society*, *130*(600 PART A), 1877–1904. https://doi.org/10.1256/qj.03.102

Field, P. R., Lawson, R. P., Brown, P. R. A., Lloyd, G., Westbrook, C., Moisseev, D., et al. (2017). Chapter 7. Secondary Ice Production - current state of the science and recommendations for the future. *Meteorological Monographs*, *58*. https://doi.org/10.1175/amsmonographs-d-16-0014.1

Findeisen, W. (1938). Die kolloidmeteorologischen vorgänge bei der niederschlagsbildung. *Meteorologische Zeitschrift*, *55*, 121–133.

Foskinis, R., Nenes, A., Papayannis, A., Georgakaki, P., Eleftheriadis, K., Vratolis, S., et al. (2022). Towards reliable retrievals of cloud droplet number for non-precipitating planetary boundary layer clouds and their susceptibility to aerosol. *Frontiers in Remote Sensing*, *3*. https://doi.org/10.3389/frsen.2022.958207

Fountoukis, C., & Nenes, A. (2005). Continued development of a cloud droplet formation parameterization for global climate models. *Journal of Geophysical Research*, *110*, *D1121*. https://doi.org/10.1029/2004JD005591

Fountoukis, C., Nenes, A., Meskhidze, N., Bahreini, R., Conant, W. C., Jonsson, H., et al. (2007). Aerosol-cloud drop concentration closure for clouds sampled during the International Consortium for Atmospheric Research on Transport and Transformation 2004 campaign. *Journal of Geophysical Research*, *112*. https://doi.org/10.1029/2006JD007272

Fridlind, Ann M., Ackerman, A. S., McFarquhar, G., Zhang, G., Poellot, M. R., DeMott, P. J., et al. (2007). Ice properties of single-layer stratocumulus during the Mixed-Phase Arctic Cloud Experiment: 2. Model results. *Journal of Geophysical Research Atmospheres*, *112*(24), 1–25. https://doi.org/10.1029/2007JD008646

Fu, S., Deng, X., Shupe, M. D., & Xue, H. (2019). A modelling study of the continuous ice formation in an autumnal Arctic mixed-phase cloud case. *Atmospheric Research*, *228*(March), 77–85. https://doi.org/10.1016/j.atmosres.2019.05.021

Fugal, J. P., Schulz, T. J., & Shaw, R. A. (2009). Practical methods for automated reconstruction and characterization of particles in digital in-line holograms. *Measurement Science and Technology*, *20*. https://doi.org/10.1088/0957-0233/20/7/075501

Geerts, B., Pokharel, B., & Kristovich, D. A. R. (2015). Blowing snow as a natural glaciogenic cloud seeding mechanism. *Monthly Weather Review*, *143*(12), 5017–5033. https://doi.org/10.1175/MWR-D-15-0241.1

Gentine, P., Pritchard, M., Rasp, S., Reinaudi, G., & Yacalis, G. (2018). Could Machine Learning Break the Convection Parameterization Deadlock? *Geophysical Research Letters*, *45*(11), 5742–5751. https://doi.org/10.1029/2018GL078202

Georgakaki, P., Bougiatioti, A., Wieder, J., Mignani, C., Ramelli, F., Kanji, Z. A., et al. (2021). On the drivers of droplet variability in alpine mixed-phase clouds. *Atmospheric Chemistry and Physics*, *21*(14), 10993–11012. https://doi.org/10.5194/acp-21-10993-2021

Georgakaki, P., Sotiropoulou, G., Vignon, É., Billault-Roux, A. C., Berne, A., & Nenes, A. (2022). Secondary ice production processes in wintertime alpine mixed-phase clouds. *Atmospheric Chemistry and Physics*, *22*(3), 1965–1988. https://doi.org/10.5194/acp-22-1965-2022

Gerber, F., Sharma, V., & Lehning, M. (2023). CRYOWRF—Model Evaluation and the Effect of Blowing Snow on the Antarctic Surface Mass Balance. *Journal of Geophysical Research: Atmospheres*, *128*(12), 1–19. https://doi.org/10.1029/2022jd037744

Gerber, H. (1991). Direct measurement of suspended particulate volume concentration and far-infrared extinction coefficient with a laser diffraction instrument. *Applied Optics*, *30*, 4824–4831. https://doi.org/10.1016/0021-8502(89)90880-X

Gettelman, A., Hannay, C., Bacmeister, J. T., Neale, R. B., Pendergrass, A. G., Danabasoglu, G., et al. (2019). High Climate Sensitivity in the Community Earth System Model Version 2 (CESM2). *Geophysical Research Letters*, *46*(14), 8329–8337. https://doi.org/10.1029/2019GL083978

Gettelman, A., Gagne, D. J., Chen, C. C., Christensen, M. W., Lebo, Z. J., Morrison, H., & Gantos, G. (2021). Machine Learning the Warm Rain Process. *Journal of Advances in Modeling Earth Systems*, *13*(2). https://doi.org/10.1029/2020MS002268

Ghan, S. J., Guzman, G., & Abdul-Razzak, H. (1998). Competition between sea salt and sulfate particles as cloud condensation nuclei. *Journal of the Atmospheric Sciences*, *55*(22), 3340–3347. https://doi.org/10.1175/1520-0469(1998)055<3340:CBSSAS>2.0.CO;2

Ghan, S. J., Abdul-Razzak, H., Nenes, A., Ming, Y., Liu, X., Ovchinnikov, M., et al. (2011). Droplet nucleation: Physically-based parameterizations and comparative evaluation. *Journal of Advances in Modeling Earth Systems*, *3*(4), 1–34. https://doi.org/10.1029/2011ms000074

Giangrande, S. E., Toto, T., Bansemer, A., Kumjian, M. R., Mishra, S., & Ryzhkov, A. V. (2016). Insights into riming and aggregation processes as revealed by aircraft, radar, and disdrometer observations for a 27 April 2011 widespread precipitation event. *Journal of Geophysical Research: Atmospheres*, *121*, 5846–5863. https://doi.org/10.1002/2015JD024537

Goosse, H., Kay, J. E., Armour, K. C., Bodas-Salcedo, A., Chepfer, H., Docquier, D., et al. (2018). Quantifying climate feedbacks in polar regions. *Nature Communications*, *9*(1). https://doi.org/10.1038/s41467-018-04173-0

Grazioli, J., Lloyd, G., Panziera, L., Hoyle, C. R., Connolly, P. J., Henneberger, J., & Berne, A. (2015). Polarimetric radar and in situ observations of riming and snowfall microphysics during CLACE 2014. *Atmospheric Chemistry and Physics*, *15*, 13787–13802. https://doi.org/10.5194/acp-15-13787-2015

Grazioli, Jacopo, Ghiggi, G., Billault-Roux, A. C., & Berne, A. (2022). MASCDB, a database of images, descriptors and microphysical properties of individual snowflakes in free fall. *Scientific Data*, *9*(1), 1–16. https://doi.org/10.1038/s41597-022-01269-7

Griesche, H. J., Seifert, P., Ansmann, A., Baars, H., Barrientos Velasco, C., Bühl, J., et al. (2020). Application of the shipborne remote sensing supersite OCEANET for profiling of Arctic aerosols and clouds during Polarstern cruise PS106,. *Atmospheric Measurement Techniques*, *13*, 5335–5358. https://doi.org/https://doi.org/10.5194/amt-13-5335-2020

Griggs, D. J., & Choularton, T. W. (1983). Freezing modes of riming droplets with application to ice splinter production. *Quarterly Journal of the Royal Meteorological Society*, *109*(459), 243–253. https://doi.org/10.1002/qj.49710945912

Griggs, D. J., & Choularton, T. W. (1986). A laboratory study of secondary ice particle production by the fragmentation of rime and vapour-grown ice crystals. *Quarterly Journal of the Royal Meteorological Society*, *112*(471), 149–163. https://doi.org/10.1256/smsqj.47108

Grosvenor, D. P., Sourdeval, O., Zuidema, P., Ackerman, A., Alexandrov, M. D., Bennartz, R., et al. (2018). Remote Sensing of Droplet Number Concentration in Warm Clouds: A Review of the Current State of Knowledge and Perspectives. *Reviews of Geophysics*, *56*(2), 409–453. https://doi.org/10.1029/2017RG000593

Grubisic, V., & Billings, B. J. (2008). Climatology of the Sierra Nevada mountain-wave events. *Monthly Weather Review*, *136*, 757–768. https://doi.org/10.1175/2007MWR1902.1

Grundner, A., Beucler, T., Gentine, P., Iglesias-Suarez, F., Giorgetta, M. A., & Eyring, V. (2022). Deep Learning Based Cloud Cover Parameterization for ICON. *Journal of Advances in Modeling Earth Systems*, *14*(12), 1–24. https://doi.org/10.1029/2021MS002959

Grzegorczyk, P., Yadav, S., Zanger, F., Theis, A., Mitra, S. K., Borrmann, S., & Szakáll, M. (2023). Fragmentation of ice particles : laboratory experiments on graupel-graupel and graupel-snowflake collisions. *Atmospheric Chemistry and Physics Discussion*. https://doi.org/10.5194/egusphere-2023-1074

Guyot, G., Gourbeyre, C., Febvre, G., Shcherbakov, V., Burnet, F., Dupont, J. C., et al. (2015). Quantitative evaluation of seven optical sensors for cloud microphysical measurements at the Puy-de-Dôme Observatory, France. *Atmospheric Measurement Techniques*, *8*(10), 4347–4367. https://doi.org/10.5194/amt-8-4347-2015

Hallett, J., & Mossop, S. C. (1974). Production of secondary ice particles during the riming process. *Nature*, *249*, 26–28. https://doi.org/10.1038/249026a0

Hammer, E., Bukowiecki, N., Gysel, M., Jurányi, Z., Hoyle, C. R., Vogt, R., et al. (2014). Investigation of the effective peak supersaturation for liquid-phase clouds at the high-alpine site Jungfraujoch , Switzerland (3580 m a . s . l .). *Atmospheric Chemistry and Physics*, *14*, 1123–1139. https://doi.org/10.5194/acp-14-1123- 2014

Hammer, E., Bukowiecki, N., Luo, B. P., Lohmann, U., Marcolli, C., Weingartner, E., et al. (2015). Sensitivity estimations for cloud droplet formation in the vicinity of the high-alpine research station Jungfraujoch (3580 m a . s . l .). *Atmospheric Chemistry and Physics*, *15*, 10309–10323. https://doi.org/10.5194/acp-15-10309-2015

Han, Y., Zhang, G. J., Huang, X., & Wang, Y. (2020). A Moist Physics Parameterization Based on Deep Learning. *Journal of Advances in Modeling Earth Systems*, *12*(9). https://doi.org/10.1029/2020MS002076

Harris, L. M., & Durran, D. R. (2010). An Idealized Comparison of One-Way and Two-Way Grid Nesting. *Monthly Weather Review*, *138*(6), 2174–2187. https://doi.org/10.1175/2010MWR3080.1

Hartmann, M., Adachi, K., Eppers, O., Haas, C., Herber, A., Holzinger, R., et al. (2020). Wintertime Airborne Measurements of Ice Nucleating Particles in the High Arctic: A Hint to a Marine, Biogenic Source for Ice Nucleating Particles. *Geophysical Research Letters*, *47*(13). https://doi.org/10.1029/2020GL087770

Hartmann, S., Seidel, J., Keinert, A., Kiselev, A., Leisner, T., & Stratmann, F. (2023). Secondary ice production - No evidence of a productive rime-splintering mechanisms during dry and wet growth. In *EGU General Assembly 2023, Vienna, Austria*. https://doi.org/https://doi.org/10.5194/egusphere-egu23-11199

Henneberg, O., Henneberger, J., & Lohmann, U. (2017). Formation and development of orographic mixed-phase clouds. *Journal of the Atmospheric Sciences*, *74*, 3703–3724. https://doi.org/10.1175/JAS-D-16-0348.1

Henneberger, J., Fugal, J. P., Stetzer, O., & Lohmann, U. (2013). HOLIMO II: A digital holographic instrument for ground-based in situ observations of microphysical properties of mixed-phase clouds. *Atmospheric Measurement Techniques*, *6*, 2975–2987. https://doi.org/10.5194/amt-6-2975-2013

Herrmann, E., Weingartner, E., Henne, S., Vuilleumier, L., Bukowiecki, N., Steinbacher, M., et al. (2015). Analysis of long-term aerosol size distribution data from Jungfraujoch with emphasis on free tropospheric conditions, cloud influence, and air mass transport. *Journal of Geophysical Research Atmospheres*, *120*, 9459–9480. https://doi.org/10.1002/2015JD023660

Hersbach, H., Bell, B., Berrisford, P., Hirahara, S., Horányi, A., Muñoz-Sabater, J., et al. (2020). The ERA5 global reanalysis. *Quarterly Journal of the Royal Meteorological Society*, *146*(730), 1999–2049. https://doi.org/10.1002/qj.3803

Heymsfield, A., & Willis, P. (2014). Cloud conditions favoring secondary ice particle production in tropical maritime convection. *Journal of the Atmospheric Sciences*, *71*(12), 4500–4526. https://doi.org/10.1175/JAS-D-14-0093.1

Heymsfield, A. J., & Mossop, S. C. (1984). Temperature dependence of secondary ice crystal production during soft hail growth by riming. *Quarterly Journal of the Royal Meteorological Society*, *110*(465), 765–770. https://doi.org/10.1002/qj.49711046512

Heymsfield, A. J., Schmitt, C., Bansemer, A., & Twohy, C. H. (2010). Improved representation of ice particle masses based on observations in natural clouds. *Journal of the Atmospheric Sciences*, *67*(10), 3303–3318. https://doi.org/10.1175/2010JAS3507.1

Heymsfield, A. J., Schmitt, C., Chen, C. C. J., Bansemer, A., Gettelman, A., Field, P. R., & Liu, C. (2020). Contributions of the Liquid and Ice Phases to Global Surface Precipitation: Observations and Global Climate Modeling. *Journal of the Atmospheric Sciences*, *77*(8), 2629–2648. https://doi.org/10.1175/JAS-D-19-0352.1

Hoarau, T., Pinty, J. P., & Barthe, C. (2018). A representation of the collisional ice break-up process in the two-moment microphysics LIMA v1.0 scheme of Meso-NH. *Geoscientific Model Development*, *11*(10), 4269–4289. https://doi.org/10.5194/gmd-11-4269-2018

Hobbs, P. V., & Rangno, A. L. (1990). Rapid development of high ice particle concentrations in small polar maritime cumuliform clouds. *Journal of the Atmospheric Sciences*, *47*, 2710–2722. https://doi.org/10.1175/1520- 0469(1990)047,2710:RDOHIP.2.0.CO;2.

Hong, S. Y., Noh, Y., & Dudhia, J. (2006). A new vertical diffusion package with an explicit treatment of entrainment processes. *Monthly Weather Review*, *134*(9), 2318–2341. https://doi.org/10.1175/MWR3199.1

Hoose, C. (2022). Another Piece of Evidence for Important but Uncertain Ice Multiplication Processes. *AGU Advances*, *3*(2), 2021–2023. https://doi.org/10.1029/2022AV000669

Hoose, C., & Möhler, O. (2012). *Heterogeneous ice nucleation on atmospheric aerosols: A review of results from laboratory experiments*. *Atmospheric Chemistry and Physics* (Vol. 12). https://doi.org/10.5194/acp-12-9817-2012

Hourdin, F., Mauritsen, T., Gettelman, A., Golaz, J. C., Balaji, V., Duan, Q., et al. (2017). The art and science of climate model tuning. *Bulletin of the American Meteorological Society*, *98*(3), 589–602. https://doi.org/10.1175/BAMS-D-15-00135.1

Hoyle, C. R., Webster, C. S., Rieder, H. E., Nenes, A., Hammer, E., Herrmann, E., et al. (2016). Chemical and physical influences on aerosol activation in liquid clouds : a study based on observations from the Jungfraujoch , Switzerland. *Atmospheric Chemistry and Physics*, *16*, 4043–4061. https://doi.org/10.5194/acp-16-4043-2016

Hu, M., Peng, J., Sun, K., Yue, D., Guo, S., Wiedensohler, A., & Wu, Z. (2012). Estimation of size-resolved ambient particle density based on the measurement of aerosol number, mass, and chemical size distributions in the winter in Beijing. *Environmental Science and Technology*, *46*(18), 9941–9947. https://doi.org/10.1021/es204073t

Huang, Y., Wu, W., McFarquhar, G. M., Xue, M., Morrison, H., Milbrandt, J., et al. (2022). Microphysical processes producing high ice water contents (HIWCs) in tropical convective clouds during the HAIC-HIWC field campaign: Dominant role of secondary ice production. *Atmospheric Chemistry and Physics*, *22*(4), 2365–2384. https://doi.org/10.5194/acp-22-2365-2022

Ickes, L., Eriksson, P., Frostenberg, H., Ageitos, M. G., Hallborn, H., Lewinschal, A., et al. (2023). How important are secondary ice processes – preliminary results from FOR-ICE. In *EGU General Assembly 2023, Vienna, Austria*. https://doi.org/https://doi.org/10.5194/egusphere-egu23-10696

Ikawa, M., & Saito, K. (1991). Description of a Non-hydrostatic Model Developed at the Forecast Research Department of the MR. *MRI Tech. Rep.*, *28*, 238 pp. https://doi.org/https://doi.org/10.11483/mritechrepo.28

IPCC. (2013). Climate Change 2013: The Physical Science Basis. Contribution of Working Group I to the Fifth Assessment Report of the Intergovernmental Panel on Climate Change, edited by: Stocker, T. F., Qin, D., Plattner, G.-K., Tignor, M., Allen, S. K., Boschung. *Cambridge University Press, Cambridge, UK and New York, NY, USA*, 1535 pp. https://doi.org/10.1017/CBO9781107415324

Irrgang, C., Boers, N., Sonnewald, M., Barnes, E. A., Kadow, C., Staneva, J., & Saynisch-Wagner, J. (2021). Towards neural Earth system modelling by integrating artificial intelligence in Earth system science. *Nature Machine Intelligence*, *3*(8), 667–674. https://doi.org/10.1038/s42256-021-00374-3

James, R. L., Phillips, V. T. J., & Connolly, P. J. (2021). Secondary ice production during the break-up of freezing water drops on impact with ice particles. *Atmospheric Chemistry and Physics*, *21*(24), 18519–18530. https://doi.org/10.5194/acp-21-18519-2021

James, R. L., Crosier, J., & Connolly, P. J. (2023). A bin-microphysics parcel model investigation of secondary ice formation in an idealised shallow convective cloud. *Atmospheric Chemistry and Physics*, *23*, 9099–9121. https://doi.org/https://doi.org/10.5194/acp-23-9099-2023

Janjić, Z. I. (2002). Nonsingular Implementation of the Mellor-Yamada Level 2.5 Scheme in the NCEP Meso model. *NOAA/NWS/NCEP Office Note 437*, 61 pp.

Järvinen, E., McCluskey, C. S., Waitz, F., Schnaiter, M., Bansemer, A., Bardeen, C. G., et al. (2022). Evidence for Secondary Ice Production in Southern Ocean Maritime Boundary Layer Clouds. *Journal of Geophysical Research: Atmospheres*, *127*(16), 1–31. https://doi.org/10.1029/2021JD036411

Jensen, A. A., Harrington, J. Y., Morrison, H., & Milbrandt, J. A. (2017). Predicting ice shape evolution in a bulk microphysics model. *Journal of the Atmospheric Sciences*, *74*(6), 2081–2104. https://doi.org/10.1175/JAS-D-16-0350.1

Jensen, J. B., & Charlson, R. J. (1984). On the efficiency of nucleation scavenging. *Tellus B*, *36 B*(5), 367–375. https://doi.org/https://doi.org/10.3402/tellusb.v36i5.14917

Jurányi, Z., Gysel, M., Weingartner, E., Decarlo, P. F., Kammermann, L., & Baltensperger, U. (2010). Measured and modelled cloud condensation nuclei number concentration at the high alpine site Jungfraujoch. *Atmospheric Chemistry and Physics*, *10*, 7891–7906. https://doi.org/10.5194/acp-10-7891-2010

Jurányi, Z., Gysel, M., Weingartner, E., Bukowiecki, N., Kammermann, L., & Baltensperger, U. (2011). A 17 month climatology of the cloud condensation nuclei number concentration at the high alpine site Jungfraujoch. *Journal of Geophysical Research*, *116*, *D1020*. https://doi.org/10.1029/2010JD015199

Kacarab, M., Lee Thornhill, K., Dobracki, A., Howell, S. G., O'Brien, J. R., Freitag, S., et al. (2020). Biomass burning aerosol as a modulator of the droplet number in the southeast Atlantic region. *Atmospheric Chemistry and Physics*, *20*, 3029–3040. https://doi.org/10.5194/acp-20-3029-2020

Kalesse, H., Szyrmer, W., Kneifel, S., Kollias, P., & Luke, E. (2016). Fingerprints of a riming event on cloud radar Doppler spectra: Observations and modeling. *Atmospheric Chemistry and Physics*, *16*(5), 2997–3012. https://doi.org/10.5194/acp-16-2997-2016

Kalkavouras, P., Bougiatioti, A., Kalivitis, N., Stavroulas, I., Tombrou, M., Nenes, A., & Mihalopoulos, N. (2019). Regional new particle formation as modulators of cloud condensation nuclei and cloud droplet number in the eastern Mediterranean. *Atmospheric Chemistry and Physics*, *19*, 6185–6203. https://doi.org/10.5194/acp-19-6185-2019

Kammermann, L., Gysel, M., Weingartner, E., & Baltensperger, U. (2010). 13-month climatology of the aerosol hygroscopicity at the free tropospheric site Jungfraujoch (3580 m a.s.l.). *Atmospheric Chemistry and Physics*, *10*. https://doi.org/10.5194/acp-10-10717-2010

Kanji, Z. A., Ladino, L. A., Wex, H., Boose, Y., Burkert-Kohn, M., Cziczo, D. J., & Krämer, M. (2017). Overview of Ice Nucleating Particles. *Meteorological Monographs*, *58*, 1.1-1.33. https://doi.org/10.1175/amsmonographs-d-16-0006.1

Karalis, M., Sotiropoulou, G., Abel, S. J., Bossioli, E., Georgakaki, P., Methymaki, G., et al. (2022). Effects of secondary ice processes on a stratocumulus to cumulus transition during a cold-air outbreak. *Atmospheric Research*, *277*. https://doi.org/10.1016/j.atmosres.2022.106302

Kay, J. E., L'Ecuyer, T., Chepfer, H., Loeb, N., Morrison, A., & Cesana, G. (2016). Recent Advances in Arctic Cloud and Climate Research. *Current Climate Change Reports*, *2*(4), 159–169. https://doi.org/10.1007/s40641-016-0051-9

Keinert, A., Spannagel, D., Leisner, T., & Kiselev, A. (2020). Secondary ice production upon freezing of freely falling drizzle droplets. *Journal of the Atmospheric Sciences*, *77*(8), 2959–2967. https://doi.org/10.1175/JAS-D-20-0081.1

Ketterer, C., Zieger, P., Bukowiecki, N., Collaud Coen, M., Maier, O., Ruffieux, D., & Weingartner, E. (2014). Investigation of the Planetary Boundary Layer in the Swiss Alps Using Remote Sensing and In Situ Measurements. *Boundary-Layer Meteorology*, *151*(2), 317–334. https://doi.org/10.1007/s10546-013-9897-8

King, W. D., & Fletcher, N. H. (1976). Thermal Shock as an Ice Multiplication Mechanism. Part I. Theory. *Journal of the Atmospheric Sciences*, *33*, 85–96. https://doi.org/https://doi.org/10.1175/1520-0469(1976) 033<0085:TSAAIM>2.0.CO;2

Kleinheins, J., Kiselev, A., Keinert, A., Kind, M., & Leisner, T. (2021). Thermal imaging of freezing drizzle droplets: pressure release events as a source of secondary ice particles. *Journal of the Atmospheric Sciences*, *78*(5), 1–28. https://doi.org/10.1175/jas-d-20-0323.1

Kleissl, J., Honrath, R. E., Dziobak, M. P., Tanner, D., Val Martín, M., Owen, R. C., & Helmig, D. (2007). Occurrence of upslope flows at the Pico mountaintop observatory: A case study of orographic flows on a small, volcanic island. *Journal of Geophysical Research Atmospheres*, *112*, *D10S3*. https://doi.org/10.1029/2006JD007565

Kneifel, S., & Moisseev, D. (2020). Long-term statistics of riming in nonconvective clouds derived from ground-based doppler cloud radar observations. *Journal of the Atmospheric Sciences*, *77*(10), 3495–3508. https://doi.org/10.1175/JAS-D-20-0007.1

Knopf, D. A., & Alpert, P. A. (2023). Atmospheric ice nucleation. *Nature Reviews Physics*, *5*(4), 203–217. https://doi.org/10.1038/s42254-023-00570-7

Korolev, A., McFarquhar, G., Field, P. R., Franklin, C., Lawson, P., Wang, Z., et al. (2017). Mixed-Phase Clouds: Progress and Challenges. *Meteorological Monographs*, *58*, 5.1-5.50. https://doi.org/10.1175/amsmonographs-d-17-0001.1

Korolev, A. V., Emery, E. F., Strapp, J. W., Cober, S. G., Isaac, G. A., Wasey, M., & Marcotte, D. (2011). Small ice particles in tropospheric clouds: Fact or artifact? Airborne icing instrumentation evaluation experiment. *Bulletin of the American Meteorological Society*, *92*(8), 967–973. https://doi.org/10.1175/2010BAMS3141.1

Korolev, A. V., Emery, E. F., Strapp, J. W., Cober, S. G., & Isaac, G. A. (2013). Quantification of the effects of shattering on airborne ice particle measurements. *Journal of Atmospheric and Oceanic Technology*, *30*(11), 2527–2553. https://doi.org/10.1175/JTECH-D-13-00115.1

Korolev, A.i, & Isaac, G. (2003). Phase transformation of mixed-phase clouds. *Quarterly Journal of the Royal Meteorological Society*, *129*, 19–38. https://doi.org/10.1256/qj.01.203

Korolev, A., & Leisner, T. (2020). *Review of experimental studies of secondary ice production*. *Atmospheric Chemistry and Physics* (Vol. 20). https://doi.org/10.5194/acp-20-11767-2020

Korolev, A., & Milbrandt, J. (2022). How Are Mixed-Phase Clouds Mixed? *Geophysical Research Letters*, *49*(18). https://doi.org/10.1029/2022GL099578

Korolev, A., Heckman, I., Wolde, M., Ackerman, A. S., Fridlind, A. M., Ladino, L. A., et al. (2020). A new look at the environmental conditions favorable to secondary ice production. *Atmospheric Chemistry and Physics*, *20*(3), 1391–1429. https://doi.org/10.5194/acp-20-1391-2020

Korolev, A., Demott, P. J., Heckman, I., Wolde, M., Williams, E., Smalley, D. J., & Donovan, M. F. (2022). Observation of secondary ice production in clouds at low temperatures. *Atmospheric Chemistry and Physics*, *22*(19), 13103–13113. https://doi.org/10.5194/acp-22-13103-2022

Korolev, A. V., & Mazin, I. P. (2003). Supersaturation of water vapor in clouds. *Journal of the Atmospheric Sciences*, *60*(24), 2957–2974. https://doi.org/10.1175/1520-0469(2003)060<2957:SOWVIC>2.0.CO;2

Korolev, A. V., Isaac, G. A., Cober, S. G., Strapp, J. W., & Hallett, J. (2003). Microphysical characterization of mixed-phase clouds. *Quarterly Journal of the Royal Meteorological Society*, *129*(587 PART A), 39–65. https://doi.org/10.1256/qj.01.204

Krayer, M., Chouippe, A., Uhlmann, M., Dušek, J., & Leisner, T. (2021). On the ice-nucleating potential of warm hydrometeors in mixed-phase clouds. *Atmospheric Chemistry and Physics*, *21*(1), 561–575. https://doi.org/10.5194/acp-21-561-2021

Krinner, G., Derksen, C., Essery, R., Flanner, M., Hagemann, S., Clark, M., et al. (2018). ESM-SnowMIP: Assessing snow models and quantifying snow-related climate feedbacks. *Geoscientific Model Development*, *11*(12), 5027–5049. https://doi.org/10.5194/gmd-11-5027-2018

Küchler, N., Kneifel, S., Löhnert, U., Kollias, P., Czekala, H., & Rose, T. (2017). A W-band radar-radiometer system for accurate and continuous monitoring of clouds and precipitation. *Journal of Atmospheric and Oceanic Technology*, *34*(11), 2375–2392. https://doi.org/10.1175/JTECH-D-17-0019.1

Lacher, L., Lohmann, U., Boose, Y., Zipori, A., Herrmann, E., Bukowiecki, N., et al. (2017). The Horizontal Ice Nucleation Chamber (HINC): INP measurements at conditions relevant for mixed-phase clouds at the High Altitude Research Station Jungfraujoch. *Atmospheric Chemistry and Physics*, *17*(24), 15199–15224. https://doi.org/10.5194/acp-17-15199-2017

Lacher, L., Clemen, H. C., Shen, X., Mertes, S., Gysel-Beer, M., Moallemi, A., et al. (2021). Sources and nature of ice-nucleating particles in the free troposphere at Jungfraujoch in winter 2017. *Atmospheric Chemistry and Physics*, *21*(22), 16925–16953. https://doi.org/10.5194/acp-21-16925-2021

Ladino, L. A., Korolev, A., Heckman, I., Wolde, M., Fridlind, A. M., & Ackerman, A. S. (2017). On the role of ice-nucleating aerosol in the formation of ice particles in tropical mesoscale convective systems. *Geophysical Research Letters*, *44*(3), 1574–1582. https://doi.org/10.1002/2016GL072455

Ladino Moreno, L. A., Stetzer, O., & Lohmann, U. (2013). Contact freezing: A review of experimental studies. *Atmospheric Chemistry and Physics*, *13*(19), 9745–9769. https://doi.org/10.5194/acp-13-9745-2013

Lance, S., Brock, C. A., Rogers, D., & Gordon, J. A. (2010). Water droplet calibration of the Cloud Droplet Probe (CDP) and in-flight performance in liquid, ice and mixed-phase clouds during ARCPAC. *Atmospheric Measurement Techniques*, *3*(6), 1683–1706. https://doi.org/10.5194/amt-3-1683-2010

Lance, S., Shupe, M. D., Feingold, G., Brock, C. A., Cozic, J., Holloway, J. S., et al. (2011). Cloud condensation nuclei as a modulator of ice processes in Arctic mixed-phase clouds. *Atmospheric Chemistry and Physics*, *11*(15), 8003–8015. https://doi.org/10.5194/acp-11-8003-2011

Langham, E. J., & Mason, B. J. (1958). The heterogeneous and homogeneous nucleation of supercooled water. *Proceedings of the Royal Society of London. Series A. Mathematical and Physical Sciences*, *247*(1251), 493–504. https://doi.org/10.1098/rspa.1958.0207

Lanz, V. A., Prévôt, A. S. H., Alfarra, M. R., Weimer, S., Mohr, C., Decarlo, P. F., et al. (2010). Characterization of aerosol chemical composition with aerosol mass spectrometry in Central Europe: An overview. *Atmospheric Chemistry and Physics*, *10*, 10453–10471. https://doi.org/10.5194/acp-10-10453-2010

Lasher-Trapp, S., Leon, D. C., DeMott, P. J., Villanueva-Birriel, C. M., Johnson, A. V., Moser, D. H., et al. (2016). A multisensor investigation of rime splintering in tropical maritime cumuli. *Journal of the Atmospheric Sciences*, *73*, 2547–2564. https://doi.org/10.1175/JAS-D-15-0285.1

Latham, J., & Warwicker, R. (1980). Charge transfer accompanying the splashing of supercooled raindrops on hailstones. *Quarterly Journal of the Royal Meteorological Society*, *106*(449), 559–568. https://doi.org/10.1002/qj.49710644912

Lathem, T. L., Beyersdorf, A. J., Thornhill, K. L., Winstead, E. L., Cubison, M. J., Hecobian, A., et al. (2013). Analysis of CCN activity of Arctic aerosol and Canadian biomass burning during summer 2008. *Atmospheric Chemistry and Physics*, *13*, 2735–2756. https://doi.org/10.5194/acp-13-2735-2013

Lauber, A., Kiselev, A., Pander, T., Handmann, P., & Leisner, T. (2018). Secondary ice formation during freezing of levitated droplets. *Journal of the Atmospheric Sciences*, *75*(8), 2815–2826. https://doi.org/10.1175/JAS-D-18-0052.1

Lauber, A., Henneberger, J., Mignani, C., Ramelli, F., Pasquier, J., Wieder, J., & Lohmann, U. (2020). Continuous secondary ice production initiated by updrafts through the melting layer in mountainous regions.

Lauber, A., Henneberger, J., Mignani, C., Ramelli, F., Pasquier, J. T., Wieder, J., et al. (2021). Continuous secondary-ice production initiated by updrafts through the melting layer in mountainous regions. *Atmospheric Chemistry and Physics*, *21*(5), 3855–3870. https://doi.org/10.5194/acp-21-3855-2021

Lawson, R. P., Woods, S., & Morrison, H. (2015). The microphysics of ice and precipitation development in tropical cumulus clouds. *Journal of the Atmospheric Sciences*, *72*(6), 2429–2445. https://doi.org/10.1175/JAS-D-14-0274.1

Lawson, R. Paul, O'Connor, D., Zmarzly, P., Weaver, K., Baker, B., Mo, Q., & Jonsson, H. (2006). The 2D-S (stereo) probe: Design and preliminary tests of a new airborne, high-speed, high-resolution particle imaging probe. *Journal of Atmospheric and Oceanic Technology*, *23*(11), 1462–1477. https://doi.org/10.1175/JTECH1927.1

Lawson, R. Paul, Korolev, A. V., DeMott, P. J., Heymsfield, A. J., Bruintjes, R. T., Wolff, C. A., et al. (2023). The Secondary Production of Ice in Cumulus Experiment (SPICULE). *Bulletin of the American Meteorological Society*, *104*(1), E51–E76. https://doi.org/10.1175/BAMS-D-21-0209.1

Lehning, M., I.Volksch, D.Gustafsson, Nguyen, T. A., Stahli, M., & Zappa, M. (2006). ALPINE3D: A detailed model of mountain surface processes and its application to snow hydrology. *Hydrological Processes*, *20*, 2111–2128. https://doi.org/10.1002/hyp.6204

Li, H., Korolev, A., & Moisseev, D. (2021). Supercooled liquid water and secondary ice production in Kelvin-Helmholtz instability as revealed by radar Doppler spectra observations. *Atmospheric Chemistry and Physics*, *21*(17), 13593–13608. https://doi.org/10.5194/acp-21-13593-2021

Li, H., Möhler, O., Petäjä, T., & Moisseev, D. (2021). Two-year statistics of columnar-ice production in stratiform clouds over Hyytiälä, Finland: Environmental conditions and the relevance to secondary ice production. *Atmospheric Chemistry and Physics*, *21*(19), 14671–14686. https://doi.org/10.5194/acp-21-14671-2021

Libbrecht, K. G. (2017). Physical Dynamics of Ice Crystal Growth. *Annual Review of Materials Research*, *47*, 271–295. https://doi.org/10.1146/annurev-matsci-070616-124135

Listowski, C., & Lachlan-Cope, T. (2017). The microphysics of clouds over the Antarctic Peninsula - Part 2: Modelling aspects within Polar WRF. *Atmospheric Chemistry and Physics*, *17*(17), 10195–10221. https://doi.org/10.5194/acp-17-10195-2017

Liu, Yangang, Yau, M. K., Shima, S. ichiro, Lu, C., & Chen, S. (2023). Parameterization and Explicit Modeling of Cloud Microphysics: Approaches, Challenges, and Future Directions. *Advances in Atmospheric Sciences*, *40*(5), 747–790. https://doi.org/10.1007/s00376-022-2077-3

Liu, Yinghui, Key, J. R., Ackerman, S. A., Mace, G. G., & Zhang, Q. (2012). Arctic cloud macrophysical characteristics from CloudSat and CALIPSO. *Remote Sensing of Environment*, *124*, 159–173. https://doi.org/10.1016/j.rse.2012.05.006

Lloyd, G., Choularton, T. W., Bower, K. N., Gallagher, M. W., Connolly, P. J., Flynn, M., et al. (2015). The origins of ice crystals measured in mixed-phase clouds at the high-alpine site Jungfraujoch. *Atmospheric Chemistry and Physics*, *15*(22), 12953–12969. https://doi.org/10.5194/acp-15-12953-2015

Lohmann, U. (2002). A glaciation indirect aerosol effect caused by soot aerosols. *Geophysical Research Letters*, *29*(4). https://doi.org/10.1029/2001GL014357

Lohmann, U., & Feichter, J. (2005). Global indirect aerosol effects: a review. *Atmospheric Chemistry and Physics*, *5*, 715–737. https://doi.org/10.5194/acp-5-715-2005

Lohmann, U., Henneberger, J., Henneberg, O., Fugal, J. P., Bühl, J., & Kanji, Z. A. (2016). Persistence of orographic mixed-phase clouds. *Geophysical Research Letters*, *43*(19), 10,512-10,519. https://doi.org/10.1002/2016GL071036

Lohmann, Ulrike. (2017). Anthropogenic Aerosol Influences on Mixed-Phase Clouds. *Current Climate Change Reports*, *3*, 32–44. https://doi.org/10.1007/s40641-017-0059-9

Lowenthal, D., Hallar, A. G., McCubbin, I., David, R., Borys, R., Blossey, P., et al. (2016). Isotopic fractionation in wintertime orographic clouds. *Journal of Atmospheric and Oceanic Technology*, *33*(12), 2663–2678. https://doi.org/10.1175/JTECH-D-15-0233.1

Lowenthal, D. H., Hallar, A. G., David, R. O., Mccubbin, I. B., Borys, R. D., & Mace, G. G. (2019). Mixed-phase orographic cloud microphysics during StormVEx and IFRACS. *Atmospheric Chemistry and Physics*, *19*(8), 5387–5401. https://doi.org/10.5194/acp-19-5387-2019

Luke, E. P., Yang, F., Kollias, P., Vogelmann, A. M., & Maahn, M. (2021). New insights into ice multiplication using remote-sensing observations of slightly supercooled mixed-phase clouds in the Arctic. *Proceedings of the National Academy of Sciences of the United States of America*,

118(13), 1–9. https://doi.org/10.1073/pnas.2021387118

Mahesh, A., Eager, R., Campbell, J. R., & Spinhirne, J. D. (2003). Observations of blowing snow at the South Pole. *Journal of Geophysical Research: Atmospheres*, *108*(22), 1–9. https://doi.org/10.1029/2002jd003327

Mason, B. J., & Maybank, J. (1960). The fragmentation and electrification of freezing water drops. *Quarterly Journal of the Royal Meteorological Society*, *86*, 176–185. https://doi.org/10.1002/qj.49708636806

Matus, A. V., & L'Ecuyer, T. S. (2017). The role of cloud phase in Earth's radiation budget. *Journal of Geophysical Research*, *122*(5), 2559–2578. https://doi.org/10.1002/2016JD025951

McCoy, D. T., Tan, I., Hartmann, D. L., Zelinka, M. D., & Storelvmo, T. (2016). On the relationships among cloud cover, mixed-phase partitioning, and planetary albedo in GCMs. *Journal of Advances in Modeling Earth Systems*, *8*, 650–668. https://doi.org/10.1002/2015MS000589

McCoy, I. L., McCoy, D. T., Wood, R., Regayre, L., Watson-Parris, D., Grosvenor, D. P., et al. (2020). The hemispheric contrast in cloud microphysical properties constrains aerosol forcing. *Proceedings of the National Academy of Sciences of the United States of America*, *117*(32), 18998–19006. https://doi.org/10.1073/pnas.1922502117

McGovern, A., Lagerquist, R., Gagne, D. J., Jergensen, G. E., Elmore, K. L., Homeyer, C. R., & Smith, T. (2019). Making the black box more transparent: Understanding the physical implications of machine learning. *Bulletin of the American Meteorological Society*, *100*(11), 2175–2199. https://doi.org/10.1175/BAMS-D-18-0195.1

Mech, M., Maahn, M., Kneifel, S., Ori, D., Orlandi, E., Kollias, P., et al. (2020). PAMTRA 1.0: The Passive and Active Microwave radiative TRAnsfer tool for simulating radiometer and radar measurements of the cloudy atmosphere. *Geoscientific Model Development*, *13*(9), 4229–4251. https://doi.org/10.5194/gmd-13-4229-2020

Meskhidze, N., Nenes, A., Conant, W. C., & Seinfeld, J. H. (2005). Evaluation of a new cloud droplet activation parameterization with in situ data from CRYSTAL-FACE and CSTRIPE. *Journal of Geophysical Research*, *110*, *D1620*. https://doi.org/10.1029/2004JD005703

Meyers, M. P., DeMott, P. J., & Cotton, W. R. (1992). New Primary Ice-Nucleation Parameterizations in an Explicit Cloud Model. *Journal of Applied Meteorology*, *31*, 708–721. https://doi.org/10.1175/1520- 0450(1992)031<0708:NPINPI>2.0.CO;2

Mignani, C., Creamean, J. M., Zimmermann, L., Alewell, C., & Conen, F. (2019). New type of evidence for secondary ice formation at around -15 °c in mixed-phase clouds. *Atmospheric Chemistry and Physics*, *19*(2), 877–886. https://doi.org/10.5194/acp-19-877-2019

Mignani, C., Wieder, J., Sprenger, M. A., Kanji, Z. A., Henneberger, J., Alewell, C., & Conen, F. (2021). Towards parameterising atmospheric concentrations of ice-nucleating particles active at moderate supercooling. *Atmospheric Chemistry and Physics*, *21*(2), 657–664. https://doi.org/10.5194/acp-21-657-2021

Mignani, C., Zimmermann, L., Kivi, R., Berne, A., & Conen, F. (2022). Snowfall in Northern Finland derives mostly from ice clouds. *Atmospheric Chemistry and Physics*, *22*(20), 13551–13568. https://doi.org/10.5194/acp-22-13551-2022

Milbrandt, J. A., Bélair, S., Faucher, M., Vallée, M., Carrera, M. L., & Glazer, A. (2016). The pan-canadian high resolution (2.5 km) deterministic prediction system. *Weather and Forecasting*, *31*(6), 1791–1816. https://doi.org/10.1175/WAF-D-16-0035.1

Mizuno, H. (1990). Parameterization of the accretion process between different precipitation elements. *Journal of the Meteorological Society of Japan*, *68*(3), 395–398. https://doi.org/10.2151/jmsj1965.68.3_395

Möhler, O., Adams, M., Lacher, L., Vogel, F., Nadolny, J., Ullrich, R., et al. (2021). The Portable Ice Nucleation Experiment (PINE): A new online instrument for laboratory studies and automated long-term field observations of ice-nucleating particles. *Atmospheric Measurement Techniques*, *14*(2), 1143–1166. https://doi.org/10.5194/amt-14-1143-2021

Mooers, G., Pritchard, M., Beucler, T., Ott, J., Yacalis, G., Baldi, P., & Gentine, P. (2021). Assessing the Potential of Deep Learning for Emulating Cloud Superparameterization in Climate Models With Real-Geography Boundary Conditions. *Journal of Advances in Modeling Earth Systems*, *13*(5), 1–26. https://doi.org/10.1029/2020MS002385

Moore, R. H., Bahreini, R., Brock, C. A., Froyd, K. D., Cozic, J., Holloway, J. S., et al. (2011). Hygroscopicity and composition of Alaskan Arctic CCN during April 2008. *Atmospheric Chemistry and Physics*, *11*, 11807–11825. https://doi.org/10.5194/acp-11-11807-2011

Morales Betancourt, R., & Nenes, A. (2014). Understanding the contributions of aerosol properties and parameterization discrepancies to droplet number variability in a global climate model. *Atmospheric Chemistry and Physics*, *14*, 4809–4826. https://doi.org/10.5194/acp-14-4809-2014

Morales Betancourt, R., Nenes, A., Jonsson, H., Flagan, R. C., & Seinfeld, J. H. (2011). Evaluation of an entraining droplet activation parameterization using in situ cloud data. *Journal of Geophysical Research*, *116*, *D1520*. https://doi.org/10.1029/2010JD015324

Morrison, H., & Grabowski, W. (2008). Modeling Supersaturation and Subgrid-Scale Mixing with Two-Moment Bulk. *Journal of the Atmospheric Sciences*, *65*(3), 792–812. https://doi.org/10.1175/2007JAS2374.1

Morrison, H., Curry, J. A., & Khvorostyanov, V. I. (2005). A new double-moment microphysics parameterization for application in cloud and climate models. Part I: Description. *Journal of the Atmospheric Sciences*, *62*, 1678–1693. https://doi.org/10.1175/JAS3446.1

Morrison, H., Curry, J. A., Shupe, M. D., & Zuidema, P. (2005). A new double-moment microphysics scheme for application in cloud and climate models. Part II: Single-column modeling of Arctic clouds. *Journal of the Atmospheric Sciences*, *62*, 1678–1693.

Morrison, Hugh, & Grabowski, W. W. (2008). A novel approach for representing ice microphysics in models: Description and tests using a kinematic framework. *Journal of the Atmospheric Sciences*, *65*(5). https://doi.org/10.1175/2007JAS2491.1

Morrison, Hugh, & Milbrandt, J. A. (2015). Parameterization of cloud microphysics based on the prediction of bulk ice particle properties. Part I: Scheme description and idealized tests. *Journal of the Atmospheric Sciences*, *72*(1), 287–311. https://doi.org/10.1175/JAS-D-14-0065.1

Morrison, Hugh, Thompson, G., & Tatarskii, V. (2009). Impact of cloud microphysics on the development of trailing stratiform precipitation in a simulated squall line: Comparison of one- and two-moment schemes. *Monthly Weather Review*, *137*(3), 991–1007. https://doi.org/10.1175/2008MWR2556.1

Morrison, Hugh, De Boer, G., Feingold, G., Harrington, J., Shupe, M. D., & Sulia, K. (2012). Resilience of persistent Arctic mixed-phase clouds. *Nature Geoscience*, *5*(1), 11–17. https://doi.org/10.1038/ngeo1332

Morrison, Hugh, van Lier-Walqui, M., Fridlind, A. M., Grabowski, W. W., Harrington, J. Y., Hoose, C., et al. (2020). Confronting the Challenge of Modeling Cloud and Precipitation Microphysics.

Journal of Advances in Modeling Earth Systems, *12*(8). https://doi.org/10.1029/2019MS001689

Mosimann, L., Weingartner, E., & Waldvogel, A. (1994). An Analysis of Accreted Drop Sizes and Mass on Rimed Snow Crystals. *Journal of the Atmospheric Sciences*, *51*, 1548–1558. https://doi.org/10.1175/1520- 0469(1994)051<1548:AAOADS>2.0.CO;2

Motos, G., Freitas, G., Georgakaki, P., Wieder, J., Li, G., Aas, W., Lunder, C., Krejci, R., Pasquier, J. T., Henneberger, J., David, R. O., Ritter, C., Mohr, C., Zieger, P., & Nenes, A. (2023). Aerosol and dynamical contributions to cloud droplet formation in Arctic low-level clouds, Atmospheric Chemistry and Physics, 23, 13941–13956, https://doi.org/10.5194/acp-23-13941-2023

Mott, R., Scipión, D., Schneebeli, M., Dawes, N., Berne, A., & Lehning, M. (2014). Orographic effects on snow deposition patterns in mountainous terrain. *Journal of Geophysical Research*, *119*(3), 1419–1439. https://doi.org/10.1002/2013JD019880

Muhlbauer, A., & Lohmann, U. (2009). Sensitivity studies of aerosol-cloud interactions in mixed-phase orographic precipitation. *Journal of the Atmospheric Sciences*, *66*, 2517–2538. https://doi.org/10.1175/2009JAS3001.1

Mülmenstädt, J., Sourdeval, O., Delanoë, J., & Quaas, J. (2015). Frequency of occurrence of rain from liquid-, mixed-, and ice-phase clouds derived from A-Train satellite retrievals. *Geophysical Research Letters*, *42*(15), 6502–6509. https://doi.org/10.1002/2015GL064604

Murray, B. J., O'Sullivan, D., Atkinson, J. D., & Webb, M. E. (2012). Ice nucleation by particles immersed in supercooled cloud droplets. *Chem. Soc. Rev., 41*, 6519–6554. https://doi.org/10.1039/c2cs35200a

Murray, B. J., Carslaw, K. S., & Field, P. R. (2021). Opinion: Cloud-phase climate feedback and the importance of ice-nucleating particles. *Atmospheric Chemistry and Physics*, *21*(2), 665–679. https://doi.org/10.5194/acp-21-665-2021

Nakanishi, M., & Niino, H. (2006). An improved Mellor-Yamada Level-3 model: Its numerical stability and application to a regional prediction of advection fog. *Boundary-Layer Meteorology*, *119*(2), 397–407. https://doi.org/10.1007/s10546-005-9030-8

Nenes, A., & Seinfeld, J. H. (2003). Parameterization of cloud droplet formation in global climate models. *Journal of Geophysical Research*, *108*, *4415*. https://doi.org/10.1029/2002jd002911

Nenes, A., Ghan, S., Abdul-Razzak, H., Chuang, P. Y., & Seinfeld, J. H. (2001). Kinetic limitations on cloud droplet formation and impact on cloud albedo. *Tellus B: Chemical and Physical Meteorology*, *53*(2), 133. https://doi.org/10.3402/tellusb.v53i2.16569

O'Gorman, P. A., & Dwyer, J. G. (2018). Using Machine Learning to Parameterize Moist Convection: Potential for Modeling of Climate, Climate Change, and Extreme Events. *Journal of Advances in Modeling Earth Systems*, *10*(10), 2548–2563. https://doi.org/10.1029/2018ms001351

O'Shea, J. S., Choularton, W. T., Flynn, M., Bower, N. K., Gallagher, M., Crosier, J., et al. (2017). In situ measurements of cloud microphysics and aerosol over coastal Antarctica during the MAC campaign. *Atmospheric Chemistry and Physics*, *17*, 13049–13070. https://doi.org/10.5194/acp-17-13049-2017

Okamoto, S., & Tanimoto, H. (2016). A review of atmospheric chemistry observations at mountain sites. *Progress in Earth and Planetary Science*, *3*, *34*. https://doi.org/10.1186/s40645-016-0109-2

Oraltay, R. G., & Hallett, J. (1989). Evaporation and melting of ice crystals: A laboratory study. *Atmospheric Research*, *24*(1–4), 169–189. https://doi.org/10.1016/0169-8095(89)90044-6

Orr, B. W., & Kropfli, R. A. (1999). A method for estimating particle fall velocities from vertically pointing Doppler radar. *Journal of Atmospheric and Oceanic Technology*, *16*(1), 29–37. https://doi.org/10.1175/1520-0426(1999)016<0029:AMFEPF>2.0.CO;2

Oue, M., Kumjian, M. R., Lu, Y., Verlinde, J., Aydin, K., & Clothiaux, E. E. (2015). Linear depolarization ratios of columnar ice crystals in a deep precipitating system over the arctic observed by zenith-pointing Ka-band doppler radar. *Journal of Applied Meteorology and Climatology*, *54*(5), 1060–1068. https://doi.org/10.1175/JAMC-D-15-0012.1

Oue, M., Kollias, P., Ryzhkov, A., & Luke, E. P. (2018). Toward Exploring the Synergy Between Cloud Radar Polarimetry and Doppler Spectral Analysis in Deep Cold Precipitating Systems in the Arctic. *Journal of Geophysical Research: Atmospheres*, *123*, 2797–2815. https://doi.org/10.1002/2017JD027717

Oue, M., Tatarevic, A., Kollias, P., Wang, D., Yu, K., & Vogelmann, A. M. (2020). The Cloud-resolving model Radar SIMulator (CR-SIM) Version 3.3: Description and applications of a virtual observatory. *Geoscientific Model Development*, *13*(4), 1975–1998. https://doi.org/10.5194/gmd-13-1975-2020

Panziera, L., & Hoskins, B. (2008). Large snowfall events in the south-eastern Alps. *Weather*, *63*(4), 88–93. https://doi.org/10.1002/wea.178

Papakonstantinou-Presvelou, I., Sourdeval, O., & Quaas, J. (2022). Strong Ocean/Sea-Ice Contrasts Observed in Satellite-Derived Ice Crystal Number Concentrations in Arctic Ice Boundary-Layer Clouds. *Geophysical Research Letters*, *49*(13). https://doi.org/10.1029/2022GL098207

Pasquier, J. T., Henneberger, J., Korolev, A., Ramelli, F., Wieder, J., Lauber, A., et al. (2023). Understanding the History of Two Complex Ice Crystal Habits Deduced From a Holographic Imager. *Geophysical Research Letters*, *50*(1), 1–10. https://doi.org/10.1029/2022GL100247

Pasquier, Julie Thérèse, Henneberger, J., Ramelli, F., Lauber, A., David, R. O., Wieder, J., et al. (2022). Conditions favorable for secondary ice production in Arctic mixed-phase clouds. *Atmospheric Chemistry and Physics*, *22*(23), 15579–15601. https://doi.org/10.5194/acp-22-15579-2022

Passarelli, R. E. (1978). An Approximate Analytical Model of the Vapor Deposition and Aggregation Growth of Snowflakes. *Journal of the Atmospheric Sciences*, *35*(1), 118–124. https://doi.org/https://doi.org/10.1175/1520-0469(1978)035<0118:AAAMOT>2.0.CO;2

Patade, S., Waman, D., Deshmukh, A., Gupta, A. K., Jadav, A., Phillips, V. T. J., et al. (2022). The influence of multiple groups of biological ice nucleating particles on microphysical properties of mixed-phase clouds observed during MC3E. *Atmospheric Chemistry and Physics*, *22*(18), 12055–12075. https://doi.org/10.5194/acp-22-12055-2022

Pedregosa, F., Varoquaux, G., Gramfort, A., Michel, V., Thirion, B., Grisel, O., et al. (2011). Scikit-learn: Machine learning in Python. *Journal of Machine Learning Research*, *12*, 2825–2830. https://doi.org/10.1289/EHP4713

Peters, T. M., Ott, D., & O'Shaughnessy, P. T. (2006). Comparison of the Grimm 1.108 and 1.109 portable aerosol spectrometer to the TSI 3321 aerodynamic particle sizer for dry particles. *Annals of Occupational Hygiene*, *50*(8), 843–850. https://doi.org/10.1093/annhyg/mel067

Petters, M. D., & Kreidenweis, S. M. (2007). A single parameter representation of hygroscopic growth and cloud condensation nucleus activity. *Atmospheric Chemistry and Physics*, *7*, 1961–1971. https://doi.org/10.5194/acp-7-1961-2007

Phillips, V. T.J., Blyth, A. M., Brown, P. R. A., Choularton, T. W., & Latham, J. (2001). The glaciation of a cumulus cloud over New Mexico. *Quarterly Journal of the Royal Meteorological Society*,

127(575), 1513–1534. https://doi.org/10.1256/smsqj.57502

Phillips, V. T.J., Yano, J. I., & Khain, A. (2017a). Ice multiplication by breakup in ice-ice collisions. Part I: Theoretical formulation. *Journal of the Atmospheric Sciences*, *74*(6), 1705–1719. https://doi.org/10.1175/JAS-D-16-0224.1

Phillips, V. T.J., Yano, J. I., Formenton, M., Ilotoviz, E., Kanawade, V., Kudzotsa, I., et al. (2017b). Ice multiplication by breakup in ice-ice collisions. Part II: Numerical simulations. *Journal of the Atmospheric Sciences*, *74*(9), 2789–2811. https://doi.org/10.1175/JAS-D-16-0223.1

Phillips, V. T.J., Patade, S., Gutierrez, J., & Bansemer, A. (2018). Secondary ice production by fragmentation of freezing drops: Formulation and theory. *Journal of the Atmospheric Sciences*, *75*(9), 3031–3070. https://doi.org/10.1175/JAS-D-17-0190.1

Prabhakaran, P., Kinney, G., Cantrell, W., Shaw, R. A., & Bodenschatz, E. (2020). High Supersaturation in the Wake of Falling Hydrometeors: Implications for Cloud Invigoration and Ice Nucleation. *Geophysical Research Letters*, *47*(10), 1–9. https://doi.org/10.1029/2020GL088055

Pringle, K. J., Tost, H., Pozzer, A., Pöschl, U., & Lelieveld, J. (2010). Global distribution of the effective aerosol hygroscopicity parameter for CCN activation. *Atmospheric Chemistry and Physics*, *10*, 5241–5255. https://doi.org/10.5194/acp-10-5241-2010

Proske, U., Bessenbacher, V., Dedekind, Z., Lohmann, U., & Neubauer, D. (2021). How frequent is natural cloud seeding from ice cloud layers (<-35°C) over Switzerland? *Atmospheric Chemistry and Physics*, *21*(6), 5195–5216. https://doi.org/10.5194/acp-21-5195-2021

Proske, U., Ferrachat, S., Neubauer, D., Staab, M., & Lohmann, U. (2022). Assessing the potential for simplification in global climate model cloud microphysics. *Atmospheric Chemistry and Physics*, *22*(7), 4737–4762. https://doi.org/10.5194/acp-22-4737-2022

Proske, U., Ferrachat, S., Klampt, S., Abeling, M., & Lohmann, U. (2023). Addressing Complexity in Global Aerosol Climate Model Cloud Microphysics. *Journal of Advances in Modeling Earth Systems*, *15*(5). https://doi.org/10.1029/2022MS003571

Pruppacher, H. R., & Klett, J. D. (1997). *Microphysics of Clouds and Precipitation, 2nd ed. Kluwer Academic*.

Purdy, J. C., Austin, G. L., Seed, A. W., & Cluckie, I. D. (2005). Radar evidence of orographic enhancement due to the seeder feeder mechanism. *Meteorological Applications*, *12*(3), 199–206. https://doi.org/10.1017/S1350482705001672

Qu, Y., Khain, A., Phillips, V., Ilotoviz, E., Shpund, J., Patade, S., & Chen, B. (2020). The Role of Ice Splintering on Microphysics of Deep Convective Clouds Forming Under Different Aerosol Conditions: Simulations Using the Model With Spectral Bin Microphysics. *Journal of Geophysical Research: Atmospheres*, *125*(3), 1–23. https://doi.org/10.1029/2019JD031312

Ramelli, F., Beck, A., Henneberger, J., & Lohmann, U. (2020). Using a holographic imager on a tethered balloon system for microphysical observations of boundary layer clouds. *Atmospheric Measurement Techniques*, *13*, 925–939. https://doi.org/10.5194/amt-13-925-2020

Ramelli, F., Henneberger, J., David, R., Bühl, J., Radenz, M., Seifert, P., et al. (2021a). Microphysical investigation of the seeder and feeder region of an Alpine mixed-phase cloud. *Atmospheric Chemistry and Physics*, *21*, 6681–6706. https://doi.org/10.5194/acp-21-6681-2021

Ramelli, F., Henneberger, J., David, R. O., Lauber, A., Pasquier, J. T., Wieder, J., et al. (2021b). Influence of low-level blocking and turbulence on the microphysics of a mixed-phase cloud in an inner-Alpine valley. *Atmospheric Chemistry and Physics*, *21*(6), 5151–5172.

https://doi.org/10.5194/acp-21-5151-2021

Rangno, A. L., & Hobbs, P. V. (2001). Ice particles in stratiform clouds in the Arctic and possible mechanisms for the production of high ice concentrations. *Journal of Geophysical Research Atmospheres*, *106*(D14), 15065–15075. https://doi.org/10.1029/2000JD900286

Rasmussen, R. M., Geresdi, I., Thompson, G., Manning, K., & Karplus, E. (2002). Freezing drizzle formation in stably stratified layer clouds: The role of radiative cooling of cloud droplets, cloud condensation nuclei, and ice initiation. *Journal of the Atmospheric Sciences*, *59*(4), 837–860. https://doi.org/10.1175/1520-0469(2002)059<0837:FDFISS>2.0.CO;2

Rasp, S. (2020). Coupled online learning as a way to tackle instabilities and biases in neural network parameterizations : general algorithms and Lorenz 96 case study (v1.0). *Geoscientific Model Development*, *13*, 2185–2196.

Rasp, S., Pritchard, M. S., & Gentine, P. (2018). Deep learning to represent subgrid processes in climate models. *Proceedings of the National Academy of Sciences of the United States of America*, *115*(39), 9684–9689. https://doi.org/10.1073/pnas.1810286115

Reichstein, M., Camps-Valls, G., Stevens, B., Jung, M., Denzler, J., Carvalhais, N., & Prabhat. (2019). Deep learning and process understanding for data-driven Earth system science. *Nature*, *566*(7743), 195–204. https://doi.org/10.1038/s41586-019-0912-1

Reinking, R. F., Snider, J. B., & Coen, J. L. (2000). Influences of storm-embedded orographic gravity waves on cloud liquid water and precipitation. *Journal of Applied Meteorology*, *39*(6), 733–759. https://doi.org/10.1175/1520-0450(2000)039<0733:IOSEOG>2.0.CO;2

Reisner, J., Rasmussen, R. M., & Bruintjes, R. T. (1998). Explicit forecasting of supercooled liquid water in winter storms using the MM5 mesoscale model. *Quarterly Journal of the Royal Meteorological Society*, *124*(548), 1071–1107. https://doi.org/10.1002/qj.49712454804

Reutter, P., Su, H., Trentmann, J., Simmel, M., Rose, D., Gunthe, S. S., et al. (2009). Aerosol- and updraft-limited regimes of cloud droplet formation: Influence of particle number, size and hygroscopicity on the activation of cloud condensation nuclei (CCN). *Atmospheric Chemistry and Physics*, *9*, 7067–7080. https://doi.org/10.5194/acp-9-7067-2009

Riihimaki, L. D., Mcfarlane, S. A., & Comstock, J. M. (2012). Climatology and formation of tropical midlevel clouds at the Darwin ARM Site. *Journal of Climate*, *25*(19), 6835–6850. https://doi.org/10.1175/JCLI-D-11-00599.1

Roberts, G. C., & Nenes, A. (2005). A continuous-flow streamwise thermal-gradient CCN chamber for atmospheric measurements. *Aerosol Science and Technology*, *39*(3), 206–221. https://doi.org/10.1080/027868290913988

Roe, G. H. (2005). Orographic Precipitation. *Annual Review of Earth and Planetary Sciences*, *33*, 645–671. https://doi.org/10.1146/annurev.earth.33.092203.122541

Rogers, D. C., & Vali, G. (1987). Ice Crystal Production by Mountain Surfaces. *Journal of Climate and Applied Meteorology*, *26*, 1152–1168. https://doi.org/10.1175/1520-0450(1987)026<1152:ICPBMS>2.0.CO;2

Rose, D., Gunthe, S. S., Mikhailov, E., Frank, G. P., Dusek, U., Andreae, M. O., & Pöschl, U. (2008). Calibration and measurement uncertainties of a continuous-flow cloud condensation nuclei counter (DMT-CCNC): CCN activation of ammonium sulfate and sodium chloride aerosol particles in theory and experiment. *Atmospheric Chemistry and Physics*, *8*(5), 1153–1179. https://doi.org/10.5194/acp-8-1153-2008

Rotunno, R., & Houze, R. A. (2007). Lessons on orographic precipitation from the Mesoscale Alpine Programme. *Quarterly Journal of the Royal Meteorological Society*, *133*, 811–830. https://doi.org/10.1002/qj.67

Saleeby, S. M., Cotton, W. R., Lowenthal, D., & Messina, J. (2013). Aerosol impacts on the microphysical growth processes of orographic snowfall. *Journal of Applied Meteorology and Climatology*, *52*, 834–852. https://doi.org/10.1175/JAMC-D-12-0193.1

Schlenczek, O., Fugal, J., Bower, K. N., Crosier, J., Flynn, M. J., Lloyd, G., & Borrmann, S. (2014). Properties of pure ice clouds in an alpine environment. *14th Conf. on Cloud Physics, Boston, MA, Amer. Meteor. Soc.*

Schmidt, R. A. (1984). Measuring particle size and snowfall intensity in drifting snow. *Cold Regions Science and Technology*, *9*, 121–129. https://doi.org/10.1016/ 0165-232X(84)90004-1

Schneider, T., Lan, S., Stuart, A., & Teixeira, J. (2017). Earth System Modeling 2 . 0 : A Blueprint for Models That Learn From Observations and Targeted High-Resolution Simulations. *Geophysical Research Letters*, *44*, 12396–12417. https://doi.org/10.1002/2017GL076101

Schuddeboom, A. J., & McDonald, A. J. (2021). The Southern Ocean Radiative Bias, Cloud Compensating Errors, and Equilibrium Climate Sensitivity in CMIP6 Models. *Journal of Geophysical Research: Atmospheres*, *126*(22), 1–16. https://doi.org/10.1029/2021JD035310

Schwarzenboeck, A., Shcherbakov, V., Lefevre, R., Gayet, J. F., Pointin, Y., & Duroure, C. (2009). Indications for stellar-crystal fragmentation in Arctic clouds. *Atmospheric Research*, *92*(2), 220–228. https://doi.org/10.1016/j.atmosres.2008.10.002

Seifert, A, & Beheng, K. D. (2006). A two-moment cloud microphysics parameterization for mixed-phase clouds . Part 1: Model description. *Meteorology and Atmospheric Physics*, *92*, 45–66. https://doi.org/10.1007/s00703-005-0112-4

Seifert, A. (2008). On the parameterization of evaporation of raindrops as simulated by a one-dimensional rainshaft model. *Journal of the Atmospheric Sciences*, *65*(11), 3608–3619. https://doi.org/10.1175/2008JAS2586.1

Seifert, Axel, & Rasp, S. (2020). Potential and Limitations of Machine Learning for Modeling Warm-Rain Cloud Microphysical Processes. *Journal of Advances in Modeling Earth Systems*, *12*(12). https://doi.org/10.1029/2020MS002301

Seinfeld, J. H., & Pandis, S. N. (2006). *Atmospheric Chemistry and Physics: From Air Pollution to Climate Change, 2nd Edn., John Wiley, edited by: Hoboken, N. J.*

Seinfeld, J. H., Bretherton, C., Carslaw, K. S., Coe, H., DeMott, P. J., Dunlea, E. J., et al. (2016). Improving our fundamental understanding of the role of aerosol-cloud interactions in the climate system. *Proceedings of the National Academy of Sciences of the United States of America*, *113*, 5781–5790. https://doi.org/10.1073/pnas.1514043113

Sharma, V., Gerber, F., & Lehning, M. (2023). Introducing CRYOWRF v1.0: multiscale atmospheric flow simulations with advanced snow cover modelling. *Geoscientific Model Development*, *16*(2), 719–749. https://doi.org/10.5194/gmd-16-719-2023

Shaw, J., McGraw, Z., Bruno, O., Storelvmo, T., & Hofer, S. (2022). Using Satellite Observations to Evaluate Model Microphysical Representation of Arctic Mixed-Phase Clouds. *Geophysical Research Letters*, *49*(3), 1–10. https://doi.org/10.1029/2021GL096191

Sheikh, M. Z., Gustavsson, K., Lévêque, E., Mehlig, B., Pumir, A., & Naso, A. (2022). Colliding Ice Crystals in Turbulent Clouds. *Journal of the Atmospheric Sciences*, *79*(9), 2205–2218.

https://doi.org/10.1175/JAS-D-21-0305.1

Shupe, M. D., Matrosov, S. Y., & Uttal, T. (2006). Arctic Mixed-Phase Cloud Properties Derived from Surface-Based Sensors at SHEBA. *Journal of the Atmospheric Sciences*, *63*(2), 697–711. https://doi.org/10.1175/jas3659.1

Shupe, M. D., Walden, V. P., Eloranta, E., Uttal, T., Campbell, J. R., Starkweather, S. M., & Shiobara, M. (2011). Clouds at Arctic atmospheric observatories. Part I: Occurrence and macrophysical properties. *Journal of Applied Meteorology and Climatology*, *50*(3), 626–644. https://doi.org/10.1175/2010JAMC2467.1

Sinclair, V. A., Moisseev, D., & Von Lerber, A. (2016). How dual-polarization radar observations can be used to verify model representation of secondary ice. *Journal of Geophysical Research*, *121*(18), 10,954-10,970. https://doi.org/10.1002/2016JD025381

Skamarock, W. C., Klemp, J. B., Dudhia, J., Gill, D. O., Barker, D. M., Duda, M. G., et al. (2008). A Description of the Advanced Research WRF Version 3. *Tech. Rep., NCAR Technical Note NCAR/TN-475+STR*. https://doi.org/10.5065/D68S4MVH

Sledd, A., & L'Ecuyer, T. (2021). Uncertainty in forced and natural arctic solar absorption variations in CMIP6 models. *Journal of Climate*, *34*(3), 931–948. https://doi.org/10.1175/JCLI-D-20-0244.1

Smith, R. B. (2006). Progress on the theory of orographic precipitation. *Special Paper of the Geological Society of America*, *398*, 1–16. https://doi.org/10.1130/2006.2398(01)

Snider, J. R., Leon, D., & Wang, Z. (2017). Droplet concentration and spectral broadening in southeast pacific stratocumulus clouds. *Journal of the Atmospheric Sciences*, *74*(3), 719–749. https://doi.org/10.1175/JAS-D-16-0043.1

Sotiropoulou, Georgia, Sullivan, S., Savre, J., Lloyd, G., Lachlan-Cope, T., Ekman, A. M. L., & Nenes, A. (2020). The impact of secondary ice production on Arctic stratocumulus. *Atmospheric Chemistry and Physics*, *20*, 1301–1316. https://doi.org/10.5194/acp-20-1301-2020

Sotiropoulou, Georgia, Ickes, L., Nenes, A., & Ekman, A. (2021). Ice multiplication from ice–ice collisions in the high Arctic: sensitivity to ice habit, rimed fraction, ice type and uncertainties in the numerical description of the process. *Atmospheric Chemistry and Physics*, *21*, 9741–9760. https://doi.org/10.5194/acp-21-9741-2021

Sotiropoulou, Georgia, Vignon, E., Young, G., Morrison, H., O'Shea, S. J., Lachlan-Cope, T., et al. (2021). Secondary ice production in summer clouds over the Antarctic coast: An underappreciated process in atmospheric models. *Atmospheric Chemistry and Physics*, *21*(2), 755–771. https://doi.org/10.5194/acp-21-755-2021

Sotiropoulou, Georgia, Lewinschal, A., Georgakaki, P., Phillips, V., Patade, S., Ekman, A. M. L., & Nenes, A. (2022). Sensitivity of Arctic clouds to ice microphysical processes in the NorESM2 climate model. *Preprint on Authorea*. https://doi.org/10.1002/essoar.10512081.1

Stith, J. L., Twohy, C. H., Demott, P. J., Baumgardner, D., Campos, T., Gao, R., & Anderson, J. (2011). Observations of ice nuclei and heterogeneous freezing in a Western Pacific extratropical storm. *Atmospheric Chemistry and Physics*, *11*(13), 6229–6243. https://doi.org/10.5194/acp-11-6229-2011

Sud, Y. C., Lee, D., Oreopoulos, L., Barahona, D., Nenes, A., & Suarez, M. J. (2013). Performance of McRAS-AC in the GEOS-5 AGCM: Aerosol-cloud-microphysics, precipitation, cloud radiative effects, and circulation. *Geoscientific Model Development*, *6*(1), 57–79. https://doi.org/10.5194/gmd-6-57-2013

Sullivan, S. C., Lee, D., Oreopoulos, L., & Nenesa, A. (2016). Role of updraft velocity in temporal variability of global cloud hydrometeor number. *Proceedings of the National Academy of Sciences of the United States of America*, *113*, 5791–5796. https://doi.org/10.1073/pnas.1514039113

Sullivan, S. C., Hoose, C., Kiselev, A., Leisner, T., & Nenes, A. (2018). Initiation of secondary ice production in clouds. *Atmospheric Chemistry and Physics*, *18*(3), 1593–1610. https://doi.org/10.5194/acp-18-1593-2018

Sullivan, S. C., Barthlott, C., Crosier, J., Zhukov, I., Nenes, A., & Hoose, C. (2018). The effect of secondary ice production parameterization on the simulation of a cold frontal rainband. *Atmospheric Chemistry and Physics*, *18*, 16461–16480. https://doi.org/10.5194/acp-18-16461-2018

Takahashi, T., Nagao, Y., & Kushiyama, Y. (1995). Possible high ice particle production during graupel-graupel collisions. *Journal of the Atmospheric Sciences*, *52*, 4523–4527. https://doi.org/10.1175/1520- 0469(1995)052<4523:PHIPPD>2.0.CO;2

Takahashi, T. (2014). Influence of liquid water content and temperature on the form and growth of branched planar snow crystals in a cloud. *Journal of the Atmospheric Sciences*, *71*(11), 4127–4142. https://doi.org/10.1175/JAS-D-14-0043.1

Takahashi, Tsutomu. (1993). High ice crystal production in winter cumuli over the Japan Sea. *Geophysical Research Letters*, *20*(6), 451–454. https://doi.org/10.1029/93GL00613

Tan, I., & Storelvmo, T. (2019). Evidence of Strong Contributions From Mixed-Phase Clouds to Arctic Climate Change. *Geophysical Research Letters*, *46*(5), 2894–2902. https://doi.org/10.1029/2018GL081871

Taylor, J. W., Choularton, T. W., Blyth, A. M., Liu, Z., Bower, K. N., Crosier, J., et al. (2016). Observations of cloud microphysics and ice formation during COPE. *Atmospheric Chemistry and Physics*, *16*(2), 799–826. https://doi.org/10.5194/acp-16-799-2016

von Terzi, L., Dias Neto, J., Ori, D., Myagkov, A., & Kneifel, S. (2022). Ice microphysical processes in the dendritic growth layer: a statistical analysis combining multi-frequency and polarimetric Doppler cloud radar observations. *Atmospheric Chemistry and Physics*, *22*(17), 11795–11821. https://doi.org/10.5194/acp-22-11795-2022

Thomas, J., Barrett, A., & Hoose, C. (2023). Temperature and cloud condensation nuclei (CCN) sensitivity of orographic precipitation enhanced by a mixed-phase seeder-feeder mechanism: a case study for the 2015 Cumbria flood. *Atmospheric Chemistry and Physics*, *23*(3), 1987–2002. https://doi.org/10.5194/acp-23-1987-2023

Thompson, G., Rasmussen, R. M., & Manning, K. (2004). Explicit Forecasts of Winter Precipitation Using an Improved Bulk Microphysics Scheme. Part I: Description and Sensitivity Analysis. *Monthly Weather Review*, *132*, 519–542. https://doi.org/10.1175/1520-0493(2004)132<0519:EFOWPU>2.0.CO;2

Touloupas, G., Lauber, A., Henneberger, J., Beck, A., & Lucchi, A. (2020). A convolutional neural network for classifying cloud particles recorded by imaging probes. *Atmospheric Measurement Techniques*, *13*(5), 2219–2239. https://doi.org/10.5194/amt-13-2219-2020

Trömel, S., Simmer, C., Blahak, U., Blanke, A., Doktorowski, S., Ewald, F., et al. (2021). Overview: Fusion of radar polarimetry and numerical atmospheric modelling towards an improved understanding of cloud and precipitation processes. *Atmospheric Chemistry and Physics*, *21*(23), 17291–17314. https://doi.org/10.5194/acp-21-17291-2021

Tröstl, J., Herrmann, E., Frege, C., Bianchi, F., Molteni, U., Bukowiecki, N., et al. (2016). Contribution of new particle formation to the total aerosol concentration at the high-altitude site Jungfraujoch (3580masl, Switzerland). *Journal of Geophysical Research Atmospheres*, *121*, 11692–11711. https://doi.org/10.1002/2015JD024637

Twomey, S. A. (1974). Pollution and the planetary albedo. *Atmospheric Environment*, *8*, 1251–1256.

Vali, G., Leon, D., & Snider, J. R. (2012). Ground-layer snow clouds. *Quarterly Journal of the Royal Meteorological Society*, *138*(667), 1507–1525. https://doi.org/10.1002/qj.1882

Vali, G., DeMott, P. J., Möhler, O., & Whale, T. F. (2015). Technical Note: A proposal for ice nucleation terminology. *Atmospheric Chemistry and Physics*, *15*(18), 10263–10270. https://doi.org/10.5194/acp-15-10263-2015

Vardiman, L. (1978). The Generation of Secondary Ice Particles in Clouds by Crystal–Crystal Collision. *Journal of the Atmospheric Sciences*, *35*, 2168–2180. https://doi.org/10.1175/1520-0469(1978)035<2168:TGOSIP>2.0.CO;2,

Vassel, M., Ickes, L., Maturilli, M., & Hoose, C. (2019). Classification of Arctic multilayer clouds using radiosonde and radar data in Svalbard. *Atmospheric Chemistry and Physics*, *19*(7), 5111–5126. https://doi.org/10.5194/acp-19-5111-2019

Vavrus, S. (2006). An alternative method to calculate cloud radiative forcing: Implications for quantifying cloud feedbacks. *Geophysical Research Letters*, *33*(1), 2–5. https://doi.org/10.1029/2005GL024723

Vergara-Temprado, J., Miltenberger, A. K., Furtado, K., Grosvenor, D. P., Shipway, B. J., Hill, A. A., et al. (2018). Strong control of Southern Ocean cloud reflectivity by ice-nucleating particles. *Proceedings of the National Academy of Sciences of the United States of America*, *115*(11), 2687–2692. https://doi.org/10.1073/pnas.1721627115

Vignon, Besic, N., Jullien, N., Gehring, J., & Berne, A. (2019). Microphysics of Snowfall Over Coastal East Antarctica Simulated by Polar WRF and Observed by Radar. *Journal of Geophysical Research: Atmospheres*, *124*(21), 11452–11476. https://doi.org/10.1029/2019JD031028

Vignon, É., Alexander, S. P., DeMott, P. J., Sotiropoulou, G., Gerber, F., Hill, T. C. J., et al. (2021). Challenging and Improving the Simulation of Mid-Level Mixed-Phase Clouds Over the High-Latitude Southern Ocean. *Journal of Geophysical Research: Atmospheres*, *126*(7), 1–21. https://doi.org/10.1029/2020jd033490

Vionnet, V., Guyomarc'h, G., Naaim Bouvet, F., Martin, E., Durand, Y., Bellot, H., et al. (2013). Occurrence of blowing snow events at an alpine site over a 10-year period: Observations and modelling. *Advances in Water Resources*, *55*, 53–63. https://doi.org/10.1016/j.advwatres.2012.05.004

Vionnet, V., Martin, E., Masson, V., Guyomarc'H, G., Naaim-Bouvet, F., Prokop, A., et al. (2014). Simulation of wind-induced snow transport and sublimation in alpine terrain using a fully coupled snowpack/atmosphere model. *Cryosphere*, *8*(2), 395–415. https://doi.org/10.5194/tc-8-395-2014

Vogl, T., Maahn, M., Kneifel, S., Schimmel, W., Moisseev, D., & Kalesse-Los, H. (2022). Using artificial neural networks to predict riming from Doppler cloud radar observations. *Atmospheric Measurement Techniques*, *15*(2), 365–381. https://doi.org/10.5194/amt-15-365-2022

Vosper, S. B., Wells, H., Sinclair, J. A., & Sheridan, P. F. (2013). A climatology of lee waves over the UK derived from model forecasts. *Meteorological Applications*, *20*, 466–481. https://doi.org/10.1002/met.1311

Waman, D., Patade, S., Jadav, A., Deshmukh, A., Gupta, A. K., Phillips, V. T. J., et al. (2022). Dependencies of Four Mechanisms of Secondary Ice Production on Cloud-Top Temperature in a Continental Convective Storm. *Journal of the Atmospheric Sciences*, *79*(12), 3375–3404. https://doi.org/10.1175/JAS-D-21-0278.1

Wang, J., Lee, Y. N., Daum, P. H., Jayne, J., & Alexander, M. L. (2008). Effects of aerosol organics on cloud condensation nucleus (CCN) concentration and first indirect aerosol effect. *Atmospheric Chemistry and Physics*, *8*, 6325–6339. https://doi.org/10.5194/acp-8-6325-2008

Wegener, A. (1911). Thermodynamik der Atmosphäre. *Germany: Barth,Leipzig*, 331 pp.

Wex, H., Huang, L., Zhang, W., Hung, H., Traversi, R., Becagli, S., et al. (2019). Annual variability of ice-nucleating particle concentrations at different Arctic locations. *Atmospheric Chemistry and Physics*, *19*(7), 5293–5311. https://doi.org/10.5194/acp-19-5293-2019

Weyn, J. A., Durran, D. R., & Caruana, R. (2020). Improving Data-Driven Global Weather Prediction Using Deep Convolutional Neural Networks on a Cubed Sphere. *Journal of Advances in Modeling Earth Systems*, *12*(9). https://doi.org/10.1029/2020MS002109

Whale, T. F. (2017). *Ice Nucleation in Mixed-Phase Clouds*. *Mixed-Phase Clouds: Observations and Modeling*. Elsevier Inc. https://doi.org/10.1016/B978-0-12-810549-8.00002-7

Wieder, J., Ihn, N., Mignani, C., Haarig, M., Bühl, J., Seifert, P., et al. (2022). Retrieving ice-nucleating particle concentration and ice multiplication factors using active remote sensing validated by in situ observations. *Atmospheric Chemistry and Physics*, *22*(15), 9767–9797. https://doi.org/10.5194/acp-22-9767-2022

Willmott, C. J., Robeson, S. M., & Matsuura, K. (2012). A refined index of model performance. *International Journal of Climatology*, *32*(13), 2088–2094. https://doi.org/10.1002/joc.2419

Wilson, T. W., Ladino, L. A., Alpert, P. A., Breckels, M. N., Brooks, I. M., Browse, J., et al. (2015). A marine biogenic source of atmospheric ice-nucleating particles. *Nature*, *525*(7568), 234–238. https://doi.org/10.1038/nature14986

Xi, B., Dong, X., Zheng, X., & Wu, P. (2022). Cloud phase and macrophysical properties over the Southern Ocean during the MARCUS field campaign. *Atmospheric Measurement Techniques*, *15*(12), 3761–3777. https://doi.org/10.5194/amt-15-3761-2022

Xu, L., Russell, L. M., Somerville, R. C. J., & Quinn, P. K. (2013). Frost flower aerosol effects on Arctic wintertime longwave cloud radiative forcing. *Journal of Geophysical Research Atmospheres*, *118*(23), 13282–13291. https://doi.org/10.1002/2013JD020554

Yang, J., Lei, H., Hu, Z., & Hou, T. (2014). Particle size spectra and possible mechanisms of high ice concentration in nimbostratus over hebei province, china. *Atmospheric Research*, *142*, 79–90. https://doi.org/10.1016/j.atmosres.2013.12.018

Yano, J. I., & Phillips, V. T. J. (2011). Ice-Ice collisions: An Ice multiplication process in atmospheric clouds. *Journal of the Atmospheric Sciences*, *68*(2), 322–333. https://doi.org/10.1175/2010JAS3607.1

Yano, Jun Ichi, Phillips, V. T. J., & Kanawade, V. (2016). Explosive ice multiplication by mechanical break-up in ice-ice collisions: A dynamical system-based study. *Quarterly Journal of the Royal Meteorological Society*, *142*(695), 867–879. https://doi.org/10.1002/qj.2687

Young, G., Jones, H. M., Darbyshire, E., Baustian, K. J., McQuaid, J. B., Bower, K. N., et al. (2016). Size-segregated compositional analysis of aerosol particles collected in the European Arctic during the ACCACIA campaign. *Atmospheric Chemistry and Physics*, *16*(6), 4063–4079.

https://doi.org/10.5194/acp-16-4063-2016

Young, G., Lachlan-Cope, T., O'Shea, S. J., Dearden, C., Listowski, C., Bower, K. N., et al. (2019). Radiative Effects of Secondary Ice Enhancement in Coastal Antarctic Clouds. *Geophysical Research Letters*, *46*, 2312–2321. https://doi.org/10.1029/2018GL080551

Yuval, J., & O'Gorman, P. A. (2020). Stable machine-learning parameterization of subgrid processes for climate modeling at a range of resolutions. *Nature Communications*, *11*(1), 1–10. https://doi.org/10.1038/s41467-020-17142-3

Yuval, J., O'Gorman, P. A., & Hill, C. N. (2021). Use of Neural Networks for Stable , Accurate and Physically Consistent Parameterization of Subgrid Atmospheric Processes With Good Performance at Reduced Precision Geophysical Research Letters. *Geophysical Research Letters*, *48*, 1–11. https://doi.org/10.1029/2020GL091363

Zelinka, M. D., Myers, T. A., McCoy, D. T., Po-Chedley, S., Caldwell, P. M., Ceppi, P., et al. (2020). Causes of Higher Climate Sensitivity in CMIP6 Models. *Geophysical Research Letters*, *47*(1), 1–12. https://doi.org/10.1029/2019GL085782

Zelinka, M. D., Klein, S. A., Qin, Y., & Myers, T. A. (2022). Evaluating Climate Models' Cloud Feedbacks Against Expert Judgment. *Journal of Geophysical Research: Atmospheres*, *127*(2), 1–18. https://doi.org/10.1029/2021JD035198

Zhang, G., & Lu, Y. (2012). Bias-corrected random forests in regression. *Journal of Applied Statistics*, *39*(1), 151–160. https://doi.org/10.1080/02664763.2011.578621

Zhao, X., & Liu, X. (2021). Global Importance of Secondary Ice Production. *Geophysical Research Letters*, *48*(11), 1–11. https://doi.org/10.1029/2021GL092581

Zhao, X., & Liu, X. (2022). Primary and secondary ice production: Interactions and their relative importance. *Atmospheric Chemistry and Physics*, *22*(4), 2585–2600. https://doi.org/10.5194/acp-22-2585-2022

Zhao, X., Liu, X., Phillips, V. T. J., & Patade, S. (2021). Impacts of secondary ice production on Arctic mixed-phase clouds based on ARM observations and CAM6 single-column model simulations. *Atmospheric Chemistry and Physics*, *21*(7), 5685–5703. https://doi.org/10.5194/acp-21-5685-2021

Zhao, X., Liu, X., Burrows, S., DeMott, P. J., Diao, M., McFarquhar, G. M., et al. (2023). Important Ice Processes Are Missed by the Community Earth System Model in Southern Ocean Mixed-Phase Clouds: Bridging SOCRATES Observations to Model Developments. *Journal of Geophysical Research: Atmospheres*, *128*(4), 1–15. https://doi.org/10.1029/2022JD037513

Zubler, E. M., Lohmann, U., Lüthi, D., Schär, C., & Muhlbauer, A. (2011). Statistical analysis of aerosol effects on simulated mixed-phase clouds and precipitation in the Alps. *Journal of the Atmospheric Sciences*, *68*, 1474–1492. https://doi.org/10.1175/2011JAS3632.1

Paraskevi Georgakaki

P: (+41) 779731586

E: paraskevi.georgakaki@epfl.ch

A: Lausanne, Switzerland

ORCID: 0000-0002-4296-8779

Education

Ph.D. in Environmental Engineering
2019 – 2023

École Polytechnique Fédérale de Lausanne
School of Architecture, Civil & Environmental Engineering
Advisor: Prof. Athanasios Nenes
Ph.D. Dissertation: *The role of secondary ice production in mixed-phase clouds*

M.Sc. in Environmental Physics and Meteorology
2017 – 2019

National and Kapodistrian University of Athens
Advisor: Prof. Maria Tombrou
Master Thesis: *Numerical simulation of aerosol-cloud interactions*

B.A. in Physics
2011 – 2017

University of Crete
Advisors: Assoc. Prof. Ilias Vardavas, Prof. Maria Kanakidou, Prof. Nikolaos Hatzianastassiou
Bachelor Thesis: Aerosol direct effect on solar radiation over the eastern Mediterranean basin based on AVHRR satellite measurements and climatological aerosol data GADS

Scientific Experience & trainings

Summer school in MM-Wavelength Radar Observations for Cloud and Precipitation
June 4–9 2023

Stony Brook University, NY
Training school sponsored by the National Science Foundation: Lectures and hands-on research project on how to use multi-sensor, multi-wavelength radar data to study cloud microphysics and dynamics

Student supervision

Bachelor thesis project (Université de Neuchâtel)

- *Evaluation of a numerical weather prediction model using remote sensing observations, Eliot Perrin (2023)*

Teaching Assistant
Feb 2021 – Jan 2023

École Polytechnique Fédérale de Lausanne
Courses: Physics and chemistry of the atmosphere (bachelor) and Atmospheric processes: from cloud to global scales (master)

WRF model tutorial
Jan 2020

Basic Weather Research & Forecasting tutorial
UCAR/NCAR, Boulder, Colorado

ERASMUS Internship
Feb 2019 – May 2019

Stockholm University
Department of Meteorology
Advisor: Prof. Annica Ekman
Topic: Cloud formation in a marine environment. A simulation approach.

Honors

Schmidt Science Fellowship (in partnership with the Rhodes Trust) nominee

For postdoctoral studies awarded to 30 researchers worldwide across all areas of science (1 nomination for EPFL)

Skills

Software skills

Python, MATLAB, FORTRAN, Linux

Languages

Greek (native), English (full professional proficiency), German (limited working proficiency)

Publications

1. **Georgakaki, P.**, Billault-Roux, A.-C., Foskinis, R., Gao, K., Sotiropoulou, G., Gini, M., Takahama, S., Eleftheriadis, K., Papayannis, A., Berne, A., and Nenes, A.: Unraveling secondary ice production in winter orographic clouds through a synergy of in-situ observations, remote sensing and modeling, under review for npj Climate and Atmospheric Science, preprint accessible at: https://doi.org/10.21203/rs.3.rs-3502790/v1, 2023.
2. **Georgakaki, P.**, and Nenes, A.: RaFSIP: Parameterizing ice multiplication in models using a machine learning approach, under review for Journal of Advances in Modeling Earth Systems, 2023.
3. Motos, G., Freitas, G., **Georgakaki, P.**, Wieder, J., Li, G., Aas, W., Lunder, C., Krejci, R., Pasquier, J. T., Henneberger, J., David, R. O., Ritter, C., Mohr, C., Zieger, P., and Nenes, A.: Aerosol and dynamical contributions to cloud droplet formation in Arctic low-level clouds, Atmos. Chem. Phys., 23, 13941–13956, https://doi.org/10.5194/acp-23-13941-2023, 2023.

4. Billault-Roux, A.-C., **Georgakaki, P.**, Gehring, J., Jaffeux, L., Schwarzenboeck, A., Coutris, P., Nenes, A., and Berne, A.: Distinct secondary ice production processes observed in radar Doppler spectra: insights from a case study, Atmos. Chem. Phys., 23, 10207–10234, https://doi.org/10.5194/acp-23-10207-2023, 2023.
5. Sotiropoulou, G., Lewinschal, A., **Georgakaki, P.**, Phillips, V., Patade, S., Ekman, A. M. L., and Nenes, A.: Sensitivity of Arctic clouds to ice microphysical processes in the NorESM2 climate model, in review for J.Clim., preprint accessible at: https://www.authorea.com/doi/full/10.1002/essoar.10512081.1, 2022.
6. Foskinis, R., Nenes, A., Papayannis, A., **Georgakaki, P.**, Eleftheriadis, K., Vratolis, S., Gini, M. I., Komppula, M., Vakkari, V. and Kokkalis, P.: Towards reliable retrievals of cloud droplet number for non-precipitating planetary boundary layer clouds and their susceptibility to aerosol, Front. Remote Sens., 3, https://www.frontiersin.org/articles/10.3389/frsen.2022.958207, 2022.
7. Karalis, M., Sotiropoulou, G., Abel, S. J., Bossioli, E., **Georgakaki, P.**, Methymaki, G., Nenes, A., and Tombrou, M.: Effects of secondary ice processes on a stratocumulus to cumulus transition during a cold-air outbreak, Atmos. Res., 277, https://doi.org/10.1016/j.atmosres.2022.106302, 2022.
8. **Georgakaki, P.**, Sotiropoulou, G., Vignon, É., Billault-Roux, A.-C., Berne, A., and Nenes, A.: Secondary ice production processes in wintertime alpine mixed-phase clouds, Atmos. Chem. Phys., 22, 1965–1988, https://doi.org/10.5194/acp-22-1965-2022, 2022.
9. **Georgakaki, P.**, Bougiatioti, A., Wieder, J., Mignani, C., Ramelli, F., Kanji, Z. A., Henneberger, J., Hervo, M., Berne, A., Lohmann, U., and Nenes, A.: On the drivers of droplet variability in alpine mixed-phase clouds, Atmos. Chem. Phys., 21, 10993–11012, https://doi.org/10.5194/acp-21-10993-2021, 2021.

Scientific conferences & workshops

1. **Georgakaki, P.**, Billault-Roux, A-C., Perrin, E., Foskinis, R., Sotiropoulou, G., Vogel, F., Gini, M., Eleftheriadis, K., Moehler, O., Takahama, S., Berne, A., and Nenes, A.: Unraveling secondary ice production in winter orographic clouds through a synergy of in-situ observations, remote sensing and modeling, EGU General Assembly 2023, Vienna, Austria, 23–28 April 2023, (poster presentation).
2. Costa-Surós, M., Gonçalves, M., Chatziparaschos, M., **Georgakaki, P.**, Ilić, L., Montane, G., Myriokefalitakis, S., van Noije, T., Le Sager, P., Kanakidou, M., Nenes, A., and Pérez García-Pando, C: Dust-induced ice formation processes and its impact on the representation of clouds in an Earth System Model, EGU General Assembly 2023, Vienna, Austria, 23–28 April 2023.
3. Ickes, L., Costa Surós, M., Eriksson, P., Frostenberg, H., **Georgakaki, P.**, Gonçalves Ageitos, M., Hallborn, H., Lewinschall, A., May, E., Nenes, A., Neubauer, D., Pérez García-Pando, C., Proske, U., and Sotiropoulou, G.: How important are secondary ice processes – preliminary results from FOR-ICE, EGU General Assembly 2023, Vienna, Austria, 23–28 April 2023.
4. Motos, G., Freitas, G., **Georgakaki, P.,** Wieder, J., Aas, W., Lunder, C., Krejci, R., Pasquier, J., Henneberger, J., David, R., Mohr, C., Zieger, P., and Nenes, A.: Linking aerosol size distribution and hygroscopicity to cloud droplet formation at an Arctic mountain site, EGU General Assembly 2023, Vienna, Austria, 23–28 April 2023, EGU23-13074.
5. **Georgakaki, P.**, Sotiropoulou, G., and Nenes, A.: Parameterizing secondary ice production in Arctic mixed-phase clouds, EGU General Assembly 2022, Vienna, Austria, 23–27 May 2022, EGU22-11263, https://doi.org/10.5194/egusphere-egu22-11263, 2022, (oral presentation).
6. **Georgakaki, P.**, Sotiropoulou, G., and Nenes, A.: Parameterizing secondary ice production in Arctic mixed-phase clouds, QuIESCENT Arctic workshop 2022, Arctic Science Summit Week, Tromsø, Norway, 30 March–1 April 2022, (oral presentation).
7. Motos, G., Freitas, G., **Georgakaki, P.**, Wieder, J., Aas, W., Lunder, C., Krejci, R., Mohr, C., Zieger, P., Lohmann, U., and Nenes, A.: Arctic aerosol size distribution, hygroscopicity and cloud formation from fall to spring, QuIESCENT Arctic workshop 2022, Arctic Science Summit Week, Tromsø, Norway, 30 March–1 April 2022.

8. Motos, G., **Georgakaki, P.**, Zieger, P., Wieder, J., Lohmann, U., and Nenes, A.: In-Situ Observations Of Aerosol Hygroscopicity And Cloud Droplet Formation In Ny-Ålesund, Svalbard, During Fall 2019 And Spring 2020, AGU Fall Assembly Meeting, 13-17 December 2021, New Orleans.
9. **Georgakaki, P.**, Sotiropoulou, G., Vignon, E., Berne, A., and Nenes, A., 2021: The impact of secondary ice processes on orographic mixed-phase clouds, European Aerosol Conference (EAC), Online, 30 August - 3 September 2021, (poster presentation).
10. **Georgakaki, P.**, Sotiropoulou, G., Vignon, E., Berne, A., and Nenes, A., 2021: The relative contribution of secondary ice processes in Alpine mixed-phase clouds, EGU General Assembly 2021, Online, 19–30 April 2021, (PICO presentation).
11. Motos, G., **Georgakaki, P.**, Zieger, P., Wieder, J., Lohmann, U., and Nenes, A.: In-situ observations of aerosol-cloud interactions in Ny-Ålesund, Svalbard, during fall 2019 and spring 2020, EGU General Assembly 2021, Online, 19–30 Apr 2021, https://doi.org/10.5194/egusphere-egu21-15775, 2021.
12. Karalis, M., Sotiropoulou, G., Abel, S. J., Bossioli, E., **Georgakaki, P.**, Methymaki, G., Nenes, A., and Tombrou, M.: The impact of Secondary Ice Processes on a stratocumulus-to-cumulus transition during a Cold-Air Outbreak, EGU General Assembly 2021, Online, 19–30 April 2021, EGU21-3369, https://doi.org/10.5194/egusphere-egu21-3369, 2021.
13. **Georgakaki, P.**, Sotiropoulou, G., Vignon, E., Lloyd, G., Berne, A., and Nenes, A.: The Relative Contribution of Secondary Ice Production Mechanisms in Alpine Mixed-Phase Clouds, AGU Fall Assembly Meeting, 1-17 December 2020, Online, (poster presentation).
14. **Georgakaki, P.**, Bougiatioti, A., Wieder, J., Kanji, Z. A., Ramelli, F., Henneberger, J., Mignani, C., Hervo, M., Berne, A., Lohmann, U., and Nenes, A.: Analysis of CCN number, hygroscopicity and cloud formation over the Swiss Alps, American Association for Aerosol Research, 38th Annual Conference, Online, 5-9 October 2020, (poster presentation).
15. **Georgakaki, P.**, Bougiatioti, A., and Nenes, A.: The observed impact of aerosols on cloud droplet formation during the RACLETS campaign, EGU General Assembly 2020, Online, 4–8 May 2020, EGU2020-18123, https://doi.org/10.5194/egusphereegu2020-18123, 2020, (poster presentation).
16. **Georgakaki, P.**, Papadimas, C. D., Hatzianastassiou, N., Fotiadi, A., Matsoukas, C., Stackhouse, P., Kanakidou, M., and Vardavas, I. M.: Aerosol direct effect on solar radiation over the eastern Mediterranean Sea based on AVHRR satellite measurements, EGU General Assembly 2017, 23-28 April 2017, Vienna, Austria (poster presentation).
17. **Georgakaki, P.**, Papadimas, C. D., Hatzianastassiou, N., Fotiadi, A., Matsoukas, C., Stackhouse, P., Kanakidou, M., and Vardavas, I. M.: Direct Effect of Aerosols on Solar Radiation over the Eastern Mediterranean Basin on a daily 1˚ by 1˚ Resolution, 13th International Conference of Meteorology, Climatology and Atmospheric Physics COMECAP 2016, 19-21 September 2016, Thessaloniki, Greece, https://doi.org/10.1007/978-3-319-35095-0_175, (poster presentation).

"*In order to succeed, we must first believe that we can.*"

– Nikos Kazantzakis

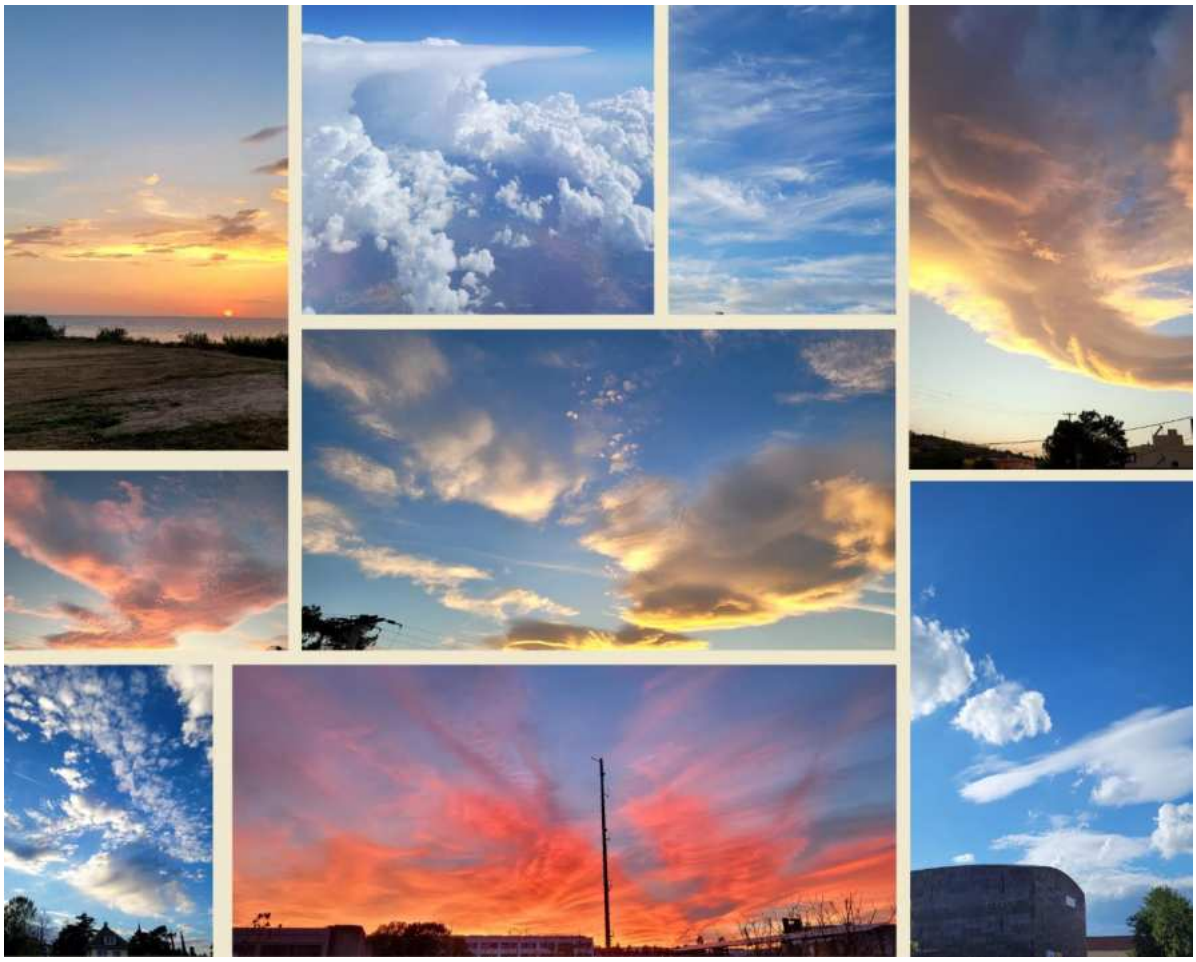

Collage capturing some of the moments when I was captivated by the cloudy sky. Photographs taken in various locations including Lausanne, Patras, Vienna, and my hometown – Rethymno.